Physics Reports 565 (2015) 1–107

Contents lists available at ScienceDirect

Physics Reports

journal homepage: www.elsevier.com/locate/physrep

The Lagrange-mesh method

Daniel Baye

Physique Quantique and Physique Nucléaire Théorique et Physique Mathématique, C.P. 229, Université Libre de Bruxelles (ULB), B-1050 Brussels, Belgium

ARTICLE INFO

Article history:
Accepted 26 November 2014
Available online 15 December 2014
editor: A. Schwenk

Keywords:
Lagrange-mesh method
Gauss quadrature
Orthogonal polynomials
Schrödinger and Dirac equations
Two-body bound states and continuum
Three-body bound states

ABSTRACT

The Lagrange-mesh method is an approximate variational method taking the form of equations on a grid thanks to the use of a Gauss-quadrature approximation. The variational basis related to this Gauss quadrature is composed of Lagrange functions which are infinitely differentiable functions vanishing at all mesh points but one. This method is quite simple to use and, more importantly, can be very accurate with small number of mesh points for a number of problems. The accuracy may however be destroyed by singularities of the potential term. This difficulty can often be overcome by a regularization of the Lagrange functions which does not affect the simplicity and accuracy of the method.

The principles of the Lagrange-mesh method are described, as well as various generalizations of the Lagrange functions and their regularization. The main existing meshes are reviewed and extensive formulas are provided which make the numerical calculations simple. They are in general based on classical orthogonal polynomials. The extensions to non-classical orthogonal polynomials and periodic functions are also presented.

Applications start with the calculations of energies, wave functions and some observables for bound states in simple solvable models which can rather easily be used as exercises by the reader. The Dirac equation is also considered. Various problems in the continuum can also simply and accurately be solved with the Lagrange-mesh technique including multichannel scattering or scattering by non-local potentials. The method can be applied to three-body systems in appropriate systems of coordinates. Simple atomic, molecular and nuclear systems are taken as examples. The applications to the time-dependent Schrödinger equation, to the Gross–Pitaevskii equation and to Hartree–Fock calculations are also discussed as well as translations and rotations on a Lagrange mesh.

Contents

E-mail address: dbaye@ulb.ac.be.

http://dx.doi.org/10.1016/j.physrep.2014.11.006
0370-1573/

1. Introduction

The continuous expansion of computing power leads to attempts for solving with numerical techniques increasingly complicated problems [1–3]. Consequently, efficient numerical approximations are needed more than ever. Ideally they should provide the highest accuracy with minimal computing efforts and maximal flexibility.

Quantum mechanics requires solutions of a variety of Schrödinger or Schrödinger-like equations. Approximations describing bound states or various types of continuum states are needed. Even for two-body problems few practical cases allow an analytical solution. Hence one is obliged to make use of approximations. A large number of variants of approximations exist. Roughly speaking, for bound states, they belong to two main families: variational techniques and numerical resolutions. For scattering states describing collisions, many more variants exist but usually with an important numerical component, specially when the Coulomb force plays a role.

An ideal numerical method would involve (i) limited or no analytical calculations, (ii) short computation times and (iii) high accuracy. Such a perfect method does of course not exist. However, under some conditions, the above criteria are met with the Lagrange-mesh method (LMM) [4–6]. The LMM is an approximate variational calculation using a special basis of functions, hereafter called Lagrange functions, related to a set of mesh points and to the Gauss quadrature associated with this mesh. It has the high accuracy of a variational approximation and the simplicity of a calculation on a mesh. Computing times depend on the duration of the search of the lowest eigenvalue(s) of a matrix that can be large in multidimensional problems, but is rather sparse.

The Lagrange functions are N infinitely differentiable functions that vanish at all points of this mesh, except one. They form an orthonormal set. Used as a variational basis in a quantum-mechanical calculation, the Lagrange functions lead to a simple algebraic system when matrix elements are computed with the associated Gauss quadrature. The variational equations take the form of mesh equations with a diagonal representation of the potential only depending on values of this potential at the mesh points [4–6]. The most striking property of the LMM is that, in spite of its simplicity, the obtained energies and wave functions can be as accurate with the Gauss-quadrature approximation as in the original variational method with an exact calculation of the matrix elements [7,6]. The accuracy of the lowest energies exceeds by far the accuracy of the Gauss quadrature for individual matrix elements.

The LMM allows very accurate calculations in simple quantum-mechanical problems. In some exceptional cases, it can even give numerically exact results with small numbers of mesh points. This occurs for the harmonic oscillator and for the hydrogen atom, both non-relativistic and relativistic. But the LMM is also very accurate though rather simple in various more complicated (and more realistic) applications in atomic [8–10] and nuclear [11–13] physics. In particular, combined with the R-matrix theory [14], it offers practical solutions to scattering problems with local or non-local potentials.

As mentioned above, this method does not always work, unfortunately. Its high accuracy depends on the validity of the Gauss quadrature. Though the expected accuracy of the LMM is much higher than the accuracy of the Gauss quadrature on individual matrix elements, it fails when the Gauss quadrature is inaccurate. The error of the Gauss quadrature involves a high derivative of the integrated function, the order of which increases with the number of mesh points [15,16]. Hence, if the Gauss quadrature is not valid somewhere, the LMM is inaccurate. This means that singularities or discontinuities of the

potential or of its derivatives may kill the accuracy. In some cases, this problem can be circumvented by a regularization technique [4–7] but, in many other cases, accurate calculations may not be possible. A simple example is given by a system with Coulomb-like singularities. These singularities can be 'regularized' for two and three particles but not – or not yet – for more particles.

The LMM is a global method, using information from the whole domain of definition of the studied problem. For well conditioned problems, i.e. when infinitely differentiable solutions exist almost everywhere, global methods provide a better accuracy than local methods using information from pieces of the domain. Among global approaches, two important and efficient approximations are the collocation and variational (or Galerkin) methods [1–3]. Nearly optimal techniques can be looked for by keeping the advantages of both approaches such as in the LMM. In the mathematical vocabulary, the LMM is a pseudospectral method, i.e. an approximate spectral method taking the form of a collocation method. Collocation methods [17] correspond to the discretization of a differential equation on a mesh but are usually not related to a variational principle. Pseudospectral methods are characterized by a fast, exponential, convergence.

The first aim of this review is to present the LMM in a way that allows using the different available meshes in practical calculations. A large number of examples, several of them easily reproducible by the reader, will illustrate the technique. These examples are taken in various types of physical applications in the context of atomic, molecular and nuclear physics. They should help showing when the Lagrange-mesh technique is applicable and how to choose the appropriate mesh in such a case. Some examples are academic but familiar to the reader. They offer simple tests of the accuracy of the LMM. Other are more realistic. They are more easily solved with the LMM than with most other techniques.

My hope is that this text can provide hints for further developments of the full LMM, i.e., involving the associated Gauss-quadrature approximation, but also for useful applications of Lagrange bases in large-scale computations. The realistic examples of the full LMM presented here could inspire ameliorations or simplifications of codes involving bases made of polynomials multiplied by some function. These bases can in general be replaced by an equivalent Lagrange basis allowing the use of the associated Gauss quadrature. This should be particularly, but not exclusively, useful for multichannel scattering problems with or without non-local terms or for iterative methods of resolution of non-linear Schrödinger-like equations. But, in addition, techniques where the Gauss quadrature is not valid could also benefit from the replacement of the basis by Lagrange functions with a partial use of the Gauss quadrature. Such a hybrid approach might in particular be interesting in atomic physics and in few-body problems where pieces of matrix elements would be simplified with a Gauss quadrature while the remaining terms would be computed with another technique.

Although the authors of Ref. [4] were not aware of this fact, the Lagrange-mesh method has a number of common points with other methods. Since the introduction of the LMM, many more works share part of its properties. To name only a few of these methods for the moment, let us mention the discrete-variable-representation method (DVR) [18,19] and the quadrature discretization method (QDM) [20,21]. Another aim of the present review is to discuss the main related methods and to explain the similarities and differences with the LMM.

This method also has a pedagogical interest. When the zeros and weights of the relevant Gauss quadrature and a diagonalization method are available, the Lagrange-mesh techniques allows very simple numerical solutions of a number of problems such as those presented in this report. Several interesting physical problems were solved with the LMM by undergraduate students within their end-of-studies research work. Codes are short and can be rather easily debugged. The method is so simple and efficient that one has to insist on its limitations to avoid an overestimation of its possibilities.

In Section 2, the principle of the LMM is explained. The notion of regularization is introduced. The extension to several dimensions is discussed. In Section 3, explicit expressions are given for the main families of Lagrange meshes based on classical and non-classical orthogonal polynomials and on periodic functions. This section contains many useful formulas about Lagrange functions and matrix elements at the Gauss-quadrature approximation. In many cases, their exact counterparts are also given, as well as explanations. Section 3 should be very useful for practitioners but can be skipped or partly skipped at first reading. In Section 4, the main methods sharing common points with the LMM are introduced in Lagrange-mesh notation and discussed. Some historical aspects are mentioned. In Section 5, simple applications to the determination of the energies and wave functions of two-body bound states are presented: the one-dimensional and three-dimensional harmonic oscillators, the non-relativistic and relativistic hydrogen atom. The hydrogen atom in a strong magnetic field illustrates the use of Lagrange meshes for several coordinates. The application of the method in momentum space is also discussed. Most of these applications can serve as simple numerical exercises. In Section 6, various calculations involving continuum wave functions are presented and compared. Practical methods to calculate phase shifts and collision matrices combine the LMM with the R-matrix technique and with the complex-scaling method. Section 7 is devoted to three-body systems. The reason for the different treatments of atomic or molecular applications on one hand and nuclear applications on the other hand are discussed. The LMM in perimetric coordinates is applied to the helium atom, the hydrogen molecular ion and the antiprotonic helium atom. The LMM in hyperspherical coordinates is applied to the helium trimer and to halo nuclei. Miscellaneous applications are presented in Section 8: the resolutions of the time-dependent Schrödinger equation and of the Gross–Pitaevskii and nuclear Hartree–Fock equations. Translations and rotations are also considered. Section 9 is devoted to conclusions and an outlook. All numerical calculations are performed in double precision.

Given the variety of discussed topics, the bibliography cannot be exhaustive. In each case, I give some key references and/or the references that were most useful to me. These references are aimed to help the reader to start a more complete bibliographic search.

2. Presentation of the Lagrange-mesh method

2.1. Gauss quadrature

In this paper, we shall meet various forms of Gauss quadrature related to different families, classical or non-classical, of orthogonal polynomials. I shall also use the denomination Gauss quadrature in a loose sense for non-polynomial cases. Let me thus start with the traditional definitions.

Let us consider an integral over an interval (a, b) and a family of polynomials $p_k(x)$ defined on this interval, which are orthogonal with respect to a weight function $w(x)$,

$$\int_a^b p_k(x)p_{k'}(x)w(x)dx = h_k\delta_{kk'}, \tag{2.1}$$

where $\sqrt{h_k}$ is the norm of $p_k(x)$ [22]. A standard Gauss quadrature with N mesh points involves the N zeros x_i of the orthogonal polynomial of degree N,

$$p_N(x_i) = 0, \tag{2.2}$$

and the N associated weights w_i [22,15,16]. The quadrature approximation reads

$$\int_a^b f(x)w(x)\,dx \approx \sum_{k=1}^{N} w_k f(x_k). \tag{2.3}$$

By definition, this quadrature gives the exact result if $f(x)$ is any polynomial of degree at most $2N-1$. Otherwise the error R_N on the quadrature is related to some value of the $2N$th-derivative of function $f(x)$ in the interval [22],

$$R_N \propto f^{(2N)}(\xi) \quad (a < \xi < b), \tag{2.4}$$

where the proportionality constant depends on N. It vanishes for polynomials of degree at most $2N-1$. It will not be small when the involved derivative does not exist at some point, i.e. in case of a discontinuity or divergence. The weights w_i can be obtained from values of $p'_N(x_i)$ and $p_{N-1}(x_i)$ (see Section 3.1.1).

The choice of Gauss quadrature depends on the interval. For example, on $(-\infty, +\infty)$, the Hermite polynomials are orthogonal with respect to the weight function $\exp(-x^2)$. The simplest Gauss quadrature on this interval is based on their properties and is called the Gauss–Hermite quadrature. Similarly, the standard Gauss quadratures on $(0, \infty)$ are the Gauss–Laguerre quadratures based on the Laguerre or generalized Laguerre polynomials. On finite intervals, the standard Gauss quadratures are Gauss–Legendre or Gauss–Jacobi, properly shifted and scaled from the $(-1, +1)$ interval. Non-standard quadratures based on other weight functions can also be defined.

In Lagrange-mesh calculations however, we shall not use (2.3) to avoid the explicit occurrence of the weight function $w(x)$ in the integral. The quadrature formula is rewritten as

$$\int_a^b g(x)\,dx \approx \sum_{k=1}^{N} \lambda_k g(x_k), \tag{2.5}$$

where the weight function is included in $g(x)$. Hence the N new weights λ_k which will be important in the following sections are given by

$$\lambda_k = w_k/w(x_k). \tag{2.6}$$

This form is valid both for classical and non-classical orthogonal polynomials. The weights λ_k are given by Eq. (3.7) and, for classical polynomials, by Eq. (3.23).

There exist families of functions $\varphi_j(x), j = 1, \ldots, N$, for which a quadrature formula similar to (2.5) is also very accurate. More precisely, the Gauss-like quadrature formula

$$\int_a^b \varphi_j^*(x)\varphi_{j'}(x)dx = \sum_{k=1}^{N} \lambda_k \varphi_j^*(x_k)\varphi_{j'}(x_k) \tag{2.7}$$

is exact for all products involving functions of this family, $j,\ j' = 1, \ldots, N$. Orthogonal polynomials are a particular case with $\varphi_j(x) = \sqrt{w(x)}p_j(x)$. Other examples will be encountered in Section 3, such as orthogonal polynomials with a change of variable, various kinds of periodic functions and the cardinal sine (sinc) functions. When Eq. (2.7) is valid, I shall also call the corresponding quadrature a Gauss quadrature, to unify the vocabulary.

In the following, for the matrix element

$$\langle f|O|g\rangle = \int_a^b f^*(x)[Og](x)dx \tag{2.8}$$

of some operator O between two functions f and g calculated at the Gauss-quadrature approximation, I shall use the notation

$$\langle f|O|g\rangle_G = \sum_{k=1}^{N} \lambda_k f^*(x_k)[Og](x_k). \tag{2.9}$$

The notation Og represents the action of O on $g(x)$. The index G will denote the use of the Gauss-quadrature approximation (when it is not exact).

2.2. Lagrange functions

For simplicity, the Lagrange functions are assumed to be real. Let us consider N abscissas x_i and weights λ_i of a Gauss quadrature over interval (a, b). A Lagrange function $f_i(x)$ over this interval (a, b) is associated with each mesh point x_i. A set of Lagrange functions is subjected to two conditions.

(i) The Lagrange functions $f_i(x)$ are infinitely differentiable functions which satisfy the Lagrange conditions

$$f_i(x_j) = \lambda_i^{-1/2}\delta_{ij}. \tag{2.10}$$

For $i = j$, the N conditions fix the normalization of $f_i(x)$.

(ii) The Gauss quadrature is exact for products of Lagrange functions,

$$\langle f_i|f_j\rangle = \int_a^b f_i(x)f_j(x)dx = \langle f_i|f_j\rangle_G. \tag{2.11}$$

This definition requires a number of comments. The common indices of the mesh points x_i and Lagrange functions $f_i(x)$ are arbitrary. One usually uses $i = 1$ to N or $i = 0$ to $N - 1$. When the mesh and the set of wave functions are symmetric, a useful numbering is $i = -(N - 1)/2$ to $(N - 1)/2$ by unit step. Index i is then integer for N odd and half-integer for N even. This notation then simplifies parity projection (see Section 2.6).

Property (i) is, except for the multiplicative factor, typical of Lagrange interpolation polynomials. This is the origin of the name 'Lagrange function' introduced in Ref. [4]. However, contrary to Lagrange polynomials which are often defined on various subintervals, the Lagrange functions are all defined on a single interval and are not necessarily polynomials, even when they are based on classical orthogonal polynomials (see Section 3). Indeed, for these polynomials, property (2.11) imposes that the Lagrange functions include the square root of the weight function $w(x)$.

Properties (i) and (ii) have an important corollary: Lagrange functions are orthonormal. Because of conditions (2.10), the Lagrange functions are orthonormal when the overlap is calculated with the Gauss quadrature,

$$\langle f_i|f_j\rangle_G = \sum_{k=1}^{N} \lambda_k \lambda_i^{-1/2}\delta_{ik}\lambda_j^{-1/2}\delta_{jk} = \delta_{ij}. \tag{2.12}$$

Hence, since the quadrature in (2.11) is exact, one can write

$$\langle f_i|f_j\rangle = \int_a^b f_i(x)f_j(x)dx = \delta_{ij}, \tag{2.13}$$

which establishes the orthonormality.

In Ref. [4], the factor $\lambda_i^{-1/2}$ was not introduced in Eq. (2.10) but a factor λ_i appeared in the right-hand side of Eq. (2.13). Functions that satisfy (2.10) without this factor are usually called cardinal functions. This earlier normalization convention soon appeared less elegant and less practical than the present one for which the orthonormality (2.13) can be used. It was abandoned in our later works [23].

In Section 2.7, a generalized type of Lagrange functions will be introduced: the regularized Lagrange functions, for which property (ii) and thus its corollary (2.13) are not true. However, property (2.12) remains valid, i.e. these functions are still orthonormal at the Gauss approximation. The result (2.12) is usually a rather poor approximation for each overlap but, surprisingly, considering the regularized Lagrange functions as if they were orthonormal will be shown to be an excellent approximation in practice. But let me delay this discussion to Sections 2.7 and 5.4.2. First I consider that property (ii) is satisfied.

I will use the wording 'Lagrange mesh' not only for the set of mesh points but for the mesh points, weights and Lagrange functions together. In this sense, two different 'Lagrange meshes' may share exactly the same mesh points but be nevertheless different. We shall see examples in Section 3.7. In many calculations, the weights and Lagrange functions do not appear explicitly. Different meshes with the same mesh points then differ by the matrix elements of the kinetic energy defined in Section 2.5.

Two main techniques can be used to construct Lagrange functions, when possible: expansions in an orthonormal basis and ratios of functions with well defined zeros. Let us first consider a set of N orthonormal basis functions $\varphi_k(x)$ ($k = 1$ to

N) verifying the conditions

$$\sum_{k=1}^{N} \varphi_k^*(x_i)\varphi_k(x_j) = \lambda_i^{-1}\delta_{ij}, \quad i, j = 1, \ldots, N, \tag{2.14}$$

at all mesh points of a Gauss quadrature. The number of Lagrange conditions (2.14) is $\frac{1}{2}N(N-1)$. They can only be satisfied in specific cases, for example when the functions $\varphi_k(x)$ are related to orthogonal polynomials. The cases $i = j$ are not conditions but fix a relation between the Gauss weights and the $\varphi_k(x)$. Eqs. (2.14) imply that the matrix with elements $\lambda_i^{1/2}\varphi_k(x_i)$ is unitary, or orthogonal when the $\varphi_k(x)$ are real. Hence the Lagrange conditions can be written equivalently

$$\sum_{i=1}^{N} \lambda_i \varphi_k^*(x_i)\varphi_l(x_i) = \delta_{kl}, \quad k, l = 1, \ldots, N. \tag{2.15}$$

This means that the Gauss quadrature is exact for all products $\varphi_k^*(x)\varphi_l(x)$ involving functions of the set.

When conditions (2.14) and (2.15) are satisfied, the Lagrange functions are defined as

$$f_i(x) = \lambda_i^{1/2} \sum_{k=1}^{N} \varphi_k^*(x_i)\varphi_k(x). \tag{2.16}$$

With (2.14), they clearly verify property (2.10). Although this is not yet obvious (see Section 3), the sum in (2.16) can usually be performed analytically so that the Lagrange functions have in general a compact expression. This is better seen with the other technique of construction.

Another way of defining Lagrange functions starts from a function $F(x)$ with N real zeros in (a, b) at the N mesh points x_i of a Gauss quadrature and a function $G(x)$ with a single zero at $x = 0$. The following ratios provide a family of N interpolation functions

$$f_i(x) = \lambda_i^{-1/2} \frac{G'(0)}{F'(x_i)} \frac{F(x)}{G(x - x_i)}. \tag{2.17}$$

These functions satisfy condition (i). They are Lagrange functions if they also satisfy condition (ii). Anyway, they are orthonormal at the Gauss approximation [Eq. (2.12)]. An important particular case of (2.17) is $G(x) = x$ or

$$f_i(x) = \frac{\lambda_i^{-1/2}}{F'(x_i)} \frac{F(x)}{x - x_i} \tag{2.18}$$

which appears in relation with classical orthogonal polynomials (Section 3.1).

For most Lagrange functions described in this text, both forms (2.16) and (2.17) are available and can be shown to be equivalent. However the compact form (2.17) reflects the real spirit of the LMM. Expression (2.16) is more in the spirit of the DVR [18] (see Section 4.2).

2.3. Lagrange-mesh equations for bound states

Let me start by recalling the variational principle. Consider a one-dimensional Schrödinger equation,

$$H\psi = E\psi \tag{2.19}$$

with the Hamiltonian

$$H = -\frac{\hbar^2}{2m}\frac{d^2\psi}{dx^2} + V(x) \tag{2.20}$$

where m is the mass of a particle with coordinate x affected by potential V or the reduced mass of two particles at distance x interacting with potential V. A variational approximation of the wave function is given by a linear combination of N linearly independent functions $\varphi_j(x)$,

$$\psi(x) = \sum_{j=1}^{N} c_j \varphi_j(x). \tag{2.21}$$

The trial function (2.21) leads to the system of variational equations

$$\sum_{j=1}^{N} \left(\frac{\hbar^2}{2m} T_{ij} + V_{ij} - E\langle\varphi_i|\varphi_j\rangle \right) c_j = 0, \quad i = 1, \ldots, N \tag{2.22}$$

where

$$T_{ij} = \langle\varphi_i|T|\varphi_j\rangle = -\int_a^b \varphi_i^*(x)\varphi_j''(x)dx \tag{2.23}$$

is a matrix element of the kinetic-energy operator $T = -d^2/dx^2$ and

$$V_{ij} = \langle\varphi_i|V|\varphi_j\rangle = \int_a^b \varphi_i^*(x)V(x)\varphi_j(x)dx. \tag{2.24}$$

When the algebraic system (2.22) is solved, each eigenvalue is an upper bound of the corresponding eigenvalue of H [24,25]. The accuracy improves when N increases. Since such an eigenvalue problem can be solved for large N values with computers, the main difficulty usually lies in the calculation of the matrix elements V_{ij}.

In the LMM, the variational approximation (2.21) of the wave function is replaced by an expansion in Lagrange functions,

$$\psi(x) = \sum_{j=1}^{N} c_j f_j(x). \tag{2.25}$$

In this basis, because of conditions (2.10), the coefficients have a simple physical interpretation,

$$c_j = \lambda_j^{1/2}\psi(x_j). \tag{2.26}$$

They provide a sampling of the approximate wave function. With a systematic use of the Gauss-quadrature approximation for the potential, the trial function (2.25) leads to the variational system of equations

$$\sum_{j=1}^{N}\left(\frac{\hbar^2}{2m}T_{ij}^{(G)} + V_{ij}^{G}\right)c_j = Ec_i \tag{2.27}$$

where the parentheses on the superscript of $T_{ij}^{(G)}$ mean that the kinetic-energy matrix element may be exact, $T_{ij} = \langle f_i| - d^2/dx^2|f_j\rangle$, or approximated as T_{ij}^{G} with the Gauss quadrature. Exact and approximate expressions of T_{ij} are discussed in Section 2.5 and given explicitly in Section 3. The crucial aspect of the LMM is that the matrix elements V_{ij}^{G} of the potential are approximated with the Gauss quadrature consistent with the mesh,

$$V_{ij} \approx V_{ij}^{G} = \sum_{k=1}^{N}\lambda_k f_i(x_k)V(x_k)f_j(x_k) = V(x_i)\delta_{ij}. \tag{2.28}$$

Hence, Eqs. (2.22) are approximated as

$$\sum_{j=1}^{N}\left(\frac{\hbar^2}{2m}T_{ij}^{(G)} + V(x_i)\delta_{ij}\right)c_j = Ec_i. \tag{2.29}$$

They have the aspect and simplicity of mesh equations but they are approximately variational and, as we shall see, they may be very accurate.

A striking feature of the linear system of equations (2.29) is that it does not seem to depend any more on global properties of the Lagrange functions $f_i(x)$ or equivalently of the basis functions $\varphi_k(x)$. With (2.35), it depends only on the mesh points x_i and on the numerical values of $T_{ij}^{(G)}$. In fact, the system (2.29) has also sometimes been obtained more or less phenomenologically without any reference to the Lagrange functions and to the variational principle. However, in that way [18,26,27], its high accuracy is more difficult to understand.

The remarkable simplification in the LMM is that in place of a potential matrix with elements (2.24) to be calculated, the potential matrix is diagonal and only requires *values* of the potential at the mesh points. This aspect is very similar to collocation methods which share the same simplicity but not necessarily the same accuracy.

In the mesh equations (2.29), the Lagrange basis is hidden: it only appears through the mesh points x_i and kinetic matrix elements T_{ij}. The Lagrange functions $f_j(x)$ and weights λ_j are only needed to evaluate the wave function $\psi(x)$ and some types of matrix elements. Contrary to finite-difference techniques, the approximate wave function $\psi(x)$ is known everywhere under the form (2.25).

The method remains valid when the Schrödinger equation contains a non-local potential term with kernel $W(x, x')$ [28]. The mesh equations take the form

$$\sum_{j=1}^{N}\left(\frac{\hbar^2}{2m}T_{ij} + V(x_i)\delta_{ij} + (\lambda_i\lambda_j)^{1/2}W(x_i, x_j)\right)c_j = Ec_i. \tag{2.30}$$

Here also, only values at mesh points of the non-local potential are needed but the potential matrix is no longer diagonal and the weights λ_i are explicitly needed. The role of the Gauss quadrature (and the difference with collocation methods) clearly appears here.

2.4. Comments

As emphasized in the Introduction, the Lagrange-mesh equations (2.29) or (2.30) can give very accurate results. These results have often an accuracy similar to that of the variational calculation (2.22) performed with the same Lagrange basis $f_j(x)$ or with the equivalent basis $\varphi_k(x)$ related by (2.16). The two calculations only differ by the use of the Gauss quadrature in the LMM. The variational accuracy of this method presenting the aspect of a mesh method and its near insensitivity to the quite simplifying use of the consistent Gauss quadrature are not fully explained yet [7].

An explanation of the high accuracy is available in particular cases where the exact wave functions are known and a related mesh is used such as the one-dimensional harmonic oscillator with the Hermite mesh (Sections 3.2, 5.2, 5.8 and 8.5), the three-dimensional harmonic oscillator with the modified Laguerre mesh (Sections 3.3.6 and 5.2) and the hydrogen atom with the regularized Laguerre mesh (Sections 3.3.4, 5.4 and 5.9) [4]. In these cases, the LMM with a proper scaling (see next subsection) can be exact for one, most or all eigenvalues. The analysis has been extended in Ref. [29] to polynomial potentials studied with a regularized Laguerre mesh. There, it is shown by using the equivalent basis $\varphi_k(x)$ that matrix elements are exact for a number of the lowest k values. The authors argue that this explains the accuracy of the lowest eigenvalues. In some particular cases, one can show that the orders of magnitudes of the variational and Gauss-quadrature errors are similar [30]. See also the discussion in Ref. [31] in the DVR context.

Anyway, a general proof explaining the accuracy of the LMM does not exist for all meshes described in Section 3. However, I now show that the Lagrange-mesh equations (2.29) can be derived as exact variational equations but for different non-local potentials $\tilde{V}_N(x, x')$ depending on the number of basis functions. This justifies to some extent the variational behaviour of the LMM. Let me define these non-local potentials as

$$\tilde{V}_N(x, x') = \sum_{k=1}^{N} V(x_k) f_k(x) f_k(x'). \tag{2.31}$$

They have the property

$$\tilde{V}_N(x_i, x_j) = \lambda_i^{-1} V(x_i) \delta_{ij}. \tag{2.32}$$

The exact matrix elements of these potentials are given by

$$\langle f_i | \tilde{V}_N | f_j \rangle = \sum_{k=1}^{N} V(x_k) \int_a^b f_i(x) f_k(x) dx \int_a^b f_k(x') f_j(x') dx' = V(x_i) \delta_{ij} \tag{2.33}$$

because of the orthonormality (2.13) of the basis. Hence the variational equations (2.22) for this potential with a basis of N Lagrange functions $f_j(x)$ are exactly given by the Lagrange-mesh equations (2.29) with the exact kinetic matrix elements T_{ij}. Even more strikingly, when the Gauss quadrature is used to calculate the matrix elements (2.33), one obtains with (2.32),

$$\langle f_i | \tilde{V}_N | f_j \rangle_G = (\lambda_i \lambda_j)^{1/2} \tilde{V}_N(x_i, x_j) = V(x_i) \delta_{ij}, \tag{2.34}$$

i.e. exactly the same result. The Lagrange-mesh equations (2.30) for potential $W(x, x') = \tilde{V}_N(x, x')$ are also exactly the variational equations for this potential.

The striking properties of potentials $\tilde{V}_N(x, x')$ and a comparison with the local potential $V(x)\delta(x - x')$ might open the way to a general proof of the high accuracy of the LMM.

2.5. Exact and approximate matrix elements

The exact kinetic-energy matrix elements T_{ij} are simple symmetric functions of x_i and x_j. Their expressions for various meshes can be found in Section 3 and in Refs. [4,5,32]. They can be approximated with a Gauss quadrature as

$$T_{ij} \approx T_{ij}^G = -\sum_{k=1}^{N} \lambda_k f_i(x_k) f_j''(x_k) = -\lambda_i^{1/2} f_j''(x_i). \tag{2.35}$$

In fact, the *exact* kinetic-energy matrix elements are sometimes given by Eq. (2.35). This is for example the case for the Legendre (Section 3.4), Fourier (Section 3.7.1) and sinc (Section 3.7.5) meshes [4].

When the Gauss approximation is used for T_{ij}, the Lagrange-mesh equations become identical to those of a collocation method,

$$\sum_{j=1}^{N} \left(-\lambda_i^{1/2} f_j''(x_i) + V(x_i) \delta_{ij} \right) c_j = E c_i. \tag{2.36}$$

If approximation (2.35) is not symmetrical, one can use, assuming here $f_j(a)f_j'(a) = f_j(b)f_j'(b) = 0$,

$$T_{ij}^{G,\mathrm{sym}} = \int_a^b f_i'(x)f_j'(x)dx \approx \sum_{k=1}^{N} \lambda_k f_i'(x_k)f_j'(x_k). \tag{2.37}$$

Matrix elements of other operators are often given with a high accuracy by the Gauss quadrature. Useful approximations are

$$\langle f_i|\frac{d}{dx}|f_j\rangle_G = \lambda_i^{1/2} f_j'(x_i) \tag{2.38}$$

(which is in fact exact in a number of cases, see Section 3) and, for an infinitely differentiable function $g(x)$,

$$\langle f_i|g(x)|f_j\rangle_G = g(x_i)\delta_{ij}. \tag{2.39}$$

The latter expression is very useful to calculate various types of radii and transition probabilities.

Some matrix elements require an exact calculation based on the explicit expression of Lagrange functions. For example, the matrix elements

$$\langle f_i|\delta(x-a)|f_j\rangle = f_i(a)f_j(a) \tag{2.40}$$

are easy to compute.

2.6. Translation, scaling, mapping, parity projection

The list of existing Lagrange functions can be extended by translating, scaling and mapping them or projecting them on parity.

Translations are elementary. They only affect the mesh points and Lagrange functions. The kinetic matrix elements remain unchanged. Translations are often combined with scaling.

For the scaling, let us start from a Gauss quadrature (2.5),

$$\int_{a'}^{b'} f(u)du \approx \sum_{k=1}^{N} \lambda_k f(u_k), \tag{2.41}$$

with zeros u_k and weights λ_k over an interval (a', b'). The change of variable

$$x = hu \tag{2.42}$$

leads to the modified quadrature

$$\int_a^b g(x)dx \approx h\sum_{k=1}^{N} \lambda_k g(hu_k) \tag{2.43}$$

over an interval $(a, b) = (ha', hb')$.

The wave function is expanded over scaled Lagrange functions as

$$\psi(x) = h^{-1/2}\sum_{j=1}^{N} c_j f_j(x/h). \tag{2.44}$$

The factor $h^{-1/2}$ keeps the unit norm. The coefficients are given by

$$c_j = (h\lambda_j)^{1/2}\psi(hu_j). \tag{2.45}$$

The scaled equations read

$$\sum_{j=1}^{N}\left(\frac{\hbar^2}{2mh^2}T_{ij} + V(hu_i)\delta_{ij}\right)c_j = Ec_i \tag{2.46}$$

where T_{ij} is expressed as a function of the zeros u_i and u_j. Scaling allows a modification of the definition interval. Intervals $(0, \infty)$ and $(-\infty, +\infty)$ are not modified. In such intervals, scaling can be used to fit the mesh-point distributions to the physical problem. To some extent, the scaling parameter h can then be used as a variational parameter: the eigenvalues are essentially independent of h over some plateau. However, because of the approximation introduced by the Gauss quadrature, this plateau is in general not a minimum and even not always a local minimum.

A monotonous mapping $u = t(x)$ is a more general transformation. It leads to a new interval $(a, b) = (t^{-1}(a'), t^{-1}(b'))$ where t^{-1} is the inverse function of t. The mesh points are transformed according to

$$\hat{x}_i = t^{-1}(u_i) \tag{2.47}$$

and the weights according to

$$\hat{\lambda}_i = \lambda_i / t'(\hat{x}_i). \tag{2.48}$$

If $w(u)$ is the weight function associated with the scalar product of the orthogonal polynomials $p_k(u)$ in Eq. (2.1), the weight function associated with the scalar product of functions $p_k[t(x)]$ reads

$$\hat{w}(x) = t'(x) w[t(x)]. \tag{2.49}$$

The Lagrange functions are now defined as

$$\hat{f}_j(x) = [t'(x)]^{1/2} f_j[t(x)]. \tag{2.50}$$

They still verify the Lagrange conditions

$$\hat{f}_j(\hat{x}_i) = [t'(\hat{x}_i)]^{1/2} f_j(u_i) = \hat{\lambda}_i^{-1/2} \delta_{ij}. \tag{2.51}$$

A simple example is presented in Section 3.3.6. The simplest cases are the scaling $u = x/h$ described above and linear changes of variable aimed at moving and scaling an interval.

Parity projection is useful to derive new Lagrange meshes on half the interval or to simplify the problem when the potential is even [5]. Here I assume that the interval, mesh and Lagrange functions are symmetric around $x = 0$ and index j takes N values from $-(N-1)/2$ to $(N-1)/2$. Then one can construct Lagrange functions of parity $p = \pm 1$ over the positive half interval. For $N = 2M$ even, they are defined for $x \geq 0$ and $j = 1/2$ to $M - 1/2$ as

$$f_j^p(x) = 2^{-1/2}[f_j(x) + p f_{-j}(x)]. \tag{2.52}$$

After projection, the dummy index j can be modified to run from 1 to M for simplicity, or left unchanged. For $N = 2M + 1$ odd, definition (2.52) is still valid for $j = 1$ to M. But in addition, for positive parity, the function

$$f_0^+(x) = f_0(x) \tag{2.53}$$

corresponding to $x_0 = 0$ must be included.

The projected Lagrange functions are orthonormal,

$$\langle f_j^p | f_{j'}^{p'} \rangle = \delta_{jj'} \delta_{pp'}. \tag{2.54}$$

For N even, the kinetic matrix elements are simply given by

$$T_{ij}^p = T_{ij} + p T_{i,-j}. \tag{2.55}$$

For N odd and $p = +1$, one needs the additional elements

$$T_{0j}^+ = 2^{-1/2}(T_{0j} + T_{0,-j}), \quad T_{00}^+ = T_{00}. \tag{2.56}$$

The mesh equations (2.46) still keep the simple form

$$\sum_{j=1}^{M} \left(\frac{\hbar^2}{2mh^2} T_{ij}^p + V(hu_i)\delta_{ij} \right) c_j = E c_i \tag{2.57}$$

for $i = 1, \ldots, M$ where $M = N/2$ for N even and $M = (N+p)/2$ for N odd.

Examples of construction of new meshes by parity projection are given in Sections 3.7 and 3.6.4. Examples of exploitation of symmetries can be found in Section 8.

2.7. Regularization of a singularity

The Lagrange-mesh technique is often very accurate. It is much more accurate than the corresponding Gauss approximation on individual matrix elements [7]. However, singularities destroy the accuracy of the Gauss quadrature and hence the interest of the LMM. Singularities naturally occur in a number of potentials. Well-known examples are the $1/r$ singularity of the Coulomb potential and the $1/r^2$ singularity of the centrifugal term at the origin in spherical coordinates.

This problem can sometimes be solved with a regularization technique [5,7]. In its original version [5], the regularization was introduced as a modification of the operator. It is however simpler to consider a modification of the basis functions. Let $f_j(x)$ be a set of N Lagrange functions as defined in Section 2.2. Regularized functions are defined as

$$\hat{f}_j(x) = \frac{R(x)}{R(x_j)} f_j(x) \tag{2.58}$$

where $R(x)$ is a regularization function usually aimed at eliminating some unwanted inaccuracy of the Gauss quadrature in the matrix elements of the potential (or of the kinetic-energy operator when it is more complicated than $-d^2/dx^2$). The regularized functions still verify the Lagrange conditions (2.10) at the Gauss-quadrature mesh points

$$\hat{f}_j(x_i) = \lambda_i^{-1/2}\delta_{ij}. \tag{2.59}$$

However, if the functions f_j are exactly orthogonal, this is in general not the case any more for the regularized functions $\hat{f}_j$.

To date, the regularization has only been used for Lagrange functions based on classical orthogonal polynomials with $R(x)$ a power of a polynomial (Sections 3.3–3.5). Whether more general cases can be interesting is still an open question.

The principle is illustrated here for a singularity at $x = 0$. Regularized Lagrange functions can be defined as

$$\hat{f}_j(x) = \left(\frac{x}{x_j}\right)^n f_j(x), \tag{2.60}$$

for various integer of half-integer values of n. The Lagrange conditions (2.10) are still verified over the same mesh. However, although these functions are orthogonal at the Gauss approximation, the orthogonality is not any more exact for $n > 1/2$ [11,32]. An advantage is that the Gauss quadrature is now exact or accurate for potentials containing $1/x$ ($n \geq 1/2$) or $1/x^2$ ($n \geq 1$) singularities.

The Gauss approximation $\hat{T}_{ij}^G$ for the kinetic-energy matrix elements can be obtained from

$$\lambda_i^{1/2}\hat{f}_j''(x_i) = \frac{1}{R(x_j)}\left[R(x_i)\lambda_i^{1/2}f_j''(x_i) + 2R'(x_i)\lambda_i^{1/2}f_j'(x_i) + R''(x_i)\delta_{ij}\right]. \tag{2.61}$$

When this approximation is not symmetrical, it is preferable to use

$$\hat{T}_{ij}^G = -\left[\hat{f}_i\hat{f}_j'\right]_a^b + \sum_{k=1}^{N}\lambda_k\hat{f}_i'(x_k)\hat{f}_j'(x_k). \tag{2.62}$$

In practical applications, the algebraic system (2.46) is still often used, as if the Lagrange basis was exactly orthogonal. This might seem a rather rough approximation but numerical studies indicate that ignoring the non-orthogonality does not introduce any significant loss of accuracy. Indeed a calculation with an exact treatment of the overlap is in general possible, but more complicated since it leads to a generalized eigenvalue problem. Strikingly, such a complication does not introduce any improvement of accuracy, in general. Let us try to understand why taking the exact overlap into account is not necessary.

As we shall see in Section 3, for classical orthogonal polynomials, the exact overlap between Lagrange functions regularized with a polynomial factor can be written under the form

$$\langle\hat{f}_i|\hat{f}_j\rangle = \delta_{ij} + \sum_m (v_{mi}w_{mj} + w_{mi}v_{mj}) \tag{2.63}$$

where the sum runs over few values and v_{mi} and w_{mj} are the respective components of vectors $\boldsymbol{v}_m$ and $\boldsymbol{w}_m$ which only depend on the mesh points x_i. To simplify the discussion, let me discuss the importance of neglecting the sum in Eq. (2.63) and thus treating the basis as orthonormal in a frequent particular case, i.e. the regularization (2.60) with $n = 1$. In this case, the sum reduces to a single term. An example with several m values can be found in Section 3.4.7 [Eq. (3.139)] and is useful in Section 5.5.

For simplicity, let me thus assume that the sum in (2.63) contains a single, separable, term, i.e.

$$\langle\hat{f}_i|\hat{f}_j\rangle = \delta_{ij} + v_iv_j. \tag{2.64}$$

The mesh equations can be written in matrix form as

$$\boldsymbol{H}^G\boldsymbol{c} = E\boldsymbol{c} \tag{2.65}$$

where $\boldsymbol{H}^G$ is the Hamiltonian matrix with the potential calculated with the Gauss-quadrature approximation like in (2.46) and $\boldsymbol{c} = (c_1, c_2, \ldots, c_N)^T$ is a vector containing the coefficients c_j of expansion (2.44). The exact Lagrange-mesh equations with the regularized basis $\hat{f}_j$ can be written as

$$\boldsymbol{H}^G\tilde{\boldsymbol{c}} = \tilde{E}(\boldsymbol{I} + \boldsymbol{v}\boldsymbol{v}^T)\tilde{\boldsymbol{c}} \tag{2.66}$$

where $\boldsymbol{I}$ is the $N \times N$ unit matrix, $\boldsymbol{v} = (v_1, v_2, \ldots, v_N)^T$ is a vector with components v_i and $\tilde{\boldsymbol{c}}$ is a vector solution of (2.66).

Numerical experiments show that the eigenvalues E and $\tilde{E}$ are very close to each other. In order to understand the origin of this closeness, one can start from Eq. (2.65) and treat the additional term in Eq. (2.66) as a perturbation. One obtains at first order

$$\tilde{E} = E - \tilde{E}(\boldsymbol{v}^T\boldsymbol{c})^2 \approx E[1 - (\boldsymbol{v}^T\boldsymbol{c})^2]. \tag{2.67}$$

The closeness of the results implies that the scalar product $\boldsymbol{v}^T\boldsymbol{c}$ is small,

$$|\boldsymbol{v}^T\boldsymbol{c}| \ll 1. \tag{2.68}$$

This is not at all obvious since $\boldsymbol{c}$ results from an approximate variational calculation and $\boldsymbol{v}$ is a fixed vector depending on the mesh choice. Numerical experiments confirm the smallness of this scalar product (see Section 5.3). A proof of this property is given in Appendix A for Lagrange functions based on classical orthogonal polynomials, regularized by x/x_i. This proof is based on properties given in Section 3 and on the accuracy of the Gauss quadrature. I conjecture that similar proofs exist for other types of regularization. In the case of the hydrogen atom, one can show analytically that $\boldsymbol{v}^T\boldsymbol{c}$ vanishes identically (see Section 5.4.2).

Property (2.68) also shows that the scalar product of two approximate wave functions ψ_k and ψ_l obtained from Eq. (2.65) can be accurately given by the Gauss quadrature in spite of the non-orthogonality of the basis. Indeed, the exact scalar product is given by Eq. (2.64) as

$$\begin{aligned}\langle\psi_k|\psi_l\rangle &= \boldsymbol{c}_k^T\boldsymbol{c}_l + (\boldsymbol{c}_k^T\boldsymbol{v})(\boldsymbol{v}^T\boldsymbol{c}_l)\\ &\approx \boldsymbol{c}_k^T\boldsymbol{c}_l = \delta_{kl}\end{aligned} \tag{2.69}$$

since the eigenvectors of matrix $\boldsymbol{H}^G$ are orthonormal.

Finally, one observes that Eq. (2.66) can be recast into a standard eigenvalue problem. By factorizing the matrix in the right-hand side as

$$\boldsymbol{I} + \boldsymbol{v}\boldsymbol{v}^T = [(\boldsymbol{I} - \gamma\boldsymbol{v}\boldsymbol{v}^T)^{-1}]^2 \tag{2.70}$$

where

$$\gamma = \frac{1}{v^2}\left(1 \pm \frac{1}{\sqrt{1+v^2}}\right) \tag{2.71}$$

with the squared norm v^2 of $\boldsymbol{v}$, Eq. (2.66) can be rewritten as

$$\left[\boldsymbol{H}^G - \gamma(\boldsymbol{H}^G\boldsymbol{v}\boldsymbol{v}^T + \boldsymbol{v}\boldsymbol{v}^T\boldsymbol{H}^G) + \gamma^2\boldsymbol{v}\boldsymbol{v}^T\boldsymbol{H}^G\boldsymbol{v}\boldsymbol{v}^T\right]\tilde{\boldsymbol{c}} = \tilde{E}\tilde{\boldsymbol{c}}. \tag{2.72}$$

This is valid for both signs in the definition of γ. Here also, one observes that $E \approx \tilde{E}$ if $|\boldsymbol{v}^T\tilde{\boldsymbol{c}}| \ll 1$.

A similar discussion applies to the accuracy of the replacement of the exact kinetic-energy matrix element T_{ij} by its expression T_{ij}^G calculated at the Gauss-quadrature approximation. In the Lagrange-mesh practice, this replacement does in general not cost a loss of accuracy (in fact, it can lead to a slight improvement, see Section 5.2). For Lagrange meshes based on orthogonal polynomials, the expressions of T_{ij} and T_{ij}^G differ like in (2.63),

$$T_{ij} = T_{ij}^G + \sum_m (v'_{mi}w'_{mj} + w'_{mi}v'_{mj}) \tag{2.73}$$

where the vectors $\boldsymbol{v}'_m$ and $\boldsymbol{w}'_m$ may present similarities with those appearing in the overlap $\langle\hat{f}_i|\hat{f}_j\rangle$ (see Section 3).

2.8. Multidimensional Lagrange meshes

The simplest way to treat multidimensional calculations is by constructing Lagrange functions as tensor products of one-dimensional Lagrange functions [23,33]. For example, in Cartesian coordinates, three-dimensional (3D) Lagrange functions can be written as

$$F_{ijk}(x,y,z) = (h_xh_yh_z)^{-1/2}f_i(x/h_x)g_j(y/h_y)h_k(z/h_z), \tag{2.74}$$

where f_i, g_j, h_k can be any of the examples discussed in Section 3, N_x, N_y, N_z are the respective sizes of the one-dimensional bases and h_x, h_y, h_z are the respective scaling factors. The mesh associated with F_{ijk} is

$$(h_xu_i,\, h_yv_j,\, h_zw_k) \tag{2.75}$$

where u_i, v_j, w_k are the mesh points associated with the Lagrange functions $f_i(u)$, $g_j(v)$, $h_k(w)$, respectively. The Lagrange conditions are satisfied,

$$F_{ijk}(h_xu_{i'}, h_yv_{j'}, h_zw_{k'}) = (h_xh_yh_z\lambda_i\mu_j\nu_k)^{-1/2}\delta_{ii'}\delta_{jj'}\delta_{kk'}, \tag{2.76}$$

where λ_i, μ_j, ν_k are the corresponding weights.

The wave function is then approximated as

$$\psi(x,y,z) = \sum_{i=1}^{N_x}\sum_{j=1}^{N_y}\sum_{k=1}^{N_z} c_{ijk}F_{ijk}(x,y,z). \tag{2.77}$$

With the Lagrange property (2.76), the values of the approximate wave function at mesh points are

$$\psi(h_x u_i, h_y v_j, h_z w_k) = (h_x h_y h_z \lambda_i \mu_j \nu_k)^{-1/2} c_{ijk} \tag{2.78}$$

and provide a simple physical interpretation of the coefficients c_{ijk}.

The matrix elements of Hamiltonian

$$H = -\frac{\hbar^2}{2m}\Delta + V(x,y,z) \tag{2.79}$$

are given by [23,33]

$$H_{ijk,i'j'k'} = \frac{\hbar^2}{2m}\left(h_x^{-2} T_{ii'}\delta_{jj'}\delta_{kk'} + h_y^{-2}\delta_{ii'}T_{jj'}\delta_{kk'} + h_z^{-2}\delta_{ii'}\delta_{jj'}T_{kk'}\right) + V(h_x u_i, h_y v_j, h_z w_k)\delta_{ii'}\delta_{jj'}\delta_{kk'}, \tag{2.80}$$

where $T_{ii'}$, $T_{jj'}$, and $T_{kk'}$ are given by the Gauss approximation (2.35) or by the corresponding exact matrix elements. The matrix representing the potential is diagonal.

The advantage of the method is that the 3D kinetic-energy matrix is sparse as it represents only one-body operators. Since the 3D potential matrix is diagonal, the resulting Hamiltonian matrix is also sparse.

If the potential is even in some direction, say with respect to x, expressions (2.74) and (2.80) remain valid with the replacements $f_i(x) \to f_i^{p_x}(x)$ [Eq. (2.52)] and $T_{ii'} \to T_{ii'}^{p_x}$ [Eq. (2.55)]. This allows a significant reduction of the size of the matrix. Another reduction occurs if two particles are identical (see Section 7.2).

Other types of multidimensional Lagrange functions can be established by using tensor products in other coordinate systems [23,8,31] (see Sections 5.6 and 7.2). However, a Lagrange mesh and basis in spherical angular coordinates (θ, φ) is still lacking. Approximate Lagrange meshes on the sphere are developed and used in Refs. [5,34,35].

2.9. Mean values and transition matrix elements

With the Gauss quadrature (2.5), one can easily calculate mean values of a number of operators. Let me start with the one-dimensional case. For the frequently encountered scaled wave function (2.44) corresponding to energy E, the mean value $\langle T\rangle = \langle\psi|T|\psi\rangle$ of the kinetic-energy operator $T = -d^2/dx^2$ is given at the Gauss approximation by

$$\langle T\rangle_G = \frac{1}{h^2}\sum_{i,j=1}^{N} c_i T_{ij}^G c_j \tag{2.81}$$

where the value of T_{ij}^G of the kinetic-energy matrix element should be identical to the value used for the calculation of the coefficients c_i. For a local potential as well as for any function $V(x)$ of the coordinate, the mean value is simply

$$\langle V\rangle_G = \sum_{j=1}^{N} c_j^2 V(hu_j). \tag{2.82}$$

The approximation of the mean value of a non-local potential $W(x,x')$ reads

$$\langle W\rangle_G = \int_a^b dx \int_a^b dx' \psi(x) W(x,x')\psi(x') \approx h\sum_{i,j=1}^{N} (\lambda_i\lambda_j)^{1/2} c_i W(hu_i, hu_j) c_j. \tag{2.83}$$

Let us note that the Gauss approximation of the mean value of the Hamiltonian is exactly equal (up to rounding errors) to the Lagrange-mesh energy E,

$$\langle H\rangle_G = \sum_{i,j=1}^{N} c_i \left[\frac{\hbar^2}{2mh^2}T_{ij}^{(G)} + V(hu_i)\delta_{ij}\right] c_j = E, \tag{2.84}$$

since vector $\boldsymbol{c}$ is an exact eigenvector of the Hamiltonian matrix. This equality may sometimes be lost when the Lagrange basis is regularized and thus not exactly orthogonal.

Transition matrix elements involving a local operator $O(x)$ between an initial state $\psi_i(x)$ and a final state $\psi_f(x)$ are given by

$$\langle\psi_f|O(x)|\psi_i\rangle_G = \sum_{j=1}^{N} c_j^{(f)} O(hu_j) c_j^{(i)}. \tag{2.85}$$

Expressions can also easily be established for operators involving derivatives.

These expressions can be generalized to three dimensions. Matrix elements of observables which do not include derivatives are very simply evaluated with the Gauss quadrature, since (2.74) and (2.76) lead to

$$\langle F_{i'j'k'}|O(x,y,z)|F_{ijk}\rangle \approx O(h_x u_i, h_y v_j, h_z w_k)\delta_{ii'}\delta_{jj'}\delta_{kk'}. \tag{2.86}$$

These properties are or can be useful in many applications such as the resolution of the Gross–Pitaevskii equation [36] (Section 8.3), nuclear Hartree–Fock calculations [37] (Section 8.4), and density functional theory [38,39]. For example, the 3D extensions of (2.82) and (2.85) are with (2.77)

$$\langle\psi|V(x,y,z)|\psi\rangle_G = \sum_{i=1}^{N_x}\sum_{j=1}^{N_y}\sum_{k=1}^{N_z} c_{ijk}^2 V(h_x u_i, h_y v_j, h_z w_k) \tag{2.87}$$

and

$$\langle\psi^{(f)}|O(x,y,z)|\psi^{(i)}\rangle_G = \sum_{i=1}^{N_x}\sum_{j=1}^{N_y}\sum_{k=1}^{N_z} c_{ijk}^{(f)} O(h_x u_i, h_y v_j, h_z w_k) c_{ijk}^{(i)}, \tag{2.88}$$

respectively.

3. Explicit expressions for various Lagrange meshes

At first reading, this section may be skipped or restricted to Sections 3.2, 3.8 and 3.7.5.

3.1. Lagrange meshes from orthogonal polynomials

3.1.1. Summary of properties of orthogonal polynomials

Notations and most properties described below are taken from Ref. [22]. Proofs can be found in Refs. [15,16]. Polynomials $p_N(x)$ orthogonal on interval (a, b) with weight function $w(x)$ verify

$$\int_a^b w(x)p_N(x)p_{N'}(x)dx = h_N\delta_{NN'} \tag{3.1}$$

where N is the degree of $p_N(x)$ and h_N is the square of its norm. The coefficients of the highest powers of x are denoted according to

$$p_N(x) = k_N x^N + k'_N x^{N-1} + \cdots \tag{3.2}$$

An important property of orthogonal polynomials is that they satisfy the three-term recurrence relation

$$\frac{k_N}{k_{N+1}}\,p_{N+1}(x) = \left(x - \frac{k'_N}{k_N} + \frac{k'_{N+1}}{k_{N+1}}\right)p_N(x) - \frac{k_{N-1}h_N}{k_N h_{N-1}}\,p_{N-1}(x). \tag{3.3}$$

They verify the Christoffel–Darboux relation

$$\sum_{m=0}^{N-1}\frac{p_m(x)p_m(y)}{h_m} = \frac{k_{N-1}}{h_{N-1}k_N}\,\frac{p_N(x)p_{N-1}(y) - p_{N-1}(x)p_N(y)}{x-y} \tag{3.4}$$

with the limit when $y \to x$,

$$\sum_{m=0}^{N-1}\frac{p_m(x)^2}{h_m} = \frac{k_{N-1}}{h_{N-1}k_N}\left[p'_N(x)p_{N-1}(x) - p'_{N-1}(x)p_N(x)\right]. \tag{3.5}$$

3.1.2. Lagrange functions

Let x_i, $i = 1, \ldots, N$ be the zeros of the orthogonal polynomial p_N,

$$p_N(x_i) = 0. \tag{3.6}$$

These zeros are all real and distinct. They define a Gauss quadrature with the weights

$$\lambda_i = \frac{k_N h_{N-1} p'_N(x_i)}{k_{N-1}w(x_i)p_{N-1}(x_i)}. \tag{3.7}$$

The corresponding Lagrange functions are defined from (2.18) as

$$f_j(x) = \lambda_j^{-1/2} \left(\frac{w(x)}{w(x_j)} \right)^{1/2} \frac{p_N(x)}{p'_N(x_j)(x - x_j)}. \tag{3.8}$$

A Taylor expansion of $p_N(x)$ around $x = x_j$ shows that they satisfy property (i) [Eq. (2.10)] of the definition of a Lagrange function. Since polynomial $p_N(x)$ is divided by one of its factors, the Lagrange function is a polynomial of degree $N - 1$ multiplied by the square root of its weight function. Hence the Gauss quadrature is exact for products of Lagrange functions and property (ii) [Eq. (2.11)] is also satisfied. The Lagrange functions satisfy for $n < N$ the sum rules

$$\sum_{j=1}^{N} \sqrt{\lambda_j w(x_j)}\, x_j^n f_j(x) = \sqrt{w(x)}\, x^n \tag{3.9}$$

since (2.25) and (2.26) are exact for polynomials of degree smaller than N.

Expression (3.8) can also be obtained from Eq. (2.16) with the orthonormal set of basis functions [4]

$$\varphi_k(x) = h_k^{-1/2} \sqrt{w(x)} p_k(x). \tag{3.10}$$

Indeed, introducing the Christoffel–Darboux relation (3.4) into the variant (2.16) of the expression of Lagrange functions and taking account of (3.6) also leads to (3.8).

Gauss approximations of matrix elements of the kinetic-energy operator can then be obtained from derivatives of (3.8), as in Eq. (2.35). Using a Taylor expansion of $p_N(x)$, the calculation is easy for $i \neq j$ and a little more involved for $i = j$. Whether these (in principle approximate) expressions are in fact exact depends on the properties of the derivatives of the weight function $w(x)$, as we shall see in the next subsections.

3.1.3. Exact matrix elements

The matrix elements of x are exactly given by the Gauss quadrature as

$$\langle f_i | x | f_j \rangle = x_i \delta_{ij} \tag{3.11}$$

since $x f_i(x) f_j(x)$ is a polynomial of degree $2N - 1$ times the weight function [15]. The exact matrix elements of x^2 are obtained by writing

$$x^2 = (x - x_i)(x - x_j) + (x_i + x_j)x - x_i x_j. \tag{3.12}$$

The matrix elements of the first term can be obtained from the squared norm h_N. The other ones are exactly given by the Gauss quadrature and lead to the first term of the equation below. With the expression (3.7) of the weights, one derives

$$\langle f_i | x^2 | f_j \rangle = x_i^2 \delta_{ij} + (-1)^{i-j} \frac{k_{N-1} h_N}{k_N h_{N-1}} \sqrt{\frac{p_{N-1}(x_i) p_{N-1}(x_j)}{p'_N(x_i) p'_N(x_j)}}. \tag{3.13}$$

The phase involves $i - j$ which is an integer even if i and j are half integers. When i and j are integers, the phase can be written $(-1)^{i+j}$ as well. This expression provides the overlap of Lagrange functions regularized by a factor x. Matrix elements of higher powers of x can also be exactly calculated with expansions similar to (3.12).

Simple exact expressions for the matrix elements of d/dx can also be derived. Since a Lagrange function is the product of the square root of the wave function by a polynomial of degree $N - 1$, one easily derives

$$D_{ij} = \langle f_i | \frac{d}{dx} | f_j \rangle \tag{3.14}$$

$$= \frac{1}{2} \left[\langle f_i | \frac{w'}{w} | f_j \rangle - \frac{w'(x_i)}{w(x_i)} \delta_{ij} \right] + \lambda_i^{1/2} f_j'(x_i). \tag{3.15}$$

The last term is the Gauss-quadrature approximation. The terms in the square bracket show that this approximation is exact if the Gauss quadrature is exact for w'/w. This is the case for the Legendre (Section 3.4 with $m = 0$), Laguerre (Section 3.3 with $\alpha = 0$) and, because of (3.11), Hermite (Section 3.2) classical polynomials. With Eq. (10) of Ref. [40], one obtains

$$D_{ij} = \frac{1}{2} \left[\lambda_i^{1/2} f_j'(x_i) - \lambda_j^{1/2} f_i'(x_j) + f_i(b) f_j(b) - f_i(a) f_j(a) \right]. \tag{3.16}$$

This simple result can also be obtained by integrating by parts half the integral and by noting that $f_i f_j' - f_i' f_j$ is the product of the weight w by a polynomial of degree $2N - 4$. When the last two terms of (3.16) vanish or cancel each other, the matrix element is antisymmetric: $D_{ij} = -D_{ji}$, $D_{ii} = 0$.

3.1.4. Classical orthogonal polynomials

Of special importance are the so-called *classical* orthogonal polynomials. Their weight function satisfies the simple differential equation [16]

$$[\sigma(x)w(x)]' = \tau(x)w(x) \tag{3.17}$$

where $\tau(x)$ is a polynomial of first degree and $\sigma(x)$ is given by

$$\sigma(x) = \begin{cases} (x-a)(b-x) & \text{for } a, b \text{ finite,} \\ x-a & \text{for } a \text{ finite, } b=\infty, \\ 1 & \text{for } a=-\infty, b=\infty. \end{cases} \tag{3.18}$$

The polynomials then verify the second-order differential equation

$$\sigma(x)p_N''(x) + \tau(x)p_N'(x) + Nd_N p_N(x) = 0 \tag{3.19}$$

where the constant d_N is defined by

$$d_N = -\tau' - \frac{1}{2}(N-1)\sigma''. \tag{3.20}$$

The Rodrigues formula [15,16] reads

$$p_N(x) = \frac{(-1)^N k_N}{\prod_{k=0}^{N-1} d_{N+k}} \frac{1}{w(x)} \frac{d^N}{dx^N}[\sigma(x)^N w(x)]. \tag{3.21}$$

From this formula, one derives

$$\sigma(x)p_N'(x) = \left[N\sigma'(0) - \frac{k_N'\sigma''}{2k_N} + \frac{N\sigma''}{2}x\right]p_N(x) + \frac{k_{N-1}}{k_N}\frac{h_N}{h_{N-1}}d_{2N}p_{N-1}(x). \tag{3.22}$$

For classical orthogonal polynomials, expression (3.7) of the weights can be rewritten with (3.22) and (3.6) as

$$\lambda_i = \frac{d_{2N}h_N}{\sigma(x_i)w(x_i)[p_N'(x_i)]^2} = \left(\frac{k_N h_{N-1}}{k_{N-1}}\right)^2 \frac{\sigma(x_i)}{d_{2N}h_N w(x_i)[p_{N-1}(x_i)]^2}. \tag{3.23}$$

Expression (3.8) of the Lagrange functions can be simplified as

$$f_j(x) = (-1)^{j-j_0}\left[\frac{\sigma(x_j)}{d_{2N}}\right]^{1/2}\frac{\varphi_N(x)}{x-x_j} \tag{3.24}$$

where $\varphi_N(x)$ is given by Eq. (3.10) and j_0 is chosen such that all $f_j(x_j)$ are positive. Eq. (3.13) becomes

$$\langle f_i|x^2|f_j\rangle = x_i^2\delta_{ij} + (-1)^{i-j}\sqrt{\sigma(x_i)\sigma(x_j)}/d_{2N}. \tag{3.25}$$

3.2. Lagrange–Hermite mesh

The Lagrange–Hermite mesh is based on the classical Hermite polynomials [4]. It can be useful for solving one-dimensional Schrödinger equations (Section 5.2), time-dependent Schrödinger equations (Section 8.1) and 3D problems in cartesian coordinates (Section 8.3).

The Hermite polynomials [22] are defined over $(-\infty, +\infty)$ with the weight function

$$w(x) = e^{-x^2}. \tag{3.26}$$

This weight function is a particular solution of (3.17) corresponding to

$$\sigma(x) = 1, \qquad \tau(x) = -2x, \qquad d_N = 2. \tag{3.27}$$

Hence the differential equation (3.19) becomes

$$H_N'' - 2xH_N' + 2NH_N = 0. \tag{3.28}$$

The squared norm of $H_N(x)$ is given by

$$h_N = \sqrt{\pi}\,2^N N! \tag{3.29}$$

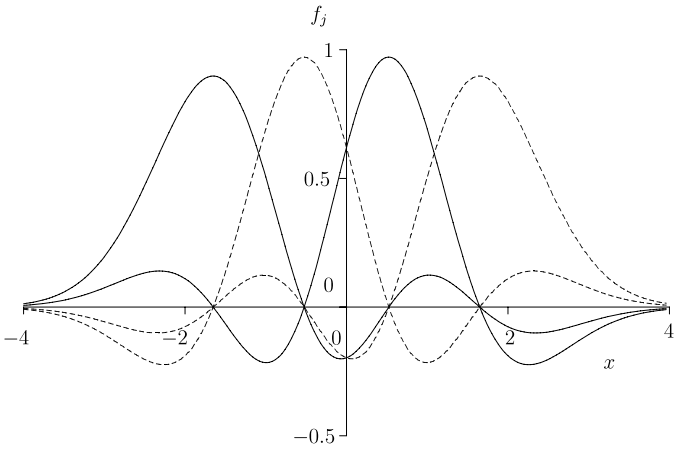

Fig. 1. Lagrange–Hermite functions (3.35) for $N = 4$.

and the first coefficients of the explicit expression (3.2) by

$$k_N = 2^N, \quad k'_N = 0. \tag{3.30}$$

The recurrence relation (3.3) reads

$$H_{N+1} = 2xH_N - 2NH_{N-1} \tag{3.31}$$

and the derivative (3.22) is given by

$$H'_N = 2NH_{N-1}. \tag{3.32}$$

Because of the symmetry of the mesh and of the weight function, it is convenient to use the increasing integer or half-integer indices $i = -(N-1)/2, \ldots, (N-1)/2$ for the mesh points defined by

$$H_N(x_i) = 0. \tag{3.33}$$

The numerical values of the mesh points can be calculated with many program libraries or as explained in Section 3.6.1. The corresponding Gauss-quadrature weights (3.23) read

$$\lambda_i = \frac{2h_N e^{x_i^2}}{[H'_N(x_i)]^2} = \frac{h_{N-1} e^{x_i^2}}{N[H_{N-1}(x_i)]^2}. \tag{3.34}$$

The Lagrange–Hermite functions are defined from (3.8) or (3.24) as [4]

$$f_j(x) = (-1)^{N-j}(2h_N)^{-1/2} \frac{H_N(x)}{x - x_j} e^{-x^2/2}. \tag{3.35}$$

The phase factor in Eq. (3.35) is needed to obtain positive coefficients in the right-hand side of the Lagrange condition (2.10). These functions verify the differential equation

$$f_j'' + (2N + 1 - x^2) f_j + \frac{2f_j'}{x - x_j} = 0. \tag{3.36}$$

This equation can be useful to express the second derivative f_j'' as a function of f_j and f_j', for example in the calculation of the kinetic-energy matrix elements. The Lagrange–Hermite functions are depicted for $N = 4$ in Fig. 1. One observes that three of them vanish at each mesh point. The one that does not vanish is associated with the mesh point.

According to Eq. (3.15) or Eq. (3.16), the matrix elements of $D_{ij} = \langle f_i | d/dx | f_j \rangle$ are exactly given by the first derivatives at mesh points as

$$D_{i \neq j} = D^G_{i \neq j} = \lambda_i^{1/2} f_j'(x_i) = (-1)^{i-j} \frac{1}{x_i - x_j} \tag{3.37}$$

and

$$D_{ii} = D^G_{ii} = \lambda_i^{1/2} f_i'(x_i) = 0. \tag{3.38}$$

As expected, they are antisymmetric. From (3.25) and (3.27), the exact matrix elements of x^2 read [4]

$$\langle f_i|x^2|f_j\rangle = x_i^2\delta_{ij} + (-1)^{i-j}\frac{1}{2}. \tag{3.39}$$

At the Gauss-quadrature approximation, the kinetic-energy matrix elements of $-d^2/dx^2$ are given by Eqs. (2.35) and (3.36)–(3.38) as

$$T^G_{i\neq j} = (-1)^{i-j}\frac{2}{(x_i-x_j)^2} \tag{3.40}$$

and

$$T^G_{ii} = \frac{1}{3}(2N+1-x_i^2). \tag{3.41}$$

They are not exact since $-f_if_j''$ contains a polynomial of degree $2N$. The exact matrix elements can be obtained by separating the term $(-1)^{i-j+1}(2h_N)^{-1}[H_N(x)]^2\exp(-x^2)$ of degree $2N$, calculating its integral with (3.29) and using the exact Gauss quadrature for the rest, i.e. [4],

$$T_{ij} = T^G_{ij} - (-1)^{i-j}\frac{1}{2}. \tag{3.42}$$

The role of the difference between the exact and approximate expressions is discussed in Section 5.2.

3.3. Lagrange–Laguerre meshes

3.3.1. Generalized Laguerre polynomials

Various Lagrange meshes and bases are based on Laguerre polynomials [4]. Because of their definition interval $(0, +\infty)$, they are particularly useful for representing the radial coordinate of a bound-state problem on a mesh (Section 5, see also Section 6.6). They are also useful in relation with the perimetric coordinates (Section 7.2).

The Laguerre polynomials [22] are defined over $(0, +\infty)$ with the weight function

$$w(x) = x^\alpha e^{-x} \tag{3.43}$$

where $\alpha > -1/2$. This function corresponds to

$$\sigma(x) = x, \qquad \tau(x) = \alpha + 1 - x, \qquad d_N = 1. \tag{3.44}$$

The differential equation (3.19) becomes

$$xL_N^{\alpha\prime\prime} + (\alpha+1-x)L_N^{\alpha\prime} + NL_N^\alpha = 0. \tag{3.45}$$

The squared norm is given by

$$h_N^\alpha = \frac{\Gamma(N+\alpha+1)}{N!} \tag{3.46}$$

and the first coefficients by

$$k_N = \frac{(-1)^N}{N!}, \qquad k'_N = \frac{(-1)^{N-1}}{(N-1)!}(N+\alpha). \tag{3.47}$$

The recurrence relation (3.3) reads

$$(N+1)L^\alpha_{N+1} = (2N+\alpha+1-x)L^\alpha_N - (N+\alpha)L^\alpha_{N-1} \tag{3.48}$$

and the derivative (3.22) is given by

$$xL_N^{\alpha\prime} = NL_N^\alpha - (N+\alpha)L^\alpha_{N-1}. \tag{3.49}$$

3.3.2. Lagrange–Laguerre functions

The mesh points are defined by [4]

$$L_N^\alpha(x_i) = 0 \tag{3.50}$$

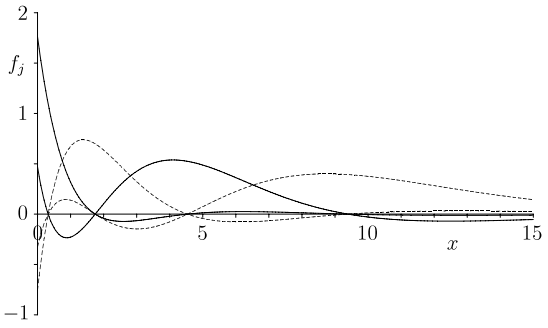

Fig. 2. Lagrange–Laguerre functions (3.52) for $\alpha = 0$ and $N = 4$.

where $i = 1$ to N correspond to increasing x_i values. The Gauss weights are

$$\lambda_i = \frac{\Gamma(N+\alpha+1)e^{x_i}}{N!x_i^{\alpha+1}[L_N^{\alpha\prime}(x_i)]^2} = \frac{\Gamma(N+\alpha)e^{x_i}}{N!(N+\alpha)x_i^{\alpha-1}[L_{N-1}^{\alpha}(x_i)]^2}. \tag{3.51}$$

The Lagrange functions are defined as

$$f_j(x) = (-1)^j x_j^{1/2}(h_N^\alpha)^{-1/2}\frac{L_N^\alpha(x)}{x-x_j}x^{\alpha/2}e^{-x/2}. \tag{3.52}$$

They satisfy the equation

$$xf_j'' + f_j' + \frac{1}{4}\left[2(2N+\alpha+1) - x - \frac{\alpha^2}{x}\right]f_j + \frac{f_j + 2xf_j'}{x-x_j} = 0. \tag{3.53}$$

The Lagrange–Laguerre functions are displayed for $\alpha = 0$ and $N = 4$ in Fig. 2.

3.3.3. *Values and matrix elements*

The first derivatives at mesh points are given by [41]

$$D_{i\neq j}^G = \lambda_i^{1/2} f_j'(x_i) = (-1)^{i-j}\sqrt{\frac{x_j}{x_i}}\frac{1}{x_i - x_j} \tag{3.54}$$

and

$$D_{ii}^G = \lambda_i^{1/2} f_i'(x_i) = -\frac{1}{2x_i}. \tag{3.55}$$

They do not provide the exact matrix elements of d/dx when $\alpha \neq 0$ because the derivative of x^α introduces a non-polynomial factor $1/x$. On the contrary, for $\alpha = 0$, the matrix elements D_{ij} of d/dx are exactly given by the above expressions. With (3.16), one obtains [41]

$$D_{i\neq j} = \frac{(-1)^{i-j}}{2\sqrt{x_i x_j}}\left(\frac{x_i + x_j}{x_i - x_j} - \delta_{\alpha 0}\right) \tag{3.56}$$

and

$$D_{ii} = -\frac{\delta_{\alpha 0}}{2x_i}. \tag{3.57}$$

For $\alpha = 0$, these results coincide with (3.54) and (3.55). For $\alpha \neq 0$, the matrix elements are antisymmetric as expected for functions vanishing at the origin and at infinity.

The second derivatives read with (3.53)–(3.55) as [41,40]

$$\lambda_i^{1/2} f_j''(x_i) = (-1)^{i-j+1}\sqrt{\frac{x_j}{x_i}}\frac{3x_i - x_j}{x_i(x_i - x_j)^2} \tag{3.58}$$

for $i \neq j$ and

$$\lambda_i^{1/2} f_i''(x_i) = -\frac{1}{12x_i}\left[2(2N+\alpha+1) - x_i - \frac{\alpha^2+8}{x_i}\right]. \tag{3.59}$$

The matrix elements of x^2 are given by (3.25) and (3.44) as

$$\langle f_i|x^2|f_j\rangle = x_i^2\delta_{ij} + (-1)^{i-j}\sqrt{x_i x_j}, \tag{3.60}$$

and those of $1/x$ and $1/x^2$ by [40]

$$\langle f_i|\frac{1}{x}|f_j\rangle = \frac{1}{x_i}\delta_{ij} + (-1)^{i-j}\frac{1}{\alpha\sqrt{x_i x_j}} \tag{3.61}$$

and

$$\langle f_i|\frac{1}{x^2}|f_j\rangle = \frac{1}{x_i^2}\delta_{ij} + (-1)^{i-j}\frac{1}{\alpha\sqrt{x_i x_j}}\left(\frac{2N+\alpha+1}{\alpha^2-1} + \frac{1}{x_i} + \frac{1}{x_j}\right). \tag{3.62}$$

If the kinetic-energy operator is defined as

$$T_\alpha = -\frac{d^2}{dx^2} + \frac{\alpha(\alpha-2)}{4x^2} \tag{3.63}$$

for $\alpha > 0$, its exact matrix elements are given after a rather heavy calculation [40] by

$$T_{i\neq j} = (-1)^{i-j}\left[\sqrt{x_i x_j}\sum_{k\neq i,j}^{N}\frac{1}{x_k(x_k-x_i)(x_k-x_j)} + \frac{\alpha+1}{2\sqrt{x_i x_j}}\left(\frac{1}{x_i}+\frac{1}{x_j}\right)\right] \tag{3.64}$$

$$= (-1)^{i-j}\frac{1}{\sqrt{x_i x_j}}\left[\frac{N}{\alpha+1} + \frac{1}{2} - \left(\frac{1}{x_i}+\frac{1}{x_j}\right) + \frac{x_i+x_j}{(x_i-x_j)^2}\right] \tag{3.65}$$

and

$$T_{ii} = x_i\sum_{k\neq i}^{N}\frac{1}{x_k(x_k-x_i)^2} + \frac{(\alpha+1)^2}{4x_i^2} \tag{3.66}$$

$$= -\frac{1}{12} + \frac{(2N+\alpha+1)(\alpha+4)}{6(\alpha+1)x_i} + \frac{(\alpha+2)(\alpha-5)}{6x_i^2}. \tag{3.67}$$

Expressions (3.65) and (3.67) simplify the respective expressions (3.64) and (3.66) given in [4].

If the kinetic-energy operator is $T_0 = -d^2/dx^2$, the matrix elements read [40]

$$\langle f_i|T_0|f_j\rangle = \frac{(-1)^{i-j+1}}{\sqrt{x_i x_j}}\left[-\frac{\alpha(2N+\alpha+1)}{4(\alpha^2-1)} + \frac{\alpha+2}{4}\left(\frac{1}{x_i}+\frac{1}{x_j}\right) - \frac{x_i+x_j}{(x_i-x_j)^2}\right] \tag{3.68}$$

and

$$\langle f_i|T_0|f_i\rangle = -\frac{1}{12}\left\{1 - \frac{\alpha+2}{x_i}\left[\frac{(2N+\alpha+1)(2\alpha-1)}{\alpha^2-1} - \frac{\alpha+4}{x_i}\right]\right\}. \tag{3.69}$$

3.3.4. *Laguerre mesh regularized by x for $\alpha \geq 0$*

When the radial wave functions in spherical coordinates are written as $r^{-1}u_l(r)$, the functions $u_l(r)$ vanish at the origin like r^{l+1}. This behaviour can be simulated with Lagrange–Laguerre functions with $\alpha = 2l+2$ but the mesh then varies with l [4]. A more serious problem is that the Gauss quadrature does not give accurate results for the matrix elements of $1/r$ and $1/r^2$. Although the exact expressions (3.61) and (3.62) are now available [40], it is more convenient to use regularized Lagrange functions for all partial waves [5]. The most important case in practical applications is the regularization by x. It can be used in studies of bound states of the radial Schrödinger (Sections 5.3–5.5) and Dirac (Section 5.9) equations or for complex scaling (Section 6.6). General expressions for a regularization by x^n are given in [11,6]. In practice, only the regularizations by x in spherical coordinates and by $x^{3/2}$ (Section 3.3.5) in hyperspherical coordinates are useful until now. Other cases usually lead to asymmetric kinetic-energy matrices.

The Lagrange functions are defined by [32,7,6]

$$\hat{f}_j(x) = \frac{x}{x_j}f_j(x) = (-1)^j(h_N^\alpha x_j)^{-1/2}\frac{L_N^\alpha(x)}{x-x_j}x^{\alpha/2+1}e^{-x/2}. \tag{3.70}$$

This basis is not orthonormal. From (3.60), one deduces

$$\langle\hat{f}_i|\hat{f}_j\rangle = \delta_{ij} + \frac{(-1)^{i-j}}{\sqrt{x_i x_j}}. \tag{3.71}$$

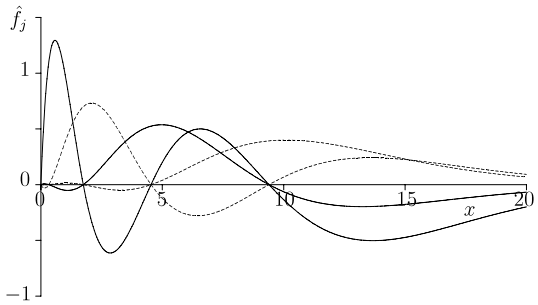

Fig. 3. Lagrange–Laguerre functions (3.70) regularized by x for $\alpha = 0$ and $N = 4$.

The regularized Lagrange–Laguerre functions are displayed for $\alpha = 0$ and $N = 4$ in Fig. 3. They all vanish at $x = 0$ and have a larger amplitude at large distances.

The matrix elements of d/dx are given at the Gauss approximation by

$$\hat{D}^G_{i\neq j} = (-1)^{i-j}\sqrt{\frac{x_i}{x_j}}\frac{1}{x_i - x_j}, \qquad \hat{D}^G_{ii} = \frac{1}{2x_i}. \tag{3.72}$$

They are not exact since the integrand $\hat{f}_i\hat{f}'_j$ involves the weight function multiplied by a polynomial of degree $2N$. But $\int_0^\infty \hat{f}_i(\hat{f}'_j + \frac{1}{2}\hat{f}_j)dx$ can be calculated exactly with the Gauss quadrature. With (3.71), the exact expressions are thus

$$\hat{D}_{ij} = \hat{D}^G_{ij} - \frac{(-1)^{i-j}}{2\sqrt{x_i x_j}}, \tag{3.73}$$

or explicitly

$$\hat{D}_{i\neq j} = (-1)^{i-j}\frac{x_i + x_j}{2\sqrt{x_i x_j}(x_i - x_j)}, \quad \hat{D}_{ii} = 0. \tag{3.74}$$

This matrix is antisymmetric as expected. The matrix elements of $T = -d^2/dx^2$ read at the Gauss approximation [32]

$$\hat{T}^G_{i\neq j} = (-1)^{i-j}\frac{x_i + x_j}{\sqrt{x_i x_j}(x_i - x_j)^2} \tag{3.75}$$

and

$$\hat{T}^G_{ii} = -\frac{1}{12x_i^2}\left[x_i^2 - 2(2N + \alpha + 1)x_i + \alpha^2 - 4\right]. \tag{3.76}$$

The exact expressions are given by

$$\hat{T}_{ij} = \hat{T}^G_{ij} - (-1)^{i-j}\frac{1}{4\sqrt{x_i x_j}}. \tag{3.77}$$

3.3.5. Laguerre mesh regularized by $x^{3/2}$ for $\alpha \geq 0$

In hyperspherical coordinates, the regularization by $x^{3/2}$ allows a better reproduction of the wave function near the singularity of the centrifugal term [11] (see Section 7.6),

$$\hat{f}_j(x) = \left(\frac{x}{x_j}\right)^{3/2} f_j(x). \tag{3.78}$$

The regularized Lagrange–Laguerre functions are displayed for $\alpha = 0$ in Fig. 4. They exhibit a marked increase of amplitude at large distances.

The matrix elements of $T = -d^2/dx^2$ read at the Gauss approximation

$$\hat{T}^G_{i\neq j} = (-1)^{i-j}\frac{2}{(x_i - x_j)^2} \tag{3.79}$$

and

$$\hat{T}^G_{ii} = -\frac{1}{12x_i^2}\left[x_i^2 - 2(2N + \alpha + 1)x_i - 1 + \alpha^2\right]. \tag{3.80}$$

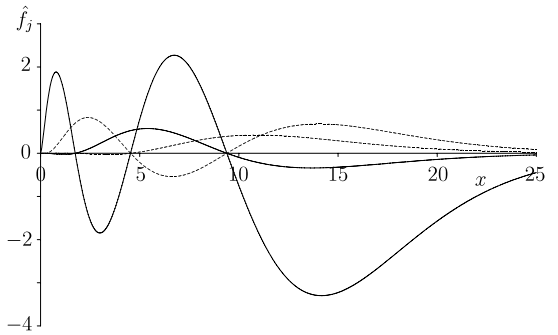

Fig. 4. Lagrange–Laguerre functions (3.78) regularized by $x^{3/2}$ for $\alpha = 0$ and $N = 4$.

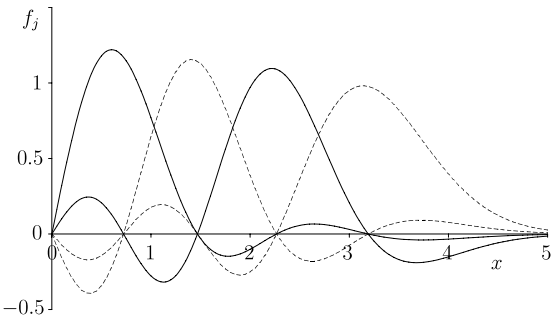

Fig. 5. Modified Lagrange–Laguerre functions (3.83) for $\alpha = 1/2$ and $N = 4$.

These expressions are not exact since the integral involves a polynomial of degree $2N + 1$. The exact expressions are given by

$$\hat{T}_{ij} = \hat{T}^G_{ij} + (-1)^{i-j}\frac{2N + \alpha + 1 - x_i - x_j}{4x_i x_j}. \tag{3.81}$$

3.3.6. Modified Laguerre mesh in x^2

We have seen in Section 2.6 that a mapping can lead to new types of Lagrange meshes. An interesting example is given by $t(x) = x^2$. The basis functions have a Gaussian asymptotic behaviour. This mesh leads to exact results for the three-dimensional harmonic oscillator for $\alpha = l + 1/2$ [4] (Section 5.2).

The mesh points verify

$$L^\alpha_N(x_i^2) = 0. \tag{3.82}$$

The Lagrange functions (2.50) read

$$f_j(x) = (-1)^j x_j (h^\alpha_N/2)^{-1/2} x^{\alpha+1/2} e^{-x^2/2}\frac{L^\alpha_N(x^2)}{x^2 - x_j^2} \tag{3.83}$$

and the Gauss weights are given by (2.48) and (3.51) as

$$\lambda_i = \frac{\Gamma(N + \alpha)}{2N!(N + \alpha)}\frac{e^{x_i^2}}{x_i^{2\alpha-1}[L^\alpha_{N-1}(x_i^2)]^2}. \tag{3.84}$$

They satisfy the equation

$$f_j'' + \left[2(2N + \alpha + 1) - x^2 - \frac{\alpha^2 - 1/4}{x^2}\right]f_j + 2\frac{f_j + 2xf_j'}{x^2 - x_j^2} = 0. \tag{3.85}$$

Modified Lagrange–Laguerre functions are displayed for $\alpha = 1/2$ in Fig. 5. They are more localized near the mesh points.

The first derivatives at mesh points are given by

$$\lambda_i^{1/2} f_j'(x_i) = (-1)^{i-j}\frac{2x_j}{x_i^2 - x_j^2} \tag{3.86}$$

for $i \neq j$ and

$$\lambda_i^{1/2} f_i'(x_i) = -\frac{1}{2x_i}. \tag{3.87}$$

The second derivatives are given by Eq. (3.85) as

$$\lambda_i^{1/2} f_j''(x_i) = (-1)^{i-j+1} \frac{8x_i x_j}{(x_i^2 - x_j^2)^2} \tag{3.88}$$

for $i \neq j$ and

$$\lambda_i^{1/2} f_i''(x_i) = \frac{1}{3}\left[x_i^2 - 2(2N + \alpha + 1) + \frac{\alpha^2 + 5/4}{x_i^2}\right]. \tag{3.89}$$

If the kinetic-energy operator reads

$$T = -\frac{d^2}{dx^2} + \frac{\alpha^2 - 1/4}{x^2}, \tag{3.90}$$

its matrix elements are exactly given by the Gauss quadrature as [4]

$$T_{ij} = -\lambda_i^{1/2} f_j''(x_i) + \frac{\alpha^2 - 1/4}{x_i^2}\,\delta_{ij}. \tag{3.91}$$

The Gauss quadrature is here exact because the integrand is x^3 multiplied by a polynomial in x^2 of degree $2N - 2$ and by $w(x^2)$. Returning to the variable $t(x) = x^2$, the weight function $w(t)$ is multiplied by a polynomial of degree $2N - 1$. But the Gauss quadrature is not exact for the matrix elements of d^2/dx^2 and $1/x^2$ separately.

The matrix elements of xd/dx can be found in Ref. [45].

3.3.7. Modified Laguerre mesh in x^2 regularized by x

The choice of α in the preceding mesh depends on the partial wave. It may be more interesting to have a single mesh for all partial waves. The regularized modified mesh also leads to exact solutions for the three-dimensional harmonic oscillator for $\alpha = -1/2$ (or $\alpha = 1/2$ for odd l values).

The Lagrange functions are regularized as usual,

$$\hat{f}_j(x) = \frac{x}{x_j} f_j(x) \tag{3.92}$$

where f_j is given by (3.83). This is convenient for the kinetic-energy operator $T = -d^2/dx^2$. Its matrix elements at the Gauss approximation read with Eqs. (2.61) and (3.86)–(3.89),

$$\hat{T}^G_{i\neq j} = (-1)^{i-j} \frac{4(x_i^2 + x_j^2)}{(x_i^2 - x_j^2)^2} \tag{3.93}$$

and

$$\hat{T}^G_{ii} = \frac{1}{3}\left[-x_i^2 + 2(2N + \alpha + 1) - \frac{\alpha^2 - 3/4}{x_i^2}\right]. \tag{3.94}$$

These expressions are not exact as the degree of the polynomial in $t(x) = x^2$ is $2N$.

A regularization by $(x/x_j)^2$ is also useful [44]. For the kinetic-energy operator T_α defined in Eq. (3.63), the matrix elements at the Gauss approximation happen to be given by the opposites of Eqs. (3.88) and (3.89). Another approach, based on an integration by parts is presented in Ref. [44] for $\alpha = 0$.

3.4. Lagrange–Legendre meshes

3.4.1. Generalized Legendre polynomials

Although they are proportional to Jacobi polynomials (Section 3.5) with $\alpha = \beta = m$, these polynomials deserve a separate treatment because of their importance in applications using spherical coordinates [5,35] (see Section 5.6). They are also very useful in other cases [42,43,28,9,44–46] (see Section 5.5 and Sections 6.1–6.5).

The generalized Legendre polynomials are defined over $(-1, +1)$ with the weight function

$$w(x) = (1 - x^2)^m \tag{3.95}$$

where $m \geq 0$ is assumed. It corresponds to

$$\sigma(x) = 1 - x^2, \qquad \tau(x) = -2(m+1)x, \qquad d_N = N + 2m + 1. \tag{3.96}$$

Hence the differential equation (3.19) is

$$(1-x^2)p_N^{m\prime\prime} - 2(m+1)xp_N^{m\prime} + N(N+2m+1)p_N^m = 0. \tag{3.97}$$

The squared norm of p_N^m is given by

$$h_N^m = \frac{2}{2N+2m+1}\frac{(N+2m)!}{N!}. \tag{3.98}$$

The first coefficients are

$$k_N^m = \frac{(2N+2m)!}{2^{N+m}N!(N+m)!}, \qquad k_N^{m\prime} = 0. \tag{3.99}$$

The recurrence relation (3.3) reads

$$(N+1)p_{N+1}^m = (2N+2m+1)xp_N^m - (N+2m)p_{N-1}^m. \tag{3.100}$$

The important expressions are the modified 'polynomials'

$$P_{N+m}^m(x) = (1-x^2)^{m/2}p_N^m(x) \tag{3.101}$$

which verify the differential equation

$$L_m^2 P_{N+m}^m = (N+m)(N+m+1)P_{N+m}^m \tag{3.102}$$

where

$$L_m^2 = -\frac{d}{dx}(1-x^2)\frac{d}{dx} + \frac{m^2}{1-x^2}. \tag{3.103}$$

Without weight function, the squared norm of P_{N+m}^m is also given by (3.98). Its derivative can be calculated with

$$(1-x^2)P_{N+m}^{m\prime} = -(N+m)xP_{N+m}^m + (N+2m)P_{N+m-1}^m. \tag{3.104}$$

3.4.2. *Lagrange–Legendre functions*

The increasing zeros of

$$p_N^m(x_i) = 0 \tag{3.105}$$

are numbered with index $i = -(N-1)/2, \ldots, (N-1)/2$. The Gauss weights are given by

$$\lambda_i = \frac{2(N+2m)!}{N!(1-x_i^2)[P_{N+m}^{m\prime}(x_i)]^2} = \frac{2(N+2m-1)!(1-x_i^2)}{N!(N+2m)[P_{N+m-1}^m(x_i)]^2}. \tag{3.106}$$

The Lagrange functions are defined as

$$f_j(x) = (-1)^{j_N - j}\left(\frac{1-x_j^2}{2N+2m+1}\right)^{1/2}(h_N^m)^{-1/2}\frac{P_{N+m}^m(x)}{x-x_j} \tag{3.107}$$

with $j_N = (N-1)/2$. They verify the differential equation

$$L_m^2 f_j = (N+m)(N+m+1)f_j + 2\frac{(1-x^2)f_j' - xf_j}{x-x_j}. \tag{3.108}$$

The Lagrange–Legendre functions are displayed for $m = 0$ and $N = 4$ in Fig. 6.

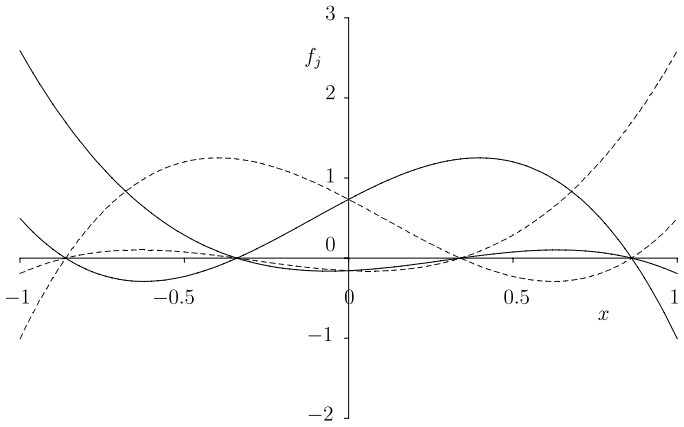

Fig. 6. Lagrange–Legendre functions (3.107) for $m = 0$ and $N = 4$.

3.4.3. Values and matrix elements

The first derivatives at mesh points are given by

$$\lambda_i^{1/2} f_j'(x_i) = (-1)^{i-j} \left(\frac{1-x_j^2}{1-x_i^2}\right)^{1/2} \frac{1}{x_i - x_j} \tag{3.109}$$

for $i \neq j$ and

$$\lambda_i^{1/2} f_i'(x_i) = \frac{x_i}{1-x_i^2}. \tag{3.110}$$

For $m = 0$, these expressions give the exact matrix elements D_{ij} [41]. Otherwise, they are not the exact matrix elements of d/dx. The second derivatives are given by

$$\lambda_i^{1/2} f_j''(x_i) = 2(-1)^{i-j+1} \frac{(1-x_j^2)^{1/2}}{(1-x_i^2)^{3/2}} \frac{1 + x_i x_j - 2x_i^2}{(x_i - x_j)^2}, \tag{3.111}$$

for $i \neq j$ and

$$\lambda_i^{1/2} f_i''(x_i) = -\frac{1}{3(1-x_i^2)} \left[(N+m)(N+m+1) + 6 - \frac{m^2+8}{1-x_i^2}\right]. \tag{3.112}$$

For $m = 0$, they give the exact matrix elements of d^2/dx^2 [41]. They are not symmetric since the Legendre polynomials $P_N(x)$ do not vanish at the extremities of the interval.

The matrix elements of x^2 read according to (3.25),

$$\langle f_i | x^2 | f_j \rangle = x_i^2 \delta_{ij} + (-1)^{i-j} \frac{\sqrt{(1-x_i^2)(1-x_j^2)}}{2N + 2m + 1}. \tag{3.113}$$

For the kinetic-energy operator $T = L_m^2$ given by (3.103), one has exactly [4]

$$T_{ij} = \lambda_i^{1/2} (L_m^2 f_j)(x_i), \tag{3.114}$$

or, explicitly,

$$T_{i \neq j} = (-1)^{i-j} (1-x_i^2)^{1/2} (1-x_j^2)^{1/2} \frac{2}{(x_i - x_j)^2} \tag{3.115}$$

and

$$T_{ii} = \frac{1}{3}(N+m)(N+m+1) + \frac{2}{3} \frac{m^2-1}{1-x_i^2}. \tag{3.116}$$

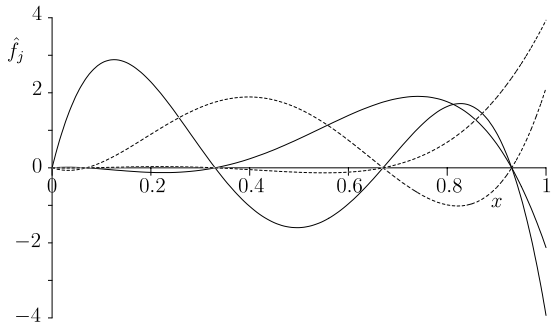

Fig. 7. Lagrange–Legendre functions (3.122) over (0, 1) regularized by x for $N = 4$.

3.4.4. Legendre mesh regularized by $\sqrt{1-x^2}$

From now on, I only consider the choice $m = 0$ in the Lagrange–Legendre functions. This choice simplifies the basis functions and provides exact matrix elements at the Gauss approximation. However, in physical applications, the magnetic quantum number m may not be zero. In this case, the Gauss quadrature is inaccurate for the term $m^2/(1-x^2)$ in operator (3.103). In order to eliminate this problem, a regularization by $(1-x^2)^{\nu/2}$ where ν is an integer is useful in problems where non-zero magnetic quantum numbers appear. This is for example the case for some coordinate systems used to describe simple molecular systems in strong magnetic fields [9,46–48].

Here, I only consider the case $\nu = 1$ for simplicity. More general expressions can be found in Refs. [9,46]. The $m = 0$ Legendre functions regularized by $\sqrt{1-x^2}$ read

$$\hat{f}_j(x) = \left(\frac{1-x^2}{1-x_j^2}\right)^{1/2} f_j(x). \tag{3.117}$$

For $T = L_0^2$, the kinetic-energy matrix elements at the Gauss approximation are given by

$$\hat{T}^G_{i\neq j} = 2(-1)^{i-j}\frac{1-x_ix_j}{(x_i-x_j)^2} \tag{3.118}$$

and

$$\hat{T}^G_{ii} = \frac{1}{3}\left[N(N+1) - \frac{11}{1-x_i^2}\right]. \tag{3.119}$$

3.4.5. Shifted Legendre mesh on (0, 1) *regularized by x*

A number of interesting problems take place in an interval $(0, a)$ which can be obtained by scaling (0, 1). The origin being often a regular singular point, a regularization is necessary [42,43,28,14] (Section 6).

A Lagrange mesh on (0, 1) is then obtained for $i = 1, \ldots, N$ from

$$P_N(2x_i - 1) = 0, \tag{3.120}$$

where $P_N(x) = P_N^0(x)$ is a standard Legendre polynomial. The corresponding Gauss weights $\hat{\lambda}_i$ are

$$\hat{\lambda}_i = \frac{\lambda_i}{2} = \frac{1}{4x_i(1-x_i)[P'_N(2x_i-1)]^2} = \frac{4x_i(1-x_i)}{N^2[P_{N-1}(2x_i-1)]^2} \tag{3.121}$$

where λ_i is given by (3.106) for $m = 0$. The Lagrange functions regularized by x are defined as

$$\hat{f}_j(x) = (-1)^{N-i}\sqrt{\frac{1-x_j}{x_j}}\,\frac{xP_N(2x-1)}{x-x_j}. \tag{3.122}$$

These regularized Lagrange–Legendre functions are depicted in Fig. 7.

The exact matrix elements of d/dx are given by the Gauss quadrature as

$$\hat{D}_{i\neq j} = (-1)^{i-j}\sqrt{\frac{x_i(1-x_j)}{x_j(1-x_i)}}\,\frac{1}{x_i-x_j} \tag{3.123}$$

and

$$\hat{D}_{ii} = \frac{1}{2x_i(1-x_i)}. \tag{3.124}$$

For $T = -d^2/dx^2$, the exact matrix elements are given by the Gauss quadrature as [42]

$$\hat{T}_{i\neq j} = (-1)^{i-j}\frac{x_i + x_j - 2x_i^2}{x_j(x_j - x_i)^2}\sqrt{\frac{x_j(1-x_j)}{x_i(1-x_i)^3}} \tag{3.125}$$

and

$$\hat{T}_{ii} = \frac{N(N+1)x_i(1-x_i) - 3x_i + 1}{3x_i^2(1-x_i)^2}. \tag{3.126}$$

These matrix elements are not symmetric because the Lagrange functions do not satisfy Hermitian boundary conditions at the right extremity of this interval.

In the R-matrix theory [14], one adds to the kinetic energy the boundary condition operator (see Section 6.1)

$$\mathcal{L} = \delta(x-1)\frac{d}{dx} \tag{3.127}$$

introduced by Bloch [49]. The matrix elements of $\mathcal{L}$ are calculated like in (2.40) and provide the symmetric expressions [50,14]

$$\langle\hat{f}_i|T + \mathcal{L}|\hat{f}_j\rangle = \frac{(-1)^{i-j}}{[x_ix_j(1-x_i)(1-x_j)]^{1/2}}\left[N^2 + N + 1 + \frac{x_i + x_j - 2x_ix_j}{(x_i - x_j)^2} - \frac{1}{1-x_i} - \frac{1}{1-x_j}\right] \tag{3.128}$$

for $i \neq j$ and

$$\langle\hat{f}_i|T + \mathcal{L}|\hat{f}_i\rangle = \frac{(4N^2 + 4N + 3)x_i(1-x_i) - 6x_i + 1}{3x_i^2(1-x_i)^2}. \tag{3.129}$$

3.4.6. *Shifted Legendre mesh on* (0, 1) *regularized by* $x^{3/2}$

In hyperspherical coordinates, the singularity at the origin leads to a half-integer power of x (see Section 7.6). This is well regularized with $x^{3/2}$ although a regularization by x can also be used [12].

The Lagrange functions are defined as

$$\hat{f}_j(x) = (-1)^{N-j}\frac{\sqrt{1-x_j}}{x_j}\frac{x^{3/2}P_N(2x-1)}{x - x_j}. \tag{3.130}$$

The Gauss approximation for the matrix elements of d/dx reads

$$\hat{D}^G_{i\neq j} = (-1)^{i-j}\sqrt{\frac{1-x_j}{1-x_i}}\frac{x_i}{x_j(x_i - x_j)} \tag{3.131}$$

and

$$\hat{D}^G_{ii} = \frac{2 - x_i}{2x_i(1-x_i)}. \tag{3.132}$$

These expressions are not exact because the degree of the polynomial integrand is $2N$. Since the integral of $f_i(x)f_j'(x) - (N + 1/2)P_N^2(2x-1)$ is exactly calculated with the Gauss quadrature, the exact matrix elements of d/dx read with (3.98),

$$\hat{D}_{ij} = \hat{D}^G_{ij} + \frac{1}{2}(-1)^{i-j}\frac{\sqrt{(1-x_j)(1-x_i)}}{x_ix_j}. \tag{3.133}$$

For $T = -d^2/dx^2$, the exact matrix elements are given by the Gauss quadrature as

$$\hat{T}_{i\neq j} = (-1)^{i-j}\frac{2x_j - x_ix_j - x_i^2}{x_j(x_j - x_i)^2}\sqrt{\frac{1-x_j}{(1-x_i)^3}} \tag{3.134}$$

and

$$\hat{T}_{ii} = \frac{[4N(N+1) - 3]x_i(1-x_i) - 9x_i + 1}{12x_i^2(1-x_i)^2}. \tag{3.135}$$

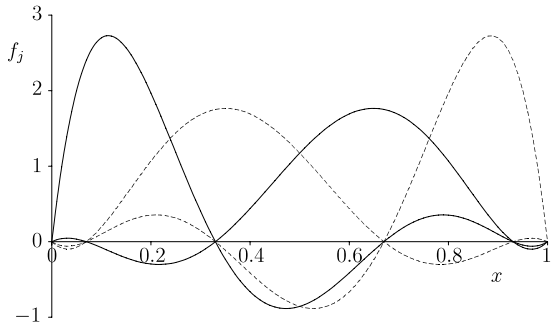

Fig. 8. Lagrange–Legendre functions (3.138) over (0, 1) regularized by $x(1-x)$ for $N = 4$.

The exact matrix elements of $-d^2/dx^2 + \mathcal{L}$ are

$$\langle \hat{f}_i|T + \mathcal{L}|\hat{f}_j\rangle = \frac{(-1)^{i+j}}{x_i x_j[(1-x_i)(1-x_j)]^{1/2}} \times \left[N(N+1) + \frac{3}{2} + \frac{x_i^2 + x_j^2 - x_i x_j(x_i + x_j)}{(x_i - x_j)^2} - \frac{1}{1-x_i} - \frac{1}{1-x_j}\right] \tag{3.136}$$

for $i \neq j$ and

$$\langle \hat{f}_i|T + \mathcal{L}|\hat{f}_i\rangle = \frac{4N(N+1)(3+x_i)(1-x_i) + 3x_i^2 - 30x_i + 7}{12x_i^2(1-x_i)^2}. \tag{3.137}$$

3.4.7. Shifted Legendre mesh on (0, 1) *regularized by* $x(1-x)$

In some problems (see Section 5.5), the wave function is confined in such a way that it must vanish at both extremities of an interval scaled from (0, 1). Convenient Lagrange functions vanishing at 0 and 1 are obtained by regularizing Lagrange–Legendre functions at both extremities with $x(1-x)/x_j(1-x_j)$ [51],

$$\hat{f}_j(x) = (-1)^{N-j}\frac{x(1-x)}{\sqrt{x_j(1-x_j)}}\frac{P_N(2x-1)}{x - x_j}. \tag{3.138}$$

The Lagrange–Legendre functions regularized at both extremities are depicted in Fig. 8.

The exact overlaps of these functions are given by

$$\langle \hat{f}_i|\hat{f}_j\rangle = \delta_{ij} + \frac{(-1)^{i-j}}{4(2N+1)R_{ij}}\left[\frac{2N^2+2N-1}{(2N-1)(2N+3)} + 1 + 4(x_i^2 + x_j^2) - 6(x_i + x_j) + 4x_i x_j\right] \tag{3.139}$$

with $R_{ij} = \sqrt{x_i(1-x_i)x_j(1-x_j)}$. They have the structure (2.63). The exact matrix elements of x^{-1} and x^{-2} are simpler,

$$\langle \hat{f}_i|\frac{1}{x}|\hat{f}_j\rangle = \frac{1}{x_i}\delta_{ij} + \frac{(-1)^{i-j}}{(2N+1)R_{ij}}\left(x_i + x_j - \frac{3}{2}\right) \tag{3.140}$$

and

$$\langle \hat{f}_i|\frac{1}{x^2}|\hat{f}_j\rangle = \frac{1}{x_i^2}\delta_{ij} + \frac{(-1)^{i-j}}{(2N+1)R_{ij}}. \tag{3.141}$$

In the last three expressions, the first term is the Gauss approximation.

The matrix elements of $T = -d^2/dx^2$ are given at the Gauss approximation by [51]

$$\hat{T}^G_{i\neq j} = (-1)^{i-j}\frac{x_i + x_j - 2x_i x_j}{R_{ij}(x_i - x_j)^2} \tag{3.142}$$

and

$$\hat{T}^G_{ii} = \frac{1}{3x_i(1-x_i)}\left[N(N+1) + \frac{1}{x_i(1-x_i)}\right]. \tag{3.143}$$

The exact matrix elements read

$$\hat{T}_{ij} = \hat{T}^G_{ij} - (-1)^{i-j}\frac{N(N+1)}{(2N+1)R_{ij}}. \tag{3.144}$$

A regularization by $1-x$, i.e. Lagrange functions vanishing at $x = 1$ but not at the origin, is also useful in three-body confinement problems. It can be obtained in a similar way [52].

3.5. Lagrange–Jacobi meshes

3.5.1. Jacobi polynomials

The Lagrange meshes based on Jacobi polynomials have not been much used yet [42] but they can lead to useful applications (Section 6.3) and interesting information about the method (Section 5.5).

The Jacobi polynomials [22] are defined over $(-1, +1)$ with the weight function

$$w(x) = (1-x)^\alpha (1+x)^\beta. \tag{3.145}$$

This function corresponds to

$$\sigma(x) = 1 - x^2, \qquad \tau(x) = -(\gamma+1)x + \beta - \alpha, \qquad d_N = N + \gamma \tag{3.146}$$

where

$$\gamma = \alpha + \beta + 1. \tag{3.147}$$

Hence the differential equation (3.19) is

$$(1-x^2)P_N^{(\alpha,\beta)\prime\prime} + [\beta - \alpha - (\gamma+1)x]P_N^{(\alpha,\beta)\prime} + N(N+\gamma)P_N^{(\alpha,\beta)} = 0. \tag{3.148}$$

The squared norm is given by

$$h_N = \frac{2^\gamma}{2N+\gamma} \frac{\Gamma(N+\alpha+1)\Gamma(N+\beta+1)}{N!\Gamma(N+\gamma)} \tag{3.149}$$

and the first coefficient by

$$k_N = \frac{\Gamma(2N+\gamma)}{2^N N!\Gamma(N+\gamma)}. \tag{3.150}$$

The recurrence relation (3.3) reads

$$\begin{aligned} 2(N+1)(N+\gamma)(2N+\gamma-1)P_{N+1}^{(\alpha,\beta)} &= (2N+\gamma)[\alpha^2 - \beta^2 + (2N+\gamma-1)(2N+\gamma+1)x]P_N^{(\alpha,\beta)} \\ &\quad - 2(N+\alpha)(N+\beta)(2N+\gamma+1)P_{N-1}^{(\alpha,\beta)}. \end{aligned} \tag{3.151}$$

The derivative of $P_N^{(\alpha,\beta)}(x)$ can be calculated with

$$(2N+\gamma-1)(1-x^2)P_N^{(\alpha,\beta)\prime} = N[\alpha - \beta - (2N+\gamma-1)x]P_N^{(\alpha,\beta)} + 2(N+\alpha)(N+\beta)P_{N-1}^{(\alpha,\beta)}. \tag{3.152}$$

3.5.2. Lagrange–Jacobi functions

Increasing mesh points x_i are defined by

$$P_N^{(\alpha,\beta)}(x_i) = 0 \tag{3.153}$$

where $i = 1, \ldots, N$. The Gauss–Jacobi weights are

$$\begin{aligned} \lambda_i &= \frac{(2N+\gamma)h_N}{(1-x_i)^{\alpha+1}(1+x_i)^{\beta+1}[P_N^{(\alpha,\beta)\prime}(x_i)]^2} \\ &= \frac{(2N+\gamma)(2N+\gamma-1)^2 h_N}{4(N+\alpha)^2(N+\beta)^2(1-x_i)^{\alpha-1}(1+x_i)^{\beta-1}[P_{N-1}^{(\alpha,\beta)}(x_i)]^2}. \end{aligned} \tag{3.154}$$

The Lagrange–Jacobi functions are defined by

$$f_j(x) = (-1)^{N-j}\sqrt{\frac{1-x_j^2}{2N+\gamma}} h_N^{-1/2}(1-x)^{\alpha/2}(1+x)^{\beta/2}\frac{P_N^{(\alpha,\beta)}(x)}{x-x_j}. \tag{3.155}$$

They verify the differential equation

$$(1-x^2)f_j'' - 2xf_j' + \frac{1}{4}\left[(2N+\gamma)^2 - 1 - 2\,\frac{\alpha^2+\beta^2+(\alpha^2-\beta^2)x}{1-x^2}\right]f_j + 2\,\frac{(1-x^2)f_j' - xf_j}{x-x_j} = 0. \tag{3.156}$$

3.5.3. Values and matrix elements

The first derivatives at mesh points are given by [41]

$$\lambda_i^{1/2} f_j'(x_i) = (-1)^{i-j} \left(\frac{1-x_j^2}{1-x_i^2}\right)^{1/2} \frac{1}{x_i - x_j} \tag{3.157}$$

for $i \neq j$ and

$$\lambda_i^{1/2} f_i'(x_i) = \frac{x_i}{1-x_i^2}. \tag{3.158}$$

The exact matrix elements of d/dx are given either by (3.16) of by (3.15) with Eq. (59) of Ref. [40]. The second derivatives at mesh points read [42]

$$\lambda_i^{1/2} f_j''(x_i) = (-1)^{i-j+1} \frac{2}{(x_i - x_j)^2} \left(\frac{1-x_j^2}{1-x_i^2}\right)^{1/2} \frac{1 + x_i x_j - 2x_i^2}{1-x_i^2} \tag{3.159}$$

for $i \neq j$ and

$$\lambda_i^{1/2} f_i''(x_i) = -\frac{1}{12(1-x_i^2)} \left[(2N+\gamma)^2 + 23 - 2\,\frac{\alpha^2 + \beta^2 + 16 + (\alpha^2 - \beta^2)x_i}{1-x_i^2}\right]. \tag{3.160}$$

The matrix elements of d^2/dx^2 can be derived from these expressions and from the matrix elements of w'/w and w''/w given in Ref. [40]. The matrix elements of x^2 read according to (3.25),

$$\langle f_i | x^2 | f_j \rangle = x_i^2 \delta_{ij} + (-1)^{i-j} \frac{\sqrt{(1-x_i^2)(1-x_j^2)}}{2N+\gamma}. \tag{3.161}$$

3.5.4. $\alpha = 0$ Lagrange–Jacobi mesh over (0, 1)

The shifted Lagrange–Legendre mesh can be generalized by shifting and scaling the Lagrange–Jacobi mesh to interval (0, 1). In practice, the most interesting case requires that the Lagrange functions do not vanish at $x = 1$. Hence we choose $\alpha = 0$. The mesh points are then given by

$$P_N^{(0,\beta)}(2x_i - 1) = 0. \tag{3.162}$$

The shifted Lagrange–Jacobi functions are defined by

$$\widetilde{f}_j(x) = (-1)^{j+N} \sqrt{x_j(1-x_j)}\, \frac{P_N^{(0,\beta)}(2x-1)}{x - x_j}\, x^{\beta/2} \tag{3.163}$$

and the Gauss weights read

$$\widetilde{\lambda}_i = \frac{\lambda_i}{2} \tag{3.164}$$

where λ_i is given by (3.154). These Lagrange–Jacobi functions are depicted for $\beta = 42$ and $N = 4$ in Fig. 9. The choice for β provides an x^{21} behaviour near the origin typical of a radial wave function of the $l = 20$ partial wave (see Section 6.3). The mesh points are then concentrated in the vicinity of $x = 1$.

The first derivatives at the mesh points are given by

$$\widetilde{\lambda}_i^{1/2} \widetilde{f}_j'(x_i) = (-1)^{i-j} \sqrt{\frac{x_j(1-x_j)}{x_i(1-x_i)}}\, \frac{1}{x_i - x_j} \tag{3.165}$$

for $i \neq j$ and

$$\widetilde{\lambda}_i^{1/2} \widetilde{f}_i'(x_i) = \frac{2x_i - 1}{2x_i(1-x_i)}. \tag{3.166}$$

The second derivatives read

$$\widetilde{\lambda}_i^{1/2} \widetilde{f}_j''(x_i) = (-1)^{i-j} \sqrt{\frac{x_j(1-x_j)}{x_i(1-x_i)}}\, \frac{4x_i^2 - 2x_i x_j - 3x_i + x_j}{2x_i(1-x_i)(x_i - x_j)^2} \tag{3.167}$$

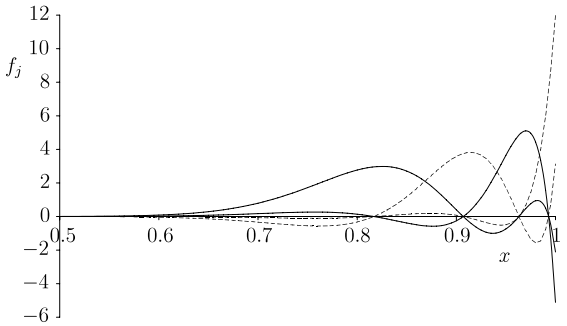

Fig. 9. Lagrange–Jacobi functions (3.163) over (0, 1) for $\beta = 42$ and $N = 4$. Notice that the abscissas start at 0.5.

for $i \neq j$ and

$$\widetilde{\lambda}_i^{1/2}\widetilde{f}_i''(x_i) = -\frac{1}{12x_i(1-x_i)}\left[(2N+\beta+1)^2+23-\frac{\beta^2+8}{x_i}-\frac{8}{1-x_i}\right]. \tag{3.168}$$

The matrix elements of $1/x$ and $1/x^2$ are given by [40]

$$\langle\widetilde{f}_i|\frac{1}{x}|\widetilde{f}_j\rangle = \frac{1}{x_i}\delta_{ij} + \frac{(-1)^{i-j}}{\beta}\sqrt{\frac{(1-x_i)(1-x_j)}{x_ix_j}} \tag{3.169}$$

and

$$\langle\widetilde{f}_i|\frac{1}{x^2}|\widetilde{f}_j\rangle = \frac{1}{x_i^2}\delta_{ij} + \frac{(-1)^{i-j}}{\beta}\sqrt{\frac{(1-x_i)(1-x_j)}{x_ix_j}}\left(\frac{2N^2}{\beta^2-1}+\frac{2N+\beta}{\beta-1}+\frac{1}{x_i}+\frac{1}{x_j}\right). \tag{3.170}$$

Let T_β be defined like in (3.63) with α replaced by β and $\mathcal{L}$ be defined by (3.127). The exact matrix elements of $T_\beta + \mathcal{L}$ read [40]

$$\begin{aligned}\langle\widetilde{f}_i|T_\beta+\mathcal{L}|\widetilde{f}_j\rangle = {}& \frac{(-1)^{i-j}}{\sqrt{x_ix_j(1-x_i)(1-x_j)}}\left\{\frac{N(N+\beta+1)}{\beta+1}[(\beta+2)x_ix_j-x_i-x_j+1]\right.\\ & - x_ix_j\left(\frac{1}{1-x_i}+\frac{1}{1-x_j}\right)-(1-x_i)(1-x_j)\left(\frac{1}{x_i}+\frac{1}{x_j}\right)\\ & \left.+\frac{x_i(1-x_i)+x_j(1-x_j)}{(x_i-x_j)^2}+\frac{\beta}{2}x_ix_j\right\}\end{aligned} \tag{3.171}$$

for $i \neq j$ and

$$\begin{aligned}\langle\widetilde{f}_i|T_\beta+\mathcal{L}|\widetilde{f}_i\rangle = {}& \frac{N(N+\beta+1)}{\beta+1}\left[\frac{\beta+4}{3x_i}+\frac{4(\beta+1)}{3(1-x_i)}-\beta-2\right]-\frac{\beta}{2}\\ & +\frac{\beta+10}{6x_i}+\frac{2\beta+5}{3(1-x_i)}+\frac{(\beta-5)(\beta+2)}{6x_i^2}-\frac{5}{3(1-x_i)^2}.\end{aligned} \tag{3.172}$$

The matrix elements of d^2/dx^2 can be obtained from Ref. [40].

3.5.5. *Regularized $\alpha = 0$ Lagrange–Jacobi mesh over* (0, 1)

The previous basis may have the drawback in physical applications that the mesh depends on β (Section 6.3). This problem can be circumvented with a regularization by x,

$$\hat{f}_j(x) = \frac{x}{x_j}\widetilde{f}_j(x) = (-1)^{N-j}\sqrt{\frac{1-x_j}{x_j}}\,\frac{P_N^{(0,\beta)}(2x-1)}{x-x_j}\,x^{\beta/2+1}. \tag{3.173}$$

The mesh and weights are unchanged. The first derivatives at mesh points read

$$\widetilde{\lambda}_i^{1/2}\hat{f}_j'(x_i) = (-1)^{i-j}\sqrt{\frac{x_i(1-x_j)}{x_j(1-x_i)}}\,\frac{1}{x_i-x_j} \tag{3.174}$$

for $i \neq j$ and

$$\widetilde{\lambda}_i^{1/2} \hat{f}_i'(x_i) = \frac{1}{2x_i(1-x_i)}. \tag{3.175}$$

They provide the exact matrix elements of d/dx. The second derivatives at mesh points read

$$\widetilde{\lambda}_i^{1/2} \hat{f}_j''(x_i) = \frac{(-1)^{i-j}}{\sqrt{x_i x_j (1-x_i)(1-x_j)}} \frac{(1-x_j)(2x_i^2 - x_i - x_j)}{(1-x_i)(x_i-x_j)^2} \tag{3.176}$$

for $i \neq j$ and

$$\widetilde{\lambda}_i^{1/2} \hat{f}_i''(x_i) = -\frac{1}{12x_i(1-x_i)} \left[(2N+\beta+1)^2 - 1 - \frac{\beta^2-4}{x_i} - \frac{8}{1-x_i} \right]. \tag{3.177}$$

They provide the exact matrix elements of d^2/dx^2.

The matrix elements of $T_0 + \mathcal{L}$ read

$$\langle \hat{f}_i | T_0 + \mathcal{L} | \hat{f}_j \rangle = \frac{(-1)^{i-j}}{\sqrt{x_i x_j (1-x_i)(1-x_j)}} \left[N(N+\beta+1) + \frac{\beta}{2} + 1 + \frac{x_i + x_j - 2x_i x_j}{(x_i-x_j)^2} - \frac{1}{1-x_i} - \frac{1}{1-x_j} \right] \tag{3.178}$$

for $i \neq j$ and

$$\langle \hat{f}_i | T_0 + \mathcal{L} | \hat{f}_i \rangle = \frac{1}{12x_i(1-x_i)} \left[4(2N+\beta+1)^2 - 3\beta^2 + 8 - \frac{\beta^2-4}{x_i} - \frac{20}{1-x_i} \right]. \tag{3.179}$$

For $\beta = 0$, one recovers (3.128) and (3.129). The matrix elements of $1/x$ and $1/x^2$ are now given exactly by the Gauss quadrature.

3.6. Lagrange meshes based on non-classical orthogonal polynomials

3.6.1. Non-classical orthogonal polynomials

All previous meshes were based on classical orthogonal polynomials. The definition of classical polynomials is given by (3.17) and (3.18). The advantage of these polynomials is that, in addition to a recurrence relation (3.3) and a Darboux–Christoffel relation (3.4), they also satisfy the self-adjoint second-order differential equation (3.19).

Certain non-classical orthogonal polynomials can have useful applications. Let us consider polynomials $\bar{p}_n(x)$ orthonormal over an interval (a, b) with respect to a non-classical weight function $w(x)$ [15,16],

$$\int_a^b w(x) \bar{p}_n(x) \bar{p}_{n'}(x) dx = \delta_{nn'}, \tag{3.180}$$

obtained by replacing $p_n(x)$ of Section 3.1 by $\bar{p}_n(x) = p_n(x)/\sqrt{h_n}$. The recurrence relation (3.3) for normed polynomials can be rewritten as

$$\beta_n \bar{p}_n(x) = (x - \alpha_n) \bar{p}_{n-1}(x) - \beta_{n-1} \bar{p}_{n-2}(x) \tag{3.181}$$

where

$$\alpha_n = \frac{k'_{n-1}}{k_{n-1}} - \frac{k'_n}{k_n} \tag{3.182}$$

and

$$\beta_n = \frac{k_{n-1}}{k_n} \sqrt{\frac{h_n}{h_{n-1}}}. \tag{3.183}$$

The first terms are $\bar{p}_{-1} = 0$ and

$$\bar{p}_0(x) = 1/\beta_0 \tag{3.184}$$

with

$$\beta_0^2 = \int_a^b w(x) dx. \tag{3.185}$$

The polynomials $\bar{p}_n(x)$ are successively obtained with [53–55]

$$\alpha_n = \int_a^b w(x) x \, [\bar{p}_{n-1}(x)]^2 \, dx \tag{3.186}$$

and

$$\beta_n = \int_a^b w(x) \, [(x-\alpha_n)\bar{p}_{n-1}(x) - \beta_{n-1}\bar{p}_{n-2}(x)]^2 \, dx. \tag{3.187}$$

In general, the coefficients in the recurrence relation are not available analytically and a numerical integration is necessary. These integrals must be calculated with high accuracy.

The zeros of $\bar{p}_N(x)$ can be obtained from the eigenvalues of the $N \times N$ matrix $\boldsymbol{X}$ with elements

$$X_{ij} = \int_a^b w(x) x \bar{p}_{i-1}(x) \bar{p}_{j-1}(x) dx \tag{3.188}$$

for $i, j = 1, \ldots, N$. This matrix is the representation of coordinate x in the basis of polynomials. It is symmetric and tridiagonal. Its non-zero matrix elements are

$$X_{ii} = \alpha_i, \qquad X_{i,i+1} = X_{i+1,i} = \beta_i. \tag{3.189}$$

Its eigenvalues are the mesh points of a Gauss quadrature. For classical orthogonal polynomials, one has $\beta_0 = \sqrt{h_0}$. The other coefficients are $\alpha_n = 0$ and $\beta_n = \sqrt{n/2}$ for Hermite, $\alpha_n = 2n + \alpha - 1$ and $\beta_n = -\sqrt{n(n+\alpha)}$ for Laguerre and $\alpha_n = 0$ and $\beta_n = \sqrt{n(n+2m)/(2n+2m+1)(2n+2m-1)}$ for Legendre. For Jacobi polynomials, they can be deduced from (3.151) and (3.149).

Let $\boldsymbol{O}$ be the matrix diagonalizing $\boldsymbol{X}$. The quadrature weights are given by [53]

$$\lambda_i = [w(x_i)]^{-1} (\beta_0 O_{1i})^2. \tag{3.190}$$

Equivalently, the weights can be obtained from (3.7) and (3.183) as [16]

$$\lambda_i^{-1} = \beta_N w(x_i) \bar{p}_{N-1}(x_i) \bar{p}'_N(x_i) \tag{3.191}$$

or with the Christoffel–Darboux relation (3.5) as

$$\lambda_i^{-1} = w(x_i) \sum_{k=1}^{N} [\bar{p}_{k-1}(x_i)]^2. \tag{3.192}$$

The accuracies of these variants may be quite different. The simpler expression (3.190) becomes rapidly inaccurate when N increases while (3.191) and specially (3.192) remain accurate up to much higher N values. A simple test is given by the exact relation

$$\sum_{i=1}^{N} \lambda_i w(x_i) = \beta_0^2 \tag{3.193}$$

derived from Eq. (3.185).

The derivatives of the polynomials are useful to compute the kinetic-energy matrix elements. They can be obtained from the derivatives of the recurrence relation (3.181) starting for the first derivative with $\bar{p}'_0(x) = 0$ and $\bar{p}'_1(x) = 1/(\beta_0\beta_1)$ and for the second derivative with $\bar{p}''_0(x) = \bar{p}''_1(x) = 0$ and $\bar{p}''_2(x) = 2/(\beta_0\beta_1\beta_2)$.

3.6.2. Symmetric Lagrange–Gaussian mesh on $(-\infty, +\infty)$

Two sets of orthogonal polynomials forming a basis equivalent to a set of shifted or distributed Gaussians have led to Lagrange meshes [56,57]. The notations in the original papers are rather different. In Ref. [56], the Gaussians have a width $1/c\sqrt{2}$ and a spacing 1. In Ref. [57], the Gaussians have a width 1 and a spacing a. The scaling parameter h introduced in the LMM [Eq. (2.44)] allows reaching arbitrary widths and spacings in both cases, but the comparison is not easy. Hence, the notations are slightly modified here to allow such a comparison. An example of use of this basis can be found in Ref. [58].

Since a mesh over $(-\infty, +\infty)$ can always be translated without difficulty, a mesh symmetric with respect to the origin is interesting. Let me start with the symmetric set of N shifted Gaussians

$$\exp[-\nu(x-n)^2], \quad n = -\frac{1}{2}(N-1), \ldots, \frac{1}{2}(N-1) \tag{3.194}$$

used in [57]. These Gaussians can be rewritten as

$$e^{-\nu(x-n)^2} = e^{-\nu(x^2+n^2)} (\cosh \nu x)^{N-1} (1 + \tanh \nu x)^{(N-1)/2+n} (1 - \tanh \nu x)^{(N-1)/2-n}. \tag{3.195}$$

This suggests the weight function

$$\hat{w}_N(x) = A_N e^{-2\nu x^2} (\cosh \nu x)^{2N-2}, \tag{3.196}$$

the basis functions being polynomials depending on $\tanh \nu x$ multiplied by its square root. Since $\hat{w}_N(x)$ depends on N, the coefficient

$$A_N = 2^{2N-2} e^{-(N-1)^2 \nu/2} \tag{3.197}$$

is chosen in such a way that the order of magnitude of $\hat{w}_N(x)$ does not vary too much with N.

The change of variable

$$t(x) = \tanh \nu x \tag{3.198}$$

where t varies over $(-1, +1)$, with inverse

$$x(t) = \frac{1}{\nu} \operatorname{arc\,tanh} t = \frac{1}{2\nu} \ln \frac{1+t}{1-t}, \tag{3.199}$$

transforms the Gaussians (3.195) into polynomials in t multiplied by the square root of the even weight function [see Eq. (2.49)]

$$w_N(t) = x'(t) \hat{w}_N[x(t)] = \nu^{-1} A_N e^{-(2\nu)^{-1}[\ln(1+t)-\ln(1-t)]^2} (1-t^2)^{-N}. \tag{3.200}$$

One can define polynomials $p_k(t)$ of degree k orthonormal with respect to $w_N(t)$. Since $w_N(t)$ is an even function of t, these polynomials are even for k even and odd for k odd. The functions

$$\varphi_k(x) = \sqrt{A_N} e^{-\nu x^2} (\cosh \nu x)^{N-1} p_k(\tanh \nu x) \tag{3.201}$$

for $k = 0$ to $N-1$ are then orthonormal over $(-\infty, +\infty)$,

$$\int_{-\infty}^{+\infty} \varphi_k(x) \varphi_{k'}(x) dx = \delta_{kk'}. \tag{3.202}$$

They are linear combinations of the Gaussians (3.194) and form an equivalent, but orthonormal, basis.

The coefficients α_n in (3.186) vanish because of parity. The coefficients β_n are given by (3.185) and (3.187), i.e. by

$$\beta_0^2 = A_N \int_{-\infty}^{+\infty} e^{-2\nu x^2} (\cosh \nu x)^{2N-2} dx \tag{3.203}$$

$$= \sqrt{\frac{\pi}{2\nu}} \sum_{j=0}^{2N-2} \binom{2N-2}{j} e^{-\nu j(2N-2-j)/2} \tag{3.204}$$

and

$$\beta_n^2 = A_N \int_{-\infty}^{+\infty} e^{-2\nu x^2} (\cosh \nu x)^{2N-2} \times [(\tanh \nu x) p_{n-1}(\tanh \nu x) - \beta_{n-1} p_{n-2}(\tanh \nu x)]^2 dx. \tag{3.205}$$

The integrals (3.205) can in principle be calculated analytically but a compact general result is not known. In practice, they can be computed accurately with the Gauss–Fourier quadrature (Section 3.7.1), i.e. with a constant step that must not be very small. The result (3.204) can be used to test the accuracy of a numerical evaluation of (3.203). Notice that it is in general very close to $\sqrt{2\pi/\nu}$.

The zeros t_i of $p_N(t)$,

$$p_N(t_i) = 0, \tag{3.206}$$

provide the mesh points of a Gauss quadrature with weights λ_i given by (3.191) or (3.192). The Lagrange mesh is defined for $i = -\frac{1}{2}(N-1), \ldots, \frac{1}{2}(N-1)$ as

$$x_i = \frac{1}{\nu} \operatorname{arc\,tanh} t_i \tag{3.207}$$

and the Lagrange functions by (2.50), (3.8) and (3.201) as

$$\hat{f}_j(x) = \hat{\lambda}_j^{-1/2} \frac{t'(x_j) \varphi_N(x)}{\varphi'_N(x_j)[t(x) - t_j]} \tag{3.208}$$

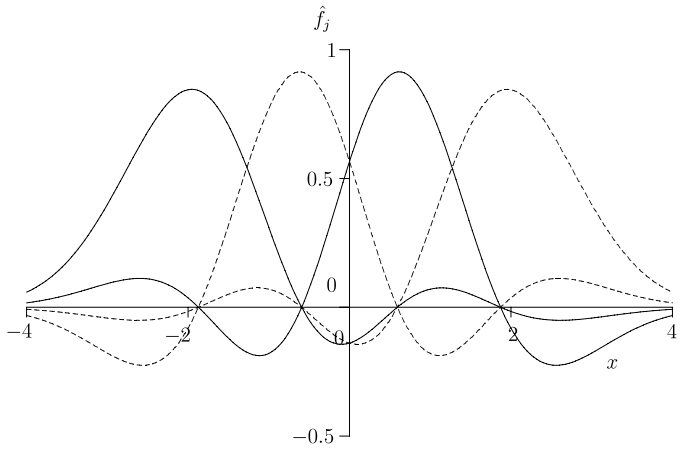

Fig. 10. Lagrange–Gaussian functions (3.208) for $\nu = 1/2$ and $N = 4$.

Table 1
Lagrange–Gaussian zeros and weights for $\nu = 1/2$ and $N = 4$.

x_i	±0.592 691 542 239 66	±1.870 672 397 539 59
λ_i	1.198 586 849 039 74	1.412 549 051 284 93

where

$$\hat{\lambda}_i = \lambda_i / t'(x_i) = \left\{ \sum_{k=1}^{N} [\varphi_{k-1}(x_i)]^2 \right\}^{-1}, \tag{3.209}$$

given by (2.48) and (3.192), is the weight corresponding to a Gauss quadrature with mesh points x_i. This quadrature is exact for the scalar products (3.202) and for integrals of products of two Gaussian functions (3.194). The Lagrange–Gaussian functions are displayed for $\nu = 1/2$ and $N = 4$ in Fig. 10. They are similar to the Lagrange–Hermite functions in Fig. 1 but one can see that the mesh points are different. The corresponding zeros and weights are given in Table 1.

The kinetic-energy matrix elements can be computed either from the matrix elements of Gaussians or with the symmetric approximation (2.37). They can also be accurately computed with the Gauss–Fourier quadrature.

3.6.3. Asymmetric Lagrange–Gaussian mesh on $(-\infty, +\infty)$

A Lagrange–Gaussian mesh based on the same principle, but different, was introduced earlier by Karabulut and Sibert [56]. It was tested numerically in Refs. [57,59]. In order to make a comparison with the previous mesh, the original basis of Ref. [56] is shifted and presented as

$$\exp[-\nu(x - n + d)^2], \quad n = 0, \ldots, N-1. \tag{3.210}$$

For $d = (N-1)/2$, this basis is equivalent to the symmetric basis (3.194). For $d = 0$, the original basis of Ref. [56] is recovered with $\nu = c^2$.

These Gaussians can be rewritten as

$$e^{-\nu(x-n+d)^2} = e^{-\nu n^2} e^{-\nu(x+d)^2} [e^{2\nu(x+d)}]^n, \tag{3.211}$$

which suggests the weight function

$$\hat{w}(x) = \sqrt{\frac{2\nu}{\pi}}\, e^{-2\nu(x+d)^2} \tag{3.212}$$

and the change of variable

$$u(x) = e^{2\nu(x+d)} \tag{3.213}$$

where u varies over $(0, \infty)$. In Ref. [56], orthogonal polynomials $p_k(u)$ are derived with the weight function

$$w(u) = x'(u)\hat{w}[x(u)] = \frac{1}{\sqrt{2\pi\nu}\, u}\, e^{-(\ln u)^2/2\nu}. \tag{3.214}$$

With this choice, one has $\beta_0 = 1$.

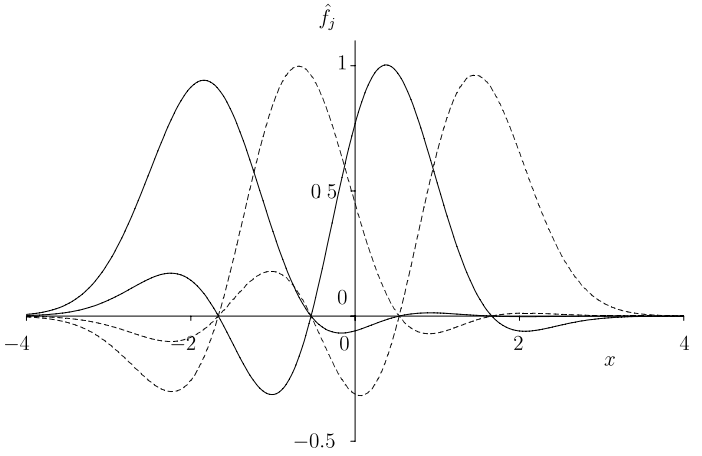

Fig. 11. Asymmetric Lagrange–Gaussian functions (3.220) for $\nu = 1/2$, $N = 4$, and $d = 7/4$.

An important advantage of these polynomials is that one can derive a recurrence relation with simple analytical expressions for the coefficients [56]. When normed, the polynomials $\bar{p}_n(u)$ satisfy the recurrence relation (3.181) with

$$\alpha_n = q^{-2n+3/2}(1 + q - q^n) \tag{3.215}$$

and

$$\beta_n = q^{-2n+1}(1 - q^n)^{1/2} \tag{3.216}$$

with $q = e^{-\nu}$. For $k = 0$ to $N - 1$, the functions

$$\varphi_k(x) = \left(\frac{2\nu}{\pi}\right)^{1/4} e^{-\nu(x+d)^2} \bar{p}_k[e^{2\nu(x+d)}] \tag{3.217}$$

are then linear combinations of the Gaussians (3.210) and are orthonormal.

With the zeros u_i of $\bar{p}_N(u)$ for $i = 1, \ldots, N$,

$$\bar{p}_N(u_i) = 0, \tag{3.218}$$

the Lagrange mesh is

$$x_i = (2\nu)^{-1} \ln u_i - d. \tag{3.219}$$

The Lagrange functions are given by

$$\hat{f}_j(x) = \hat{\lambda}_j^{-1/2} \frac{2\nu e^{2\nu(x+d)} \varphi_N(x)}{\varphi'_N(x_j)(e^{2\nu(x+d)} - u_j)} \tag{3.220}$$

where $\hat{\lambda}_j$ given by (2.48) is the weight corresponding to x_j.

Karabulut and Sibert have shown that the set of mesh points x_i is symmetric with respect to $N/2 - 1/4 - d$. For $d = (N-1)/2$, basis (3.210) [56] is equivalent to the symmetric basis (3.194) but the mesh is then slightly asymmetric. This apparently paradoxical situation is explained as follows. After the change of variables

$$u = \frac{1+t}{1-t} \tag{3.221}$$

where t belongs to $(-1, 1)$, the weight function (3.214) becomes proportional to (3.200) multiplied by the asymmetric factor $(1-t)^{2N}$. The two sets of polynomials are thus different.

The choice $d = N/2 - 1/4$ puts the middle of the set of mesh point at $x = 0$. The resulting symmetric mesh differs from the mesh of the previous subsection because it is obtained from a different – asymmetric – set of Gaussians, as is obvious from the comparison of (3.194) and (3.210) with $d \neq (N-1)/2$. These Lagrange–Gaussian functions are displayed for $\nu = 1/2$, $d = N/2 - 1/4$ and $N = 4$ in Fig. 11. They are similar to the Lagrange–Gaussian functions in Fig. 10 but the symmetric mesh is a little narrower here and the set of functions is obviously not symmetric.

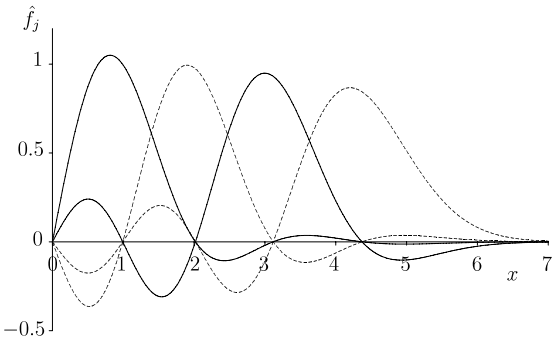

Fig. 12. Lagrange–Gaussian functions (3.229) on $(0, \infty)$ for $\nu = 1/2$ and $N = 4$.

3.6.4. Lagrange–Gaussian mesh on $(0, \infty)$

For a radial problem on the interval $(0, \infty)$, it is interesting to have a basis of functions vanishing at the origin. This can be obtained from Gaussian functions with the basis

$$\exp[-\nu(x-n)^2] - \exp[-\nu(x+n)^2] \propto \exp(-\nu x^2)\sinh(2n+1)\nu x, \quad n = 1, \ldots, N. \tag{3.222}$$

Notice the shift $n \to n + \frac{1}{2}(N+1)$ with respect to (3.194). The factor $\sinh(2n+1)\nu x$ is equal to $\sinh \nu x$ multiplied by a polynomial depending on $\sinh^2 \nu x$. Lagrange meshes corresponding to this basis can be obtained in several ways [57].

First, one can simply keep the positive sector of the mesh (3.207) with $2N$ points and project $2N$ Lagrange functions (3.208) on negative parity according to (2.52). Second, it is also possible to directly construct Lagrange functions inspired by (3.222). If the polynomials $p_k(\sinh^2 \nu x)$ are orthonormal with respect to the weight function

$$\hat{w}(x) = \exp(-2\nu x^2)\sinh^2 \nu x, \tag{3.223}$$

the basis (3.222) is equivalent to the orthonormal basis

$$\varphi_k(x) = \exp(-\nu x^2)\sinh \nu x\, \bar{p}_k(\sinh^2 \nu x) \tag{3.224}$$

with $k = 0, \ldots, N-1$. This suggests the change of variable

$$t(x) = \sinh^2 \nu x. \tag{3.225}$$

The weight function (3.223) becomes after this change of variable,

$$w(t) = x'(t)\hat{w}[x(t)] = \frac{1}{2\nu} e^{-2\nu^{-1}[\ln(\sqrt{t}+\sqrt{t+1})]^2} \sqrt{\frac{t}{t+1}} \tag{3.226}$$

and leads to the orthonormal polynomials $\bar{p}_k(t)$.

The zeros t_i of

$$\bar{p}_N(t_i) = 0 \tag{3.227}$$

provide the mesh points

$$x_i = \frac{1}{\nu}\ln(\sqrt{t_i} + \sqrt{t_i+1}). \tag{3.228}$$

The Lagrange functions are

$$\hat{f}_j(x) = \hat{\lambda}_j^{-1/2} \frac{\nu \sinh 2\nu x_j\, \varphi_N(x)}{\varphi_N'(x_j)(\sinh^2 \nu x - t_j)}. \tag{3.229}$$

They are displayed for $\nu = 1/2$ and $N = 4$ in Fig. 12. Because of their Gaussian origin, they have some resemblance with the modified Lagrange–Laguerre functions in Fig. 5.

3.7. Lagrange meshes based on periodic functions

3.7.1. Lagrange–Fourier mesh

The Lagrange–Fourier mesh is presented in [4] under the name 'Cartesian mesh'. The more appropriate denomination 'Fourier mesh' was later used by us since Ref. [37]. In fact, most properties of this mesh were first derived by Meyer for odd numbers of mesh points [60]. The corresponding Lagrange functions were obtained in Eq. (4.8) of Ref. [60]. They were rediscovered in Refs. [26,4] and employed in Ref. [33]. They are known under many different names and notations in the

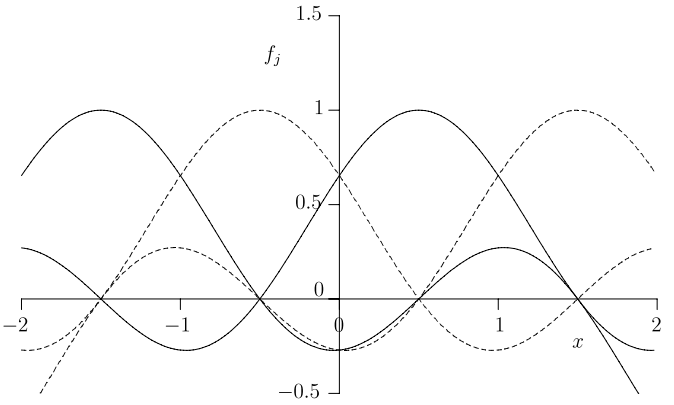

Fig. 13. Lagrange–Fourier functions (3.233) for $N = 4$. The definition interval is thus $(-2, 2)$.

literature. For example, they are called 'psinc' in Ref. [61], 'Dirichlet discrete representation' in Ref. [62] and hidden as the sum of cosines u_i^{per} in Ref. [63]. See Section 5.2 for an application of the Fourier mesh to the harmonic oscillator, Ref. [64] for applications to periodic potentials and Section 8.5 for translations and rotations on a Fourier mesh.

The Lagrange–Fourier functions are defined over the finite interval $(-\frac{1}{2}N, +\frac{1}{2}N)$. When N is large, this interval is a good approximation of $(-\infty, +\infty)$ for bound-state calculations. A variational basis over this interval is the set of N plane waves

$$\varphi_k(x) = N^{-1/2} e^{i2\pi kx/N}, \quad k = -\frac{1}{2}(N-1), \ldots, \frac{1}{2}(N-1). \tag{3.230}$$

The k values are integers if N is odd or half-integers if N is even. They can take half-integer values because differences between them remain integers. These functions are related to orthogonal polynomials of a complex variable [15,4]. The mesh points x_i are given by

$$x_i = i, \quad i = -\frac{1}{2}(N-1), \ldots, \frac{1}{2}(N-1). \tag{3.231}$$

The quadrature weights are

$$\lambda_i = 1. \tag{3.232}$$

This simple constant-step quadrature is in fact a sort of Gauss quadrature, which is named here the Gauss–Fourier quadrature, and is thus very accurate for infinitely differentiable functions [65]. It is exact for the products $\varphi_k^*(x)\varphi_{k'}(x)$ and thus for products of Lagrange functions (3.233).

The Lagrange–Fourier functions are real combinations (2.16) of the plane waves (3.230) and read [4]

$$f_j(x) = \frac{1}{N} \sum_{k=-\frac{1}{2}(N-1)}^{\frac{1}{2}(N-1)} e^{i2\pi k(x-x_j)/N} = \frac{\sin \pi (x - x_j)}{N \sin \frac{\pi}{N}(x - x_j)} \tag{3.233}$$

[see Eq. (B.1)]. The Lagrange–Fourier functions are displayed for $N = 4$ in Fig. 13.

The matrix elements of d^n/dx^n are given exactly by the Gauss–Fourier quadrature since the derivatives of $\varphi_k(x)$ are proportional to $\varphi_k(x)$ and the derivatives of the Lagrange functions are linear combinations of these Lagrange functions. They are thus obtained directly from $f_j^{(n)}(x_i)$. For d/dx, they read [60]

$$D_{i\neq j} = (-1)^{i-j} \frac{\pi}{N \sin[\pi (x_i - x_j)/N]}, \quad D_{ii} = 0. \tag{3.234}$$

The exact kinetic matrix elements of $-d^2/dx^2$ [60,4] are given by (2.35) as

$$T_{i\neq j} = (-1)^{i-j} \frac{2\pi^2 \cos[\pi (x_i - x_j)/N]}{N^2 \sin^2[\pi (x_i - x_j)/N]}, \tag{3.235}$$

$$T_{ii} = \frac{\pi^2}{3}\left(1 - \frac{1}{N^2}\right). \tag{3.236}$$

Let $\boldsymbol{D}$ and $\boldsymbol{T}$ be the corresponding matrices. With Eqs. (3.233) and (2.15), one easily proves

$$\boldsymbol{T} = -\boldsymbol{D}^2. \tag{3.237}$$

Similar relations exist for the matrix elements of higher-order derivatives.

The Lagrange–Fourier functions can also be useful for periodic problems. They are in particular very useful for treating the azimuthal angle φ on $(0, 2\pi)$. With a scaling factor $h = 2\pi/N$ and a translation, the mesh points are given for $i = 1$ to N by (2.42) as

$$x_i = \frac{2i-1}{N}\pi \tag{3.238}$$

and the weights by (2.43) as

$$\lambda_i = \frac{2\pi}{N}. \tag{3.239}$$

This quadrature has incorrectly been interpreted as corresponding to a Gauss–Chebyshev quadrature of the first kind [66]. While the meshes are similar, the basis corresponding to Chebyshev polynomials of the first kind and thus the Lagrange functions differ from (3.230) and (3.233). See Section 3.7.4 for the Lagrange mesh related to these polynomials.

The Lagrange functions can be obtained from relation (3.233), scaled with h according to (2.44). The kinetic matrix elements read according to (2.46) [5],

$$T_{i\neq j} = (-1)^{i-j}\frac{\cos\frac{1}{2}(x_i - x_j)}{2\sin^2\frac{1}{2}(x_i - x_j)}, \tag{3.240}$$

$$T_{ii} = \frac{1}{12}\left(N^2 - 1\right). \tag{3.241}$$

3.7.2. First sine meshes

The preceding constant-step mesh has been introduced for one-dimensional problems on the $(-\infty, +\infty)$ interval, approximated as a scaled symmetric finite interval $(-1, 1)$ [26,4,27,67]. It is possible to define meshes based on sine functions on the $(-1, 1)$ interval [66,33,6]. Meshes can also be derived for the $(0, 1)$ interval (see Section 5.5) that can be scaled as $(0, h)$ to approximate the $(0, \infty)$ domain useful to describe radial equations. In this case, basis functions vanishing at the origin are of particular interest. The kinetic matrix elements are derived by Muckerman [66] (see also Ref. [33]). They are rediscovered as 'little sinc functions' in Ref. [68] in a collocation context.

Different meshes are obtained according to the boundary conditions imposed on the basis functions. Let us first consider the orthonormal functions

$$\varphi_k(x) = \sqrt{2}\sin\pi kx \tag{3.242}$$

($k = 1, \ldots, N$), which vanish at both ends of the $(0, 1)$ interval. For these functions, the left-hand sides of the Lagrange conditions (2.14) read with (B.2),

$$\sum_{k=1}^{N}\varphi_k(x_i)\varphi_k(x_j) = \frac{1}{2}\left\{\frac{\sin[(2N+1)\frac{\pi}{2}(x_i - x_j)]}{\sin\frac{\pi}{2}(x_i - x_j)} - \frac{\sin[(2N+1)\frac{\pi}{2}(x_i + x_j)]}{\sin\frac{\pi}{2}(x_i + x_j)}\right\} \tag{3.243}$$

for $i \neq j$. Expression (3.243) vanishes when both terms have the common value 1 or -1 [32]. A mesh with step $1/(N+1)$ is given by

$$x_i = \frac{i}{N+1}, \quad i = 1, \ldots, N. \tag{3.244}$$

This mesh is symmetric with respect to 1/2. The number of mesh points can be even or odd. The corresponding quadrature weights are given by (2.14) as

$$\lambda_i = \frac{1}{N+1}. \tag{3.245}$$

With (3.243), a compact form for the Lagrange functions is readily established from (2.16) as

$$f_j(x) = \frac{\sqrt{N+1}}{2}\left\{\frac{\sin[(2N+1)\frac{\pi}{2}(x - x_j)]}{\sin\frac{\pi}{2}(x - x_j)} - \frac{\sin[(2N+1)\frac{\pi}{2}(x + x_j)]}{\sin\frac{\pi}{2}(x + x_j)}\right\}. \tag{3.246}$$

The first Lagrange-sine functions are displayed for $N = 4$ in Fig. 14. Notice that these Lagrange functions can also be obtained by a negative-parity projection (2.52) of the Lagrange–Fourier functions (3.233) for an odd number $2N + 1$ of mesh points, after scaling the corresponding interval $(-N - \frac{1}{2}, N + \frac{1}{2})$ to $(-1, 1)$.

A derivation of compact expressions for the matrix elements of the kinetic energy is easy with the Gauss quadrature defined by (3.244) and (3.245). With (2.35), one obtains exact expressions since $\varphi_k''(x)$ is proportional to $\varphi_k(x)$ so that the

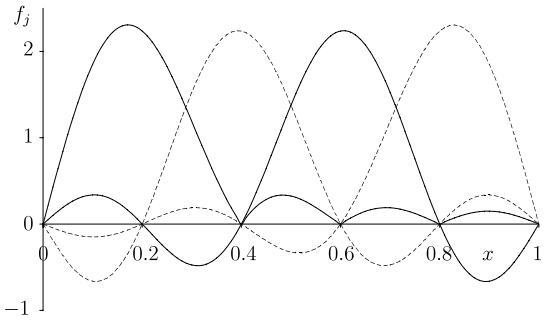

Fig. 14. First Lagrange-sine functions (3.246) over (0, 1) for $N = 4$.

Gauss-quadrature formula is exact for matrix elements of derivatives of even order. Notice that the matrix elements of the first-order derivative are thus not exactly given by the Gauss quadrature. The kinetic matrix elements read

$$T_{i\neq j} = (-1)^{i-j}\frac{\pi^2}{2}\left[\frac{1}{\sin^2\frac{\pi}{2}(x_i - x_j)} - \frac{1}{\sin^2\frac{\pi}{2}(x_i + x_j)}\right] \tag{3.247}$$

and

$$T_{ii} = \frac{\pi^2}{2}\left[\frac{2}{3}(N+1)^2 + \frac{1}{3} - \frac{1}{\sin^2\pi x_i}\right]. \tag{3.248}$$

The correctness of the numerical kinetic-energy matrix can be tested on its eigenvalues $\pi^2 k^2$, $k = 1, \ldots, N$. Eqs. (3.247) and (3.248) were derived in Ref. [69] but the authors did not use them with a diagonal potential matrix. Eqs. (3.244)–(3.248) were established by Schwartz (Eqs. (37) and (39) of Ref. [26]) in a collocation context, without mention neither of a Gauss quadrature, nor of their exactness.

As noted in Refs. [66,70], this mesh is related to the Chebyshev polynomials of the second kind. Indeed, these polynomials are defined by

$$U_n(\cos u) = \frac{\sin(n+1)u}{\sin u} \tag{3.249}$$

with $h_n = \pi/2$ and $k_n = 2^n$ [22]. One can rewrite Eq. (3.242) for $k = 1$ to N as

$$\varphi_k(x) = \sqrt{2}\sin\pi x\, U_{k-1}(\cos\pi x). \tag{3.250}$$

The mesh points are solutions of

$$U_N(\cos\pi x_i) \propto \sin(N+1)\pi x_i = 0 \tag{3.251}$$

which leads to the mesh (3.244). By using the Christoffel–Darboux relation (3.4), the Lagrange functions (2.16) can be written as

$$f_j(x) = \lambda_j^{1/2}\sin\pi x_j\, U_{N-1}(\cos\pi x_j)\,\frac{\sin\pi x U_N(\cos\pi x)}{\cos\pi x - \cos\pi x_j} \tag{3.252}$$

$$= \frac{1}{\sqrt{N+1}}\sin N\pi x_j\,\frac{\sin(N+1)\pi x}{\cos\pi x - \cos\pi x_j} \tag{3.253}$$

which is equivalent to (3.246). The Gauss quadrature associated with (3.244)–(3.245) is obtained from the Gauss–Chebyshev quadrature of the second kind [22] after a change of variable $x \to \cos\pi x$. Equivalent expressions for (3.247) and (3.248) can be derived in a similar way.

Interestingly, the same basis leads to two other meshes [32]. These meshes are asymmetric but mutually symmetric with respect to the centre 1/2 of the interval. The expressions (3.243) also vanish when both numerators are simultaneously zero. The two meshes with constant spacing $2/(2N+1)$ are for $i = 1, \ldots, N$ [32],

$$x_i = \frac{2i-1}{2N+1} \tag{3.254}$$

and

$$x_i = \frac{2i}{2N+1}. \tag{3.255}$$

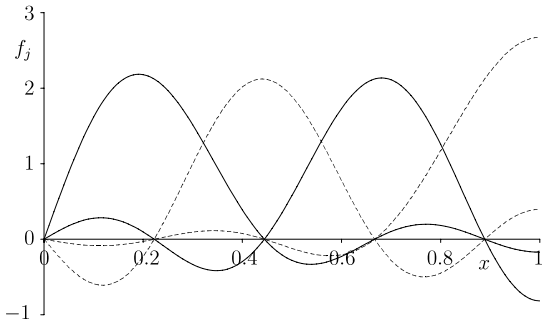

Fig. 15. Second Lagrange-sine functions (3.260) over (0, 1) for $N = 4$.

The corresponding weights λ_i are

$$\lambda_i = \frac{2}{2N+1}. \tag{3.256}$$

The Gauss formula also takes here a very simple form. See [32] for the expressions of the kinetic matrix elements. These meshes are also related to the Chebyshev polynomials of the second kind. For pairs of different zeros, the numerator of the Darboux–Christoffel relation (3.4) vanishes in a more complicated way than in Eq. (3.251).

3.7.3. Second sine meshes

Other sine meshes on the (0, 1) interval correspond to a basis that does not vanish at 1. One of them has been used in scattering problems [71,72]. The orthonormal functions

$$\varphi_k(x) = \sqrt{2}\sin\pi\left(k-\frac{1}{2}\right)x \tag{3.257}$$

($k = 1, \ldots, N$) vanish at 0 and their first derivatives vanish at 1. With Eq. (B.3), the left-hand side of the Lagrange conditions reads

$$\sum_{k=1}^{N}\varphi_k(x_i)\varphi_k(x_j) = \frac{1}{2}\left[\frac{\sin N\pi(x_i-x_j)}{\sin\frac{\pi}{2}(x_i-x_j)} - \frac{\sin N\pi(x_i+x_j)}{\sin\frac{\pi}{2}(x_i+x_j)}\right] \tag{3.258}$$

for $i \neq j$. They are satisfied when both terms have the same value $+1$ or -1. These conditions provide the asymmetric constant-step mesh

$$x_i = \frac{2i}{2N+1}, \quad i = 1, \ldots, N, \tag{3.259}$$

which is identical to the mesh (3.255) with the same weights (3.256). However, in spite of this similarity, the two meshes correspond to different Lagrange functions with different boundary conditions. Relation (3.258) provides

$$f_j(x) = \frac{1}{\sqrt{4N+2}}\left[\frac{\sin N\pi(x-x_j)}{\sin\frac{\pi}{2}(x-x_j)} - \frac{\sin N\pi(x+x_j)}{\sin\frac{\pi}{2}(x+x_j)}\right]. \tag{3.260}$$

The second Lagrange-sine functions are displayed for $N = 4$ in Fig. 15. Notice that their first derivatives all vanish at $x = 1$.

For $i \neq j$, the T_{ij} are given by (3.247),

$$T_{i\neq j} = (-1)^{i-j}\frac{\pi^2}{2}\left[\frac{1}{\sin^2\frac{\pi}{2}(x_i-x_j)} - \frac{1}{\sin^2\frac{\pi}{2}(x_i+x_j)}\right], \tag{3.261}$$

but with different values for the x_i. For $i = j$, they slightly differ from (3.248),

$$T_{ii} = \frac{\pi^2}{2}\left[\frac{2}{3}N(N+1) + \frac{1}{2} - \frac{1}{\sin^2\pi x_i}\right]. \tag{3.262}$$

The correctness of the kinetic-energy matrix can be tested on its eigenvalues $\pi^2(k-\frac{1}{2})^2$.

This mesh is related to Jacobi polynomials with $\alpha = 1/2$ and $\beta = -1/2$ [66,70] by

$$\sin(2n+1)u = \sin u\, U_{2n}(\cos u) = \sqrt{\pi}h_n^{-1/2}\sin u\, P_n^{(1/2,-1/2)}(\cos 2u), \tag{3.263}$$

[22] where $h_n = [\Gamma(n+1/2)/n!]^2$ is given by (3.149). Eq. (3.257) can be rewritten as

$$\varphi_k(x) = \sqrt{\pi} h_{k-1}^{-1/2} (1-\cos\pi x)^{1/2} P_{k-1}^{(1/2,-1/2)}(\cos\pi x). \tag{3.264}$$

The mesh points (3.259) are solutions of

$$P_N^{(1/2,-1/2)}(\cos\pi x_i) = 0. \tag{3.265}$$

By using relation (3.4), the Lagrange functions (2.16) can be written as

$$f_j(x) = \sqrt{\frac{\lambda_j}{h_{N-1}}} \sin\frac{1}{2}\pi x_j P_{N-1}^{(1/2,-1/2)}(\cos\pi x_j) \frac{\sin\frac{1}{2}\pi x P_N^{(1/2,-1/2)}(\cos\pi x)}{\cos\pi x - \cos\pi x_j} \tag{3.266}$$

$$= \sqrt{\frac{2}{2N+1}} \sin\left(N-\frac{1}{2}\right)\pi x_j \frac{\sin\left(N+\frac{1}{2}\right)\pi x}{\cos\pi x - \cos\pi x_j}, \tag{3.267}$$

which is equivalent to (3.260). The Gauss quadrature associated with (3.256) and (3.259) is obtained from the Gauss–Jacobi quadrature after a change of variable $x \to \cos\pi x$. Equivalent expressions for (3.261) and (3.262) can be derived in a similar way.

Additional meshes correspond to the same basis (3.257). The Lagrange conditions (3.258) are also satisfied when both numerators vanish simultaneously. A mesh symmetric with respect to 1/2 is

$$x_i = \frac{2i-1}{2N}, \quad i = 1, \ldots, N. \tag{3.268}$$

The weights are given by (2.14) as

$$\lambda_i = \frac{1}{N}. \tag{3.269}$$

Here the Lagrange functions are still given by (3.260) but with different mesh points. The exact expressions of the kinetic matrix elements are

$$T_{i\neq j} = (-1)^{i-j}\frac{\pi^2}{2}\left[\frac{\cos\frac{\pi}{2}(x_i-x_j)}{\sin^2\frac{\pi}{2}(x_i-x_j)} + \frac{\cos\frac{\pi}{2}(x_i+x_j)}{\sin^2\frac{\pi}{2}(x_i+x_j)}\right] \tag{3.270}$$

and

$$T_{ii} = \frac{\pi^2}{2}\left[\frac{1}{6}(4N^2-1) + \frac{\cos\pi x_i}{\sin^2\pi x_i}\right]. \tag{3.271}$$

The correctness of the kinetic-energy matrix can be tested on its eigenvalues $\pi^2(k-\frac{1}{2})^2$, $k = 1, \ldots, N$. The results (3.268)–(3.271) and (3.260) can also be obtained by projecting the Fourier-mesh results (3.231), (3.232) and (3.235), (3.236) on negative parity for even numbers $2N$ of mesh points, after scaling the interval $(-N, N)$ to $(-1, 1)$.

Another mesh satisfying (3.258),

$$x_i = \frac{i}{N}, \quad i = 1, \ldots, N, \tag{3.272}$$

is equivalent to the mesh employed in Ref. [71] and simplified in Ref. [67]. Here the spacing between successive points is $1/N$. As the last point $x_N = 1$ is at the upper boundary of the interval, the corresponding formulas are slightly more complicated since the last point requires a separate treatment. It was used in an R-matrix treatment in Ref. [71]. Drawbacks of this mesh are discussed in Refs. [42,14].

These meshes also correspond to Jacobi polynomials. For pairs of different zeros, the numerator of relation (3.4) vanishes in a more complicated way than in Eq. (3.265).

3.7.4. Cosine meshes

Let us consider the orthonormal functions

$$\varphi_k(x) = (2-\delta_{k0})^{1/2}\cos\pi kx \tag{3.273}$$

($k = 0, \ldots, N-1$), the derivatives of which vanish at both ends of the (0, 1) interval. This basis was studied in Ref. [70].

With Eq. (B.2), the left-hand sides of the Lagrange conditions (2.14) read

$$\sum_{k=0}^{N-1}\varphi_k(x_i)\varphi_k(x_j) = \frac{1}{2}\left\{\frac{\sin[(2N-1)\frac{\pi}{2}(x_i-x_j)]}{\sin\frac{\pi}{2}(x_i-x_j)} + \frac{\sin[(2N-1)\frac{\pi}{2}(x_i+x_j)]}{\sin\frac{\pi}{2}(x_i+x_j)}\right\} \tag{3.274}$$

for $i \neq j$. A mesh with step $1/N$ given by

$$x_i = \frac{2i-1}{2N} \tag{3.275}$$

for $i = 1$ to N is symmetric with respect to $1/2$. The corresponding quadrature weights are given by (2.14) as

$$\lambda_i = \frac{1}{N}. \tag{3.276}$$

Using Appendix B, the Lagrange functions can be simplified with respect to Eq. (8) of Ref. [70] as

$$f_j(x) = \frac{1}{\sqrt{N}} \left[\frac{\sin \frac{2N-1}{2}\pi(x-x_j)}{\sin \frac{\pi}{2}(x-x_j)} - \frac{\sin \frac{2N-1}{2}\pi(x+x_j)}{\sin \frac{\pi}{2}(x+x_j)} \right]. \tag{3.277}$$

The kinetic matrix elements of $-d^2/dx^2$ are exactly given by the Gauss quadrature defined by (3.275) and (3.276). They read [70]

$$T_{i\neq j} = (-1)^{i-j} \frac{\pi^2}{2} \left[\frac{1}{\sin^2 \frac{\pi}{2}(x_i - x_j)} - \frac{1}{\sin^2 \frac{\pi}{2}(x_i + x_j)} \right] \tag{3.278}$$

and

$$T_{ii} = \frac{\pi^2}{2} \left[\frac{1}{3}(2N^2+1) - \frac{1}{\sin^2 \pi x_i} \right]. \tag{3.279}$$

These expressions are almost identical to (3.247) and (3.248) with N replacing $N+1$ and different sets of mesh points x_i. The correctness of the kinetic-energy matrix can be tested on its eigenvalues $\pi^2 k^2$, $k = 0, \ldots, N-1$.

The Lagrange functions (3.277) are related to the Chebyshev polynomials of the first kind [70] since [22]

$$T_n(\cos u) = \cos nu. \tag{3.280}$$

The mesh points (3.275) are solutions of

$$T_N(\cos \pi x_i) = \cos N\pi x_i = 0. \tag{3.281}$$

The Lagrange functions can be written as

$$f_j(x) = \frac{1}{\sqrt{N}} T_{N-1}(\cos \pi x_j) \frac{T_N(\cos \pi x)}{\cos \pi x - \cos \pi x_j} \tag{3.282}$$

$$= \frac{1}{\sqrt{N}} \cos(N-1)\pi x_j \frac{\cos N\pi x}{\cos \pi x - \cos \pi x_j}, \tag{3.283}$$

which is equivalent to (3.277). The quadrature (3.274), (3.275) is obtained from the Gauss–Chebyshev quadrature of the first kind [22] after a change of variable $x \to \cos \pi x$.

Two other meshes can be obtained from (3.274) for $i = 1, \ldots, N$,

$$x_i = \frac{2i-2}{2N-1} \tag{3.284}$$

and

$$x_i = \frac{2i-1}{2N-1}. \tag{3.285}$$

They are mutually symmetric and each of them involves one extremity of the interval. These meshes also correspond to Chebyshev polynomials of the first kind. For pairs of different zeros, the numerator of relation (3.4) vanishes in a more complicated way than in Eq. (3.281). The mesh (3.284) can also be obtained by projecting the Fourier mesh (3.231) on positive parity for an odd number $2N-1$ of mesh points, after scaling the interval $(-N+\frac{1}{2}, N-\frac{1}{2})$ to $(-1, 1)$.

3.7.5. Cardinal sine (sinc) mesh

The Lagrange-sinc functions are defined over $(-\infty, +\infty)$ [26,33,37,6]. They are not periodic but they are closely related to the Fourier mesh. The corresponding mesh was first used for a quantum-mechanical problem by Schwartz in a collocation spirit [26]. Colbert and Miller introduced this basis and mesh in a variational approach in the context of the DVR as the limit of a sine mesh [33]. This mesh was rediscovered several times [62,73].

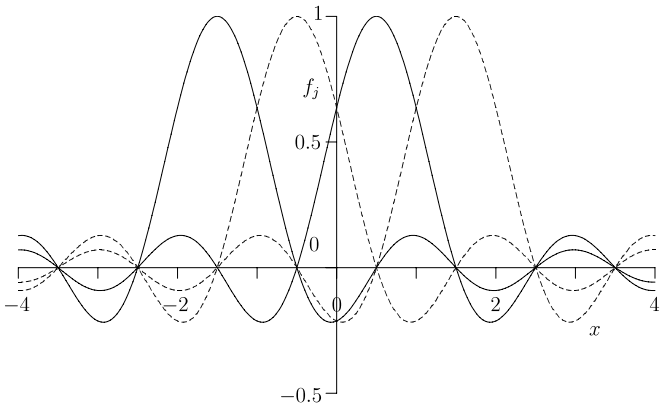

Fig. 16. Lagrange-sinc functions (3.288) for $N = 4$.

The mesh points

$$x_i = i, \quad i = -\frac{1}{2}(N-1), \ldots, \frac{1}{2}(N-1), \tag{3.286}$$

and weights

$$\lambda_i = 1 \tag{3.287}$$

are the same as those of the Fourier mesh [Eqs. (3.231) and (3.232)]. They define a Gauss-like quadrature for finite N values, identical to the Gauss–Fourier quadrature. The interest of this constant-step Gauss quadrature was first discussed by Schwartz [65]. The Lagrange-sinc functions are defined as

$$f_j(x) = \mathrm{sinc}\,(x - x_j), \tag{3.288}$$

where the sinc or cardinal sine function is given by [74]

$$\mathrm{sinc}\, x = \frac{\sin \pi x}{\pi x}. \tag{3.289}$$

The Lagrange-sinc functions are displayed for $N = 4$ in Fig. 16. They resemble the Lagrange–Fourier functions of Fig. 13, with an important difference: the interval of definition is infinite. In spite of this infinite interval, one observes in Fig. 16 that the useful part of this interval and the mesh points are located in $(-\frac{1}{2}(N+1), \frac{1}{2}(N+1))$.

Contrary to some statements in the literature, a finite Lagrange-sinc basis is orthonormal [74] and does not require additional approximations with respect to other Lagrange bases. There is no need to consider that a part of an infinite basis must be neglected as assumed in Ref. [33]. Also, the statement that there is 'no explicit reference to an underlying basis set' [33] is not correct.

The complete set of Lagrange-sinc functions can be seen as the limit of the Lagrange–Fourier functions for $N \to \infty$ [33],

$$f_j(x) = \lim_{N\to\infty} \frac{\sin \pi (x - x_j)}{N \sin \frac{\pi}{N}(x - x_j)}. \tag{3.290}$$

The matrix elements of d/dx are [26]

$$D_{i\neq j} = (-1)^{i-j} \frac{1}{x_i - x_j}, \quad D_{ii} = 0. \tag{3.291}$$

The exact kinetic matrix elements are given either by a direct calculation or by the limit of (3.235)–(3.236) for $N \to \infty$ [26,33],

$$T_{i\neq j} = (-1)^{i-j} \frac{2}{(x_i - x_j)^2}, \tag{3.292}$$

$$T_{ii} = \frac{\pi^2}{3}. \tag{3.293}$$

The Lagrange-sinc basis can be projected on parity over $(0, \infty)$ [33]. To avoid a mesh point at the origin, one chooses the even number $2N$ of points before projection. The resulting basis is scaled with $h = 1/N$, i.e. in such a way that the mesh points are inside the $(0, 1)$ interval. One obtains for $i = 1$ to N the mesh

$$x_i = \frac{2i - 1}{2N}. \tag{3.294}$$

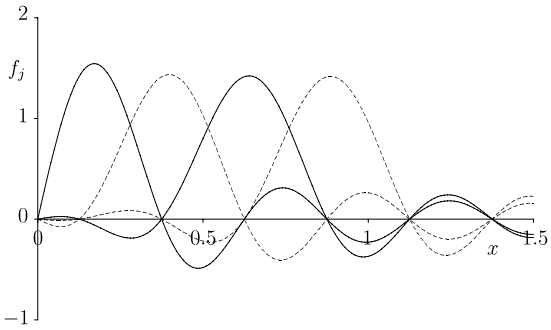

Fig. 17. Negative-parity Lagrange-sinc functions (3.296) for $N = 4$.

The Gauss-quadrature weights read

$$\lambda_i = \frac{1}{N}. \tag{3.295}$$

The Lagrange functions (2.52) for parity $p = \pm 1$ are given by

$$f_j^p(x) = (N/2)^{1/2}\{\mathrm{sinc}\,[N(x - x_j)] + p\,\mathrm{sinc}\,[N(x + x_j)]\}. \tag{3.296}$$

These functions are defined over $(0, \infty)$. For $p = -1$, they vanish at the origin and are displayed for $N = 4$ in Fig. 17. The part extending beyond $x = 9/8$ does not play a physical role.

The kinetic matrix elements (2.55) read [33]

$$T^p_{i\neq j} = (-1)^{i-j}N^2\left[\frac{2}{(x_i - x_j)^2} + \frac{2p}{(x_i + x_j)^2}\right] \tag{3.297}$$

and

$$T^p_{ii} = N^2\left(\frac{\pi^2}{3} + \frac{p}{2x_i^2}\right). \tag{3.298}$$

3.8. Numerical considerations

For calculations of bound-state energies, only the values x_i of the mesh-point locations and a method of diagonalization of a symmetric matrix are needed in Lagrange-mesh calculations. They allow calculating the values of the matrix elements D_{ij} and T_{ij} with the formulas of the present section. The weights λ_i are only needed to obtain explicit expressions of the wave functions or when the potential is non-local [Eq. (2.30)].

The zeros x_i and weights λ_i corresponding to classical orthogonal polynomials are available in most libraries of programs. Home-made values can be obtained with the technique of Section 3.6.1 using the coefficients given after Eq. (3.189).

The explicit evaluation of Lagrange functions can be obtained simply with the form (2.17) or (2.18) of these functions. However, these expressions are inaccurate in the vicinity of the zero x_j associated with a Lagrange function $f_j(x)$ since both the numerator and denominator tend to zero. In a small interval around x_j, one can evaluate $f_j(x)$ with the second-order Taylor expansion

$$f_j(x) \approx \lambda_j^{-1/2}\left[1 + f_j'(x_j)(x - x_j) + \frac{1}{2}f_j''(x_j)(x - x_j)^2\right] \tag{3.299}$$

since $f_j'(x_j)$ and $f_j''(x_j)$ are known. Another option is to use in this interval or everywhere expression (2.16), when it exists.

Some applications may require further matrix algebra such as matrix inversion (Section 6.1) or complex-matrix diagonalization (Section 6.6). For multidimensional problems, only a number of lowest eigenvalues of a large matrix are in general necessary. A diagonalization becomes unpractical and specific techniques should be used such as in Ref. [75].

4. Comparison with related methods

4.1. Historical aspects

The Lagrange-mesh method is based on three ingredients: (i) the variational method, (ii) a Gauss quadrature and (iii) Lagrange functions which are proportional to cardinal functions associated with the quadrature mesh points. All these

ingredients are well known and all three have been widely used separately or in some combinations for quantum mechanical problems. This is obvious for the variational method but the simultaneous use of the other two ingredients is less well known.

A number of papers discuss the interest of the Gauss quadrature and/or cardinal functions. I now quote important works that were not known to me when reference [4] was written. This subsection is devoted to seminal papers introducing some of the above ingredients. The next subsections are devoted to important competing techniques that are sometimes very close to the LMM or even essentially identical in particular cases.

Harris et al. have opened the way by suggesting to start with the matrix representation $\boldsymbol{X}$ of the coordinate x in some basis of N square-integrable functions $\varphi_j(x)$, i.e.,

$$X_{ij} = \langle\varphi_i|x|\varphi_j\rangle. \tag{4.1}$$

They diagonalize this matrix with an orthogonal matrix $\boldsymbol{O}$,

$$\boldsymbol{X} = \boldsymbol{O}\,\mathrm{diag}(x_1, x_2, \ldots, x_N)\boldsymbol{O}^{-1} \tag{4.2}$$

and use the resulting eigenvalues x_i and eigenvector matrix $\boldsymbol{O}$ to approximate the matrix representation $\boldsymbol{V}$ of $V(x)$ [76] as

$$\boldsymbol{V} = \boldsymbol{O}\,\mathrm{diag}[V(x_1), V(x_2), \ldots, V(x_N)]\boldsymbol{O}^{-1}. \tag{4.3}$$

Matrix $\boldsymbol{O}$ is not denoted with the usual notation $\boldsymbol{T}$ to avoid confusion with the kinetic-energy matrix. This idea is at the basis of the DVR described in Section 4.2.

Dickinson and Certain [77] made an important contribution by justifying the method of Harris et al. with the Gauss quadrature when the basis functions are constructed from orthogonal polynomials. They showed that relation (4.2) then provides the zeros of an orthogonal polynomial as eigenvalues, with an orthogonal matrix $\boldsymbol{O}$ [see Eq. (3.188)]. These zeros can thus be related to a Gauss quadrature. Relation (4.3) arises from this Gauss quadrature. Dickinson and Certain remark that '*the evaluation of the matrix elements and the convergence of the eigenvalues with increasing N need not be considered simultaneously*'. In other words, the accuracy on some eigenvalues can be better than the accuracy on individual matrix elements.

Meyer starts with the constant-step mesh (3.231) scaled over $(-\pi, +\pi)$ [60]. A Fourier expansion equivalent to basis (3.230) for an odd number N of mesh points leads to an exact derivation of the matrix elements of d/dx and d^2/dx^2. Interestingly, Meyer reinterprets these results in terms of functions denoted as $\delta_j(x)$ that are nothing but properly scaled Lagrange–Fourier functions (3.233). His application to the one-dimensional harmonic oscillator is thus equivalent to a Lagrange-mesh calculation (Section 5.2), but in a collocation spirit for the potential term. The conceptual difference with the LMM lies in the absence of the Gauss-like quadrature justification. Meyer does not notice that the developed method is also valid for even numbers of mesh points.

Manolopoulos and Wyatt proposed a method the spirit of which is very close to the LMM [78]. They start with a Gauss-like quadrature, the Lobatto quadrature [22] which includes the extremities of the interval in the mesh, and construct consistent interpolation functions equivalent to Lagrange functions. These functions are used together with the Lobatto quadrature in the Kohn variational principle to study reactions. The Lobatto quadrature is chosen in order to impose specific boundary conditions to scattering wave functions. These authors notice that their basis is not exactly orthogonal but that it is orthonormal with the Lobatto quadrature and that this approximation is at least as good as the exact calculation. This approach is close to, but slightly more complicated and slightly less accurate, than the LMM. Even for scattering problems, there is no obvious advantage in having the extremities of the interval as mesh points (see Section 6.1).

4.2. Discrete-variable representation

The method of the discrete-variable representation (DVR) has known several evolutions and still has presently several definitions. As explained below, for the meshes based on classical orthogonal polynomials, it is equivalent to the LMM, but without the use of Lagrange functions in its original form.

Ref. [79] is sometimes quoted as the origin of the DVR. In that work, a method is introduced to make use of a set of values of energy surfaces at different points in calculations of molecular spectra. This method is basically a collocation method with a freedom of choice of the mesh but the arbitrary choice of the mesh points does not lead to a high accuracy.

The real start of the DVR can be found in a 1985 paper [18] referring in his title to a '*generalized discrete-variable approximation*' but first giving a precise definition of the DVR (see below for the 'generalized' aspect). In that work, a variational approximation of the wave function

$$\psi(x) = \sum_{k=1}^{N} c_k\varphi_k(x) \tag{4.4}$$

expanded in a finite basis $\varphi_k(x)$ related to polynomials $p_{k-1}(x)$ orthogonal on interval (a, b), in the present notation, is combined with a Gauss quadrature based on these orthogonal polynomials in the spirit of Ref. [76]. This method is denoted as the Finite-Basis Representation (FBR). The N mesh points are defined as the zeros of $p_N(x)$,

$$p_N(x_i) = 0. \tag{4.5}$$

The matrix representation of the Hamiltonian is transformed with an orthogonal matrix $\boldsymbol{O}$ with elements

$$O_{ij} = \varphi_i(x_j)\sqrt{\lambda_j}, \tag{4.6}$$

where the λ_j are the Gauss weights in the present notation, into another representation in which the Gauss-quadrature approximation of the potential is diagonal. The DVR basis is related to the mesh points but is not defined explicitly; orthogonal transformations are performed at the level of matrix elements. A look at Eq. (2.16) shows that the orthogonal transformation leads to Lagrange functions.

The matrix elements of the kinetic-energy operator are calculated in the φ_k basis

$$T_{ij}^{\mathrm{FBR}} = -\frac{\hbar^2}{2m}\int_a^b \varphi_i^*(x)\frac{d^2}{dx^2}\varphi_j(x)dx \tag{4.7}$$

and the FBR kinetic matrix is transformed into the DVR basis as

$$\boldsymbol{T}^{\mathrm{DVR}} = \boldsymbol{O}\boldsymbol{T}^{\mathrm{FBR}}\boldsymbol{O}^{-1}. \tag{4.8}$$

The potential matrix elements are approximated with the Gauss quadrature as

$$V_{mn}^{\mathrm{FBR}} \approx \sum_k \lambda_k \varphi_m^*(x_k)V(x_k)\varphi_n(x_k) \tag{4.9}$$

and the potential matrix is transformed into the DVR basis as

$$(\boldsymbol{V}^{\mathrm{DVR}})_{ij} = (\boldsymbol{O}\boldsymbol{V}^{\mathrm{FBR}}\boldsymbol{O}^{-1})_{ij} = V(x_i)\delta_{ij}. \tag{4.10}$$

Hence the approximate variational equations become

$$\sum_{j=1}^{N}[T_{ij}^{\mathrm{DVR}} + (V(x_i) - E)\delta_{ij}]c_j = 0 \tag{4.11}$$

which are identical to the Lagrange-mesh equations (2.29) for orthogonal polynomials. Ref. [18] also presents a generalization attempting to get rid of the constraint (4.5) on the mesh points. The authors mention that the added freedom on the mesh points may be at the cost of accuracy.

This method [19] has known many evolutions [27,71,72]. The basis states $|x_i\rangle$ of the DVR are often named 'position states'. Although they are implicitly defined by Eq. (2.16), these states are not explicitly displayed in Ref. [18]. This ambiguity has led to misinterpretations of the DVR basis states. Some authors incorrectly consider that a representation of these states $|x_i\rangle$ is given by Dirac δ functions, $\langle x|x_i\rangle = \delta(x-x_i)$. Such a basis of non-square-integrable states cannot be used in the variational principle.

The correct interpretation of the DVR basis based on orthogonal polynomials in terms of Lagrange functions was first proposed by Szalay [41]. Formal definitions of the DVR based on projections of Dirac delta functions in a finite-dimensional space are studied in Ref. [31]. Muckerman [66] considered DVRs based on sine [Eq. (3.242)] and Fourier [Eq. (3.230)] functions and attempted to relate them to the Gauss–Chebyshev quadratures of the second and first kind, respectively (see Section 3.7). Lagrange functions are introduced under the expansion form (2.16). An advantage of the Lagrange functions is that they provide an approximate wave function at any x and not only at mesh points x_i. In addition, the existence of compact expressions for the Lagrange functions [4] provides compact expressions for the kinetic matrix elements T_{ij} or, through (2.35), compact approximations. The tedious basis transformation (4.8) from the FBR to the DVR can be avoided [80,81]. This would simplify existing DVR calculations [82]. While, in the DVR, conditions (2.14) and (2.15) which are equivalent to (2.10) and (2.13) play a central role, they do not appear explicitly in Refs. [27,71].

Another popular definition of the DVR is that it is based on the mesh points obtained by diagonalization of the matrix $\boldsymbol{X}$ representing the position operator. This is called 'real DVR' in Ref. [83]. For classical orthogonal polynomials, this definition is obviously correct [77]. For other cases, it has received a justification in Ref. [84]. However, it eliminates a number of useful Lagrange basis defined in Section 3. It is not valid for the Gaussian and sine bases, nor for regularized bases. This definition has slowed down the introduction of the regularization in the DVR. In Ref. [85], a regularization technique was introduced in the DVR, which was already used for the LMM in Ref. [9].

Various DVR bases do not have a direct counterpart in the Lagrange-mesh spirit. They are based on cardinal functions that may not be exactly orthogonal and are not related to Gauss-like quadratures. They are thus not closely related to a variational principle. A good example is given by DVR-like methods based on Bessel functions that have been proposed several times [26,86–88] (see also Refs. [72,67]) or on Coulomb functions [89–91]. These methods are not equivalent to the LMM because the finite bases are not orthogonal or not related to a Gauss quadrature.

Several authors studied various generalizations of the DVR [18,92]. The basic idea is to get rid of the constraints on the choice of the mesh points and associated weights that are common to the standard DVR and to the LMM. These generalizations return to the original goal of the DVR [79]. They are close to the collocation spirit but they cannot be so easily related to the LMM. These generalizations can give very accurate results [92].

4.3. Quadrature discretization method

The quadrature discretization method (QDM) has been applied to quantum mechanical problems in 1996 [21]. It is very similar to the DVR but is based on non-classical orthogonal polynomials.

In fact, the basic principle of the QDM is much older, appearing in problems of kinetic theory based on the Fokker–Planck and Boltzmann equations. In 1979, Shizgal combined non-classical orthogonal polynomials [93] with a collocation method used in various fields of physics, called the discrete-ordinate method, to derive eigenvalues of the Boltzmann operator [94]. The method was improved in Ref. [20]. It replaces a differential operator by a matrix. The mth derivative d^m/dx^m is represented by the mth power of a matrix representing d/dx in a basis of non-classical orthogonal polynomials. Like in the DVR, a matrix transformation leads to a basis where the potential is represented by a diagonal matrix. It was first applied to the Fokker–Planck equation [95].

The Fokker–Planck equation can be transformed into an equivalent Schrödinger equation. This led Shizgal and Chen to apply the QDM to quantum mechanical problems [21]. In a basis of N polynomials $p_k(x)$ orthogonal with respect to a weight function $w(x)$, a Gauss quadrature is obtained with the zeros x_i of $p_N(x_i)$ and weights w_i [Eq. (2.3)]. After a transformation with a matrix $\boldsymbol{O}$ defined like in Eq. (4.6), the Hamiltonian is represented by the matrix elements

$$H_{ij} = \sum_{k=1}^{N} D_{ki} D_{kj} + [V(x_i) - \widetilde{V}(x_i)]\delta_{ij} \tag{4.12}$$

where matrix $\boldsymbol{D}$ is obtained by an orthogonal transformation based on $\boldsymbol{O}$ from the matrix elements of d/dx in the polynomial basis

$$D_{ij} = \sum_k \sum_l O_{ik} O_{jl} \int_a^b w(x) p_k(x) p_l'(x) dx \tag{4.13}$$

and the auxiliary potential reads

$$\widetilde{V}(x) = \frac{w''(x)}{2w(x)} - \frac{1}{4}\left[\frac{w'(x)}{w(x)}\right]^2. \tag{4.14}$$

An interesting particular case occurs when w can be chosen in such a way that $V(x) = \widetilde{V}(x)$. This occurs when $w(x)$ is chosen as

$$w(x) = [\psi_0(x)]^2 \tag{4.15}$$

where $\psi_0(x)$ is the ground-state wave function of the Schrödinger equation with potential $V(x)$. Then (4.12) reduces to its first (kinetic) term. But $\psi_0(x)$ must be known analytically. This can occur for example with the Morse potential. As it is more convenient to have $\widetilde{V}(x)$ in an analytical form, for other potentials describing vibrations of a diatomic molecule, a conveniently fitted Morse potential provides a good choice for $\widetilde{V}(x)$.

The discrete-ordinate method of Shizgal and Blackmore [20] is completely equivalent to a DVR with non-classical orthogonal polynomials. As it starts with orthogonal polynomials, the transformation $\boldsymbol{O}$ simulates the use of polynomial Lagrange functions. The Lagrange conditions are automatically satisfied as shown by equation (12) of Ref. [20]. The QDM is thus also equivalent to the LMM, but more complicated. The matrix elements of differential operators are calculated in a rather complicated way from a combination of properties of orthogonal polynomials and of unitary transformations. Lagrange polynomials are introduced in Ref. [96] and lead to a method equivalent to the LMM with non-classical polynomials. In the QDM, there is no explicit reference to a variational principle probably because, initially, this principle did not apply simply to the Fokker–Planck equation.

The QDM has been applied to various test potentials [97–99]. It is particularly efficient for the lowest bound states of the Morse potential [21,100,96,101,98,99]. For the weakly-bound highly excited states, however, the tests show that the sinc method is competitive [62,101]. A change of variable [98] or a scaling [99] have been introduced recently to improve the description. In this case, the QDM converges faster than the LMM but requires more complicated calculations [96,101]. Its efficiency depends on the existence of a potential $\widetilde{V}(x)$ of the form (4.14) close to the studied potential $V(x)$. The QDM has not been applied yet to singular potentials such as the Coulomb or Yukawa potentials or in the presence of $l > 0$ centrifugal terms.

4.4. Sinc and Fourier methods

In 1985, Schwartz introduced a Lagrange interpolation technique in a collocation approach [26] but without mentioning that several of his examples lead to exact kinetic matrix elements and without reference to the variational method. Starting with the ratio form (2.17), he established the basic expressions for the sinc mesh (Section 3.7.5) including compact expressions for the kinetic matrix elements. With '*some experimentation*', Schwartz derived the basic results for the Fourier and first sine meshes. He also considered a mesh based on Bessel functions which has no exact relation with the LMM. Schwartz focuses on the construction of accurate interpolation functions possessing the Lagrange property (2.10). He does

not mention that most of the interpolation functions in his examples possess in addition the orthogonality property (2.13) which transforms them into a convenient basis for a variational calculation. Although Schwartz mentions a link between his interpolation technique and the Gauss approximation, he does not develop its consequences (2.13) for scalar products of basis functions. Nevertheless Schwartz was the first to derive the Fourier-mesh equations which were later obtained independently in Ref. [4]. He also derived the equations for the first sine mesh (3.244) and (3.245) discussed in Section 3.7.2. His empirical approach did not lead him to the two other meshes (3.254) and (3.255) related to the same basis.

The discrete singular convolution method introduced by Wei in 1999 and first applied to the Fokker–Planck equation is in some cases equivalent to the Fourier ('Dirichlet kernel') and sinc ('Shannon kernel') meshes [62]. It was later applied to quantum mechanics [102]. Various applications such as the Morse potential and harmonic oscillators are considered and good accuracies are found.

The Fourier-grid method [103,27] is based on a constant-step collocation and the use of a fast Fourier transform. Its presentation can be very different from the LMM. Nevertheless it is essentially equivalent to the Lagrange–Fourier method [67,104]. Extensions of the Fourier-grid method based on a mapping [105] can be very accurate as shown in Ref. [3].

The sinc mesh has been generalized to several dimensions in the DVR context by tensor product for various symmetries in Ref. [106].

4.5. Miscellaneous

A number of properties related to what I call Lagrange functions have been derived by Calogero in a mathematical work on matrix representations of differential operators based on classical orthogonal polynomials [107]. This interesting work was unfortunately only noticed by few authors in the context of the LMM or DVR methods [41,80,83].

The utility of Lagrange functions in a variational context without the associated Gauss quadrature of the LMM has been considered by several authors. This took place in the framework of atomic physics where the simultaneous occurrence of several Coulomb singularities cannot be regularized for more than three charged particles. The Helium atom (which can now be regularized in perimetric coordinates, see Section 7.2) was taken as a test problem. In Ref. [108], different techniques of calculations of two-body matrix elements of the Coulomb potential between Lagrange functions are considered and their accuracy is tested. A regularization was attempted in Ref. [109] leading to a reasonable but not high accuracy.

The Lagrange–Laguerre basis is used together with the R-matrix method in multichannel electron scattering on atoms and ions in Ref. [110]. The results obtained with this basis are more accurate than with the corresponding basis of Laguerre polynomials. A study of the Stark effect on the hydrogen atom is performed in parabolic coordinates with the same basis in Ref. [111]. With the full LMM, the calculations should be easier and, possibly, more accurate.

5. Potential and two-body bound states

5.1. On the choice of a Lagrange mesh

The choice of a Lagrange mesh first depends on the type of interval (a, b). For $(-\infty, +\infty)$, one can choose the Hermite, sinc or Gaussian meshes. It is also possible to use a finite interval scaled to a large domain. For $(0, \infty)$, the various Laguerre meshes are the main possibilities. Gaussian and projected sinc meshes are also available, mainly for cases without singularities. All finite intervals can be scaled from $(-1, +1)$. If the problem is not periodic, Legendre or Jacobi meshes are chosen depending on the type of boundary conditions. If it is periodic, various types of Fourier meshes can be useful.

When the mesh is selected, the regularization of the Lagrange functions must be considered. Regularization may be used to impose specific behaviours to the Lagrange functions at singular points. When the Hamiltonian possesses a regular singular point, it is convenient to use a regularization which allows a reproduction of the behaviour of regular wave functions in the vicinity of the singularity. However numerical experiments reveal than this regularization is less important when the singularity is strong, such as the centrifugal barrier at high orbital momentum or for singular potentials corresponding to irregular singular points.

Some of these choices are illustrated in the rest of this section. Most of the examples are very simple, with well known analytical solutions allowing an easy control of the accuracy (Sections 5.2–5.5). They should provide good exercises for a beginner. They are based on the one-dimensional Hamiltonian

$$H = -\frac{\hbar^2}{2m}\frac{d^2}{dx^2} + V(x), \tag{5.1}$$

or on the three-dimensional radial Hamiltonian of partial wave l

$$H_l = -\frac{\hbar^2}{2m}\left(\frac{d^2}{dr^2} - \frac{l(l+1)}{r^2}\right) + V(r) \tag{5.2}$$

where m is the mass or reduced mass and V is some potential. The physical eigenfunctions of (5.2) must vanish at the origin. A two-dimensional problem (Section 5.6), the momentum space (Section 5.7) and the Dirac equation (Sections 5.8–5.9) are also treated.

5.2. Harmonic oscillators

The harmonic oscillator represents an excellent simple test for numerical methods. In one dimension, with $V(x) = \frac{1}{2}m\omega^2x^2$, the Hamiltonian reads

$$H = \frac{1}{2}\left(-\frac{d^2}{dx^2} + x^2\right) \tag{5.3}$$

in units $\hbar = m = \omega = 1$.

In this case, the Hermite mesh is optimal [4]. Since a basis of N Lagrange–Hermite functions (3.35) is equivalent to a basis $H_k(x)\exp(-x^2/2)$ with $k = 0$ to $N-1$, the oscillator wave function with energy $n + \frac{1}{2}$ is exactly a linear combination of these Lagrange functions for any $N > n$ as shown by (2.25) and (2.26),

$$H_n(x)e^{-x^2/2} = \sum_{j=1}^{N} \lambda_j^{1/2} H_n(x_j) e^{-x_j^2/2} f_j(x). \tag{5.4}$$

The quality of the results also depends on the validity of the Gauss quadrature. The matrix elements of the kinetic energy are given at the Gauss approximation by (3.40) and (3.41), and exactly by (3.42). The potential matrix elements are given exactly by (3.39) as

$$\langle f_i|V(x)|f_j\rangle = \frac{1}{2}x_i^2\delta_{ij} + \frac{1}{4}(-1)^{i-j}. \tag{5.5}$$

The Gauss quadrature is not exact because the integrand contains the Hermite weight $\exp(-x^2)$ times a polynomial of degree $2N$, i.e. just one unit above the highest degree for which the quadrature is exact.

Let us first start with the instructive case already discussed in Ref. [4], i.e. with the exact expression for the kinetic energy and the Gauss approximation for the potential. Since the exact matrix element of the potential differs from its Gauss approximation, i.e. the first term in (5.5), the energies cannot all be correct. When the energies are ordered by increasing values, one observes that, except the energy numbered $[3N/4]$ (integer part of $3N/4$), the $N-1$ other energies are exact,

$$E_{n<[3N/4]} = n + \frac{1}{2}, \qquad E_{n>[3N/4]} = n - \frac{1}{2}. \tag{5.6}$$

They are exact because the N-point Gauss quadrature is exact for all matrix elements of the Hamiltonian between states (5.4) if $n < N$. The remaining eigenvalue can be obtained from the trace of the matrix using the property of the Hermite zeros [112],

$$\sum_i x_i^2 = \frac{1}{2}(N-1)N, \tag{5.7}$$

as

$$E_{[3N/4]} = \frac{1}{4}(3N-2). \tag{5.8}$$

Notice that this incorrect eigenvalue is mixed within the correct ones (5.6).

Here comes a remarkable property. When the Gauss approximation is used for both the kinetic and potential terms, the errors in (3.42) and (5.5) exactly cancel. This is not surprising: Hf_j contains a polynomial of degree one unit less than in f_j'' and x^2f_j. Hence the integrand in $\langle f_i|H|f_j\rangle$ is a polynomial of degree $2N-1$ multiplied by the Hermite weight function and the Gauss quadrature is exact. The Lagrange-mesh equations (2.29) are thus *identical* to the variational equations (2.22) which provide the *exact* energies and wave functions for the basis (5.4) and thus for the Lagrange basis with $h = 1$. For $h = 1$, all the LMM eigenvalues are thus exact. Using consistently the Gauss quadrature everywhere is not less good than using exact kinetic matrix elements and even marginally better!

The accuracies of the first eight eigenvalues are compared in Table 2 for various meshes with $N = 20$ points. Notice that N does not need to be odd as sometimes suggested for some meshes. Since the potential is even, the size of the matrices might be reduced to $N/2$ by calculating each parity separately with Eq. (2.57) but this reduction is not applied here. First, one observes that the energies are not variational: they can be lower than the exact value. The Hermite mesh is very well adapted, giving exact values only affected by rounding errors for $h = 1$. Even with the non-optimal value $h = 1.1$, the absolute error is still smaller than about 10^{-8} for $n = 7$. For the other meshes, h is optimized. The accuracy of the sinc mesh (Section 3.7.5) decreases from 10^{-13} for $n = 0$ to 10^{-6} for $n = 7$. The Gaussian meshes are peculiar. They require more fine tuning because there is an additional parameter ν related to the width $h/\sqrt{\nu}$ of the Gaussians, while the scaling parameter h controls their spacing. They allow obtaining a rather constant accuracy on a number of states. For $\nu = 0.045$ and $h = 0.28$, the accuracy of the first Gaussian mesh (Section 3.6.2) is better than 5×10^{-12} up to $n = 9$ and is still better than 10^{-7} for $n = 12$. Very similar accuracies are obtained with the second Gaussian mesh (Section 3.6.3) with $\nu = 0.04$, $h = 0.27$ and

Table 2
Hermite, sinc, Gaussian and Fourier Lagrange-mesh calculations of the energies of the first eight one-dimensional harmonic-oscillator energies with $N = 20$ mesh points.

n	Hermite $h = 1$	Hermite $h = 1.1$	sinc $h = 0.55$
0	0.500 000 000 000 007	0.499 999 999 999 997	0.500 000 000 000 1
1	1.500 000 000 000 002	1.500 000 000 000 002	1.499 999 999 999 9
2	2.499 999 999 999 992	2.499 999 999 999 992	2.500 000 000 166 3
3	3.500 000 000 000 000	3.499 999 999 999 976	3.499 999 999 925 4
4	4.500 000 000 000 012	4.500 000 000 000 650	4.500 000 045 843 9
5	5.499 999 999 999 993	5.499 999 999 978 584	5.499 999 984 469 7
6	6.500 000 000 000 019	6.500 000 000 508 817	6.500 004 462 526 1
7	7.500 000 000 000 029	7.499 999 989 301 029	7.499 998 924 452 7
n	1st Gaussian $\nu = 0.045, h = 0.28$	2nd Gaussian $\nu = 0.04, h = 0.27$	Fourier $h = 0.56$
0	0.499 999 999 998 54	0.499 999 999 998 83	0.500 000 000 000 29
1	1.499 999 999 999 37	1.500 000 000 000 93	1.499 999 999 981 69
2	2.499 999 999 999 39	2.500 000 000 003 85	2.500 000 000 5 19 31
3	3.500 000 000 001 12	3.500 000 000 002 21	3.499 999 989 746 71
4	4.500 000 000 001 85	4.500 000 000 003 17	4.500 000 133 429 74
5	5.499 999 999 997 41	5.499 999 999 993 20	5.499 998 516 804 60
6	6.500 000 000 004 39	6.500 000 000 000 94	6.500 011 564 073 72
7	7.500 000 000 002 58	7.499 999 999 999 35	7.499 913 555 983 41

Table 3
Modified Laguerre, radial Gaussian and regularized Laguerre Lagrange-mesh calculations of the energies of the first eight three-dimensional harmonic-oscillator energies for $l = 0$ with $N = 20$ mesh points.

n_r	Modified Laguerre $\alpha = 1/2, h = 1$	Gaussian $\nu = 0.045, h = 0.26$	Regularized Laguerre $\alpha = 0, h = 0.11$
0	1.499 999 999 999 99	1.500 000 000 006 37	1.499 999 999 999 96
1	3.499 999 999 999 99	3.499 999 999 993 21	3.500 000 000 025
2	5.500 000 000 000 00	5.499 999 999 996 53	5.499 999 994 0
3	7.500 000 000 000 01	7.500 000 000 007 29	7.500 000 40
4	9.500 000 000 000 01	9.500 000 000 006 54	9.499 984
5	11.500 000 000 000 01	11.499 999 999 992 86	11.500 29
6	13.499 999 999 999 98	13.499 999 999 981 62	13.495 7
7	15.499 999 999 999 97	15.499 999 999 999 07	15.527

$d = N/2 - 1/4$. Parity projection would however not be possible for this asymmetric mesh. The Fourier mesh (Section 3.7.1) is different since the interval is finite: $(-10, 10)$ for $N = 20$. However, for low bound states, it is a good approximation of $(-\infty, \infty)$ for the confining harmonic oscillator potential. Not surprisingly, its properties resemble those of the sinc mesh. For $h = 0.56$, the accuracy decreases from 3×10^{-13} for $n = 0$ to 10^{-4} for $n = 7$.

The Hermite mesh is thus a natural and efficient tool to determine accurate approximate solutions for the anharmonic oscillator [64].

Another striking example is provided by the three-dimensional harmonic oscillator. The Hamiltonian for partial wave l is given by Eq. (5.2) with $V(r) = \frac{1}{2}r^2$ in the same natural units. Here the modified Lagrange–Laguerre mesh (3.82) is optimal provided that α is properly chosen. The basis of Lagrange functions (3.83) is equivalent to the basis of harmonic-oscillator radial eigenfunctions if $\alpha = l + \frac{1}{2}$ to comply with the r^{l+1} behaviour near the origin [4]. Then the radial part of the kinetic operator has the form (3.90) and its matrix elements are exactly given by the Gauss quadrature as (3.91). Moreover the potential matrix elements

$$\langle f_i | r^2 | f_j \rangle = h^2 x_i^2 \delta_{ij} \tag{5.9}$$

where the x_i are given by (3.82) are also exact, as shown by the fact that the integrand is the product of the Laguerre weight (3.43) with x replaced by r^2 and a polynomial of degree $2N - 1$ in r^2. Again, the Lagrange-mesh equations are identical to the variational equations for $\alpha = l + \frac{1}{2}$ and $h = 1$ which provide the exact energies,

$$E_{n_r l} = 2n_r + l + \frac{3}{2} \tag{5.10}$$

where n_r is the number of radial nodes, and the exact wave functions within the computer accuracy. The same is true for the regularized modified basis (3.92) for the appropriate choice of α.

Energies obtained with three meshes are displayed in Table 3. For $h = 1$, the results of the modified Laguerre mesh with $\alpha = 1/2$ are numerically exact. When h differs from 1, the eigenvalues are not exact any more. For example, with $h = 1.1$, 14 digits remain exact for the lowest eight levels. Then, the accuracy starts decreasing from 2×10^{-13} for the $n_r = 8$ excited

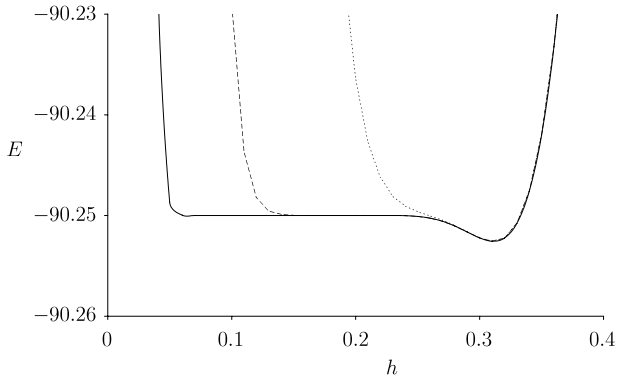

Fig. 18. Ground-state energy on a Lagrange-sinc mesh as a function of the scale parameter h for $N = 10$ (dotted line), 20 (dashed line) and 50 (full line).

Table 4
Lagrange mesh calculations of the energies of the first eight levels of the Morse potential (5.12) with $d = 100$ for $N = 50$ mesh points.

n	Exact	sinc $h = 0.16$	Shifted sinc $\Delta x = 1.5$ $h = 0.16$	Hermite $h = 0.45$	Gaussian $\nu = 0.045$ $h = 0.12$
0	−90.25	−90.249 999 999 92	−90.250 000 000 06	−90.250 000 000 000	−90.250 000 000 04
1	−72.25	−72.249 999 999 39	−72.250 000 001 07	−72.249 999 999 997	−72.250 000 000 08
2	−56.25	−56.250 000 001 09	−56.250 000 004 34	−56.249 999 999 980	−56.250 000 000 34
3	−42.25	−42.250 000 021 49	−42.249 999 999 66	−42.249 999 999 969	−42.250 000 000 17
4	−30.25	−30.250 000 065 79	−30.249 999 953 49	−30.249 999 999 986	−30.249 999 996 68
5	−20.25	−20.249 986 272 93	−20.249 999 844 10	−20.249 999 767 804	−20.249 999 976 80
6	−12.25	−12.246 629 245 07	−12.249 999 506 48	−12.249 819 599 149	−12.249 974 616 93
7	−6.25	−6.074 543 610 02	−6.249 679 795 43	−6.220 081 090 733	−6.241 591 712 63

state to 10^{-5} for the $n_r = 12$ state. For the radial Gaussian mesh (3.228) (Section 3.6.4), the accuracy remains between 10^{-12} and 10^{-11} up to $n_r = 12$. Then it drops from 3×10^{-10} for $n_r = 13$ to 10^{-6} at $n_r = 15$. This is a remarkable result with only 20 mesh points. This mesh has however the drawback that an efficient regularization, which might be useful for other partial waves, is not known (see however the comments on Table 5). The regularized Laguerre mesh with $\alpha = 0$ (Section 3.3.4) is based on exponentially decreasing functions, i.e. decreasing too slowly to efficiently describe a Gaussian behaviour. Nevertheless, the accuracy is excellent for the $n_r = 0$ ground state. It decreases rather fast with increasing n_r: from 3×10^{-11} for $n_r = 1$ to 3×10^{-3} for $n_r = 5$.

5.3. Morse potential

Another benchmark test of numerical methods is the Morse potential [113]

$$V(x) = D[\exp(-2a(x - x_e)) - 2\exp(-a(x - x_e))] \tag{5.11}$$

on the $(-\infty, +\infty)$ interval, because its exact solutions are known analytically. Let us choose the units $\hbar = 2m = a = 1$ in Hamiltonian (5.1). With the origin of the coordinate system at the minimum of the potential ($x_e = 0$), the most general Morse Hamiltonian can be written as

$$H = -\frac{d^2}{dx^2} + d[\exp(-2x) - 2\exp(-x)] \tag{5.12}$$

where d is the only parameter. Its exact eigenvalues are

$$E_n = -\left(n + \frac{1}{2} - \sqrt{d}\right)^2 \tag{5.13}$$

where n is an integer verifying $0 \leq n < \sqrt{d} - \frac{1}{2}$.

With the choice $d = 100$, the potential supports 10 bound states. The first eight energies studied with several meshes, i.e. sinc, Hermite and Gaussian, are compared with the exact results in Table 4. All calculations are performed with $N = 50$ mesh points. The scale parameter h is optimized to a 0.01 absolute accuracy.

For the sinc mesh, the choice of h is illustrated by Fig. 18. For $N = 10$, the minimum around $h = 0.31$ is below the exact value. The number of mesh points is not sufficient to obtain reliable results. For $N = 20$, a plateau appears between 0.15

Table 5
Regularized Laguerre-mesh and Gaussian-mesh calculations with $N = 40$ mesh points of the energies of the first eight states of the radial Morse potential (5.14) with $D = 0.10262$, $r_e = 2$ and $a = 0.72$ for $l = 0$ and 1. The 'exact' results are obtained with Eq. (5.15) for $l = 0$ and with a regularized Laguerre mesh with $N = 100$ for $l = 1$.

n	'Exact'	Regularized Laguerre $h = 0.04$	Gaussian ($\nu = 0.045$) $h = 0.12$
$l = 0$			
0	−0.097 307 739 656 378 9	−0.097 307 739 656 378 8	−0.097 307 739 656 371 8
1	−0.087 106 748 380 901 4	−0.087 106 748 380 912	−0.087 106 748 380 881
2	−0.077 470 462 987 776 9	−0.077 470 462 987 91	−0.077 470 462 987 758
3	−0.068 398 883 477 005 3	−0.068 398 883 473 9	−0.068 398 883 476 983
4	−0.059 892 009 848 586 7	−0.059 892 009 829	−0.059 892 009 848 624
5	−0.051 949 842 102 521 0	−0.051 949 842 33	−0.051 949 842 102 606
6	−0.044 572 380 238 808 3	−0.044 572 381 6	−0.044 572 380 238 70
7	−0.037 759 624 257 448 4	−0.037 759 620 5	−0.037 759 624 257 49
$l = 1$			
0	−0.097 040 301 141 149 1	−0.097 040 301 141 149 1	−0.097 040 301 141 142 4
1	−0.086 848 915 165 615 0	−0.086 848 915 165 625	−0.086 848 915 165 594
2	−0.077 222 734 207 089 1	−0.077 222 734 207 25	−0.077 222 734 207 070
3	−0.068 161 755 035 938 0	−0.068 161 755 033 0	−0.068 161 755 035 916
4	−0.059 665 973 015 200 3	−0.059 665 972 993	−0.059 665 973 015 240
5	−0.051 735 382 273 815 3	−0.051 735 382 48	−0.051 735 382 273 899
6	−0.044 369 975 967 572 3	−0.044 369 977 4	−0.044 369 975 967 47
7	−0.037 569 746 657 221 1	−0.037 569 743 6	−0.037 569 746 657 26

and 0.24. For lower h values, the variational basis is not good enough. Above $h \approx 0.24$, the Gauss-sinc quadrature starts to fail: the lowest eigenvalue decreases below the exact value. Beyond $h = 0.34$, the variational basis is not good enough. For $N = 50$, the plateau extends to lower h values but the problems do not change above $h \approx 0.24$. The optimal value of h is not the same for all states. Here, as a compromise, I choose $h = 0.16$. The absolute accuracy deteriorates from 10^{-10} for $n = 0$ to 2×10^{-1} for $n = 7$. Some errors are positive and some are negative. The situation changes a little when the mesh is shifted to comply with the asymmetry of the potential. With a shift $\Delta x = 1.5$ of the mesh to the right, the accuracy does not change much for the lowest bound states but improves significantly for $n = 5$ to 7.

The accuracies on the first energies are much better for the Hermite mesh: from 2×10^{-13} for $n = 0$ to 3×10^{-6} for $n = 5$. For $n = 6$ and 7, they are not better. The results are not improved by a shift. For the Gauss mesh, the parameter ν is chosen as 0.045. With $h = 0.12$, the accuracies range from 4×10^{-11} for $n = 0$ to 2×10^{-8} for $n = 5$ and 2×10^{-3} for $n = 7$. A shift may improve $n = 6$ and 7 but at the cost of some accuracy on the lowest energies.

The Morse potential is also often used as a test for the s-wave radial problem. It is then written as

$$V(r) = D[\exp(-2a(r - r_e)) - 2\exp(-a(r - r_e))] \tag{5.14}$$

with mass m and parameters a, D and r_e typical of the vibrational spectrum of some molecule. Here, after choosing the length unit a^{-1} and the energy unit $\hbar^2 a^2/2m$, the problem only depends on two independent dimensionless combinations of the parameters, $d = 2mD/\hbar^2 a^2$ and ar_e. Notice that the formula

$$E_{n0} = -\left(n + \frac{1}{2} - \sqrt{d}\right)^2 \hbar^2 a^2/2m \tag{5.15}$$

does not give the exact $l = 0$ energies. However, if ar_e is large enough, the error can be made smaller than the computer accuracy because the first term in (5.14) is highly repulsive and strongly damps the wave function at small r values [114]. The condition for the s-wave radial wave function at the origin

$$\psi_0(0) = 0 \tag{5.16}$$

is replaced by $\psi_0(0) = \epsilon$ where ϵ is of the order of $\exp[-\sqrt{d}\exp(ar_e)]$. Hence the energies (5.15) can be numerically exact if ϵ is smaller than the computer accuracy.

The accurate results obtained in Ref. [71] with the Fourier-grid method and discussed in Ref. [32] correspond to $D = 0.10262$, $r_e = 2$ and $a = 0.72$ ($2m = 1836$) in atomic units. The exact energies agree up to better than 10^{-15} with the analytical expression (5.15) with the single parameter $d = 2mD/a^2 \approx 363.445\,833\,333\,333$, where the energy is expressed in units of $a^2/2m \approx 2.823\,529\,411\,764\,706 \times 10^{-4}$. Hence the Lagrange-mesh and other methods for this radial potential can be tested with respect to (5.15).

Table 5 displays the corresponding Lagrange-mesh results obtained for $N = 40$ with the regularized Laguerre mesh (Section 3.3.4) with $h = 0.04$ and the radial Gaussian mesh (3.228) with $\nu = 0.045$ and $h = 0.12$ for $l = 0$ and 1. For $l = 1$, the 'exact' values are numerically converged results obtained with the regularized Laguerre mesh for $N = 100$. For $l = 0$, the absolute accuracy obtained with the Laguerre mesh and $N = 40$ varies from 10^{-16} for $n = 0$ to 4×10^{-9} for $n = 7$. The radial Gaussian mesh (3.228) is slightly less good for $n = 0$, though the accuracy is still 10^{-14}, probably because

Table 6
Comparison of errors on the energies of the first six $l = 0$ levels of the radial Morse potential (5.14) ($D = 0.10262$, $r_e = 2$ and $a = 0.72$) obtained with various approximations using the regularized Laguerre basis for $N = 30$ and 40: (a) variational calculation, (b) variational calculation with the basis treated as orthonormal, (c) Gauss approximation on the potential, (d) Gauss approximation on the overlap and potential and (e) LMM. The last column displays the scalar products $\boldsymbol{v}^T\boldsymbol{c}$.

n	(a)	(b)	(c)	(d)	(e)	$\boldsymbol{v}^T\boldsymbol{c}$
$N = 30$						
0	3.1(−12)	−1.2(−11)	−8.3(−12)	−2.4(−11)	−9.7(−12)	1.1(−5)
1	2.8(−10)	−2.5(−11)	−6.3(−10)	−1.4(−9)	−6.5(−10)	−7.8(−5)
2	7.1(−9)	6.6(−9)	1.7(−8)	1.6(−8)	1.7(−8)	5.8(−5)
3	3.7(−8)	−7.1(−8)	−7.1(−8)	−2.0(−7)	−5.0(−8)	1.1(−3)
4	4.2(−7)	−3.1(−7)	−2.0(−6)	−4.1(−6)	−1.5(−6)	−4.2(−3)
5	5.0(−6)	5.0(−6)	7.9(−6)	5.9(−6)	8.6(−6)	4.0(−3)
$N = 40$						
0	4.3(−15)	4.2(−15)	6.9(−17)	−6.9(−17)	1.2(−16)	1.5(−8)
1	1.2(−14)	7.2(−15)	−1.0(−14)	−1.8(−14)	−1.0(−14)	2.5(−7)
2	8.7(−14)	3.7(−14)	−1.5(−13)	−3.1(−13)	−1.4(−13)	1.2(−6)
3	1.3(−12)	1.3(−12)	3.0(−12)	2.7(−12)	3.1(−12)	−1.8(−6)
4	7.4(−12)	2.3(−12)	1.8(−11)	1.5(−11)	2.0(−11)	−6.2(−6)
5	3.3(−11)	−5.2(−11)	−2.9(−10)	−4.7(−10)	−2.2(−10)	4.3(−5)

the numerical values of the zeros are less accurate. But the accuracy remains around 10^{-13} up to $n = 7$. For $l = 1$, the accuracy does not change much. This is normal for the Laguerre mesh where the regularization eliminates the singularity problem of the centrifugal term. It is more surprising for the Gaussian mesh which is not regularized. The singularity of the centrifugal term is probably hidden by the presence of the strong repulsive core of the Morse potential. This is not true for the singularity of the Coulomb potential [4] (see Sections 5.4 and 5.5).

The errors on the energies of the $l = 0$ ground state and first five excited states for a variational calculation using the regularized Laguerre basis (3.70), or equivalently a basis of scaled Laguerre polynomials multiplied by r times the square root of their weight function $\exp(-r/2h)$ [7], are displayed in column (a) of Table 6 for $h = 0.04$ and $N = 30$ and 40. As they should, they are all positive. The accuracy increases with the number N of mesh points and decreases for more excited states. These errors do not vary much when the basis is treated as orthogonal in column (b), i.e. when the overlap matrix $I + \boldsymbol{v}^T\boldsymbol{v}$ appearing in Eq. (2.66) is replaced by the unit matrix I. However, they are not any more necessarily positive. Columns (c) to (e) correspond to various forms of Lagrange-mesh calculations. In approximation (c), the exact kinetic energy and overlap are used. Only the potential is calculated with the Gauss quadrature. The eigenvalue problem is generalized as the basis is not orthogonal. The accuracies vary randomly with respect to the previous calculations, i.e. they can be smaller or larger. In approximation (d), the basis is considered as orthonormal. The exact kinetic-energy matrix [Eq. (3.77)] is still used. The LMM with Gauss quadratures everywhere corresponds to calculation (e). On the average, the errors are a factor of 2 to 3 less good than in the variational calculation. This is a very little price to pay, given the simplicity of this approach. The scalar products $\boldsymbol{v}^T\boldsymbol{c}$ [Eq. (2.68)] are also given in that case. One can see that the calculations (b), (d), (e) are weakly affected by corrections of the order of $(\boldsymbol{v}^T\boldsymbol{c})^2$. The fact that the difference between the variational and Lagrange-mesh approximations are correlated with the square of this overlap agrees with Eq. (2.67). What is more surprising is that the accuracy of the variational calculation itself seems also to be correlated with that expression.

5.4. Hydrogen atom

The singularity of the Coulomb potential adds a difficulty for the LMM. It offers a first example of the power of the regularization technique [5]. Non regularized meshes give poor results for low l values [4].

5.4.1. Energies and wave functions

In atomic units $\hbar = m_e = e = 1$ where m_e is the electron mass, the radial Hamiltonian (5.2) reads

$$H_l = \frac{1}{2}\left(-\frac{d^2}{dr^2} + \frac{l(l+1)}{r^2}\right) - \frac{1}{r}. \tag{5.17}$$

The regularized Lagrange–Laguerre basis (3.70) plays a special role here since, for well chosen values of the scaling parameter h, the radial wave functions can be expressed exactly as finite combinations of those Lagrange functions. We limit the discussion to the regularized basis functions defined in (3.70) with $\alpha = 0$ because they vanish at the origin and solve the singularity problem induced for the Gauss quadrature by the Coulomb and centrifugal terms. This basis is not exactly orthogonal as shown by Eq. (3.71). The radial functions ψ_l are expanded on the mesh points hx_i as

$$\psi_l(r) = h^{-1/2}\sum_{j=1}^{N} c_{lj}\hat{f}_j(r/h). \tag{5.18}$$

Table 7
Regularized Lagrange–Laguerre mesh calculations of lowest $l = 0$ energies E_{n0}, mean radii $\langle r\rangle$ and virial ratios $\langle V\rangle/\langle T\rangle$ of the hydrogen atom for given N and h.

N	h	n	$2n^2E_{n0}$	$n^{-2}\langle r\rangle$	$\langle V\rangle/\langle T\rangle$
1	0.5	1	−1.000 000 000 000 00	0.500 000 000 000 00	−1.333 333 333 333 33
2	0.5	1	−1.000 000 000 000 00	1.500 000 000 000 00	−2.000 000 000 000 00
		2	12.000 000 000 000 00	0.125 000 000 000 00	−0.666 666 666 666 67
30	2	1	−1.000 000 000 057 91	1.500 000 006 059 76	−1.999 999 998 250 42
		2	−1.000 000 000 000 00	1.499 999 999 999 99	−1.999 999 999 999 97
		3	−0.999 999 999 999 99	1.500 000 000 000 01	−1.999 999 999 999 99
		4	−0.999 999 999 999 99	1.500 000 000 000 00	−1.999 999 999 999 98
		5	−1.000 000 000 000 00	1.499 999 999 999 99	−1.999 999 999 999 98
		6	−1.000 000 000 000 00	1.499 999 999 999 99	−2.000 000 000 000 00
		7	−1.000 000 000 000 00	1.499 999 999 999 31	−1.999 999 999 999 64
		8	−0.999 999 998 358 58	1.499 999 907 810 77	−1.999 999 914 270 44
		9	−0.999 992 470 317 24	1.499 788 014 433 83	−1.999 726 221 033 10
		10	−0.998 243 564 685 96	1.477 199 524 515 56	−1.961 228 457 014 62
30	3	1	−1.000 000 965 952 38	1.500 035 936 842 03	−1.999 981 926 567 99
		2	−1.000 000 000 000 76	1.500 000 000 069 15	−1.999 999 999 969 28
		3	−1.000 000 000 000 00	1.499 999 999 999 99	−1.999 999 999 999 99
		4	−1.000 000 000 000 00	1.500 000 000 000 00	−1.999 999 999 999 99
		5	−1.000 000 000 000 00	1.500 000 000 000 00	−1.999 999 999 999 99
		6	−1.000 000 000 000 00	1.499 999 999 999 99	−1.999 999 999 999 99
		7	−1.000 000 000 000 01	1.499 999 999 999 99	−2.000 000 000 000 02
		8	−1.000 000 000 000 00	1.500 000 000 000 01	−2.000 000 000 000 06
		9	−1.000 000 000 000 00	1.499 999 999 999 95	−1.999 999 999 999 95
		10	−0.999 999 999 948 43	1.499 999 995 991 69	−1.999 999 996 441 92
		11	−0.999 999 579 251 89	1.499 982 693 459 26	−1.999 979 253 619 59
		12	−0.999 795 754 594 44	1.495 672 287 930 20	−1.993 235 544 279 28
Exact			−1	1.5	−2

The Lagrange-mesh equations for orbital momentum l read

$$\sum_{j=1}^{N}(H_{lij}^{G} - E\delta_{ij})c_{lj} = 0 \tag{5.19}$$

where

$$H_{lij}^{G} = \frac{1}{2h^2}\hat{T}_{ij}^{G} + \left(\frac{l(l+1)}{2h^2x_i^2} - \frac{1}{hx_i}\right)\delta_{ij} \tag{5.20}$$

is the matrix element $\langle\hat{f}_i|H_l|\hat{f}_j\rangle_G$ calculated with approximations (3.75) and (3.76) for the kinetic energy. The Gauss quadrature is here *exact* for the Coulomb and centrifugal terms. For the scale parameter $h = n/2$, expansion (5.18) can reproduce the exact hydrogen radial functions with any principal quantum number n if N is equal to n or larger. The system (5.19) with $\hat{T}_{ij}^{G}$ replaced by $\hat{T}_{ij}$ and the coefficient of E replaced by $\langle\hat{f}_i|\hat{f}_j\rangle$ given by (3.71) would be an exact variational calculation with a basis chosen in a space supporting the exact solutions for one eigenvalue (see Section 5.4.2). For the exact energy, the corresponding expansion (5.18) is exact. In this case, the notations E_{nl}, c_{nl} and ψ_{nl} are used. A drawback is that h must be adapted to each level.

Lagrange-mesh results for the s wave obtained with the regularized Laguerre basis for various choices of N and h are displayed in Table 7 in atomic units. The mean radius $\langle r\rangle$ and virial ratio $\langle V\rangle/\langle T\rangle$ are computed using the Gauss quadrature with equations (2.81) and (2.82). The energies are multiplied by $2n^2$ to simplify the comparison with the exact value $E_n = -1/2n^2$ and the mean radii are divided by n^2 to simplify the comparison with the exact value $3n^2/2$. The virial ratio is to be compared with its exact value -2. The first calculation is performed with a single point and provides the exact energy for $h = 0.5$! This is not surprising since the Lagrange function is proportional to the radial wave function $\psi_{1s}(r) = 2r\exp(-r)$. The mean radius and kinetic energy are however not given exactly by the one-point Gauss quadrature. These problems are solved for $N = 2$ but the other eigenvalue is unphysical. Similarly, for $h = n/2$, the nth eigenvalue is correct with $N = n$ mesh points and the mean radius and virial ratio are also correct for $N = n + 1$.

Each eigenvalue can be exactly reproduced but for different values of the scaling parameter. Can one obtain several accurate eigenvalues simultaneously? This is illustrated in Table 7 by two calculations with $N = 30$ and $h = 2$ and 3. For $h = 2$, $n = 4$ is optimal and the $n = 2$ to 7 energies are very accurate. The wave functions also have an excellent accuracy as illustrated by the closeness of the mean radius and virial ratio calculated with the Gauss quadrature to the exact values. For the ground state, the accuracy is better than 10^{-10} for the energy and 10^{-8} for the other two quantities. One observes that the ground-state energy is below the exact value. The LMM converges here from below, which underlines the difference with a variational calculation. Beyond $n = 7$, the precision is progressively, and rapidly, lost. For $h = 3$, $n = 6$ is optimal

and the $n = 2$ to 9 energies are very accurate. The $n = 10$ energy is still quite good but the accuracy of the ground-state energy deteriorates to 10^{-6}.

A striking fact is that these results are obtained with a basis which is not orthonormal, but treated as orthonormal. Very similar results are obtained in an exact variational calculation with the non-orthogonal regularized Lagrange–Laguerre basis, or with the equivalent basis of Laguerre polynomials L_0 to L_{N-1} multiplied by $r\exp(-r/2h)$ [40]. Contrary to the LMM, these approaches lead to a generalized eigenvalue problem. Finally, let me mention that the Lagrange–Gaussian mesh which gives excellent results for the Morse potential does not give meaningful results here.

Numerical studies of the hydrogen atom have been performed with several methods. The mapped Fourier and sine methods are studied in Refs. [105,115]. In Ref. [89], a Lagrange-mesh calculation is performed with the Laguerre basis (3.52) with $\alpha = 1$. Collocation techniques based on Bessel and Coulomb functions are also tested. In Ref. [116], the mapped-Fourier-grid method and a pseudospectral or collocation method with Laguerre polynomials are compared. The Laguerre basis is equivalent to the non-regularized basis (3.52) with $\alpha = 0$. With 50 mesh points and a scaling factor, better results are obtained with the Laguerre basis than with the Fourier grid. A Lagrange–Lobatto method is tested on hydrogen in Refs. [117,83] and compared with a variational calculation using the same basis [83]. A Legendre–Lobatto method is also studied in Ref. [117].

5.4.2. Exactness in the regularized Laguerre-mesh method

For the regularized Laguerre mesh, it is possible to compare the Lagrange-mesh equations to the variational equations obtained with the Lagrange-mesh basis which can provide the exact wave functions. The mesh equations (5.19) can be written in matrix form as

$$\boldsymbol{H}_l^G \boldsymbol{c}_{nl} = E_{nl} \boldsymbol{c}_{nl} \tag{5.21}$$

where $\boldsymbol{H}_l^G$ is the matrix with elements (5.20) at the Gauss approximation with $h = n/2$ for some quantum number n. Vector $\boldsymbol{c}_{nl}$ defined by $\boldsymbol{c}_{nl}^T = (c_{nl1}, c_{nl2}, \ldots, c_{nlN})$ contains the coefficients of the Lagrange-mesh wave function. The exact variational equations with basis $\hat{f}_i$ (without Gauss approximation) can be written with (3.71) and (3.77) as

$$\left(\boldsymbol{H}_l^G - \frac{1}{8h^2}\boldsymbol{v}\boldsymbol{v}^T\right)\tilde{\boldsymbol{c}}_{nl} = \tilde{E}_{nl}(\boldsymbol{I} + \boldsymbol{v}\boldsymbol{v}^T)\tilde{\boldsymbol{c}}_{nl} \tag{5.22}$$

where $\boldsymbol{I}$ is the $N \times N$ unit matrix, $\tilde{\boldsymbol{c}}_{nl}$ is a vector containing the variational coefficients and $\boldsymbol{v}$ is a vector with components

$$v_i = \frac{(-1)^i}{\sqrt{x_i}}. \tag{5.23}$$

Vector $\boldsymbol{v}$ has no physical meaning since it only depends on the mesh choice. The variational equations (5.22) can provide the exact energies and wave functions for $n = 1$ to N with different values $h = n/2$. Indeed, the exact wave functions $\psi_{nl}(r)$ contain polynomials of degree n times $\exp(-r/n)$ while the regularized Lagrange functions $\hat{f}_i(r/h)$ contain polynomials of degree N times $\exp(-r/2h)$.

Let me now show that the solution vector $\tilde{\boldsymbol{c}}_{nl}$ is exactly orthogonal to $\boldsymbol{v}$ for $h = n/2$ and $N > n$. Indeed, the integral

$$\int_0^\infty r^{-1}\psi_{nl}(r)L_{N-1}(r/h)e^{-r/2h}dr \propto \int_0^\infty x^l L_{n-l-1}^{2l+2}(x)L_{N-1}(x)e^{-x}dx \tag{5.24}$$

with $x = r/h$ vanishes for $N > n$ since $L_{N-1}(x)$ is then orthogonal to any polynomial of degree $n-1$ for the weight function $\exp(-x)$. The N-point Gauss quadrature is exact for this integral since the degree of the polynomial is smaller than $2N-2$. Hence one can write for $N > n$,

$$\sum_{k=1}^N \lambda_k (hx_k)^{-1}\psi_{nl}(hx_k)L_{N-1}(x_k)e^{-x_k/2} = 0, \tag{5.25}$$

where the x_k are the zeros of $L_N(x)$. With the definition (3.51) of λ_k and the property (2.45),

$$\tilde{c}_{nlk} = h^{1/2}\lambda_k^{1/2}\psi_{nl}(hx_k), \tag{5.26}$$

one obtains for $N > n$

$$\sum_{k=1}^N \tilde{c}_{nlk}(-1)^k x_k^{-1/2} = 0 \tag{5.27}$$

or

$$\boldsymbol{v}^T\tilde{\boldsymbol{c}}_{nl} = 0. \tag{5.28}$$

If $N - n - 1 = p > 0$, replacing r^{-1} in Eq. (5.24) by r^{j-1} shows that $\tilde{\boldsymbol{c}}_{nl}$ is also orthogonal to p additional vectors with components $(-1)^i x_i^{j-1/2}$ for $j = 1$ to p.

The important consequence of Eq. (5.28) is that Eq. (5.22) reduces to Eq. (5.21) which is thus exact,

$$\tilde{E}_{nl} = E_{nl}, \quad \tilde{\boldsymbol{c}}_{nl} = \boldsymbol{c}_{nl}. \tag{5.29}$$

The Lagrange-mesh calculation with the regularized basis using the Gauss quadrature everywhere and thus treating the basis as if it were orthonormal is exact for $h = n/2$ and $N > n$. The vector of coefficients satisfies one or several orthogonality properties such as Eq. (5.28).

Another consequence of Eq. (5.28) is that the norm of the solution is exactly given by the Gauss quadrature in spite of the non-exactness of this quadrature for the scalar products of Lagrange functions $\hat{\tilde{f}}_i(r/h)$ (see Section 2.7).

5.4.3. Static polarizabilities

The accuracies on the energies and some other quantities are spectacular but many other methods are able to provide accurate results for the hydrogen atom for which almost everything is exactly known analytically. However, the LMM is sometimes also able to exactly calculate more complicated physical quantities. An interesting example is given by static polarizabilities for which a general analytical expression is available but its existence is not well known [118,119]. The exact static polarizabilities of hydrogen were also published for a limited number of states in Refs. [120–122]. Strikingly, the LMM calculation is able to provide the exact values of the hydrogen polarizabilities [123]. The interpretation of the numerical calculation requires rounding some easily identifiable digits related to the limited computer accuracy.

Expressions for static polarizabilities are summarized in Appendix C. The polarizabilities are usually defined by series which involve the continuum. These series can be summed in a compact form with the method of Dalgarno and Lewis [124]. This method is not used here but is described for the hydrogen atom in Ref. [123]. Let me consider the polarization by a multipole operator $r^\lambda Y_{\lambda\mu}$. The polarizability of state nlm for component μ of the multipole operator is given by Eq. (C.1). This expression allows a calculation for any μ and m from $3jm$ coefficients and $\lambda + 1$ reduced polarizabilities given by Eq. (C.2). The average polarizabilities (C.3) do not depend on μ. The functions $\psi_{n'l'}$ appearing in (C.2) are expanded like in Eq. (5.18) with coefficients $c_{n'l'j}$ ($j = 1, \ldots, N$) and lead to the algebraic system (5.19) with l replaced by l'. Eq. (C.3) provides at the Gauss approximation the average polarizabilities

$$\alpha_\lambda^{(nl)} = \frac{2h^{2\lambda}}{2\lambda+1} {\sum_{l'=|l-\lambda|}^{l+\lambda}}' (2l'+1) \begin{pmatrix} l' & \lambda & l \\ 0 & 0 & 0 \end{pmatrix}^2 \sum_{n'=1}^{N} \frac{[\sum_{j=1}^{N} c_{n'l'j} x_j^\lambda c_{nlj}]^2}{E_{n'l'} - E_{nl}}, \tag{5.30}$$

where the prime means that the sum runs by steps of two.

As we have seen, for $h = n/2$, the wave function ψ_{nl} given by (5.18) is exact. When the LMM version of the Dalgarno–Lewis method presented in Ref. [123] (see Eqs. (C.4) and (C.5) in Appendix C) gives exact results, one easily shows that Eq. (5.30) also gives exact results despite that the energies $E_{n'l'}$ are not exact. This is a straight application of the spectral decomposition of an inverse matrix and of the exactness of matrix elements calculated with the Gauss quadrature [125]. Hence, the coefficients $c_{n'l'}$ obtained from the system (5.19), give the exact polarizabilities when $h = n/2$. The average polarizabilities (C.3) are then obtained with the Gauss quadrature in (5.30) which is exact for $N \geq n + \lambda + 1$. With an infinite number of digits, the polarizabilities would be exact. Here they contain rounding errors related to the computer accuracy.

The two reduced dipole polarizabilities (C.2) obtained with the regularized Lagrange–Laguerre mesh of Section 3.3.4 with $\alpha = 0$ are displayed in Table 8. The conditions of the calculation are $N = n+2$ and $h = n/2$. The results are close to integers or simple fractions, which can easily be guessed. Exact theoretical values for their average are also given in the table. The $1s$ case is known for a long time [126]. For $l = 0$, exact analytical expressions were derived in Ref. [120]. The average dipole polarizability of an arbitrary state nl is given by

$$\alpha_1^{(nl)} = \frac{1}{4} n^4 [2(2n^2+7) + 7l(l+1)]. \tag{5.31}$$

This formula has first been proven analytically in Refs. [118,119] and rediscovered on the basis of LMM results in Ref. [123]. Notice that five Lagrange-mesh points give better results than eighty B splines [121].

5.5. Confined hydrogen atom

An hydrogen atom confined in an impenetrable spherical cavity of radius R offers an interesting example of the efficiency of the LMM and of some of its subtleties [51]. The radial Hamiltonian remains given by (5.17) in atomic units but in the interval $r \in (0, R)$ with the condition

$$\psi_l(R) = 0 \tag{5.32}$$

in addition to $\psi_l(0) = 0$. The problem can be solved analytically but provides a transcendental quantification equation so that analytical energies are not available in general. Extremely accurate numerical values of these energies can be found in Ref. [127]. However a look at the wave functions of the unconfined hydrogen atom shows that particular cases exist where one energy is known analytically. For example, for $R = 2$, the $2s$ unconfined radial function vanishes at the boundary. Hence

Table 8
Reduced dipole polarizabilities (C.2) for $l' = l+1$ (second column) and $l' = l-1$ (third column) obtained on a Laguerre mesh with $N = n+2$ points and $h = n/2$. The rounded average polarizabilities obtained with (5.30) or (C.3) displayed in the last column agree with Eq. (5.31).

nl	$\alpha_1^{(nll+1)}$	$\alpha_1^{(nll-1)}$	$\alpha_1^{(nl)}$
1s	13.500 000 000 00		4.5
2s	360.000 000 000 00		120
2p	520.000 000 000 00	8.000 000 000 00	176
3s	3 037.500 000 000 02		1 012.5
3p	3 780.000 000 000 01	108.000 000 000 00	1 296
3d	5 783.399 999 999 98	−194.400 000 000 00	1 863
4s	14 976.000 000 000 03		4 992
4p	17 023.999 999 999 96	640.000 000 000 01	5 888
4d	24 192.000 000 000 02	−1152.000 000 000 00	7 680
4f	34 559.999 999 999 70	−3455.999 999 999 99	10 368

it is a solution of the confined problem. As it does not vanish between $r = 0$ and $r = R$, it describes the ground state of the confined atom. The exact 1s confined energy is the 2s unconfined energy,

$$E_{1s}(R = 2) = E_{2s}(R = \infty) = -1/8. \tag{5.33}$$

The energies of the excited states for $R = 2$ do not have a simple expression.

Various numerical techniques have been used to solve this problem. Here I only mention those having some relation with the LMM. In Refs. [128,129], a mapped Fourier grid method has been applied. However, the convergence can be much faster with the LMM [51]. Let me apply several variants of the LMM to the ground-state energy of the hydrogen atom confined in a sphere of radius $R = 2$.

I first consider the approach employed in Ref. [51], i.e. a Lagrange mesh based on shifted Legendre polynomials regularized at 0 and R obtained by scaling the expressions of Section 3.4.7. For $i = 1$ to N, the Lagrange basis (3.138) reads

$$f_i(r) = (-1)^{i+N} \frac{r(R-r)}{\sqrt{R^3 x_i(1-x_i)}} \frac{P_N(2r/R-1)}{r - Rx_i}. \tag{5.34}$$

The mesh points Rx_i are given by (3.120),

$$P_N(2x_i - 1) = 0. \tag{5.35}$$

This basis is not orthonormal. The overlaps are given by

$$\langle f_i | f_j \rangle = \delta_{ij} + \frac{(-1)^{i+j}}{4(2N+1)\sqrt{x_i(1-x_i)x_j(1-x_j)}} \times \left[\frac{3}{2} + \frac{1}{2(2N-1)(2N+3)} + 4(x_i^2 + x_i x_j + x_j^2) - 6(x_i + x_j) \right]. \tag{5.36}$$

In spite of this complicated expression, the basis is treated below as orthonormal, as it is orthonormal at the Gauss approximation. The kinetic matrix elements are given at the Gauss approximation by scaling Eqs. (3.142) and (3.143). The Gauss quadrature is also not exact here as shown by (3.144).

Results with this mesh are presented in the upper lines of the left-hand side of Table 9. The mean radius is calculated simply as

$$\langle r \rangle = R \sum_{j=1}^{N} x_j c_j^2, \tag{5.37}$$

where the c_j are the coefficients in expansion (2.25). With the Legendre mesh, the convergence of the energy and of the mean radius are extremely fast for a calculation without any evaluation of integral. Notice that the convergence is reached from below, in sharp contrast with a real variational calculation. With only 8 mesh points, the error on the energy is 10^{-14}. Adding two points improves the wave functions and thus the mean radius.

It is interesting to compare basis (5.34) with another Lagrange basis, also vanishing at 0 and R, based on the $\alpha = \beta = 2$ Jacobi polynomials. By scaling and shifting (3.155), one obtains

$$f_i(r) = (-1)^{i+N} \sqrt{\frac{(N+4)(N+3)x_i(1-x_i)}{2(N+2)(N+1)R^3}}\, r(R-r) \frac{P_N^{(2,2)}(2r/R-1)}{r - Rx_i} \tag{5.38}$$

with mesh points given by (3.153),

$$P_N^{(2,2)}(2x_i - 1) = 0. \tag{5.39}$$

Table 9
Lagrange-mesh calculations of the ground-state energy E and mean radius $\langle r\rangle$ of the hydrogen atom confined in a sphere of radius $R = 2$ with the shifted Legendre mesh regularized by $r(R-r)$ (left, upper lines), the $(\alpha, \beta) = (2, 0)$ shifted Jacobi mesh regularized by r (left, lower lines), the $(\alpha, \beta) = (2, 2)$ shifted Jacobi mesh (right, upper lines) and the first sine mesh (right, lower lines). The exact mean radius comes from Ref. [127].

Regularized Legendre			Jacobi (2, 2)		
Regularized Jacobi (2, 0)			First sine mesh		
N	E	$\langle r\rangle$	N	E	$\langle r\rangle$
4	−0.125 061	0.860 9	20	−0.124 70	0.859 5
	−0.124 999 906	0.859 364		−0.118 4	0.861 6
6	−0.125 000 001 4	0.859 353 32	40	−0.124 977	0.859 36
	−0.124 999 999 999 35	0.859 353 174 4		−0.123 2	0.860 0
8	−0.125 000 000 000 03	0.859 353 174 268 1	60	−0.124 995 0	0.859 355
	−0.125 000 000 000 18	0.859 353 174 267 0		−0.124 53	0.859 63
10	−0.125 000 000 000 01	0.859 353 174 266 77	80	−0.124 998 4	0.859 354
	−0.124 999 999 999 78	0.859 353 174 266 87		−0.124 79	0.859 51
Exact	−0.125	0.859 353 174 266 771			

Here the factor $r(R-r)$ is the square root of the weight function $w(r)$. This basis is exactly orthonormal. The bases (5.34) and (5.38) are equivalent since they both involve N linearly independent polynomials of degree $N-1$ multiplied by the same factor $r(R-r)$. However, as shown below, this Jacobi (2, 2) mesh gives very poor results. For the kinetic matrix elements, the Gauss quadrature is here catastrophic as suggested by the asymmetry of expression (3.159) because the derivatives of the square root of the weight function $r(R-r)$ are not proportional to this weight function and thus introduce singularities at both 0 and R incompatible with an accurate Gauss quadrature. Numerically exact values of the kinetic matrix elements are however easily obtained with a Gauss–Legendre numerical quadrature involving at least $N+1$ mesh points since the integrand is a polynomial of degree $2N$. The integrand is the product $f_i' f_j'$ calculated by differentiating (5.38). An optimal accuracy is obtained with $N+2$ points.

With the (2, 2) Jacobi mesh, the calculation slowly converges from above (see the upper lines in right-hand side of Table 9). The accuracy on the energy for $N = 80$ is 2×10^{-6}. Even with the numerically exact expressions for the kinetic matrix elements, the singularity at $r = 0$ of the potential strongly hinders the accuracy. Notice that without potential, the accuracy of the hard-sphere energies is as good with this Jacobi mesh as with the regularized Legendre mesh. This confirms that the much slower convergence arises from the Coulomb singularity. Regularizing Coulomb singularities is often crucial.

This interpretation is confirmed with another Lagrange basis derived from Jacobi polynomials with $(\alpha, \beta) = (2, 0)$ regularized by r,

$$f_i(r) = (-1)^{i+N} \sqrt{\frac{1-x_i}{2x_i R^3}}\, r(R-r) \frac{P_N^{(2,0)}(2r/R-1)}{r - Rx_i} \tag{5.40}$$

with the zeros

$$P_N^{(2,0)}(2x_i - 1) = 0. \tag{5.41}$$

Here r is thus the regularization factor and $(R-r)$ is the square root of the weight function $w(r)$. The basis (5.40) is equivalent to the other two bases. It is not orthonormal. The overlap is given by (3.25) and (3.146) as

$$\langle f_i | f_j \rangle = \delta_{ij} + \frac{(-1)^{i+j}}{4(2N+3)} \sqrt{\frac{(1-x_i)(1-x_j)}{x_i x_j}}. \tag{5.42}$$

Because of the regularizing factor, the Gauss quadrature is exact for the Coulomb term. Here also, exact expressions T_{ij} are obtained by integrating the product $f_i' f_j'$ with a Gauss–Legendre numerical quadrature involving $N+2$ mesh points.

The results are presented below the Legendre results in Table 9. One observes an even faster convergence. With only four points, the accuracy of the energy is already 10^{-7} and the accuracy of the mean radius is 10^{-5}. For $N = 6$, these numbers become 10^{-12} and 2×10^{-10}, respectively. This can be understood by the fact that the Gauss–Jacobi quadrature associated with the mesh points is more accurate here since the polynomial multiplying the weight is of degree $2N$, thus smaller than the degree $2N+2$ for the Legendre functions (5.34). For $N = 8$ and 10 however, the accuracy is less good because of the rounding errors in the numerical integration of the kinetic matrix elements. The Legendre mesh remains the most interesting choice because of its analytical simplicity.

Problems of slow convergence occur with other Lagrange meshes for which the Gauss quadrature is not accurate with the Coulomb singularity, like the first sine mesh (Section 3.7.2) as shown in the lower rows on the right-hand side of Table 9.

5.6. Hydrogen atom in a strong magnetic field

The hydrogen atom in a homogeneous magnetic field is a simple example of non-separable system for which a two-dimensional Lagrange mesh is useful. An analytical solution is available which provides essentially exact results from low to

very high fields in the infinite-proton-mass approximation [130,131]. However, those calculations are not easy to perform and the corresponding wave functions are given in the form of series. For these reasons, accurate numerical approximations are still interesting [44,132–134]. Among them, Lagrange-mesh approximate calculations [23,44] are particularly simple. They provide accurate wave functions that can easily be used in more elaborate applications such as the determination of transition probabilities [45].

The non-relativistic Hamiltonian for the hydrogen atom in a magnetic field in the z direction is given in atomic units by

$$H = -\frac{1}{2}\Delta - \frac{1}{r} + \frac{1}{2}\gamma\, L_z + \frac{1}{8}\gamma^2 r_\perp^2. \tag{5.43}$$

In Eq. (5.43), $\boldsymbol{r}$ is the electron coordinate, z is its component along the field axis, $\boldsymbol{r}_\perp$ is its component perpendicular to the field axis, and L_z is the z component of the orbital angular momentum. The parameter γ expresses the magnetic field B in atomic units of $B_0 = \hbar/a_0^2 e \approx 2.35 \times 10^5$ T. In the form (5.43) of H, the proton mass is assumed to be infinite. This approximation becomes inaccurate at very high fields (see Ref. [135] and references therein). Since L_z and the parity operator are constants of motion of H in Eq. (5.43), the eigenstates belong to a subspace corresponding to a fixed eigenvalue m of L_z and a fixed z-parity p.

Several coordinates systems can be used to solve Eq. (5.43). They lead to different Lagrange-mesh treatments [44]. Although the use of semi-parabolic coordinates [23] seems optimal, I present here the Lagrange mesh in spherical coordinates as it is more instructive. In spherical coordinates r, θ, φ, the wave function is factorized as

$$\Psi_m^p(\boldsymbol{r}) = r^{-1}\psi_m^p(r,u)e^{im\varphi}, \tag{5.44}$$

where $u = \cos\theta$ varies over $(-1,+1)$. The Schrödinger equation (5.43) becomes in this coordinate system,

$$\left[\frac{1}{2}\left(-\frac{d^2}{dr^2} + \frac{L_m^2}{r^2}\right) + V(r,u) + \frac{1}{2}m\gamma - E\right]\psi_m^p = 0 \tag{5.45}$$

where L_m^2 is given by (3.103) and the Coulomb and diamagnetic potential reads

$$V(r,u) = -\frac{1}{r} + \frac{1}{8}\gamma^2(1-u^2)r^2. \tag{5.46}$$

The volume element is $drdu$.

The Laguerre zeros x_i $(i = 1,\ldots,N_r)$ are given by (3.50) with $\alpha = 0$. The Lagrange–Laguerre functions $\hat{f}_i(x)$ are regularized as defined in Eq. (3.70). The regularization is necessary because of the r^{-1} and r^{-2} singularities in Eqs. (5.45) and (5.46). The $2N_u$ Legendre mesh points are defined according to Eq. (3.105) but only the N_u positive values are necessary, $0 \le u_j < 1$. Notice that this mesh depends on m. The $2N_u$ associated Lagrange–Legendre functions $g_j(u)$ given by Eq. (3.107) are projected on z parity $p = \pm 1$ [Eq. (2.52)] as

$$g_j^p(u) = 2^{-1/2}[g_j(u) + p g_{-j}(u)] \tag{5.47}$$

where index j then varies from $1/2$ to $N_u - 1/2$.

On the $N_r N_u$ mesh points (hx_i, u_j), the wave function ψ_m^p is expanded as

$$\psi_m^p(r,u) = h^{-1/2}\sum_{i=1}^{N_r}\sum_{j=1/2}^{N_u-1/2} C_{ij}^p \hat{f}_i(r/h) g_j^p(u). \tag{5.48}$$

The Lagrange-mesh system of equations then reads

$$\sum_{i=1}^{N_r}\sum_{j=1/2}^{N_u-1/2}\left\{h^{-2}T_{ij,i'j'}^p + \left[V(hx_i,u_j) + \frac{1}{2}m\gamma - E\right]\delta_{ii'}\delta_{jj'}\right\} C_{ij}^p = 0. \tag{5.49}$$

The kinetic-energy matrix elements are given by the Gauss-quadrature formula as

$$T_{ij,i'j'}^p = \frac{1}{2}[\hat{T}_{ii'}^{rG}\delta_{jj'} + x_i^{-2}(T_{jj'}^u + pT_{j-j'}^u)\delta_{ii'}] \tag{5.50}$$

where $\hat{T}_{ii'}^{rG}$ is given by (3.75) and (3.76) while $T_{jj'}^u$ is given by (3.115) and (3.116). The present calculation is very similar to the one in Ref. [82] but simplified by compact expressions for the kinetic energy. Other matrix elements are then easily calculated [44,45].

Results are presented in Table 10 for $m = 0, -1$ and -2. Positive m values lead to much higher energies because of the $\frac{1}{2}\gamma L_z$ term in (5.43). Two cases are presented: the field $\gamma = 1$ where the magnetic and Coulomb effects have the same order of magnitude and the strong field $\gamma = 1000$. The binding energies $E_B = \frac{1}{2}(|m| + m + 1)\gamma - E$ are compared with accurate literature results [131–134]. The corresponding r.m.s. radii and quadrupole moments are also given [44].

The size of the basis is $N_r N_u$. Very accurate results are obtained with sizes ranging from 300 $(m = 0)$ or 672 $(m = -2)$ for $\gamma = 1$, to 8000 $(m = 0)$ or 12,800 $(m = -2)$ for $\gamma = 1000$. It is shown in Ref. [44] that the role of the regularization is not important for $m = -1$ and $m = -2$.

Table 10
Binding energies E_B, r.m.s. radii $\langle r^2\rangle^{1/2}$, and quadrupole moments Q of the $m = 0$, -1 and -2 states as a function of the magnetic field γ (a). Comparison with (b) energies of Ref. [131] and quadrupole moments of Ref. [136] and (c) energies of Refs. [132–134] (all digits not shown).

γ		N_r	$2N_u$	h	E_B (Hartree)	$\langle r^2\rangle^{1/2}$	Q
$m = 0$							
1	a	20	30	0.2	0.831 168 896 733 2	1.347 711 846 509	0.417 654 244 94
	b				0.831 168 896 733		0.415 5
	c				0.831 168 896 733 158		
1000	a	80	200	0.03	7.662 423 238	0.228 181 387	0.098 159 819
	b				7.662 423 247 755		0.098 1
$m = -1$							
1	a	24	40	0.2	0.456 597 058 423 8	2.270 800 579 23	0.454 199 198 8
	b				0.456 597 058 424		
	c				0.456 597 058 423 752		
1000	a	80	300	0.03	5.638 421 084 6	0.277 223 496	0.141 726 625
	b				5.638 421 08		
	c				5.638 421 079 484 214		
$m = -2$							
1	a	28	48	0.2	0.353 048 025 149 6	2.858 521 188 61	0.110 861 229 2
	b				0.353 048 025 149		
1000	a	80	320	0.03	4.805 110 675	0.307 979 592	0.171 721 29
	b				4.805 110 67		

5.7. Lagrange-mesh method in momentum space

Numerical solutions of the Schrödinger equation in momentum space have been studied with the LMM by Semay and coworkers [137,138]. The basic motivation of working in momentum space is the possibility of using kinetic operators $T(p^2)$ more complicated than the non-relativistic operator $T_{NR}(p^2) = p^2/2m$. For example, working in momentum space [137,138] allows a simpler treatment of the semirelativistic kinetic expression $T_{SR}(p^2) = \sqrt{p^2c^2 + m_1^2c^4} + \sqrt{p^2c^2 + m_2^2c^4}$, where m_1 and m_2 are the masses of the interacting particles, than in configuration space [139].

If the non-local potential $V_l(p, p')$ for partial wave l in momentum space is known or if the Fourier transform of the potential $V(r)$ in configuration space is available, the Schrödinger equation reads

$$T(p^2)\psi_l(p) + \int_0^\infty pV_l(p, p')p'\psi_l(p')dp' = E\psi_l(p) \tag{5.51}$$

where $T(p^2)$ can be $T_{NR}(p^2)$ or $T_{SR}(p^2)$. The solution $\psi_l(p)$ vanishes at the origin and is square integrable over $(0, \infty)$ for bound states. If $\psi_l(p)$ is expanded in regularized Lagrange–Laguerre functions (3.70) as

$$\psi_l(p) = h^{-1/2}\sum_{j=1}^{N} c_j\hat{f}_j(p/h), \tag{5.52}$$

the Gauss quadrature with mesh points hx_i leads to the mesh equations

$$\sum_{j=1}^{N}[T(h^2x_i^2)\delta_{ij} + h^3\sqrt{\lambda_i\lambda_j}x_ix_jV_l(hx_i, hx_j)]c_j = Ec_i. \tag{5.53}$$

The matrix appearing in this eigenvalue problem displays different properties from the configuration-space matrix. In r space, the potential matrix is diagonal and the weights λ_j do not appear. The weights are needed only if the wave function must be constructed. In p space, the kinetic-energy matrix is diagonal and the weights appear in the potential matrix.

Another interesting case, not considered in Refs. [137,138] but based on some of their results in §III.E, occurs when the Fourier transform of a potential $V(r)$ is not available. It is based on the expression $\boldsymbol{r} = i\nabla_{\boldsymbol{p}}$. Then the matrix elements $\langle f_i|V(r)|f_j\rangle$ between scaled Lagrange functions in p space can be obtained [138] from

$$(r^2)_{ij} = \langle\hat{f}_i| - \frac{d^2}{dp^2} + \frac{l(l+1)}{p^2}|\hat{f}_j\rangle_G = h^{-2}\left(T_{ij}^G + \frac{l(l+1)}{x_i^2}\delta_{ij}\right) \tag{5.54}$$

where T_{ij}^G is the Gauss approximation for the matrix element of $-d^2/dp^2$ which is derived in position space for $-d^2/dx^2$ in previous sections. For the regularized Laguerre mesh, the T_{ij}^G are given by (3.75) and (3.76). If the positive definite symmetric matrix with elements $(r^2)_{ij}$ is diagonalized into a diagonal matrix $\boldsymbol{D}$ with diagonal elements d_k by an orthogonal matrix $\boldsymbol{O}$, one obtains

$$\langle\hat{f}_i|V(r)|\hat{f}_j\rangle_G = [\boldsymbol{O}V(\sqrt{\boldsymbol{D}})\boldsymbol{O}^T]_{ij} \tag{5.55}$$

Table 11
Ground-state energy of the Gaussian potential (5.57) with $g = 15$ by three different methods on regularized Laguerre meshes with $h = 0.4$: in r space, in p space with Eqs. (5.53) and (5.59), and with Eq. (5.56).

N	r space	p space	
		Eq. (5.53)	Eq. (5.56)
10	−5.389 8	−5.377 602 13	−5.377 599 166
20	−5.377 858	−5.377 599 907 062 3	−5.377 599 907 034
40	−5.377 599 897 6	−5.377 599 907 068 446	−5.377 599 907 068 483
60	−5.377 599 907 206	−5.377 599 907 068 436	−5.377 599 907 067 966
80	−5.377 599 907 068 667	−5.377 599 907 068 435	−5.377 599 907 068 306
100	−5.377 599 907 068 927	−5.377 599 907 068 442	−5.377 599 907 068 586

Table 12
Ground-state energy of the Yukawa potential (5.60) with $g = 10$ on a regularized Laguerre mesh: in r space ($h = 0.1$) and in p space with Eq. (5.56) ($h = 10$).

N	r space	N	$p$space Eq. (5.56)
5	−16.340 425 965	50	−16.337 0
10	−16.340 425 568 459 64	100	−16.340 148
20	−16.340 425 568 459 81	200	−16.340 365
30	−16.340 425 568 459 52	300	−16.340 399
		400	−16.340 410
		500	−16.340 416

where $V(\sqrt{\boldsymbol{D}})$ is a diagonal matrix containing the diagonal elements $V(\sqrt{d_k})$. The Schrödinger equation thus reads

$$\sum_{j=1}^{N}\left[T(h^2x_i^2)\delta_{ij}+\sum_{k=1}^{N}O_{ik}V\left(\sqrt{d_k}\right)O_{jk}\right]c_j = Ec_i. \tag{5.56}$$

The need for a Fourier transform is then avoided.

Like in Ref. [138], let us consider the simple non-relativistic example, with $T_{NR}(p^2)$, of a Gaussian interaction

$$V(r) = -g\ \exp(-r^2) \tag{5.57}$$

in units $\hbar = 2m = a = 1$ where a is the range of the potential. The Fourier transform is also a Gaussian that leads for partial wave l to

$$V_l(p,p') = -\frac{g}{2\sqrt{\pi}}\,e^{-(p^2+p'^2)/4}i_l(pp'/2) \tag{5.58}$$

where i_l is a spherical Hankel function [22]. For example, the s-wave potential reads

$$V_0(p,p') = -\frac{g}{2\sqrt{\pi pp'}}\,e^{-(p-p')^2/4}\left(1-e^{-pp'}\right). \tag{5.59}$$

In Table 11, the ground-state energy is obtained on regularized Laguerre meshes for the potential with $g = 15$ as a function of the number N of mesh points in three different ways: in r space, in p space with Eqs. (5.53) and (5.59), and in p space with Eq. (5.56). The optimal scale factor takes the same value $h = 0.4$ in both spaces. In r space, a 10^{-8} accuracy is reached with $N = 40$ and a 10^{-12} accuracy is reached with $N = 80$. In p space with the analytical potential, the convergence is much faster. The accuracy is already about 2×10^{-6} with $N = 10$. A 10^{-14} accuracy is reached with $N = 40$. In p space with approximation (5.56), the convergence is almost as fast but the results are less stable for high N. This is understandable since the calculation in Eq. (5.55) requires matrix multiplications which increase the role of rounding errors.

Let us now consider the other example of Ref. [138], the Yukawa potential

$$V(r) = -g\,\frac{e^{-r}}{r} \tag{5.60}$$

with $g = 10$. In Table 12, the ground-state energy is obtained on a regularized Laguerre mesh in r space and with Eq. (5.56) to avoid the complicated expression of this potential in p space [138]. The optimal scale factors now take different values. For this potential, the convergence in r space is much faster. The optimal scale factor is close to $h = 0.1$. With only 5 points, the absolute accuracy is better than 10^{-6}. With 10 points, it reaches 10^{-12}. The calculations in p space are performed with Eq. (5.56) (see Ref. [138] for a calculation with the analytical Fourier-transformed potential which involves a Legendre function of the second kind). The optimal h is quite large. It is taken as $h = 10$. The convergence is slow. Even with $N = 500$, the accuracy is only 10^{-5}. In Ref. [138], a slightly faster convergence is obtained with the analytical formula.

For the Schrödinger equations considered here, the treatment in momentum space is much more interesting for the fast-decreasing Gaussian potential than for the Yukawa potential. See Ref. [138] for applications involving more complicated kinetic energies $T_{SR}(p^2)$.

5.8. One-dimensional Dirac oscillator

In one dimension, the Dirac oscillator [140] can be written as a two-component problem. It provides a simple preliminary example of the Dirac equation [141]. Like the Dirac equation, it involves the use of first-order differential operators.

The two-component Dirac equation in one dimension is written with $\hbar = c = m = 1$ as

$$H_D\phi = \{\alpha[p_x - i\beta V(x)] + \beta\}\phi = E\phi \tag{5.61}$$

where $\alpha = \sigma_y$ and $\beta = \sigma_z$ are 2×2 Pauli matrices and

$$V(x) = \omega x. \tag{5.62}$$

Let us write $\phi(x)$ as

$$\phi(x) = \begin{pmatrix} P(x) \\ Q(x) \end{pmatrix}. \tag{5.63}$$

The coupled Dirac equations become in matrix form

$$\begin{pmatrix} 1 & -\dfrac{d}{dx} + V(x) \\ \dfrac{d}{dx} + V(x) & -1 \end{pmatrix} \begin{pmatrix} P(x) \\ Q(x) \end{pmatrix} = E \begin{pmatrix} P(x) \\ Q(x) \end{pmatrix}. \tag{5.64}$$

The exact eigenvalues of the Dirac oscillator are [140,141]

$$E_n = \pm\sqrt{1 + 2|n|\omega}, \quad n = 0, \pm1, \pm2, \ldots \tag{5.65}$$

Hence the squares of the energies have the simple form $1 + 2|n|\omega$. The energies appear in opposite pairs except for $n = 0$.

The components $P(x)$ and $Q(x)$ are expanded in Lagrange functions as

$$\begin{pmatrix} P(x) \\ Q(x) \end{pmatrix} = h^{-1/2} \begin{pmatrix} \displaystyle\sum_{j=1}^{N} p_j f_j(x/h) \\ \displaystyle\sum_{j=1}^{N} q_j f_j(x/h) \end{pmatrix} \tag{5.66}$$

with the mesh points hu_i. A projection on the Lagrange functions leads to the $2N \times 2N$ algebraic system of equations

$$\begin{pmatrix} I & H^{(1,2)} \\ H^{(2,1)} & -I \end{pmatrix} \begin{pmatrix} (p_1, p_2, \ldots, p_N)^T \\ (q_1, q_2, \ldots, q_N)^T \end{pmatrix} = E \begin{pmatrix} (p_1, p_2, \ldots, p_N)^T \\ (q_1, q_2, \ldots, q_N)^T \end{pmatrix} \tag{5.67}$$

with

$$H_{ij}^{(1,2)} = H_{ji}^{(2,1)} = -\frac{1}{h}D_{ij} + V(hu_i)\delta_{ij}. \tag{5.68}$$

The matrix elements D_{ij} for the Hermite mesh are given by (3.37) and (3.38) where the Gauss quadrature is exact, and those of the sinc mesh by (3.291). Notice that the trace of the Hamiltonian matrix is zero.

The P_n and Q_n components of the wave function corresponding to energy E_n are respectively proportional to oscillator wave functions $H_{|n|}(x)\exp(-x^2/2)$ and $H_{|n|-1}(x)\exp(-x^2/2)$ (except $Q_0 = 0$). For the Hermite mesh, the Lagrange-mesh equations are exact variational equations for any N since the matrix elements of both the potential and the first derivative are exactly given by the Gauss quadrature. According to (5.4), both components can be expressed exactly by a sufficiently large expansion in Lagrange–Hermite functions. Hence the energies and wave functions must be exact for the Hermite mesh, up to rounding errors.

Numerical values for the squares of the eigenvalues obtained for $\omega = 1$ with the Hermite and sinc meshes are presented in Table 13. The Hermite results are optimal with $h = 1/\sqrt{\omega}$ and are in this case all exact. This is confirmed by the results obtained with $N = 5$. Nine of the $2N = 10$ eigenvalues correspond to the exact energies and wave functions for quantum numbers $n = -4$ to 4. The tenth eigenvalue (indicated by a star) is equal to 1 as expected from the fact that the trace of the matrix vanishes. It corresponds to an eigenvector with $p_i = 0$ and $q_j = (-1)^j$. For $h = 1/\sqrt{\omega}$, this exact but unphysical solution is due to the exactness of the matrix elements (3.37) and (3.38) and to the Stieltjes sum rule [142]

$$\sum_{j\neq k}^{N} \frac{1}{x_j - x_k} = x_k, \quad k = 1, \ldots, N. \tag{5.69}$$

The mean square radii are also shown in the table. They are exact for $|n| \leq 3$ but not for $|n| = 4$ because the degree of the polynomial is one unit too high. With $N = 6$, one obtains 23/6 for $n = -4$ and 25/6 for $n = +4$. The radius for the non-physical eigenvalue is meaningless and is just given for information.

Table 13
Squared energies and mean square radii of the $n = -4$ to 4 states of the Dirac oscillator with $\omega = 1$ calculated with the Hermite mesh ($N = 5, h = 1$) and sinc mesh ($N = 20, h = 0.5$). The row indicated by a star and the numbers in parentheses have no physical meaning (see text).

n	Hermite		sinc	
	E_n^2	$\langle x^2\rangle$	E_n^2	$\langle x^2\rangle$
−4	9.000 000 000 000 005	(3.000 000 000 000 9)	9.000 000 977	3.833 322
−3	7.000 000 000 000 003	2.811 017 763 495 7	7.000 000 004 6	2.811 017 685
−2	5.000 000 000 000 004	1.776 393 202 250 5	5.000 000 004 6	1.776 393 150
−1	3.000 000 000 000 003	0.711 324 865 405 3	3.000 000 000 003 3	0.711 324 865 33
*	0.999 999 999 999 999	(2.000 000 000 000 1)	1.000 000 000 003 3	(9.30 027 802 160)
0	1.000 000 000 000 002	0.500 000 000 000 1	1.000 000 000 003 3	0.499 999 999 96
1	3.000 000 000 000 001	1.288 675 134 595 3	3.000 000 000 003 3	1.288 675 134 45
2	4.999 999 999 999 993	2.223 606 797 750 5	5.000 000 004 6	2.223 606 741
3	7.000 000 000 000 005	3.188 982 236 505 7	7.000 000 004 6	3.188 982 134
4	8.999 999 999 999 995	(2.500 000 000 000 9)	9.000 000 977	4.166 656

The sinc mesh gives accurate but non-exact results after h has been roughly optimized to $h = 10/N\sqrt{\omega}$. With $N = 20$ points, good results are obtained for low $|n|$ values. The accuracy decreases when $|n|$ increases. The mean square radii are also accurate. For $|n| = 4$ the accuracy is still better than 10^{-5}. An unphysical eigenvalue very close to 1 also appears, as expected from the trace of the matrix. The p_i components of the corresponding eigenvector are small and the absolute values of the q_i components do not vary much. Some relation similar to an approximate Stieltjes sum rule is also at work here.

5.9. Dirac equation for hydrogenic atoms

Until now, most published Lagrange-mesh calculations are non-relativistic. A semi-relativistic approach based on the Salpeter equation has been developed by Semay and coworkers [139,143,144]. The difference with the Schrödinger equation lies in a relativistic kinetic energy $\sqrt{p^2c^2 + m^2c^4}$ whose matrix elements can be obtained by diagonalizing the matrix representing p^2. The Dirac equation allows a simpler Lagrange-mesh treatment. In the case of hydrogenic atoms, it can even provide numerically exact energies and wave functions, with very low numbers of mesh points [145].

In atomic units, the Dirac Hamiltonian reads

$$H_D = c\alpha \cdot \boldsymbol{p} + \beta c^2 + V(r), \tag{5.70}$$

where α and β are the traditional Dirac matrices and the speed of light $c = 1/\alpha$ is the inverse of the fine-structure constant. Its eigenenergies are denoted $c^2 + E$. The Dirac spinors are written as

$$\phi_{\kappa m}(\boldsymbol{r}) = \frac{1}{r}\begin{pmatrix} P_\kappa(r)\chi_{\kappa m} \\ iQ_\kappa(r)\chi_{-\kappa m}\end{pmatrix} \tag{5.71}$$

as a function of the large and small radial components $P_\kappa(r)$ and $Q_\kappa(r)$. The spinors $\chi_{\kappa m}$ are eigenstates of $\boldsymbol{L}^2, \boldsymbol{S}^2, \boldsymbol{J}^2$ and J_z with respective eigenvalues $l(l+1)$, $3/4$, $j(j+1)$ and m where

$$j = |\kappa| - \frac{1}{2}, \quad l = j + \frac{1}{2}\,\mathrm{sgn}\,\kappa. \tag{5.72}$$

The coupled radial Dirac equations read in matrix form

$$H_\kappa\begin{pmatrix} P_\kappa(r) \\ Q_\kappa(r)\end{pmatrix} = \begin{pmatrix} V(r) & c\left(-\dfrac{d}{dr} + \dfrac{\kappa}{r}\right) \\ c\left(\dfrac{d}{dr} + \dfrac{\kappa}{r}\right) & V(r) - 2c^2\end{pmatrix}\begin{pmatrix} P_\kappa(r) \\ Q_\kappa(r)\end{pmatrix} = E\begin{pmatrix} P_\kappa(r) \\ Q_\kappa(r)\end{pmatrix}. \tag{5.73}$$

The Dirac spinors (5.71) are normed if

$$\int_0^\infty \left\{[P_\kappa(r)]^2 + [Q_\kappa(r)]^2\right\} dr = 1. \tag{5.74}$$

The radial functions $P_\kappa(r)$ and $Q_\kappa(r)$ are expanded in regularized Lagrange functions (3.70) as

$$\begin{pmatrix} P_\kappa(r) \\ Q_\kappa(r)\end{pmatrix} = h^{-1/2}\begin{pmatrix} \displaystyle\sum_{j=1}^N p_j \hat{f}_j^{(\alpha')}(r/h) \\ \displaystyle\sum_{j=1}^N q_j \hat{f}_j^{(\alpha')}(r/h)\end{pmatrix}. \tag{5.75}$$

The superscript added to the Lagrange functions corresponds to the superscript of the generalized Laguerre polynomials in Eq. (3.70). It is denoted here α' to avoid confusion with the fine-structure constant. A projection on the Lagrange functions leads to the $2N \times 2N$ algebraic system of equations

$$\begin{pmatrix} H^{(1,1)} & H^{(1,2)} \\ H^{(2,1)} & H^{(2,2)} \end{pmatrix} \begin{pmatrix} \boldsymbol{p} \\ \boldsymbol{q} \end{pmatrix} = E \begin{pmatrix} \boldsymbol{p} \\ \boldsymbol{q} \end{pmatrix} \tag{5.76}$$

with $\boldsymbol{p}^T = (p_1, p_2, \ldots, p_N), \boldsymbol{q}^T = (q_1, q_2, \ldots, q_N)$. The diagonal blocks have elements

$$H_{ij}^{(1,1)} = V(hx_i)\delta_{ij}, \qquad H_{ij}^{(2,2)} = (V(hx_i) - 2c^2)\delta_{ij}. \tag{5.77}$$

For the non-diagonal blocks, the matrix representing the term $c\kappa/r$ is exactly given by the Gauss quadrature and is diagonal. For the matrix elements of the first derivative d/dr, several options are possible. One can use the exact expressions (3.73) since they are available, or use the Gauss approximation. In the spirit of the LMM, I use the Gauss quadrature for the (2, 1) block and define the (1, 2) block by symmetry, i.e.,

$$H_{ij}^{(1,2)} = H_{ji}^{(2,1)} = \frac{c}{h}\left(D_{ij}^G + \frac{\kappa}{x_i}\delta_{ij}\right) \tag{5.78}$$

where D_{ij}^G is given by (3.72). It is also possible to use the Gauss quadrature for $H_{ij}^{(2,1)}$ and symmetrize. This leads to another matrix [145]. One can show that half the eigenvalues of the Hamiltonian matrix are large and negative. The lowest slightly negative ones approximate bound-state energies. The corresponding eigenvectors normalized according to

$$\sum_{i=1}^{N}\left(p_i^2 + q_i^2\right) = 1, \tag{5.79}$$

which corresponds to a Gauss quadrature of (5.74), provide the normed wave functions. In the hydrogenic cases, Eq. (5.79) is numerically exact.

For a relativistic hydrogenic atom, the potential is

$$V(r) = -\frac{Z}{r}. \tag{5.80}$$

As a function of the principal quantum number n, the energies are given analytically as [146]

$$E_{n\kappa} = c^2\left\{\left[1 + \frac{\alpha^2 Z^2}{(n - |\kappa| + \gamma)^2}\right]^{-1/2} - 1\right\} \tag{5.81}$$

with the parameter γ defined by

$$\gamma = \sqrt{\kappa^2 - \alpha^2 Z^2}. \tag{5.82}$$

They can be written in a form minimizing rounding errors as

$$E_{n\kappa} = -\frac{Z^2}{\mathcal{N}(\mathcal{N} + n - |\kappa| + \gamma)} \tag{5.83}$$

with the *effective* principal quantum number

$$\mathcal{N} = [(n - |\kappa| + \gamma)^2 + \alpha^2 Z^2]^{1/2}. \tag{5.84}$$

This number is equal to n when $|\kappa| = n$. Otherwise, it is not an integer.

Before choosing the LMM basis, it is important to first analyse the behaviour of the wave functions near the origin. It is well known [146] that the radial functions behave near the origin as

$$P_{n\kappa}(r),\ Q_{n\kappa}(r) \underset{r\to 0}{\to} r^{\gamma}, \tag{5.85}$$

i.e. the wave functions $\phi_{n\kappa m}$ are singular for $|\kappa| = 1$. This singularity is weak for the hydrogen atom but can be important for hydrogenic ions with high charges Z. The Lagrange functions (3.70) behave as

$$\hat{f}_j^{(\alpha')}(x) \underset{x\to 0}{\to} x^{1+\alpha'/2}. \tag{5.86}$$

Table 14
Regularized Lagrange–Laguerre mesh calculations of $n \leq 3$ energies of the relativistic $Z = 1$ hydrogen atom and $Z = 100$ hydrogenic ion for given N and h ($c = 137.035999074$ [147]).

nlj	κ	h	N	$E_{n\kappa}$ ($\alpha' = 2\gamma - 2$)	N	$E_{n\kappa}$ ($\alpha' = 0$)
$Z = 1$						
$1s1/2$	-1	0.5	3	−0.500 006 656 596 554	3	−0.500 006 656 715
$2s1/2$	-1	1	5	−0.125 002 080 189 192	5	−0.125 002 080 208
$2p1/2$	$+1$	1	4	−0.125 002 080 189 192	4	−0.125 002 080 192 9
$2p3/2$	-2	1	4	−0.125 000 416 028 976	4	−0.125 000 416 029 9
$3s1/2$	-1	1	7	−0.055 556 295 176 422	7	−0.055 556 295 183
$3p1/2$	$+1$	1.5	5	−0.055 556 295 176 422	5	−0.055 556 295 195
$3p3/2$	-2	1.5	5	−0.055 555 802 091 367	5	−0.055 555 802 096
$3d3/2$	$+2$	1.5	5	−0.055 555 802 091 367	5	−0.055 555 802 091 398
$3d5/2$	-3	1.5	5	−0.055 555 637 733 815	5	−0.055 555 637 733 829
$Z = 100$						
$1s1/2$	-1	0.005	3	−5939.195 192 426 652	100	−5932.765
$2s1/2$	-1	0.009 175	5	−1548.656 111 829 165	100	−1545.707
		0.010	6	−1548.656 126	100	−1545.359
$2p1/2$	$+1$	0.009 175	4	−1548.656 111 829 167	100	−1548.567
		0.010	5	−1548.656 670	100	−1548.556
$2p3/2$	-2	0.010	4	−1294.626 149 195 190	100	−1294.626 143
$3s1/2$	-1	0.013 906	7	−657.945 199 521 658 9	100	−656.436
		0.015	8	−657.945 199 577	100	−656.284
$3p1/2$	$+1$	0.013 906	5	−657.945 199 521 658 8	100	−657.890
		0.015	6	−657.946 487	100	−657.883
$3p3/2$	-2	0.014 768	5	−582.139 046 840 141 8	100	−582.139 036
		0.015	6	−582.139 046 840 163	100	−582.139 036
$3d3/2$	$+2$	0.014 768	5	−582.139 046 840 141 9	100	−582.139 046 829
		0.015	6	−582.139 046 840 143	100	−582.139 046 828
$3d5/2$	-3	0.015	5	−564.025 853 485 845 0	100	−564.025 853 485 675

Hence rather than choosing $\alpha' = 0$ like in the non-relativistic case (Section 5.4), it is convenient to choose

$$\alpha' = 2(\gamma - 1). \tag{5.87}$$

The choice $\alpha' = 2(\gamma - |\kappa|)$ can also be convenient [125]. The radial functions $P_{n\kappa}$ and $Q_{n\kappa}$ are polynomials multiplied by r^γ and the exponential $\exp(-Zr/2\mathcal{N})$. With α' given by (5.87) and

$$h = \mathcal{N}/2Z, \tag{5.88}$$

the LMM is thus able to reproduce the exact $n\kappa$ eigenfunctions if $N > n$. This remains true even when the approximate expressions D^G_{ij} are used. Indeed, like in Section 5.4.2, one can show that vectors $\boldsymbol{p}_{n\kappa}$ and $\boldsymbol{q}_{n\kappa}$ corresponding to the exact eigenvalue $E_{n\kappa}$ are orthogonal to the vector $\boldsymbol{v}$ defined by (5.23). Since the matrix with elements (3.73) can be rewritten as

$$\boldsymbol{D}^G = \boldsymbol{D} + \frac{1}{2}\boldsymbol{v}\boldsymbol{v}^T, \tag{5.89}$$

the use of the Gauss approximation in any of the non-diagonal blocks does not affect the eigenvector corresponding to the exact eigenvalue.

The trace of the Hamiltonian matrix in (5.76), and thus the sum of all eigenvalues, is

$$-2Nc^2 - 2\sum_{i=1}^{N}\frac{Z}{hx_i} = -2N\left[c^2 + \frac{Z}{h(\alpha'+1)}\right] \tag{5.90}$$

and supports the fact that half the eigenvalues are large and negative.

Exact energies for principal quantum number n can be obtained with $N = n + 1$. For example, $N = 2$ provides the exact ground-state eigenvalue and eigenfunction (see Appendix D).

The energies of hydrogenic atoms obtained with different calculations are displayed in Table 14 for $n \leq 3$ in the cases $Z = 1$ and $Z = 100$. The calculations are performed with $N = n + 2$, except for s states ($n > 1$) where a slightly larger value is used to move spurious eigenvalues to higher energies. The choice $N = n + 2$ leads below to a number of accurate mean radii. The first $E_{n\kappa}$ column contains energies obtained with the optimal α' defined in Eq. (5.87). These energies coincide with the exact ones (5.83) except possibly for one or two units on the last displayed digit. For $Z = 1$, the energies are shown as obtained with $h = n/2Z$ but calculations with the optimal value (5.88) lead to exactly the same displayed digits because the difference between the h values is smaller than 10^{-5}. As in most other cases, the results are not very sensitive to the precise choice of h. Nevertheless, at some higher accuracy level, calculations with more digits should be made with (5.88) to provide the exact values. For $Z = 100$, results are displayed for both choices of h. All digits of h need not be specified. Since the difference between both h values decreases when $n - |\kappa|$ increases, the difference between energies is more important

Table 15
Lagrange-mesh calculations of the mean values $\langle r^k \rangle$ ($k = -2, -1, 1$ et 2) for the Dirac hydrogen atom with $N = 6$ and $N = 8$ mesh points. Exact values are obtained from analytical expressions of Refs. [146,148].

k	N	$1s1/2$	$2s1/2$	$2p1/2$	$2p3/2$
-2	6	2.000 159 766 117 41	0.250 028 292 269 08	0.083 342 024 388 25	0.083 334 627 656 44
	8	2.000 159 766 115 35	0.250 028 292 269 07	0.083 342 024 388 25	0.083 334 627 656 58
[148]		2.000 159 766 116 23	0.250 028 292 269 07	0.083 342 024 388 25	0.083 334 627 656 58
-1	6	1.000 026 626 741 00	0.250 008 320 873 09	0.250 008 320 873 08	0.250 001 664 121 28
	8	1.000 026 626 740 53	0.250 008 320 873 09	0.250 008 320 873 08	0.250 001 664 121 46
[146]		1.000 026 626 740 70	0.250 008 320 873 09	0.250 008 320 873 09	0.250 001 664 121 44
1	6	1.499 973 373 967 93	5.999 883 511 520 98	4.999 883 511 521 05	4.999 973 374 235 24
	8	1.499 973 373 968 37	5.999 883 511 521 02	4.999 883 511 521 02	4.999 973 374 233 82
[146]		1.499 973 373 968 26	5.999 883 511 521 01	4.999 883 511 521 01	4.999 973 374 234 12
2	6	2.999 906 809 597 00	41.998 495 647 329 0	29.998 735 280 817 7	29.999 707 117 288 4
	8	2.999 906 809 598 03	41.998 495 647 329 3	29.998 735 280 817 4	29.999 707 117 282 1
[146]		2.999 906 809 597 87	41.998 495 647 329 2	29.998 735 280 817 3	29.999 707 117 284 2

for the $3s1/2$ state than for the other displayed states. The relative error with the non-relativistic value $h = n/2Z$ is about 10^{-10}.

The last column presents calculations with standard Laguerre polynomials ($\alpha' = 0$). For $Z = 1$, the difference with the fourth column is tiny when the same number of mesh points is kept. It decreases when $|\kappa|$ increases. For $Z = 100$, with the same N, the results are very bad. Even with the much larger $N = 100$ value, the accuracy remains poor except when $|\kappa|$ is close to n.

These results are obtained with h values varying from shell to shell and sometimes from level to level. At least three numerically exact eigenvalues can be obtained simultaneously with only $N = 20$ mesh points in some average range of scaling parameters [145].

The obtained wave functions and the corresponding Gauss quadrature lead to the exact mean values for the operators r^{-2}, r^{-1}, r, r^2 and r^3 with

$$\langle \phi_{n\kappa m} | r^k | \phi_{n\kappa m} \rangle = h^k \sum_{j=1}^{N} (p_{n\kappa j}^2 + q_{n\kappa j}^2) x_j^k. \tag{5.91}$$

The exact mean values of higher positive integer powers of r can also be obtained but with increasing numbers N of mesh points. These values are displayed Table 15. The numerical results agree with the analytical expressions from Table 3.2 of Ref. [146] for $k = -1$, 1 and 2 or from Ref. [148] for $k = -2$.

The calculation of dipole polarizabilities is more instructive. As now shown, while some partial polarizabilities (C.7) or (C.10) of the hydrogenic atoms are exact like in the non-relativistic case, others are not when $|\kappa'| \neq |\kappa|$. The exact polarizability for the ground state is calculated in [149,150]. The $\kappa' = +1$ partial polarizability (C.7) is simply given by [150]

$$\alpha_1^{(1s,-1,+1)} = \frac{1}{36Z^4} \gamma(\gamma+1)(2\gamma+1)(4\gamma+5). \tag{5.92}$$

The expression of the $\kappa' = -2$ partial polarizability is very complicated; it involves ${}_3F_2$ hypergeometric functions. Not surprisingly, the LMM only gives the exact value for $\kappa' = 1$.

In order to use the LMM, I first analyse Eq. (C.9) for $|\kappa'| = |\kappa|$. The components $P_{n\kappa}$ and $Q_{n\kappa}$ in the right-hand side contain an exponential multiplied by r^γ and by polynomials. The singularity in the l.h.s. is the same. The functions $P^{(1)}_{n\kappa\kappa'}$ and $Q^{(1)}_{n\kappa\kappa'}$ are thus also polynomials multiplied by the same exponential and the same power r^γ. Hence the LMM can solve exactly Eq. (C.9) and the equivalent polarizabilities (C.7) and (C.10) are both exact. This is not true for $\kappa' = -2$ because the factors r^γ and $r^{\gamma'}$ are now different. The scale factor in the exponential is still given by (5.88) but there is no simple polynomial factor any more. The matrix element in (C.7) is given by

$$\int_0^\infty [P_{n'\kappa'}(r) P_{n\kappa}(r) + Q_{n'\kappa'}(r) Q_{n\kappa}(r)] r^\lambda dr = h^\lambda \sum_{j=1}^{N} [p_{n'\kappa' j} p_{n\kappa j} + q_{n'\kappa' j} q_{n\kappa j}] x_j^\lambda. \tag{5.93}$$

The relative errors on partial ground-state polarizabilities are displayed in Fig. 19 for $Z = 1$ and $Z = 100$ as a function of the number N of mesh points. The exact values are either given by Eq. (5.92) or by subtraction from the accurate numerical results of Ref. [151]. For $\kappa' = 1$, the calculation is exact and the errors at all displayed N values are close to the computer accuracy for both Z values ($Z = 1$ is not shown). The errors of course depend on the code writing and machine implementation. Due to rounding errors, the accuracy slightly *deteriorates* when N increases. For $\kappa' = -2$, the calculation of the partial polarizability is not exact. Since the values of γ and γ' are very close for $Z = 1$, the calculation converges extremely fast. One observes that the error is slightly larger for $N = 4$ than for $N = 6$–20. For $Z = 100$, the results are poor for low N values. The error progressively decreases and reaches 4×10^{-9} at $N = 80$. These results can be significantly

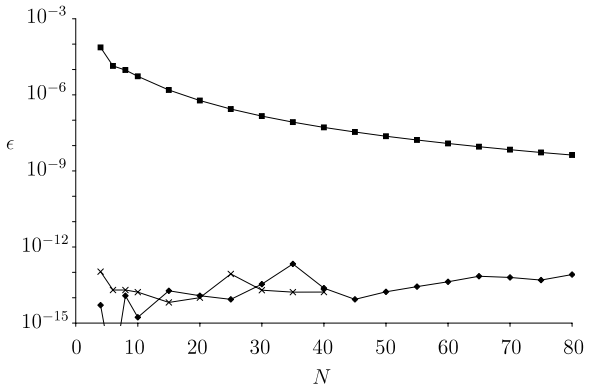

Fig. 19. Relative errors ϵ on the partial ground-state polarizabilities for $Z = 1$ (crosses: $\kappa' = -2$) and $Z = 100$ (diamonds: $\kappa' = 1$; squares: $\kappa' = -2$).

improved by using different meshes for the initial and final states and an adapted Gauss quadrature [125]. Such calculations however require explicit evaluations of the Lagrange functions (3.70).

6. Two-body continuum

6.1. R-matrix method on a Lagrange mesh

The physical information about collisions is contained in the collision matrix $\boldsymbol{S}$ or, in single-channel cases, in the phase shifts. There exist many different techniques of calculation of the phase shifts. It is impossible to quote them all (see also Section 6.6). Here I focus on the R-matrix method. To simplify the presentation, I first consider a single channel. The multichannel case (Section 6.4) is a straightforward extension described in detail in Refs. [43,14].

The R matrix (or reaction matrix) was introduced by Wigner and Eisenbud with the goal of obtaining parametrizations of resonances [152]. It became soon an efficient tool to parametrize cross sections not only at resonances but also between them [153,14]. Later it was progressively realized that it also provides an accurate technique of solution of the Schrödinger equation for collisions (see references in [14]). When combined with the LMM [154], it becomes quite simple. It can be very accurate and allows a treatment of bound states and resonances [154,42,43,28,14] and of the effective-range expansion [155] (Section 6.2). It is very economical in the sense that a good accuracy can be obtained with a small number of evaluations of the potential when the conditions of validity of the LMM are met. This property remains true for non-local potentials if they are short-ranged [28]. It makes the Lagrange-mesh R-matrix method particularly useful for microscopic models of nuclear collisions where the evaluation of the values of the local and non-local potentials takes a very long time [156,157].

The radial Schrödinger equation is

$$H_l\psi_l = E\psi_l \tag{6.1}$$

with the action of the Hamiltonian on partial wave l,

$$H_l\psi_l = \left[-\frac{\hbar^2}{2\mu}\left(\frac{d^2}{dr^2} - \frac{l(l+1)}{r^2}\right) + V(r)\right]\psi_l(r) + \int_0^\infty W(r,r')\psi_l(r')dr', \tag{6.2}$$

where μ is the reduced mass of colliding nuclei with charges Z_1e and Z_2e. In the Hamiltonian appears a non-local potential with a symmetric kernel $W(r,r')$. The local potential is assumed to have the asymptotic form

$$V(r) \underset{r\to\infty}{\longrightarrow} \frac{Z_1Z_2e^2}{r}, \tag{6.3}$$

i.e. it vanishes for large r, except for a possible Coulomb interaction. The non-local potential $W(r,r')$ is assumed to be short-ranged. Also for the sake of simplicity, these potentials are assumed here to be independent of the spins of the nuclei.

The collision matrix $S_l(E)$ in partial wave l is obtained from the asymptotic behaviour of a bounded solution at energy E vanishing at the origin,

$$\psi_l(r) \underset{r\to\infty}{\to} I_l(\eta, kr) - S_l(E)O_l(\eta, kr). \tag{6.4}$$

In this equation, $k = \sqrt{2\mu E/\hbar^2}$ is the wavenumber of the relative motion between the particles and I_l and O_l are incoming and outgoing Coulomb functions

$$I_l(\eta,x) = G_l(\eta,x) - iF_l(\eta,x), \qquad O_l(\eta,x) = G_l(\eta,x) + iF_l(\eta,x), \tag{6.5}$$

where $F_l(\eta, x)$ and $G_l(\eta, x)$ are the regular and irregular Coulomb functions, respectively [22]. They depend on the Sommerfeld parameter $\eta = Z_1 Z_2 e^2/\hbar v$ where $v = \hbar k/\mu$ is the relative velocity between the colliding nuclei. For a single-channel collision, the collision matrix S_l reduces to a single complex number. It is related to the scattering phase shift δ_l by

$$S_l(E) = e^{2i\delta_l(E)}. \tag{6.6}$$

The phase shift is real if $V(r)$ and $W(r, r')$ are real.

The principle of the R matrix is a division of the configuration space into two regions at the channel radius a. The Schrödinger equation is solved with some approximate method in the internal region $r < a$. In the external region $r > a$, the solution is approximated by its asymptotic form (6.4). The channel radius must be large enough so that the potential V has reached its asymptotic form (6.3) with a good approximation and the non-local potential W has become negligible. In microscopic models [158,28], this second condition is equivalent to requiring that antisymmetrization effects are negligible. The reader is sent to Refs. [153,14] and to the references therein for details and for proofs.

By introducing the Bloch operator generalizing (3.127)

$$\mathcal{L}(L) = \frac{\hbar^2}{2\mu}\delta(r-a)\left(\frac{d}{dr} - \frac{L}{r}\right) \tag{6.7}$$

in the Schrödinger equation (6.1), one obtains the Bloch–Schrödinger equation

$$(H_l + \mathcal{L}(L) - E)\psi_l^{\rm int}(r) = \mathcal{L}(L)\psi_l^{\rm ext}(r), \tag{6.8}$$

where the operator $H_l + \mathcal{L}(0)$ is Hermitian in the internal region. The results are independent of the choice of parameter L which can be chosen as zero [14]. This parameter is however useful for the study of bound states [14] (see also Section 6.5). In the r.h.s. of Eq. (6.8), $\psi_l^{\rm ext}$ is approximated by the asymptotic expression (6.4). In the internal region, one introduces an expansion in shifted Lagrange–Legendre functions (3.122) regularized by x and scaled to $(0, a)$,

$$\psi_l^{\rm int}(r) = a^{-1/2}\sum_{j=1}^{N} c_j \hat{f}_j(r/a). \tag{6.9}$$

The mesh points ax_i are based on the zeros x_i of $P_N(2x-1)$ [Eq. (3.120)]. Here also, the Lagrange basis is treated as if it were orthonormal.

Notice that the logarithmic derivatives of the basis functions $\hat{f}_j(r/a)$ at $r = a$ do not take a fixed value but, on the contrary, take a large variety of values. Contrary to a common belief in the literature, the use of a fixed value for the logarithmic derivative has unfavourable effects on the accuracy of the calculations as explained in Refs. [42,14]. The origin of this problem takes place in a misinterpretation of the seminal paper of Wigner and Eisenbud [152]. In that work, the R matrix is derived analytically as an infinite series with a basis of functions having all the same logarithmic derivative. A discontinuity appears in the derivative of the wave function at the channel radius but it plays no role in the derivation of the correct R matrix. In numerical calculations using a finite basis with a common logarithmic derivative, this discontinuity prevents a uniform convergence of the calculation. With the present choice of basis, the continuity of the logarithmic derivative of the wave function is ensured by the Bloch operator thanks to the variety of behaviours of the basis functions $\hat{f}_j$ [42]. The method can thus lead to very accurate results.

The matrix elements C_{ij} of the operator $H_l + \mathcal{L}(0)$ between the Lagrange functions $\hat{f}_i$ and $\hat{f}_j$ defined in Eq. (3.122) become with the Gauss-quadrature approximation,

$$C_{ij} = \langle \hat{f}_i | T + \mathcal{L}(0) | \hat{f}_j \rangle + \left[\frac{\hbar^2\, l(l+1)}{2\mu a^2 x_i^2} + V(ax_i)\right]\delta_{ij} + (\lambda_i\lambda_j)^{1/2} a W(ax_i, ax_j), \tag{6.10}$$

where the matrix elements $\langle f_i | T + \mathcal{L}(0) | \hat{f}_j \rangle$ are given by the symmetric expressions (3.128) and (3.129) multiplied by $\hbar^2/2\mu a^2$. Notice that the weights λ_i appear in the non-local term of this expression. The R matrix at energy E is defined under the form [43,14]

$$R_l(E, a) = \frac{\hbar^2}{2\mu a}\sum_{i,j=1}^{N} \hat{f}_i(1)(\boldsymbol{C} - E\boldsymbol{I})^{-1}_{ij}\hat{f}_j(1) \tag{6.11}$$

with, from Eq. (3.122),

$$\hat{f}_j(1) = (-1)^{N-j}\frac{1}{\sqrt{x_j(1-x_j)}}. \tag{6.12}$$

The R matrix depends on a. The collision matrix is given by

$$S_l(E) = \frac{I_l(\eta, ka) - kaR_l(E, a)I_l'(\eta, ka)}{O_l(\eta, ka) - kaR_l(E, a)O_l'(\eta, ka)}. \tag{6.13}$$

Table 16
s-wave scattering phase shift δ_0 (in degrees) at energy E and scattering length a_0 (in fm) for the Yamaguchi potential (6.14), obtained by the R-matrix method with channel radius a on a regularized Lagrange–Legendre mesh with N points.

a	N	$E = 0.1$ MeV	$E = 10$ MeV	a_0
8	10	−15.076 62	85.637 12	5.422 26
	15	−15.076 66	85.637 06	5.422 27
10	15	−15.078 49	85.634 42	5.422 93
	20	−15.078 49	85.634 42	5.422 93
15	15	−15.078 687 7	85.634 562 0	5.422 999 3
	20	−15.078 688 9	85.634 560 2	5.422 999 7
Exact		−15.078 689 581	85.634 560 008	5.422 999 858

This approximate collision matrix is automatically unitary if V and W are real. Physically, it should be independent of a, if a is large enough. In practice, the independence with respect to a is an important test of the accuracy.

The determination of phase shifts with the R-matrix method requires the inversion of matrix $\boldsymbol{C} - E\boldsymbol{I}$. This inversion must be performed at each energy. When the matrix can be diagonalized in a reasonable time, it is thus preferable to invert $\boldsymbol{C} - E\boldsymbol{I}$ with its spectral decomposition which must be performed only once. However, for large numbers of channels, the diagonalization may become impractical while inversion remains possible.

The techniques described above are illustrated with the Yamaguchi potential [159]. This purely non-local potential ($V = 0$) reads

$$W(r, r') = -\frac{\hbar^2}{2\mu} 2\beta(\alpha + \beta)^2 e^{-\beta(r+r')}, \tag{6.14}$$

where α and β are positive parameters. With this separable potential, the Schrödinger equation (6.1) can be solved analytically. The s-wave phase shift is given by [159]

$$k \cot \delta_0 = -\frac{\alpha\beta(\alpha + 2\beta)}{2(\alpha + \beta)^2} + \frac{\alpha^2 + 2\alpha\beta + 3\beta^2}{2\beta(\alpha + \beta)^2} k^2 + \frac{1}{2\beta(\alpha + \beta)^2} k^4. \tag{6.15}$$

The values $\alpha = 0.231\,605\,3$ fm^{-1}, $\beta = 1.391\,832\,4$ fm^{-1} and $\hbar^2/2\mu = 41.472$ MeV fm^2 reproduce the bound-state energy -2.2246 MeV of the deuteron and the neutron–proton triplet scattering length 5.423 fm (Section 6.2). With a Lagrange–Laguerre basis (3.70) with $\alpha = 0$ regularized by x and a scale factor of 0.8 fm, the deuteron energy is obtained with an accuracy of 4×10^{-7} MeV with only 10 mesh points. With $N = 20$, the error on the energy decreases to 10^{-13} MeV.

In Table 16 are displayed results for the s-wave phase shift obtained by a regularized Lagrange–Legendre calculation with the R-matrix method at two energies, $E = 0.1$ and 10 MeV. The last line in the table corresponds to the exact value of the phase shift. When the channel radius a is equal to 8 fm, a Legendre mesh of only 10 points provides the phase shift with a small error of a few times 10^{-3} degrees. Without changing a, an increase of the number of mesh points does not improve the accuracy, as shown by the calculation with $a = 8$ fm and $N = 15$. With 15 mesh points, the error on the phase shift becomes smaller than 10^{-3} and 10^{-5} degrees when a is increased to 10 fm and 15 fm, respectively. For $a = 15$ fm, an accuracy better than 10^{-6} degrees is obtained with $N = 20$.

Let me briefly comment on other methods. A method based on the Jost functions has recently been adapted to the Lagrange-mesh technique [160]. Its originality is to contain first-order derivatives only. For the Laguerre mesh, it makes use of the expressions (3.72) for $\alpha = 0$. An excellent accuracy is also obtained in various tests.

The method of Siegert pseudostates has strong similarities with the R-matrix method [161,162]. Siegert states (or Gamow states in a nuclear context) are solutions of the Schrödinger equation at complex energies with a purely outgoing asymptotic behaviour. Since these states are not easy to use, a boundary radius a is introduced in practice like in the R-matrix approach. In Refs. [161,162], Siegert pseudostates are constructed with an expansion in Legendre polynomials in the spirit of the DVR (Section 4.2). The resulting equations have a strong similarity with the present ones. In fact, it is shown in Ref. [50] that this method is strictly equivalent to the R-matrix method on a Lagrange mesh except for the fact that the kinetic terms are simpler and more compact with the Lagrange mesh. Moreover the Siegert basis can be considered as orthogonal without loss of accuracy.

6.2. Effective-range expansion

The effective-range expansion is a Taylor expansion in powers of k^2 of an analytic function based on the phase shift. In the case of a collision involving a neutral particle, for partial wave l, this function is $k^{2l+1} \cot \delta_l$ and the effective-range expansion reads

$$k^{2l+1} \cot \delta_l = -\frac{1}{a_l} + \frac{1}{2} r_l k^2 + \cdots \tag{6.16}$$

where a_l is the scattering length and r_l is the effective range. It is more complicated for charged particles (see references in Ref. [155]). The R matrix gives an easy access to the parameters of the effective-range expansion [155]. In the neutral case, the scattering length of partial wave l reads

$$a_l = \frac{(2l+1)a^{2l+1}}{(2l+1)!!^2}\,\frac{1-(l+1)R_l(0,a)}{1+lR_l(0,a)}, \tag{6.17}$$

where $R_l(0,a)$ is the R matrix (6.11) at zero energy. The scattering length of the lth partial wave for a collision between charged particles is given by

$$a_l = \frac{1}{4}l!^2 a_N^{2l+1}\,\frac{[2-R_l(0,a)]I_{2l+1}(x)-xR_l(0,a)I'_{2l+1}(x)}{[2-R_l(0,a)]K_{2l+1}(x)-xR_l(0,a)K'_{2l+1}(x)}, \tag{6.18}$$

where I_n and K_n are modified Bessel functions [22], x is the dimensionless quantity

$$x = 2(2a/a_N)^{1/2} \tag{6.19}$$

and a_N is the nuclear Bohr radius

$$a_N = \hbar^2/\mu Z_1 Z_2 e^2. \tag{6.20}$$

The effective range and higher coefficients of the effective-range expansion can be obtained as explained in Refs. [155,163].

For the Yamaguchi potential (6.14), expression (6.15) has the form of an effective-range expansion with a limited number of terms. The scattering length is thus $2(\alpha+\beta)^2/\alpha\beta(\alpha+2\beta)$. Formula (6.17) based on the Lagrange-mesh expressions (6.10) and (6.11) is illustrated for potential (6.14) by the last column in Table 16. The convergence as a function of N and a follows the same pattern as for the low energy $E = 0.1$ MeV. The scattering length is obtained with 3, 4 and about 7 correct digits with $a = 8$, 10 and 15, respectively.

6.3. R matrix at high orbital momenta

High orbital momenta are encountered in various types of coupled-channel calculations, as, for example, in recent applications of the continuum-discretized coupled-channel method (CDCC) [13,164]. When using the R matrix, for high l values, the Legendre mesh has a drawback: many points near $x = 0$ are useless because of the high centrifugal barrier. A mesh over the interval (0, 1) where the mesh points are less numerous around 0 than around 1 would be more economical. This problem is not academic. In coupled-channel calculations with many channels, even a limited reduction of the number of mesh points may usefully reduce the computer times.

Such a mesh can be obtained with the zeros given by (3.162) and the shifted Lagrange functions $\widetilde{f}_j$ defined by (3.163) based on the shifted Jacobi polynomials $P_N^{(0,\beta)}$ with $\beta = 2l+2$ [40]. The basis then simulates the r^{l+1} behaviour of the solutions $\psi_l(r)$ near the origin. The kinetic-energy operator is given by (3.63) with α replaced by $2l+2$ and the matrix elements of $T_{2l+2}+\mathcal{L}(0)$ are given by (3.171) and (3.172). This mesh is thus valid for a single l value. If used with a higher value $l' > l$, the matrix element of the rest of the centrifugal term must be calculated with the Gauss quadrature,

$$\langle\widetilde{f}_i|T_{2l'+2}+\mathcal{L}(0)|\widetilde{f}_j\rangle = \langle\widetilde{f}_i|T_{2l+2}+\mathcal{L}(0)|\widetilde{f}_j\rangle + \frac{\hbar^2}{2\mu a^2}\,\frac{l'(l'+1)-l(l+1)}{x_i^2}\,\delta_{ij}. \tag{6.21}$$

The singularity renders this quadrature less accurate for small l values but not any more when l is high enough because the integrand is damped by a factor r^{2l+2} near the singularity.

Lagrange functions regularized by x are easier to use since the Gauss approximation remains exact for the centrifugal term. In this case, the mesh is still given by Eq. (3.162) but the Lagrange functions are defined by (3.173) with $\beta = 2l$. The matrix elements of $T_0+\mathcal{L}(0)$ are given by (3.178) and (3.179). Here the kinetic-energy term must be introduced explicitly. The matrix elements of $1/x$ and $1/x^2$ are exact.

As a simple example, let us consider a high partial wave of the $\alpha+\alpha$ nuclear plus Coulomb potential [165]

$$V(r) = -122.6225\,e^{-(r/2.132)^2} + 4e^2\,\frac{\mathrm{erf}\,(0.75\,r)}{r} \tag{6.22}$$

in MeV where r is in fm, $\hbar^2/2\mu = 10.368$ MeV fm^2 and $e^2 = 1.44$ MeV fm. The phase shift at $E = 500$ MeV calculated in different ways for $l = 20$ is presented in degrees in Table 17 for increasing numbers of mesh points. The channel radius is fixed at $a = 8$ fm. With this value the R-matrix method can reach an accuracy of 10^{-6} degrees.

The first calculation is performed with the Legendre mesh as explained in subsection 6.1. The convergence is good. The absolute accuracy in degrees on the phase shift is better than 0.1 for $N = 30$. It reaches 10^{-6} at $N = 38$. Higher accuracies would require increasing a. However, an even faster convergence is obtained with the Jacobi mesh. The value $\beta = 42$ simulates the r^{21} behaviour of the wave function near the origin. The 0.1 and 10^{-6} accuracies are obtained with $N = 18$ and 26, respectively, i.e. a gain of more than 30%. The most interesting point is that the loss of accuracy with the non-optimal

Table 17
$l = 20\alpha + \alpha$ phase shift (in degrees) at 500 MeV for potential (6.22) obtained by the R-matrix method on various Lagrange meshes as a function of N for $a = 8$ fm: regularized Legendre mesh, Jacobi mesh with $\beta = 42$ and 34, regularized Jacobi mesh with $\beta = 40$ and 32.

N	Legendre	Jacobi		Regularized Jacobi	
	$\beta = 0$	$\beta = 42$	$\beta = 34$	$\beta = 40$	$\beta = 32$
16		9.55	10.74	9.77	7.07
18		13.929	13.856	13.801	13.432
20		14.034	14.029 9	14.027 8	14.001
22		14.036 103	14.036 081	14.036 071	14.034 86
24		14.036 209	14.036 211	14.036 210	14.036 175
26	10.90	14.036 213	14.036 213	14.036 213	14.036 212
28	13.662	14.036 213	14.036 213	14.036 213	14.036 213
30	13.998	14.036 213	14.036 213	14.036 213	14.036 213
32	14.032 6	14.036 213	14.036 213	14.036 213	14.036 213
34	14.035 96	14.036 213	14.036 213	14.036 213	14.036 213
36	14.036 200	14.036 213	14.036 213	14.036 213	14.036 213
38	14.036 212	14.036 213	14.036 213	14.036 213	14.036 213
40	14.036 213	14.036 213	14.036 213	14.036 213	14.036 213

value $\beta = 34$ is small in spite of the singularity of the centrifugal correction in (6.21). The same accuracies are obtained with the regularized Jacobi mesh with $\beta = 40$ which leads to the same low r behaviour. Here also, the loss of accuracy with $\beta = 32$ is small. This means that, for a total angular momentum $J = 18$, the various orbital momenta $l = 16$ to 20 coupled by a channel spin $I = 2$ can be treated simultaneously with fewer mesh points than with the Legendre mesh. Although it does not improve the accuracy, the regularized Jacobi mesh has the advantage over the non-regularized Jacobi mesh that the same formula can be used for several l values.

The R-matrix method can be used to solve the CDCC equations [13]. A preliminary calculation making use of the regularized Jacobi mesh indicates that the number of mesh points in the internal region can be usefully reduced with respect to the regularized Legendre mesh without loss of accuracy.

6.4. Multichannel R matrix

The multichannel extension of the R-matrix method on a Lagrange mesh has been performed in Ref. [43] (see also Ref. [14]). The principle remains similar. The R matrix really becomes a matrix, the size of which is equal to the number M of channels c (open or closed) included in the calculation. For channels $c = 1$ to M, it is obtained from a matrix $\boldsymbol{C}$ given for diagonal and coupling local potentials $V_{cc'}(r)$ by

$$C_{ci,c'i'} = \langle \hat{f}_i | T + \mathcal{L}(0) | \hat{f}_{i'} \rangle \delta_{cc'} + \left[\frac{\hbar^2}{2\mu_c a^2 x_i^2} l_c(l_c+1) + E_c \right] \delta_{cc'} + V_{cc'}(ax_i)\delta_{ii'} \tag{6.23}$$

where E_c is the threshold energy of channel c with orbital momentum l_c and reduced mass μ_c. The size of this matrix becomes $NM \times NM$. A diagonalization may then take a too long time. To calculate the $M \times M$ R matrix, it is then faster to invert matrix $\boldsymbol{C} - E\boldsymbol{I}$ at each energy,

$$R_{cc'}(E,a) = \frac{\hbar^2}{2\sqrt{\mu_c \mu_{c'}}\, a} \sum_{i,i'=1}^{N} \hat{f}_i(1) [(\boldsymbol{C} - E\boldsymbol{I})^{-1}]_{ci,c'i'} \hat{f}_{i'}(1). \tag{6.24}$$

See Refs. [43,14] for the expression of the collision matrix as a function of the R matrix.

As an example, let us consider the solvable two-channel potential of Ref. [166],

$$V(r) = \frac{2(\kappa_2 - \kappa_1)}{\cosh^2 y} \begin{pmatrix} \kappa_1 & \sqrt{\kappa_1 \kappa_2}\sinh y \\ \sqrt{\kappa_1 \kappa_2}\sinh y & -\kappa_2 \end{pmatrix} \tag{6.25}$$

with

$$y = (\kappa_2 - \kappa_1) r - \operatorname{arc\,cosh} \sqrt{\kappa_1 \kappa_2 / \beta^2} \tag{6.26}$$

and $\hbar = 2\mu_1 = 2\mu_2 = 1$. The first channel has threshold energy zero and the second channel has threshold energy Δ. This potential possesses a Feshbach resonance at energy $E_R < \Delta$ with width Γ, if the parameters are defined as

$$2\kappa_{1,2}^2 = \sqrt{E_R^2 + \Gamma^{2/4}} + \sqrt{(E_R - \Delta)^2 + \Gamma^{2/4}} \mp \Delta, \tag{6.27}$$

$$4\beta^4 = \left(E_R + \sqrt{E_R^2 + \Gamma^{2/4}} \right) \left(E_R - \Delta + \sqrt{(E_R - \Delta)^2 + \Gamma^{2/4}} \right). \tag{6.28}$$

Table 18
Eigenphase shifts δ_1 and δ_2 (in rad) and mixing parameter ϵ for the two-channel potential (6.23) ($\hbar = 2\mu_1 = 2\mu_2 1$) at two energies E, obtained with the multichannel R matrix with a channel radius a and N mesh points.

E	a	N	δ_1	δ_2	ϵ
50	5	20	0.728	−0.152	−0.116
		25	0.740 41	−0.047 91	−0.125 797
		30	0.740 538	−0.047 854 0	−0.125 782 2
	6	30	0.740 562	−0.047 867	−0.125 784 27
		40	0.740 540 85	−0.047 854 26	−0.125 782 82
	7	40	0.740 541 35	−0.047 854 28	−0.118 5
		50	0.740 540 91	−0.047 854 26	−0.125 782 80
	exact		0.740 540 91	−0.047 854 27	−0.125 782 80
100	5	30	0.508 82	−0.041 4	−0.119 7
	6	40	0.508 86	−0.032 7	−0.109 9
		50	0.508 86	−0.032 7	−0.109 9
	7	40	0.508 11	−0.049	−0.118 5
		50	0.509 948 2	−0.033 892	−0.121 194
	exact		0.509 945 23	−0.033 877 78	−0.121 155 68

The complex collision matrix is given by Eqs. (5) and (17) of Ref. [166]. It can be diagonalized with an orthogonal matrix as

$$\boldsymbol{S} = \boldsymbol{O}\,\mathrm{diag}(e^{i\delta_1}, e^{i\delta_2})\,\boldsymbol{O}^T \tag{6.29}$$

where δ_1 and δ_2 are the eigenphase shifts and $\boldsymbol{O}$ is a rotation matrix depending on the mixing parameter ϵ.

For $\Delta = 10$, $E_R = 7$ and $\Gamma = 1$, the R matrix results are compared with the exact results in Table 18. The potential is shown in Fig. 1 of Ref. [166]. It is smaller than 10^{-5} at $r = 5$ and about 10^{-8} at $r = 7$. At $E = 50$, fair results are already obtained with $a = 5$ and 25 points. With $N = 30$, the accuracy reaches 6 digits. To improve it, one has to increase a and hence also N. With $a = 7$ and $N = 50$, one obtains 9 exact digits. At $E = 100$, the convergence of the mixing parameter requires $a = 7$. With $N = 50$, the accuracy is not far from 10^{-5}. The phase shifts obtained with this potential are displayed in Figs. 2 of Refs. [166,167].

This method has been used in the Lagrange-mesh version of CDCC [13]. The pseudostates or bins describing the discretized continuum of the projectile are also treated with the LMM. The large spatial extension of some pseudostates leads to long-range couplings which require a large channel radius. In this case, it is convenient to use propagation methods, i.e. to divide the internal region into subregions and to propagate the R matrix between these subregions [168]. The propagation is particularly simple with Lagrange meshes since the potential remains diagonal in all subregions. The subregion containing the origin is treated as explained above. In the other subregions, the shifted Legendre mesh must not be regularized (see Refs. [14,164]).

Because the method is accurate with rather few mesh points, it is particularly useful to study problems where the calculation of the potential matrix elements is very much time-consuming. This is the case for three-body scattering in hyperspherical coordinates as defined in Section 7.6 [12]. See the references in Section 7.6 for details and applications. *Ab initio* studies of nuclear reactions make also use of this technique [156,157]. It is also employed to study reactions involving the antiprotonic helium ions [169].

6.5. Strength functions

A strength function measures the response of a system to an excitation into the continuum. In particular, the electric dipole strength is the response to an E1 excitation. It plays an important role in the study of weakly bound exotic nuclei [170].

In a two-body model based on a potential V, the dipole strength is defined as

$$\frac{dB(\mathrm{E1})}{dE} = \frac{1}{\hbar v}\sum_{m\mu}\left|\langle\phi_{klm}|\mathcal{M}_{1\mu}|\phi_0\rangle\right|^2 \tag{6.30}$$

where $\mathcal{M}_{1\mu} = erY_{1\mu}(\Omega)$ is the dipole operator. The initial bound state is assumed for simplicity to be an s state with wave function $\phi_0(\boldsymbol{r}) = r^{-1}Y_{00}(\Omega)\psi_0(r)$. The final scattering wave functions $\phi_{klm}(\boldsymbol{r}) = r^{-1}Y_{lm}(\Omega)\psi_l(k,r)$ with orbital momentum l and wavenumber k are normalized according to $\langle\phi_{klm}|\phi_{k'lm}\rangle = \delta(k-k')$. After integration over the angular variables, the final orbital momentum is $l = 1$ and the expression of the E1 strength becomes

$$\frac{dB(\mathrm{E1})}{dE} = \frac{3e^2}{4\pi\hbar v}\left|\int_0^\infty \psi_1(k,r)\,r\,\psi_0(r)dr\right|^2 \tag{6.31}$$

where $\psi_1(k,r)$ is the radial scattering wave function of the p wave at energy $E = \hbar^2 k^2/2\mu$.

In previous sections, we have seen that bound and scattering states are easily calculated with the LMM. However, the simplest calculations involve different Lagrange meshes for the bound and scattering states, i.e. Laguerre and Legendre,

respectively. The calculation of the integral in Eq. (6.31) can thus not be done simply and elegantly. This drawback can be circumvented by using the R matrix also for the bound state. Here I prefer to apply a general method [171] that leads to a simple Lagrange-mesh adaptation.

Let $\phi_\mu^{(1)}(\boldsymbol{r})$ be the unique solution of the driven Schrödinger equation [172]

$$(H-E)\phi_\mu^{(1)} = -\mathcal{M}_{1\mu}\phi_0 \tag{6.32}$$

with an outgoing asymptotic behaviour. The strength (6.30) can be rewritten as

$$\frac{dB(\mathrm{E1})}{dE} = \frac{1}{\pi}\mathrm{Im}\,\langle\phi_\mu^{(1)}|\mathcal{M}_{1\mu}|\phi_0\rangle. \tag{6.33}$$

The radial functions are determined over the internal region $(0, a)$ on a Lagrange–Legendre mesh with the help of the Bloch operator (6.8), where a is the radius of the internal region and L is some complex constant. The regularized Lagrange–Legendre mesh involves N points ax_j. The initial 0s radial function is expanded as in Eq. (6.9). Its variational energy and coefficients are given by the mesh equations

$$\sum_{j=1}^{N}[\langle\hat{f}_i|T_0 + \mathcal{L}(0)|\hat{f}_j\rangle + V(ax_i)\delta_{ij}]c_j = E_0 c_i \tag{6.34}$$

provided that a is large enough. The matrix elements of $T_0 + \mathcal{L}(0)$ at the Gauss approximation are given by (3.128) and (3.129).

In order to calculate the E1 strength, Eq. (6.32) is solved with $\phi_\mu^{(1)} = (4\pi)^{-1/2}er^{-1}Y_{1\mu}(\Omega)\psi^{(1)}(r)$ where $\psi^{(1)}(r)$ is the solution of

$$(H_1 - E)\psi^{(1)} = -r\psi_0 \tag{6.35}$$

with the outgoing asymptotic behaviour $\psi^{(1)}(r) \underset{r\to\infty}{\to} e^{ikr}$. In Eq. (6.35), H_1 is the p-wave radial Hamiltonian (5.2). Eq. (6.35) can be rewritten in an essentially equivalent way as

$$(H_1 + \mathcal{L}(ik) - E)\psi^{(1)} = -r\psi_0 \tag{6.36}$$

since (6.7) shows that $\mathcal{L}(ik)\psi^{(1)} = 0$. This equation is solved on a mesh with an expansion similar to Eq. (6.9) with coefficients $c_j^{(1)}$. Eq. (6.36) becomes

$$\sum_{j=1}^{N}\left[\langle\hat{f}_i|T_0 + \mathcal{L}(ik)|\hat{f}_j\rangle + \left(\frac{\hbar^2\, l(l+1)}{2\mu a^2} + V(ax_i) - E\right)\delta_{ij}\right]c_j^{(1)} = -ax_i c_i \tag{6.37}$$

with $l = 1$. This complex system can be solved by inverting a real matrix as shown in Appendix E where A_{ij} is the real part of the square brackets in (6.37), $b_i = ax_i c_i$, $\alpha = \hbar^2\, k/2\mu a$ and $v_j = \hat{f}_j(1)$ [Eq. (6.12)]. If a is large enough, the external part of the integral in the E1 matrix elements (6.33) becomes negligible because of the exponential decrease of ψ_0. The remaining internal part is given at the Gauss approximation by

$$\langle\psi^{(1)}|r|\psi_0\rangle \approx a\sum_{i=1}^{N} x_i c_i c_i^{(1)}. \tag{6.38}$$

The strength function (6.33) simply reads

$$\frac{dB(\mathrm{E1})}{dE} = -\frac{e^2 a}{4\pi^2}\sum_i x_i c_i\,\mathrm{Im}\,c_i^{(1)}. \tag{6.39}$$

Like in Ref. [173], the strength function for the test potential [174]

$$V(r) = -8e^{-0.16r^2} + 4e^{-0.04r^2} \tag{6.40}$$

with $\hbar = m = e = 1$ is presented in Fig. 20. Results with $N = 30$ and $a = 12$ are presented as a full line. They have a 10^{-4} relative accuracy. Results with $a = 10$ would hardly differ at the scale of the figure. For $a = 9$ (dotted line), the difference becomes visible.

6.6. Complex scaling

The complex-scaling method consists in replacing a coordinate $\boldsymbol{r}$ by a scaled or 'rotated' coordinate $\boldsymbol{r}\exp(i\theta)$ where θ is a real parameter [175,176]. The momentum $\boldsymbol{p}$ transforms into $\boldsymbol{p}\exp(-i\theta)$. An eigenstate behaving as an outgoing exponential

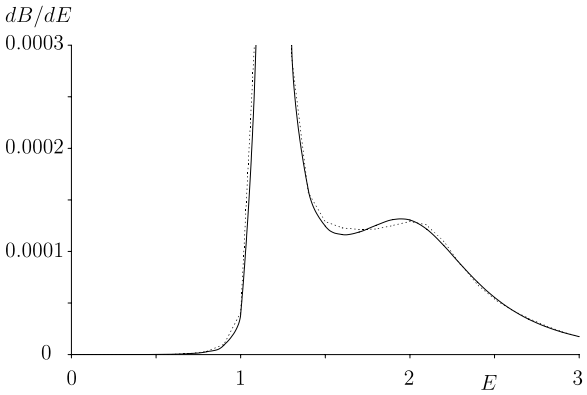

Fig. 20. E1 strength for potential (6.40) obtained with Eq. (6.39) for $N = 30$ and $a = 12$ (full line) or $a = 9$ (dotted line). Results obtained with the complex scaling equation (6.52) on a Lagrange–Laguerre mesh with $N = 30$, $h = 0.3$ and $\theta = 10^\circ$ or 20° (Section 6.6) are indistinguishable from the full line.

$\exp(ikr)$ with a complex k value ($\mathrm{Re}\, k > 0$) becomes $\exp[ir\ \mathrm{Re}\ (ke^{i\theta})]\exp[-r\ \mathrm{Im}\ (ke^{i\theta})]$. It can be transformed into a square-integrable function, if θ is large enough. The complex-scaling method is thus particularly useful to study resonances with a square-integrable basis, and in particular with a Lagrange basis.

The Schrödinger equation becomes

$$H(\theta)\psi(\theta) = E(\theta)\psi(\theta) \tag{6.41}$$

with the scaled Hamiltonian

$$H(\theta) = e^{-2i\theta}T + V(re^{i\theta}). \tag{6.42}$$

The energies $E(\theta)$ are complex.

Let us consider an $\alpha = 0$ Laguerre mesh with N points scaled as hx_j where h is a real scaling parameter. The wave functions are expanded in regularized Lagrange–Laguerre functions (3.70) as

$$\psi(\theta) = h^{-1/2}\sum_{j=1}^{N} d_j(\theta)\hat{f}_j(r/h). \tag{6.43}$$

The Schrödinger equation on a Lagrange mesh reads

$$\sum_{j=1}^{N}\left\{\frac{\hbar^2}{2\mu h^2}e^{-2i\theta}\left[\hat{T}^G_{ij} + \frac{l(l+1)}{x_i^2}\delta_{ij}\right] + V(hx_ie^{i\theta})\delta_{ij}\right\} d_j(\theta) = E(\theta)d_i(\theta) \tag{6.44}$$

where the kinetic-energy matrix elements are given by (3.75) and (3.76) for $\alpha = 0$. The wave functions are normalized according to

$$\int_0^\infty \psi(\theta)^2 dr \approx \sum_{j=1}^{N} d_j(\theta)^2 = 1. \tag{6.45}$$

Notice the absence of complex conjugation.

The real eigenvalues $E_j(\theta)$ of Eq. (6.44) provide the bound-state energies. The stable complex eigenvalues give the energies $E_{\mathrm{res},j}$ and widths Γ_j of resonances,

$$E_j(\theta) = E_{\mathrm{res},j} - \frac{1}{2}i\Gamma_j, \tag{6.46}$$

provided θ is large enough to transform the resonance into a square integrable state, i.e.

$$\tan 2\theta > \frac{\Gamma_j}{2E_{\mathrm{res},j}}. \tag{6.47}$$

In Table 19 are presented bound-state and resonance energies for potential (6.40). The calculation is performed for various values of N and θ and compared with the results of Ref. [173]. The roughly optimized value 0.3 is taken for the scale factor h. The real and complex energies converge rather fast. A 4-digit accuracy is already obtained with $N = 20$ and an about 6-digit accuracy is reached for $N = 40$. For $\theta = 10^\circ$, the complex energy of the narrow first resonance is obtained. A second, broader, resonance appears for $\theta = 20^\circ$.

Table 19
Bound-state and resonance energies for the p wave of potential (6.40) ($\hbar = m = 1$) obtained by the complex-scaling method on a Lagrange–Laguerre mesh for various N and θ values ($h = 0.3$).

θ	N	E_B	E_{r1}	E_{r2}
10	10	−0.676 6	1.191 − i0.001 6	
10	20	−0.674 661	1.170 983 − i0.004 807	
10	30	−0.674 654	1.171 042 − i0.004 864	
20	30	−0.674 658	1.170 963 − i0.004 867	2.017 589 − i0.486 121
10	40	−0.674 655	1.171 041 − i0.004 864	
20	40	−0.674 655	1.171 042 − i0.004 864	2.017 500 − i0.486 304
10	50	−0.674 654	1.171 041 − i0.004 864	
20	50	−0.674 654	1.171 041 − i0.004 864	2.017 498 − i0.486 300
Ref. [173]		−0.67	1.1710 − i0.049	2.0175 − i0.4863

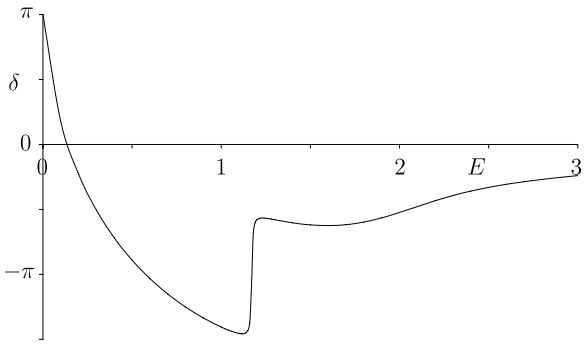

Fig. 21. p-wave phase shift of the potential (6.40) obtained with the complex-scaling method on a Lagrange mesh. The R-matrix results are superimposed.

The complex-scaling method on a Lagrange mesh has been used to study resonances of the hydrogen atom in a strong magnetic field in Ref. [177]. The convergence would have been even faster if a real scale parameter h had been introduced in the mesh calculation. The same method under the DVR name has been used in Ref. [178] to calculate photoionization cross sections of the hydrogen, lithium and sodium atoms.

The complex-scaling method has been extended to other applications such as the calculation of phase shifts [173]. As explained in Ref. [173], the phase shift $\delta(E)$ is related to the continuum level density $\Delta(E)$ by

$$\Delta(E) = \frac{1}{\pi}\frac{d\delta(E)}{dE}. \tag{6.48}$$

The continuum level density is given by the LMM as

$$\Delta(E) = \sum_{j=1,\mathcal{E}^\theta_{Rj}>0}^{N} \frac{\mathcal{E}^\theta_{Ij}}{(E-\mathcal{E}^\theta_{Rj})^2+(\mathcal{E}^\theta_{Ij})^2} - \sum_{j=1}^{N} \frac{\mathcal{E}^\theta_{0Ij}}{(E-\mathcal{E}^\theta_{0Rj})^2+(\mathcal{E}^\theta_{0Ij})^2} \tag{6.49}$$

where $E^\theta_j = \mathcal{E}^\theta_{Rj} + i\mathcal{E}^\theta_{Ij}$ are the energies obtained from Eq. (6.47) and $E_{0j}e^{2i\theta} = \mathcal{E}^\theta_{0Rj} + i\mathcal{E}^\theta_{0Ij}$ are the corresponding energies of the unscaled problem multiplied by $e^{2i\theta}$. The bound states are eliminated from the first term. Hence, an integration of (6.48) from zero to E leads to the phase shift

$$\delta(E) = \sum_{j=1,\mathcal{E}^\theta_{Rj}>0}^{N} \left[\arctan\frac{E-\mathcal{E}^\theta_{Rj}}{\mathcal{E}^\theta_{Ij}} + \arctan\frac{\mathcal{E}^\theta_{Rj}}{\mathcal{E}^\theta_{Ij}}\right] - \sum_{j=1}^{N}\left[\arctan\frac{E-\mathcal{E}^\theta_{0Rj}}{\mathcal{E}^\theta_{0Ij}} + \arctan\frac{\mathcal{E}^\theta_{0Rj}}{\mathcal{E}^\theta_{0Ij}}\right]. \tag{6.50}$$

The p-wave phase shift of the potential (6.40) obtained with this method is depicted in Fig. 21. It starts from 180° because of the bound state (see Table 19). The narrow and broad resonances are also visible.

The accuracy of the phase shifts and their sensitivity to the parameters are tested in Table 20 by comparison with accurate R-matrix results (Section 6.1). A typical accuracy is 0.1 degree for $N = 80$. The results do not depend much on θ. They are significantly less accurate than with the R matrix for comparable numbers of mesh points.

Strength functions can also be obtained with complex scaling [176]. The initial 0s ground-state scaled radial function is expanded over a Lagrange–Laguerre basis as in Eq. (6.43) with coefficients $c_j(\theta)$. These coefficients are obtained with a system similar to (6.44). The E1 matrix elements read

$$(\phi^\theta_f|re^{i\theta}|\phi^\theta_i) \approx he^{i\theta}\sum_{j=1}^{N} d_j(\theta)x_j c_j(\theta) \tag{6.51}$$

Table 20
p-wave scattering phase shifts (in degrees) at energies E for potential (6.40) obtained by the complex-scaling method on a Lagrange–Laguerre mesh for various N and θ values ($h = 0.3$). The results are compared with the accurate phase shifts from the R-matrix method on a Lagrange–Legendre mesh (Section 6.1) with $a = 25$ and $N = 50$.

θ	N	$E = 1$	$E = 2$	$E = 3$
10	40	−253.43	−95.12	−44.97
10	60	−253.71	−95.59	−45.80
5	80	−253.69	−95.54	−45.73
10	80	−253.80	−95.75	−46.05
20	80	−253.86	−95.86	−46.22
R matrix		−253.924 135	−95.981 653	−46.402 841

where ϕ_f^θ is not conjugated. The strength function is approximated as

$$\frac{dB(\mathrm{E1})}{dE} = -\frac{e^2}{\pi}\mathrm{Im}\sum_{f=1}^{N}\frac{(\phi_f^\theta|re^{i\theta}|\phi_i^\theta)^2}{E-E_f^\theta}. \tag{6.52}$$

For potential (6.40), the strength functions (6.52) obtained with $N = 30$, $h = 0.3$ and $\theta = 10$ or 20 degrees are indistinguishable from the full line in Fig. 20.

It is interesting to compare the complex-scaling method with the R-matrix method. Complex scaling is based on a single Laguerre mesh but requires complex arithmetics in the code. The R-matrix treatment is purely real but the LMM is used only in the internal region. While resonance properties can be obtained with the R matrix [50,14], their treatment is simpler with complex scaling. With similar mesh sizes, phase shifts are much more accurate with the R matrix. The R matrix allows a generalization to large coupled-channel problems. The evaluation of strength functions which requires a simultaneous treatment of bound and scattering states (including resonances) has similar advantages in both approaches.

7. Three-body bound states

7.1. Choice of coordinate system

The Hamiltonian of three particles $i = 1, 2, 3$ with masses m_i, charges $Z_i e$ and coordinates $\boldsymbol{r}_i$ reads

$$H = \sum_{i=1}^{3} T_i + \sum_{i>j=1}^{3} V_{ij} + V_{123} - T_{\mathrm{c.m.}}. \tag{7.1}$$

In this expression, $T_i = p_i^2/2m_i$ is the kinetic-energy operator of particle i, V_{ij} is the interaction between particles i and j, V_{123} is a possible three-body force and $T_{\mathrm{c.m.}}$ is the kinetic energy of the centre of mass. To calculate approximate eigenvalues and eigenfunctions of this Hamiltonian, a coordinate system must be chosen [179]. The choice of this system depends on the types of potential and in particular on their singularities.

As we have seen, a single singularity is not a problem as it can easily be regularized. But in systems of three charged particles such as atoms and molecules, several singularities occur, one for each pair of charged particles. Since potentials present a singularity for $\boldsymbol{r}_i = \boldsymbol{r}_j$ ($i \neq j = 1, 2, 3$), a regularization is necessary. This is easy in the system of perimetric coordinates [180–182]. As we shall see (Section 7.2), the regularization of the Coulomb singularities is automatic in this system and the problem can be solved on a three-dimensional Lagrange mesh [8,179] (Section 2.8). The perimetric system is of course valid for many other potentials, including non-singular potentials [183].

The perimetric coordinates are expressed as three Euler angles defining the orientation of the triangle formed by the three particles, and three internal coordinates describing the shape of this triangle [181]. Each of these coordinates is the sum of two of the side lengths of the triangle minus the third one. They have the advantage of varying from zero to infinity. This system is optimal for three-body atoms and molecules with the LMM.

The perimetric coordinates are however not convenient for interactions which depend on the angular momentum, as it is the case in many nuclear-physics problems concerning three nucleons or three clusters of nucleons. In this case, a system of hyperspherical coordinates (Section 7.6) is well adapted [184,185]. The advantage of this system is that forces depending on the angular momentum can easily be incorporated.

The hyperspherical coordinates are defined from one of the three possible systems of Jacobi coordinates. Four angles describe the orientations of the two chosen Jacobi coordinates. The dimensionless hyperangle α is related to the ratio of their lengths. The only dimensioned coordinate is the hyperradius ρ which gives information on the extension of the three-body system. The dependences on the various angles, including the hyperangle, are treated analytically. The LMM is applied to the resulting system of coupled differential equations depending on the hyperradius ρ. Only a singularity at $\rho = 0$ can be regularized. Singularities at special values of α can in principle be treated analytically. This coordinate system is less convenient for Lagrange-mesh calculations involving the Coulomb potential (7.13).

The type of application dictates the choices of coordinate system and of Lagrange mesh. The two systems of coordinates only compete for non-singular angular-momentum independent forces. In this case, the LMM can also be accurate with other coordinate systems [179]. Let me mention that a system based on a transformation of the Hylleraas coordinates also allows a regularization of potentials with a Coulomb-like singularity but in a more complicated way [179].

7.2. Lagrange-mesh method in perimetric coordinates

The system of perimetric coordinates [180,181] is defined by the three Euler angles ψ, θ, ϕ and the three coordinates

$$\begin{aligned} x &= r_{12} - r_{23} + r_{31}, \\ y &= r_{12} + r_{23} - r_{31}, \\ z &= -r_{12} + r_{23} + r_{31}, \end{aligned} \tag{7.2}$$

where r_{ij} is the distance between particles i and j. The coordinates x, y and z vary in the interval $(0, \infty)$. They thus present the advantage over other coordinate systems that they vary over a fixed interval. Fixed intervals are crucial for the LMM. The kinetic energy for S states is given, e.g., in Ref. [182]. The general expression for arbitrary states can be found in Ref. [186]. The volume element reads [8,187]

$$dV = (x+y)(y+z)(z+x)\sin\theta\, d\psi d\theta d\phi\, dxdydz. \tag{7.3}$$

The kinetic matrix elements are automatically regularized by this volume element [8,187,186], i.e. no singular term appears when these matrix elements are calculated with the Gauss quadrature. The potential matrix is diagonal and involves values of the total potential $V(x,y,z) = \sum_{i>j} V_{ij} + V_{123}$ at the three-dimensional mesh points. Coulomb potentials and other singular potentials such as the Yukawa potentials encountered for charged particles in a Debye plasma [188] (see Section 7.3) are also automatically regularized. A multidimensional basis involving non-regularized Lagrange–Laguerre functions (Section 3.3.2) is thus convenient since coordinates x, y, z vary from zero to infinity.

Let me describe the LMM in the important case where two particles are identical, say 1 and 2. The wave function with total orbital momentum L, parity π, and spatial symmetry σ of the identical particles is expanded as [186]

$$\Psi_M^{(L^\pi)\sigma} = \sum_{K=0}^{L} \mathcal{D}_{MK}^{L\pi}(\psi,\theta,\phi)\Phi_K^{(L^\pi)\sigma}(x,y,z). \tag{7.4}$$

In some cases (Sections 7.4 and 7.5), for $L > 0$, the sum can be truncated with excellent accuracy at some value $K_{\max}$. The normalized angular functions $\mathcal{D}_{MK}^{L\pi}(\psi,\theta,\phi)$ are defined for $K \geq 0$ by

$$\mathcal{D}_{MK}^{L\pi}(\psi,\theta,\phi) = \frac{\sqrt{2L+1}}{4\pi}(1+\delta_{K0})^{-1/2}\left[D_{MK}^{L}(\psi,\theta,\phi) + \pi(-1)^{L+K} D_{M\,-K}^{L}(\psi,\theta,\phi)\right] \tag{7.5}$$

where $D_{MK}^{L}(\psi,\theta,\phi)$ represents a Wigner matrix element. They have parity π and change as $\pi(-1)^K$ under permutation of the identical particles.

The 3D Lagrange functions analog to (2.74) associated with the mesh $(h_x u_i, h_y v_j, h_z w_k)$ similar to (2.75) are regularized as

$$F_{ijk}^{K}(x,y,z) = \mathcal{N}_{Kijk}^{-1/2}\mathcal{R}_K(x,y,z) f_i(x/h_x) f_j(y/h_y) f_k(z/h_z), \tag{7.6}$$

where $f_i(x/h_x), f_j(y/h_y), f_k(z/h_z)$ are Lagrange–Laguerre functions (3.52) for $\alpha = 0$ with respective numbers of mesh points N_x, N_y, N_z and respective scaling factors h_x, h_y, h_z. The basis formed of products of Lagrange functions is equivalent to the basis of products of Laguerre polynomials employed in Ref. [189]. The function $\mathcal{R}_K(x,y,z)$ is a regularization factor introduced because of the presence of singularities in the kinetic-energy part of the Hamiltonian operator when L differs from zero (see Refs. [187,186] for details). It is equal to 1 when $K = 0$ and to $\sqrt{xyz(x+y+z)}$ otherwise. The normalization factor $\mathcal{N}_{Kijk}$ is defined as

$$\mathcal{N}_{Kijk} = h_x h_y h_z (h_x u_i + h_y v_j)(h_x u_i + h_z w_k)(h_y v_j + h_z w_k)\mathcal{R}_{Kijk}^2 \tag{7.7}$$

where $\mathcal{R}_{Kijk} = \mathcal{R}_K(h_x u_i, h_y v_j, h_z w_k)$. The $\Phi_K^{(L^\pi)\sigma}(x,y,z)$ functions in Eq. (7.4) are expanded in the Lagrange basis as

$$\Phi_K^{(L^\pi)\sigma}(x,y,z) = \sum_{i=1}^{N}\sum_{j=1}^{i-\delta_K}\sum_{k=1}^{N_z} C_{Kijk}^{(L^\pi)\sigma}\left[2(1+\delta_{ij})\right]^{-1/2}\left[F_{ijk}^{K}(x,y,z) + \sigma\pi(-1)^K F_{jik}^{K}(x,y,z)\right] \tag{7.8}$$

where the same number $N = N_x = N_y$ of mesh points and the same scale factor $h = h_x = h_y$ are used for the two perimetric coordinates x and y in order to take advantage of the Lagrange conditions (2.76) when the two coordinates are exchanged, and δ_K is equal to 0 when $(-1)^K = \sigma\pi$ and 1 when $(-1)^K = -\sigma\pi$. The variational calculation then reduces to the mesh equations

$$\sum_{Kijk}\left\{\langle F_{i'j'k'}^{K'}|T_{K'K}^{L^\pi}|F_{ijk}^{K}\rangle_G + \sigma\pi(-1)^K\langle F_{i'j'k'}^{K'}|T_{K'K}^{L^\pi}|F_{jik}^{K}\rangle_G + \left[V(h_x u_i, h_y v_j, h_z w_k) - E\right]\delta_{KK'}\delta_{ii'}\delta_{jj'}\delta_{kk'}\right\} C_{Kijk}^{(L^\pi)\sigma} = 0 \tag{7.9}$$

where $T^{L^\pi}_{K'K}$ is the matrix element of the kinetic-energy operator $\sum_i T_i - T_{\rm c.m.}$ between functions $\mathcal{D}^{L\pi}_{MK'}$ and $\mathcal{D}^{L\pi}_{MK}$. The expression of the kinetic-energy part calculated with a three-dimensional Gauss quadrature is rather long but not very complicated to compute. It is given in the appendix of Ref. [186]. It only involves Laguerre zeros and weights, and values (3.54) and (3.55) of the first derivatives of the Lagrange functions at mesh points. The time-consuming part of the calculation consists in the determination of a few low eigenvalues of the Hamiltonian matrix when it is large. Note however that this matrix is sparse. It has a structure a little more complicated than Eq. (2.80).

The wave functions are normed according to

$$\sum_{Kijk} (C^{(L^\pi)\sigma}_{Kijk})^2 = 1. \tag{7.10}$$

Several mean values are easily obtained at the Gauss approximation by using Eq. (2.86). For example, the mean distance between particles 1 and 2 is given by

$$\langle r_{12}\rangle = \frac{1}{2} h \sum_{Kijk} (C^{(L^\pi)\sigma}_{Kijk})^2 (u_i + u_j) \tag{7.11}$$

and the mean distance between particle 1 or 2 and particle 3 reads

$$\langle r_{13}\rangle = \langle r_{23}\rangle = \frac{1}{2} \sum_{Kijk} (C^{(L^\pi)\sigma}_{Kijk})^2 (h u_i + h_z w_k). \tag{7.12}$$

7.3. Unconfined and confined helium atom

The most typical three-body system is the non-relativistic helium atom with only Coulomb forces. The ground-state eigenvalue of the Hamiltonian is now known with an extraordinary accuracy of about 30 or more digits [190,191], far beyond the physical needs. These benchmark values are usually obtained with an infinite mass for the helium nucleus to avoid the problems related with the experimental uncertainties on this mass. The LMM is in principle able to reach such accuracies but with very large matrices and an eigenvalue search in multiple precision. The LMM rather easily provides a 13-digit accuracy together with tractable wave functions. This is also true for a realistic helium mass. More interestingly, replacing the Coulomb potential in the code by other continuous potentials such as some forms of confinement potentials is extremely easy since only values at mesh points are needed.

In the absence of external fields, the Coulomb potentials read

$$V_C = \frac{Z_1 Z_2 e^2}{r_{12}} + \frac{Z_2 Z_3 e^2}{r_{23}} + \frac{Z_3 Z_1 e^2}{r_{31}}, \tag{7.13}$$

where

$$\boldsymbol{r}_{ij} = \boldsymbol{r}_i - \boldsymbol{r}_j. \tag{7.14}$$

In atomic units, it becomes in perimetric coordinates,

$$V_C = \frac{2Z_1 Z_2}{x+y} + \frac{2Z_2 Z_3}{y+z} + \frac{2Z_3 Z_1}{z+x}. \tag{7.15}$$

As already mentioned, it is automatically regularized by the Jacobian in the volume element (7.3), i.e. no singular term appears in the potential matrix elements.

Let us start with the $L = 0$ ground state of the helium atom [8]. Particle 3 represents an infinite-mass helium nucleus ($Z_3 = 2$, $m_3 = \infty$) and particles 1 and 2 are the electrons ($Z_1 = Z_2 = -1$, $m_1 = m_2 = 1$). The spatial wave function is symmetrized in x and y. An important improvement with respect to Ref. [8] is the use of a faster search of the lowest eigenvalues with the computer code JADAMILU based on the Jacobi–Davidson algorithm [75]. A search of a stability plateau has been performed with $N = 30$ and $N_z = 20$. For $h = 0.25$–0.3 and $h_z = 0.35$–0.4, the stability reaches 2×10^{-13}. I thus choose $h = 0.3$ and $h_z = 0.4$ like in Refs. [8,187]. The convergence obtained with these parameters is displayed in Table 21. The basis size is denoted as N_T. One already obtains 11 digits with $N = N_z = 20$. The accuracy reaches 10^{-14} for $N = 40$ and $N_z = 30$. Further increasing the mesh size shows the apparition of rounding errors which may then reduce the accuracy.

The convergence of energies is accompanied by a convergence of the wave functions. These functions accurately satisfy the cusp and virial conditions (see Ref. [8]). The mean interelectron distances $\langle r_{ee}\rangle$ and the mean electron–nucleus distance $\langle r_{\alpha e}\rangle$ calculated with (7.11) and (7.12) are displayed in Table 21. They also converge with a 12-digit accuracy.

As already mentioned, an important advantage of the LMM is that one can easily perform calculations with other potentials by changing only a few lines in the code. Two examples illustrate this flexibility: the helium atom with a Gaussian confinement and the helium atom in a Debye plasma. These examples also clarify the optimal choice of the scale parameters.

Table 21
Ground-state energy $E(^\infty\mathrm{He})$ and mean distances $\langle r_{ee}\rangle$ and $\langle r_{\alpha e}\rangle$ in atomic units of the infinite-mass helium atom as a function of the numbers N and N_z of mesh points and the mesh size N_T. The last line displays rounded energies of Refs. [190,191] and radii of Ref. [192].

N	N_z	N_T	$E(^\infty\mathrm{He})$	$\langle r_{ee}\rangle$	$\langle r_{\alpha e}\rangle$
20	20	4 200	−2.903 724 377 031 83	1.422 070 255 530 6	0.929 472 294 855 6
30	20	9 300	−2.903 724 377 036 42	1.422 070 255 563 3	0.929 472 294 872 1
30	30	13 950	−2.903 724 377 033 97	1.422 070 255 565 9	0.929 472 294 873 7
40	30	24 600	−2.903 724 377 034 21	1.422 070 255 565 8	0.929 472 294 873 6
40	40	32 800	−2.903 724 377 034 14	1.422 070 255 565 9	0.929 472 294 873 7
50	30	38 250	−2.903 724 377 034 24	1.422 070 255 565 6	0.929 472 294 873 5
[190–192]			−2.903 724 377 034 119 6	1.422 070 255 566	0.929 472 294 874

Table 22
Ground-state energy and mean interparticle distances (in atomic units) of a confined helium atom and a helium atom in a Debye plasma as a function of the numbers N and N_z of mesh points and the mesh size N_T. The results are compared with Refs. [193–195].

N	N_z	N_T	E	$\langle r_{ee}\rangle$	$\langle r_{\alpha e}\rangle$
Confined helium with $V_0 = 100$ and $R_c = 4$ ($h = 0.1, h_z = 0.15$)					
10	10	950	2.389 517 6	0.717 239 6	0.487 082 6
15	15	1 800	2.389 521 083 273	0.717 240 933 789	0.487 083 296 959
20	20	4 200	2.389 521 083 370 12	0.717 240 933 821 11	0.487 083 296 966 06
25	25	8 125	2.389 521 083 370 12	0.717 240 933 821 10	0.487 083 296 966 08
[193]			2.389 531		
Helium in a Debye plasma with $D = 1$ ($h = 0.53, h_z = 0.5$)					
10	10	950	−0.818 214 178 5	1.809 952	1.176 124 8
15	15	1 800	−0.818 214 182 550	1.809 989 685	1.176 144 046
20	20	4 200	−0.818 214 182 665	1.809 989 639 447	1.176 144 022 339
25	25	8 125	−0.818 214 182 783	1.809 989 639 897	1.176 144 022 536
30	30	13 950	−0.818 214 182 806	1.809 989 639 808	1.176 144 022 484
[194]			−0.818 214 182 80		
[195]			−0.817 04	1.782 67	1.160 18

A potential with a penetrable confinement is taken as [193]

$$V = V_C + V_0\left[2 - e^{-(r_{13}/R_c)^2} - e^{-(r_{23}/R_c)^2}\right] \tag{7.16}$$

where V_C is the Coulomb potential defined by (7.15) and V_0 and R_c are parameters. This penetrable confinement is limited to the height $2V_0$ and is mostly significant when the electrons are at a distance from the nucleus larger than R_c. Lagrange-mesh results are presented in Table 22 for $V_0 = 100$ and $R_c = 4$. The ground-state energy becomes positive but the three-body system is nevertheless deeply bound with respect to the value $2V_0$ of the confinement potential. Hence the wave function decreases rather fast. Good values of the scale factors are thus much smaller than for the free atom. Here they are roughly optimized as $h = 0.1, h_z = 0.15$. The convergence is very fast. Very good results are already obtained with $N = N_z = 10$. An accuracy of 11 or 12 digits is obtained with $N = N_z = 20$ for the energy and for the mean distances. The mean distances are scaled down by about a factor of two with respect to the free atom but $\langle r_{ee}\rangle$ and $\langle r_{\alpha e}\rangle$ indicate that the shape does not seem to change.

Notice that the impenetrable confinement studied in Ref. [193], i.e. $r_{13} < R_c, r_{23} < R_c$, is not accurately described within the Lagrange-mesh approximation in perimetric coordinates because of the discontinuity of a sharp confinement. In other coordinate systems, it may also be inaccurate because of the Coulomb singularities. Treating this case requires developing the LMM in a dedicated coordinate system [52].

Bound states of the helium atom in a Debye plasma are studied in Ref. [194]. The potential reads

$$V = \frac{Z_1Z_2}{r_{12}}e^{-r_{12}/D} + \frac{Z_2Z_3}{r_{13}}e^{-r_{13}/D} + \frac{Z_3Z_1}{r_{23}}e^{-r_{23}/D} \tag{7.17}$$

where the Debye length D is a parameter depending on the electron density and temperature of the plasma [194]. The Coulomb potential (7.13) is recovered for $D \to \infty$. Here, because of the finite range of the potential, the binding energy of the ground state is smaller and the wave function is more extended. Hence the scale parameters must be increased. For $D = 1$, the optimal values are close to $h = 0.53$ and $h_z = 0.5$. The energies for $D = 1$ are presented in Table 22. An excellent energy is already obtained with $N = N_z = 10$ but the convergence is slower than in the confined case. With $N = N_z = 30$, one has at least 11 correct digits for the energy and radii. The energy is in excellent agreement with Ref. [194]. The mean radii improve those of Ref. [195]. As expected from the reduction of energy with respect to the free case, the atom is larger by more than 25%.

The examples discussed here concern the ^1S ground state of helium. Good results can also be obtained for excited S states. However, the accuracy for other L values is less good. The accuracy for the ^1P states of the free helium atom is only of about 8 digits with mesh sizes similar to those at the end of Table 21. This is not specific of the LMM but rather related to

Table 23
Energies of the three lowest vibrational bound states in the Σ_g rotational band of the H_2^+ molecular ion for some L values. Each first line contains the Lagrange-mesh energies. Each last line displays the results of Moss [201]. Other references are [a]: [202], [b]: [203], [c]: [197], [d]: [204]. The proton mass is taken as $m_p = 1836.152701\, m_e$.

L	$v = 0$	$v = 1$	$v = 2$
0	−0.597 139 063 123 3	−0.587 155 679 207	−0.577 751 904 49
	−0.597 139 063 123 405[a,b]	−0.587 155 679 212 747[b]	−0.577 751 904 595 47[c]
	−0.597 139 063 123 41	−0.587 155 679 212 76	−0.577 751 904 595 47
10	−0.583 508 206 414 4	−0.574 252 249 872	−0.565 552 133 03
	−0.583 508 206 414 57[d]	−0.574 252 249 85	−0.565 552 133 10
20	−0.553 011 863 258 8	−0.545 468 326 311	−0.538 439 001 16
	−0.553 011 863 22	−0.545 468 326 30	−0.538 439 001 20
30	−0.518 362 395 936 9	−0.513 052 130 786	−0.508 263 438 21
	−0.518 362 395 87	−0.513 052 130 73	−0.508 263 438 18

Table 24
Average electric dipole polarizabilities $\alpha^{(L)}$ of some $v = 0$ vibrational bound levels in the Σ_g electronic configuration of the H_2^+ molecular ion.

L	$\alpha^{(L)}$	Ref. [206]
0	3.168 725 803	3.168 725 802 67
10	3.721 926 908	
20	5.670 458 508	
30	11.277 509 727	

the basis choice. The convergence for P states can be significantly accelerated by redefining the expanded wave functions [196,197,187]. This makes the method less simple. LMM calculations with a similar improvement of convergence are not available yet for $L > 1$. Fortunately, for systems with two heavy particles and one light particle, this problem does not appear as shown in the next subsections.

7.4. Hydrogen molecular ion

The hydrogen molecular ion is treated as a three-body system without reference to the Born–Oppenheimer approximation. The calculations can be accurately performed on a Lagrange mesh in perimetric coordinates for any orbital momentum L [8,187,186]. The Born–Oppenheimer approximation remains useful for studies of this ion and its isotopomers in strong magnetic fields [9,46–48] for which the three-body treatment is still too heavy [198].

The H_2^+ hydrogen molecular ion and its HD^+ and D_2^+ isotopomers contain two heavy particles and one light particle, contrary to the helium atom. In this situation, the quantum number K in Eq. (7.4) is much closer to a good quantum number. Small values of $K_{\max}$ can be used, which allows an excellent accuracy even for high L values. Typical examples of energies obtained for H_2^+ with $N_x = N_y = 40$ and $N_z = 20$ are presented in Table 23 for $h_x = h_y = 0.14$ and $h_z = 0.4$. They are compared with accurate values of the literature. Three-body Lagrange-mesh treatments of HD^+ and D_2^+ can be found in Refs. [199,200].

An important advantage of the LMM is that the approximate wave functions are both precise and easy to use, specially for matrix elements calculated with the associated Gauss quadrature. These wave functions have been used to calculate mean values [8,187,186], transition probabilities [205,199,200] and polarizabilities [188]. Let me again take the example of the polarizabilities. An equation similar to Eq. (C.4) becomes an algebraic system on a mesh and can still be solved in spite of the large basis size. Then the polarizabilities are obtained with a generalization of Eq. (C.5) [188].

Some polarizabilities $\alpha^{(L)}$ are given for the $v = 0$ states in Table 24. Literature results only exist for $L = 0$. The Lagrange-mesh polarizabilities are obtained with the wave functions corresponding to the energies of Table 23 with a 9-digit accuracy. For $L = 0$, it is confirmed by the most accurate literature result [206]. More results including quadrupole polarizabilities and dynamical dipole polarizabilities can be found in Ref. [188].

7.5. Antiprotonic helium atom

Experiments show that the antiproton can survive in helium for a few microseconds, i.e. an exceptionally long time in matter before annihilation [207]. This long lifetime is explained by the formation of metastable states of the antiprotonic helium atom $\bar{p}He^+$, i.e. the He^{++} nucleus (or α particle) + antiproton + electron system. This property allowed the observation and measurement of radiative transitions near $L = 35$. This high value can be explained by the fact that the antiproton replaces an electron in its orbital. At the radius of the electron orbital, the antiproton lies in an excited hydrogenic orbital with $n \approx \sqrt{m_{\bar{p}} m_\alpha / m_e (m_{\bar{p}} + m_\alpha)} \approx 38$, where $m_{\bar{p}}$ is the antiproton mass and m_α is the mass of the helium nucleus. When the capture occurs in a circular orbit, the annihilation is strongly hindered. Combined with accurate

Table 25
Energies and average distances for the ground state and low excited states of the antiprotonic helium atom (in atomic units) obtained with $N_x = N_y = N_z = 20$ and $h_x = h_y = 0.0005$, $h_z = 0.4$.

L	E	$E - E_{\rm app}$	$\langle r_{\alpha\bar p}\rangle$	$\langle r_{\alpha e}\rangle$	$\langle r_{\bar p e}\rangle$
0	−2934.297 142 225 0	-1.46×10^{-7}	0.000 511 282 784 555 5	1.500 163 851	1.500 163 921
1	−733.949 246 29	-1.84×10^{-6}	0.001 704 275 955 7	1.500 158 8	1.500 159 6
2	−326.477 42	$\approx -10^{-5}$	0.003 578 977	1.500 13	1.500 14

theoretical calculations, measurements of transitions in the $\bar p$He$^+$ spectrum allowed the most precise determination of the antiproton mass [208,209].

The model presented here is simplified in the fact that only Coulomb forces are considered. The nuclear interaction between the helium nucleus and the antiproton is neglected. This interaction should be complex to simulate the annihilation channel. The purely Coulombic approximation may not be very good for the ground and low excited states but the calculation of their energies provides interesting numerical information about the stability of Coulomb three-body systems.

Some properties of the $L = 0$ ground state and the lowest excited states for $L = 1$ and 2 of the purely Coulombic $\bar p$He$^+$ three-body system obtained with the LMM are presented in Table 25. The masses are $m_\alpha = 7294.299\,508$ and $m_{\bar p} = 1836.152\,667\,5$. The results are obtained in perimetric coordinates with $N_x = N_y = N_z = 20$ and $h_x = h_y = 0.0005$, $h_z = 0.4$. For the ground state, excellent results are already obtained with $N_x = N_y = 12$ and $N_z = 18$. The choice in Table 25 is a compromise for the lowest three levels.

The important difference with three-body molecular ions is that the heavy particles now attract each other. The binding energy of the $L = 0$ ground state is thus very large. The energies of the low-L states are very close to the approximation

$$E_{\rm app} = -\frac{2m_{\bar p}m_\alpha}{(L+1)^2(m_{\bar p}+m_\alpha)} - \frac{m_e(m_{\bar p}+m_\alpha)}{2(m_e+m_{\bar p}+m_\alpha)} \tag{7.18}$$

where the first term is the energy of the lowest state with orbital momentum L of the $\bar p$He^{++} hydrogenic ion and the second term is the energy of the 1s ground state of an hydrogenic atom with a nucleus of charge $Z = 1$ and mass $m_{\bar p} + m_\alpha$. The slightly negative differences $E - E_{\rm app}$ is also displayed in Table 25 as well as mean radii. This property is well justified by the average distances between the particles. The $\alpha\bar p$ radius is very close to the hydrogenic value for a maximum orbital momentum,

$$\langle r_{\alpha\bar p}\rangle = \frac{(m_{\bar p}+m_\alpha)}{4m_{\bar p}m_\alpha}\,(L+1)(2L+3). \tag{7.19}$$

The αe and $\bar p e$ distances are very close to the hydrogen ground-state value. For $L = 0$, the distance between the He^{++} nucleus and the antiproton is so small that the electron 'sees' to a good approximation a point nucleus. Notice that this distance expressed in fm is quite large, i.e. about 27 fm. The nuclear correction and the disintegration width should be rather small. When L increases, the mean distance $\langle r_{\alpha\bar p}\rangle$ rapidly increases according to (7.19) and the electron becomes affected by the presence of two separate charges with opposite signs.

Energies and radii are also presented for the lowest $L = 1$ and $L = 2$ levels. For $L = 1$, using $K_{\rm max} = 0$ in place of 1 in Eq. (7.4) introduces an error of about 10^{-7} but the results remain stable. For $L = 2$, changing $K_{\rm max}$ leads to an instability around 10^{-5}. This can be understood as follows. The three levels are bound by about 0.5 Hartree with respect to the emission of an s electron. However, only the ground state of the purely Coulombic system is stable. The two excited states can dissociate by emitting a p electron (or a d electron for $L = 2$). The implicit bound-state approximation made when using a square-integrable basis remains a good approximation because the overlaps of the $\bar p$He^{++} parts of the initial and final three-body wave functions are small. When L becomes equal to 2 or larger than 2, the emission of a p electron becomes more and more probable and the energies cannot any more be calculated to a good accuracy with the present approximation. The autoionization (or Auger electron emission) width becomes too large. But this ceases to be true at L values around $L = 30$ and higher.

Indeed, when L reaches 28, the channels for the emission of p and d electrons are closed. The Auger electrons must progressively carry higher orbital momenta with much smaller emission widths. For the Lth partial wave, the threshold of the closest open channel can be expressed as

$$E_{\rm thr} = -\frac{2m_{\bar p}m_\alpha}{(L+1-\Delta L)^2(m_{\bar p}+m_\alpha)} \tag{7.20}$$

where ΔL is the orbital momentum carried by the Auger electron. For example, the $L = 31$ energy given below in Table 26 is below the $\Delta L \le 2$ thresholds and above the $\Delta L \ge 3$ thresholds. The open threshold with the smallest ΔL is the most important since the coupling is weaker for channels with larger ΔL. For $\Delta L \ge 3$, the bound-state approximation improves and accurate energies can again be obtained. At these high orbital momenta, the nuclear interaction represents a very small correction [209] and the purely Coulombic model is valid. However, the narrow levels lie in the continuum and the bound-state approximation also provides many pseudostates, i.e. approximations of continuum states, with energies that can be

Table 26
Energies and average distances of high-L levels of the antiprotonic helium atom in atomic units for $N_x = N_y = 28, N_z = 16$ and $h_x = h_y = 0.025, h_z = 0.4$.

L	E	Refs. [208,209]	$\langle r_{\alpha\bar{p}}\rangle$	$\langle r_{\alpha e}\rangle$	$\langle r_{\bar{p}e}\rangle$
31	−3.507 635 033 6	−3.507 635 035	0.372 444 233	1.208 301 1	1.332 379 9
32	−3.353 757 863 8	−3.353 757 863	0.399 974 560 4	1.179 592 373	1.319 125 694
33	−3.216 244 232 5	−3.216 244 231	0.429 496 612 1	1.150 265 157	1.307 160 237
34	−3.093 466 901 9	−3.093 466 899	0.461 315 255 4	1.120 373 761	1.296 759 963
35	−2.984 020 954 24	−2.984 020 954	0.495 800 309 9	1.090 035 860	1.288 324 993

close to the searched for physical energy. Pseudostates can easily be discriminated from physical states by their large mean radii of the electron with respect to the heavy particles. It is however useful to approximately know the location of the physical energy to speed up its determination. Its accuracy may slightly drop when the energy of a pseudostate is very close to the physical eigenvalue but this only occurs for some choices of the conditions of the calculation and can easily be avoided.

High-L energies with parity $(-1)^L$ are presented in Table 26 and compared with the accurate results of Kamimura and coworkers [208,209]. The selected levels correspond to $\Delta L \geq 4$ to minimize the role of their width. Preliminary results were given in Ref. [210]. The calculations are performed for $K_{\max} = 3$ with $N = N_x = N_y = 28, N_z = 16$ and $h = h_x = h_y = 0.025$, $h_z = 0.4$ (50,176 basis functions). The accuracy is estimated from comparisons with calculations involving $(N-2, N_z-2)$, (N, N_z-2) and $(N-2, N_z)$ mesh points. The difference with energies calculated for $K_{\max} = 2$ is of one or two units on the last displayed digit for $L \geq 32$. For $L = 31$, it is an order of magnitude larger probably because the width of this level is larger. These energies have nine digits in common with the accurate results of Refs. [208,209]. The distance between α and $\bar{p}$ increases with the centrifugal effect. Consistently, the distances between the electron and the heavy particles are reduced because the charge of the α particle is less screened by the antiproton. The electron is closer to the attracting α particle than to the repulsing antiproton.

These results should be improved by calculating widths. This can be performed with complex scaling (Section 6.6) but requires making an eigenvalue search of a large sparse complex matrix.

7.6. Lagrange-mesh method in hyperspherical coordinates

Several definitions exist for the hyperspherical coordinates and in particular for the hyperradius. For l dependent forces, it is convenient to use the system introduced by Delves [184]. Three sets of Jacobi coordinates can be defined as

$$\boldsymbol{x}_k = \sqrt{\frac{m_i m_j}{m_0(m_i+m_j)}}\,(\boldsymbol{r}_j - \boldsymbol{r}_i), \tag{7.21}$$

$$\boldsymbol{y}_k = \sqrt{\frac{(m_i+m_j)m_k}{m_0(m_i+m_j+m_k)}}\left(\boldsymbol{r}_k - \frac{m_i\boldsymbol{r}_i + m_j\boldsymbol{r}_j}{m_i+m_j}\right), \tag{7.22}$$

where (i, j, k) is an even permutation of $(1, 2, 3)$ and m_0 is some unit of mass. Eqs. (7.21) and (7.22) define six coordinates which are transformed to the hyperspherical coordinates as four angles, the hyperradius

$$\rho = \sqrt{x_k^2 + y_k^2} \tag{7.23}$$

and the hyperangle

$$\alpha_k = \arctan\frac{y_k}{x_k}. \tag{7.24}$$

The hyperradius ρ is independent of the choice k of Jacobi coordinates. It varies from 0 to ∞. Other definitions of ρ in the literature differ by a multiplicative factor. The hyperangle α_k varies between 0 and $\pi/2$. It can also be defined as the complement of the present angle. With the angular variables $\Omega_{x_k} = (\theta_{x_k}, \varphi_{x_k})$ and $\Omega_{y_k} = (\theta_{y_k}, \varphi_{y_k})$, Eqs. (7.23) and (7.24) define a set of hyperspherical coordinates, depending on k. Let us denote the set of five angles as

$$\Omega_{5k} = (\alpha_k, \Omega_{x_k}, \Omega_{y_k}). \tag{7.25}$$

The kinetic energy reads

$$\sum_{i=1}^{3} T_i - T_{\text{c.m.}} = -\frac{\hbar^2}{2m_0}\left(\frac{\partial^2}{\partial\rho^2} + \frac{5}{\rho}\frac{\partial}{\partial\rho} - \frac{K^2(\Omega_{5k})}{\rho^2}\right), \tag{7.26}$$

where K^2 is a five-dimensional generalization of the angular momentum [211,185]. The eigenfunctions of K^2,

$$K^2\mathcal{Y}^{l_x l_y}_{KLM_L}(\Omega_5) = K(K+4)\mathcal{Y}^{l_x l_y}_{KLM_L}(\Omega_5), \tag{7.27}$$

are the hyperspherical harmonics

$$\mathcal{Y}^{l_x l_y}_{KLM_L}(\Omega_5) = \phi^{l_x l_y}_K(\alpha)\left[Y_{l_x}(\Omega_x)\otimes Y_{l_y}(\Omega_y)\right]^{LM_L}. \tag{7.28}$$

The hypermomentum quantum number K extends the concept of angular momentum to three-body systems [211]. The functions $\phi^{l_x l_y}_K(\alpha)$ are defined as a function of Jacobi polynomials (Section 3.5.1) by

$$\phi^{l_x l_y}_K(\alpha) = \mathcal{N}^{l_x l_y}_K(\cos\alpha)^{l_x}(\sin\alpha)^{l_y}P_n^{(l_y+\frac{1}{2},l_x+\frac{1}{2})}(\cos 2\alpha), \tag{7.29}$$

where n is the positive integer $(K-l_x-l_y)/2$ and the normalization factor $\mathcal{N}^{l_x l_y}_K$ is given by

$$\mathcal{N}^{l_x l_y}_K = \left[\frac{2n!(K+2)(n+l_x+l_y+1)!}{\Gamma(n+l_x+\frac{3}{2})\Gamma(n+l_y+\frac{3}{2})}\right]^{\frac{1}{2}}. \tag{7.30}$$

Let S be the total spin of the three particles. With the spinor χ^{SM_S}, generalized hyperspherical harmonics with total angular momentum J are defined as

$$\mathcal{Y}^{JM}_{\gamma K}(\Omega_5) = \left[\mathcal{Y}^{l_x l_y}_{KL}(\Omega_5)\otimes\chi^S\right]^{JM}, \tag{7.31}$$

where index γ stands for $(l_x l_y LS)$. The set of hyperspherical coordinates, i.e. the value of k in Eq. (7.23), can be chosen freely.

A wave function with total angular momentum J, projection M and parity π is expanded as

$$\Psi^{JM\pi}(\rho,\Omega_5) = \rho^{-5/2}\sum_{\gamma K}\chi^{J\pi}_{\gamma K}(\rho)\,\mathcal{Y}^{JM}_{\gamma K}(\Omega_5). \tag{7.32}$$

The factor $\rho^{-5/2}$ allows to obtain an infinite system of coupled equations under the self-adjoint form

$$\left[-\frac{\hbar^2}{2m_0}\left(\frac{d^2}{d\rho^2}-\frac{(K+3/2)(K+5/2)}{\rho^2}\right)-E\right]\chi^{J\pi}_{\gamma K}(\rho)+\sum_{K'\gamma'}V^{J\pi}_{K'\gamma',K\gamma}(\rho)\,\chi^{J\pi}_{\gamma' K'}(\rho)=0. \tag{7.33}$$

For two-body forces, the matrix elements of the potential term in Eq. (7.1) read

$$V^{J\pi}_{K'\gamma',K\gamma}(\rho) = V^{J\pi(1)}_{K'\gamma',K\gamma}(\rho)+V^{J\pi(2)}_{K'\gamma',K\gamma}(\rho)+V^{J\pi(3)}_{K'\gamma',K\gamma}(\rho). \tag{7.34}$$

A difficulty of the hyperspherical coordinates is that the three two-body terms of the potential in Eq. (7.1) depend respectively on the three coordinates $\boldsymbol{x}_1, \boldsymbol{x}_2, \boldsymbol{x}_3$ which belong to different sets of Jacobi coordinates. If set k is chosen, the matrix element of the potential term depending on $\boldsymbol{r}_i-\boldsymbol{r}_j$ is directly given by

$$V^{J\pi(k)}_{K'\gamma',K\gamma}(\rho) = \int \mathcal{Y}^{JM*}_{\gamma' K'}(\Omega_{5k})\,V_{ij}\left(\sqrt{\frac{m_0(m_i+m_j)}{m_i m_j}}\,\rho\cos\alpha_k\right)\mathcal{Y}^{JM}_{\gamma K}(\Omega_{5k})d\Omega_{5k}. \tag{7.35}$$

The other potential terms depend on $\boldsymbol{x}_i$ and $\boldsymbol{x}_j$ and the integrals in their matrix elements are performed after the hyperspherical harmonics are transformed from coordinate system k to coordinate system j, for example, according to

$$\mathcal{Y}^{l_x l_y}_{KLM_L}(\Omega_{5k}) = \sum_{l'_x l'_y}\langle l'_x l'_y \mid l_x l_y\rangle_{KL}\,\mathcal{Y}^{l'_x l'_y}_{KLM_L}(\Omega_{5j}) \tag{7.36}$$

with the Raynal–Revai coefficients $\langle l'_x l'_y \mid l_x l_y\rangle_{KL}$ [185].

The three-body problem can be described with an analytical treatment of the five angles and a one-dimensional Lagrange mesh for ρ [11]. The hyperradial functions are expanded in N regularized Lagrange functions (3.78) as

$$\chi^{J\pi}_{\gamma K}(\rho) = h^{-1/2}\sum_{n=1}^{N}C^{J\pi}_{\gamma K n}\hat{f}_n(\rho/h), \tag{7.37}$$

where h is a scaling parameter. To take account of the centrifugal singularity in the system (7.33), the Lagrange functions must be regularized. Since a single choice must be made for all K values, the $x^{3/2}$ regularization in (3.78) is optimal as it allows simulating all $\rho^{K+5/2}$ behaviours at the origin. Regularizing with $x^{5/2}$ does not lead to a symmetric matrix. The problem of regularization is discussed in detail on a simple example in the next subsection.

In summary, with the LMM, this coordinate system is mostly useful for non-singular interactions that can depend on the relative two-body angular momentum. However, the hypercentrifugal term involves a ρ^{-2} factor and must be regularized. The following applications are limited to the study of bound states. When combined with the R matrix, the Schrödinger equation in hyperspherical coordinates is also useful to study the continuum of three particles [12,212].

7.7. Particles in a hyperradial potential

The treatment in hyperradial coordinates is made difficult by the presence of an infinite system of coupled equations. In order to have a simple example, I first consider a schematic problem with a hyperradial potential, i.e. a potential $V(\rho)$ depending only on the hyperradius. This corresponds to Eq. (7.1) with a three-body potential $V_{123} \equiv V(\rho)$ but with two-body potentials $V_{ij} = 0$. An advantage of this model is that one can treat without additional difficulty an arbitrary number P of particles.

With a hyperradial potential, Eqs. (7.33) are uncoupled. One can thus independently study each K value. For $K = 0$, the Schrödinger equation describing P particles reads

$$\left[\frac{\hbar^2}{2m_0} T_{3P-4} + V(\rho) - E\right] \chi_0(\rho) = 0 \tag{7.38}$$

where the kinetic-energy operator (3.63) reads

$$T_\alpha = -\frac{d^2}{d\rho^2} + \frac{\alpha(\alpha-2)}{4\rho^2}. \tag{7.39}$$

For $P = 3$, the $K = 0$ equation in system (7.33) reduces to (7.38).

For a bounded potential or a potential less singular than ρ^{-2} at the origin, $\rho = 0$ is a regular singular point leading to the behaviour

$$\chi_0(\rho) \underset{\rho\to 0}{\longrightarrow} \rho^{(3P-4)/2} \tag{7.40}$$

of the physical solutions. Various choices of Lagrange functions are compatible with (7.40). Let us choose the expansion

$$\chi_0(\rho) = h^{-1/2} \sum_{j=1}^{N} c_j f_j^{(\alpha)}(\rho/h) \tag{7.41}$$

where the $f_j^{(\alpha)}(x)$ are the Lagrange–Laguerre functions (3.52) associated with the mesh (3.50) for some α value. In this case, the kinetic energy T_α defined in Eq. (7.39) should be used to avoid numerical problems with the singularity of the centrifugal term. Another choice is to use the Lagrange–Laguerre functions $\hat{f}_j^{(\alpha)}(x)$ regularized by x defined in (3.70). Then one has more freedom in the choice of α and one can use the kinetic energy T_0. These various cases are tested below.

When using T_α with $\alpha = 3P - 4$ to simulate the behaviour (7.40), one obtains the Lagrange-mesh equations

$$\sum_{j=1}^{N} \left\{ \langle f_i^{(3P-4)} | T_{3P-4} | f_j^{(3P-4)} \rangle + [V(hx_i) - E]\delta_{ij} \right\} c_j = 0. \tag{7.42}$$

When using T_0 with regularized Lagrange functions behaving as $x^{\alpha/2+1}$ at the origin, one obtains

$$\sum_{j=1}^{N} \left\{ \langle \hat{f}_i^{(\alpha)} | T_0 | \hat{f}_j^{(\alpha)} \rangle + \left[\frac{\hbar^2}{2m_0} \frac{(3P-4)(3P-6)}{4(hx_i)^2} + V(hx_i) - E\right] \delta_{ij} \right\} c_j = 0 \tag{7.43}$$

with various choices for α.

Let us test these variants with $\hbar = m_0 = 1$ and the potential

$$V(\rho) = -P^{4/3} \exp[-(\rho/3)^2]. \tag{7.44}$$

The coefficient has been devised in a way to provide energies within the same order of magnitude for various values of P. In Table 27, results for numbers $P = 2$ to 5 of particles are compared with numerically exact results obtained with a higher number of mesh points ($N = 50$). The scale parameter is $h = 0.2$.

Let us start with a kinetic-energy operator T_{3P-4} which includes the centrifugal term. Lagrange–Laguerre functions $f_j^{(\alpha)}$ with $\alpha = 3P - 4$ have the right behaviour (7.40) at the origin. Since potential (7.44) is regular and since the matrix elements of T_{3P-4} are exactly given by Eqs. (3.65) and (3.67), this calculation can be expected to be good. Indeed, the absolute accuracy for $N = 10$ varies between 10^{-9} for $P = 2$ and 3×10^{-6} for $P = 4$. For $N = 20$, these numbers respectively become 10^{-13} and 2×10^{-11}. When the kinetic energy T_0 is used, the singularity of the centrifugal term becomes a problem for the Gauss quadrature. This problem is illustrated by a calculation using non-regularized Lagrange functions with $\alpha = 3P - 4$ shown in the second rows. For $P = 2$, the accuracy remains good since the centrifugal term vanishes. The accuracy is only 2×10^{-4} for $P = 3$ with $N = 10$ and 3×10^{-7} for $P = 4$ with $N = 20$.

As expected, this problem is solved by a regularization. The third rows display a regularization by ρ of the $\alpha = 0$ Lagrange functions. They do not have the behaviour (7.40) at the origin but the results are better with accuracies varying between 2×10^{-8} for $P = 3$ and 3×10^{-4} for $P = 5$ with $N = 10$ and between 3×10^{-9} for $P = 3$ and 2×10^{-8} for $P = 5$ with $N = 20$. The fourth rows display results with regularized functions with the correct behaviour (7.40) obtained for $\alpha = 3P - 6$. These results are better, very close to those of the first rows. These calculations present however the advantage over the calculations with T_{3P-4} that the results would remain good even for a potential with a Coulomb-like singularity at the origin. For arbitrary potentials, they also allow coupling different K values without loss of accuracy.

Table 27
Energies for numbers of particles $P = 2$ to 5 in the hyperradial potential (7.44) on a Laguerre mesh with 10 and 20 points ($h = 0.2$). Calculations performed with non-regularized Lagrange functions ($\alpha = 3P - 4$) and kinetic energies T_{3P-4} and T_0, and with regularized (R) Lagrange functions ($\alpha = 0$ and $3P - 6$) and T_0.

α	T	$P = 2$	$P = 3$	$P = 4$	$P = 5$
$N = 10$					
$3P - 4$	T_{3P-4}	−1.505 127 079 2	−1.739 830 796	−1.752 141 5	−1.572 827 58
$3P - 4$	T_0	−1.505 127 079 2	−1.739 98	−1.752 149 6	−1.572 825 7
0 (R)	T_0	−1.505 127 006	−1.739 830 949	−1.752 221	−1.573 17
$3P - 6$ (R)	T_0	−1.505 127 006	−1.739 831 26	−1.752 148 4	−1.572 815
$N = 20$					
$3P - 4$	T_{3P-4}	−1.505 127 078 069 2	−1.739 830 938 012	−1.752 144 002 085	−1.572 827 730 13
$3P - 4$	T_0	−1.505 127 078 069 2	−1.739 845 938 53	−1.752 144 28	−1.572 827 745
0 (R)	T_0	−1.505 127 078 069 1	−1.739 830 935 1	−1.752 144 002 92	−1.572 827 746
$3P - 6$ (R)	T_0	−1.505 127 078 069 1	−1.739 830 938 006	−1.752 144 002 050	−1.572 827 731 1
Exact		−1.505 127 078 069 2	−1.739 830 938 010 8	−1.752 144 002 068 1	−1.572 827 730 372 7

Table 28
Energies (in mK) of the ground and first excited levels and corresponding average distances $\langle r_{ij}\rangle$ (in a.u.) of the ^{4}He trimer for potentials (7.45) and (7.46) calculated on a Lagrange–Laguerre mesh with $N = 30$ mesh points for each perimetric coordinate. The scaling parameter is $h = 8$ for the ground state and $h = 18$ for the excited state. The error should be at most of a few units on the last displayed digit.

W_0 (K)	ρ_0 (a_0)	E_0(mK)	$\langle r_{ij}\rangle(a_0)$	E_1(mK)	$\langle r_{ij}\rangle(a_0)$
0	–	−150.426 094 3	16.345 629 05	−2.468 3	147.1
0.279	16	−126.380 75	17.470 748 7	−2.303 5	157.0
306.9	4	−126.5	17.67	−2.28	158.5

7.8. Helium trimer

In order to study the binding energies of the helium trimer, a weakly bound system of three helium atoms, I first calculate the binding energies of the helium dimer. The Gaussian two-body potential of Refs. [213,214],

$$V(r) = -1.227e^{-(r/10.03)^2}\,\mathrm{K}, \tag{7.45}$$

reproduces the binding energy and the effective-range expansion of two helium atoms. Here the lengths are expressed in Bohr radii a_0 and the energies in Kelvins (or more precisely in k_BK $\approx 3.1668 \times 10^{-6}$ a.u. where k_B is the Boltzmann constant). The value $\hbar^2/m = 43.281\,307 a_0^2$ K where m is the mass of the helium atom is used like in Ref. [214]. The binding energy of this extended system is tiny. With the above constants, it can be obtained on a regularized Lagrange mesh ($\alpha = 0$) with $N = 100$ mesh points and the large scaling parameter $h = 8$ as −1.295 891 133 43 mK. The corresponding mean radius is 98.489 782 159 a_0.

With this potential, the trimer binding energy −150.4 mK is however too large (see the $W_0 = 0$ row in Table 28). Hence, the authors of Ref. [214] have introduced various repulsive three-body interactions to simulate a realistic binding energy −126.4 mK for the trimer,

$$W(\rho) = W_0 e^{-4(r_{12}^2+r_{23}^2+r_{31}^2)/3\rho_0^2} \tag{7.46}$$

where W_0 and ρ_0 are parameters. For illustrating the properties of Lagrange meshes, I select the two extreme cases, i.e. the steepest and shallowest repulsive terms.

To test the approach in hyperspherical coordinates, the calculation is first performed in perimetric coordinates. In these coordinates, the hyperradius reads

$$\rho^2 = \frac{2}{3}(r_{12}^2 + r_{23}^2 + r_{31}^2) = \frac{1}{3}(x^2 + y^2 + z^2 + xy + yz + zx). \tag{7.47}$$

The same Laguerre mesh is used for the three coordinates. The full symmetry of the trimer is not exploited since expansion (7.8) is used. With $N = 30$ and $h = 8$ (13,950 basis functions), one obtains in Table 28 an accuracy of about 10^{-7} mK for the ground-state energy E_0 with only two-body forces (7.45), i.e. $W_0 = 0$. The average distance between the atoms is about 16.3. The excited state requires a larger $h = 18$ to reach convergence since the average distance between atoms is as large as 147. The estimated accuracy is below 10^{-4} mK. The result improves the value −2.467 of Ref. [214]. The introduction of a weak repulsion ($W_0 = 0.279$ K) reduces a little the accuracy which remains much better than in Ref. [214]. The average distance increases to about 17.5 as a result of a larger extension of the wave function. The energy E_1 is close to the result −2.302 of Ref. [214]. With a steep repulsive term however ($W_0 = 306.9$ K), the convergence is very slow and the accuracy drops to 0.1 mK for E_0 and 0.01 mK for E_1. The radius is a bit larger than with the smooth repulsion. The value of E_1 in Ref. [214] is −2.283 mK.

Table 29
Convergence of the energy of the ground state (in mK) of the ^{4}He trimer for potentials (7.45) and (7.46) as a function of the maximum hypermomentum K_{max}. The calculation is performed on a Lagrange–Laguerre mesh regularized by $\rho^{3/2}$ with N mesh points for the hyperradial coordinate and a scaling parameter $h = 1$.

W_0 (K)	0	0.279	306.9
ρ_0 (a_0)	–	16	4
N	30	40	60
$K_{max} = 20$	−150.421 06	−126.371 77	−126.414 18
$K_{max} = 22$	−150.423 53	−126.376 02	−126.418 51
$K_{max} = 24$	−150.424 92	−126.378 50	−126.421 03
$K_{max} = 26$	−150.425 43	−126.379 45	−126.422 00
$K_{max} = 28$	−150.425 74	−126.380 03	−126.422 59
$K_{max} = 30$	−150.425 91	−126.380 38	−126.422 95
Perimetric	−150.42609	−126.38075	≈ − 126.5

In hyperradial coordinates, the system (7.33) truncated at $K = K_{max}$ is solved on a Lagrange–Laguerre mesh regularized by $\rho^{3/2}$ (Section 3.3.5). Before comparing with the previous results, one needs to evaluate the convergence of the calculation with respect to the maximum hypermomentum K_{max}. For $W_0 = 0$, the convergence is fast with respect to N over a broad plateau of h values. The number $N = 30$ of mesh points ensures a good convergence for $h = 1$. Results for some K_{max} values are presented in Table 29. The convergence is slow but rather uniform with respect to the choice of W_0. The accuracy should be about 2×10^{-4} mK. When the repulsive potential is introduced, the number of mesh points must be increased: $N = 40$ for the shallow repulsion and $N = 60$ for the steep one (4320 basis functions for $K_{max} = 30$). When compared with the results in perimetric coordinates, one observes a less good accuracy except when the repulsive term is steep. In this case, the energy seems to converge to −126.424 mK. For the excited state, the convergence is too slow to reach good results.

Both treatments have advantages and drawbacks. In perimetric coordinates, a high accuracy can be reached when the potential is smooth. A repulsive potential peak leads to convergence problems. This problem is less serious with the hyperspherical coordinates. The convergence with respect to K_{max} is slow but one can easily put more points in the Lagrange mesh to cope with the bump around the origin in hyperradius space. Notice that while the basis is much larger in perimetric coordinates than in hyperspherical coordinates, computer times are similar because of the lengthy calculation of the potential matrix elements in (7.34).

7.9. Two-neutron halo nuclei

The halo nuclei with two loosely bound neutrons such as ^{6}He, ^{11}Li, ^{14}Be can be described as three-body systems made of a core and two distant neutrons forming the halo. These nuclei have a much larger radius than the famous approximation $1.25\,A^{1/3}$ fm. The core (^{4}He, ^{9}Li, ^{12}Be) is considered as close to a normal nucleus in its ground state and is described as one of the three particles. This model offers a good opportunity to compare the merits of different coordinate systems. Several coordinate systems (Jacobi coordinates, hyperspherical coordinates, etc.) have been successfully used in studies of halo nuclei [215]. Only some of them allow an efficient treatment on a Lagrange mesh. Two of these systems have already been presented. Let me briefly introduce a third one to clarify its properties [216–218] and drawbacks [11].

Let $\boldsymbol{r}_1$ and $\boldsymbol{r}_2$ be the coordinates of two neutrons with respect to a core particle with mass $A_c m_N$ where m_N is the nucleon mass, and let $\boldsymbol{p}_1$ and $\boldsymbol{p}_2$ be the corresponding momenta. The Hamiltonian describing the relative motion of two nucleons with respect to a core in a halo nucleus of mass number $A = A_c + 2$ is given by [219,216]

$$H = \frac{\boldsymbol{p}_1^2}{2\mu} + \frac{\boldsymbol{p}_2^2}{2\mu} + \frac{\boldsymbol{p}_1 \cdot \boldsymbol{p}_2}{(A_c+1)\mu} + V_{cn}(\boldsymbol{r}_1) + V_{cn}(\boldsymbol{r}_2) + V_{nn}(|\boldsymbol{r}_1 - \boldsymbol{r}_2|) + \Lambda \sum_{FS} |\psi_{FS}\rangle\langle\psi_{FS}|, \tag{7.48}$$

where $\mu = A_c m_N/(A_c + 1)$ is the core–neutron reduced mass. The core–neutron interaction is described by potential V_{cn} which may contain central and spin–orbit terms. The neutron–neutron interaction is represented by V_{nn}. The eigenvalues of H provide binding energies with respect to the decay into the core and two free neutrons. The potential V_{cn} often displays non-physical bound states called forbidden states (FS) whose role is to simulate the Pauli antisymmetrization principle between the nucleon and the core. The forbidden states $|\psi_{FS}\rangle$ can be eliminated with a pseudopotential involving projectors [220] which increases their energies by a large quantity Λ like in Eq. (7.48) or with a supersymmetric transformation [221] which removes them.

The wave function is expanded over coupled spherical harmonics. For $J = 0$ and positive parity, it reads

$$\Psi(\boldsymbol{r}_1, \boldsymbol{r}_2) = \sum_{Sl} [[Y_l(\Omega_1) \otimes Y_l(\Omega_2)]^L \otimes \chi^S]^{00} \psi_{Sl}(r_1, r_2), \tag{7.49}$$

where χ^S is a spin state. The total spin S of the neutrons is 0 or 1. When the nucleus has a total angular momentum $J = 0$ and a positive parity, the total orbital momentum L is equal to S. The positive parity then imposes a common orbital momentum l for both neutrons. In practice, the sum over l is limited by some value l_{max}.

Table 30
Comparison of Lagrange-mesh calculations of the ground-state energy of ^{6}He (in MeV) in perimetric, core–neutron and hyperspherical coordinates. Potential 1 is given by Eq. (7.52). Potential 2 is given by (7.52) for even partial waves and vanishes for odd partial waves. The last column corresponds to the α–n potential of Ref. [223].

Perimetric coordinates				
$N_x = N_y$	N_z	Pot. 1		
20	16	−0.929 041		
22	16	−0.929 049		
22	18	−0.929 049		
24	18	−0.929 050		
Core–neutron coordinates				
$l_{\max}$	N	Pot. 1	Pot. 2	Pot. [223]
16	20	−0.925 3	−0.851 6	−0.748 3
18	20	−0.926 2	−0.852 5	−0.749 9
	24	−0.927 4	−0.853 9	−0.750 9
	30	−0.927 7	−0.854 3	−0.751 0
20	20	−0.926 8	−0.853 1	−0.750 8
Hyperspherical coordinates				
$K_{\max}$	N	Pot. 1	Pot. 2	Pot. [223]
26	20	−0.923 7	−0.901 0	−0.418 5
28	20	−0.925 0	−0.902 2	−0.420 9
30	20	−0.926 0	−0.903 2	−0.422 7
	30	−0.926 2	−0.903 5	−0.423 1

The volume element is $dr_1 dr_2 d\Omega_1 d\Omega_2$. The spin and angular parts in the matrix elements are treated analytically. This requires an expansion of the neutron–neutron potential in multipoles. The remaining problem involves the two radial coordinates r_1 and r_2. The radial part of (7.49) is expanded in Lagrange functions as

$$\psi_{Sl}(r_1, r_2) = \sum_{i_1 \geq i_2 = 1}^{N} C^S_{li_1i_2} F_{i_1 i_2}(r_1, r_2), \tag{7.50}$$

where the $C^S_{li_1i_2}$ are variational coefficients and $i_1 \geq i_2$ because of the identity of the neutrons. The two-dimensional Lagrange functions are defined as

$$F_{i_1 i_2}(r_1, r_2) = [2(1+\delta_{i_1 i_2})]^{-1/2} h^{-1} [\hat{f}_{i_1}(r_1/h)\hat{f}_{i_2}(r_2/h) + \hat{f}_{i_2}(r_1/h)\hat{f}_{i_1}(r_2/h)]. \tag{7.51}$$

The functions $\hat{f}_i(x)$ are Lagrange–Laguerre functions (3.70) with $\alpha = 0$ regularized by x. This allows a common treatment of all partial waves.

The $(\boldsymbol{r}_1, \boldsymbol{r}_2)$ system of coordinates leads to incorrect results when the core–neutron interaction depends on the orbital angular momentum [11], either because the interaction is different for the various partial waves or because the treatment of Pauli-forbidden states affects some partial waves. This is illustrated with an α+n+n description of the ^{6}He halo nucleus. The neutron–neutron interaction is the Minnesota potential defined below in Eq. (8.34) where the operator P^M_{ij} can be replaced by its eigenvalue +1 and the operator P^σ_{ij} can be replaced by its eigenvalue $(-1)^S$. As the form factor in the Minnesota interaction is a linear combination of Gaussians [222], the expansion in multipoles can be performed analytically. The LMM is now discussed for various forms of α–n interactions. The value of $\hbar^2/2m_N$ is 20.736 MeV fm^2.

Let me now compare the core–neutron coordinate system described above with other systems of coordinates within the LMM. A first α–n interaction called 'Potential 1' does not depend on the angular momentum

$$V_{\alpha n}(r) = -60e^{-r^2} \tag{7.52}$$

in MeV and fm. For $S = 0$, it reproduces the order of magnitude of the two-neutron separation energy of ^{6}He, $S_{2n} = 0.975$ MeV. In perimetric coordinates, an accurate energy is obtained with $N_x = N_y = 22, N_z = 16$ and $h_x = h_y = h_z = 0.75$. It serves as a benchmark for the other calculations. Table 30 shows that the other two systems of coordinates lead to similar energies within less than 3 keV from the exact value. The scaling parameter is $h = 0.3$ in both cases. The convergences with respect to $l_{\max}$ and $K_{\max}$ are rather slow. The convergence with respect to the number of mesh points is faster in hyperspherical coordinates.

Let us now consider l-dependent potentials. Such potentials cannot be studied in a simple way in perimetric coordinates. Potential 2 is given by (7.52) for even l and vanishes for odd l. One observes the same convergence properties as before but the two limits now differ by about 0.05 MeV, a value larger than the 3 keV convergence uncertainty obtained with Potential 1 which should remain approximately valid here. With a parity-dependent phenomenological potential reproducing the properties of the α + n phase shifts [223] and the elimination of the $l = 0$ forbidden states with $\Lambda = 5000$ MeV, the results

are even more different, in particular because the elimination of the forbidden state by the pseudopotential [220] leads to a different treatment of the dominant s wave. The elimination with the supersymmetric technique [221] would lead to similar effects. While both systems seem to be correct with Potential 1, a problem appears with the l-dependent potentials.

The problem encountered here is an error introduced by the $(\boldsymbol{r}_1, \boldsymbol{r}_2)$ coordinate system when it is used with an l-dependent potential. This error is independent of the LMM. It can be explained as follows. The coordinates $\boldsymbol{r}_1$ and $\boldsymbol{r}_2$ do not form an orthogonal system. An l-dependent core–neutron potential can be written more precisely as

$$V_{cn}(r) = \sum_l V_{\rm cn}^{(l)}(r) P_l \tag{7.53}$$

where P_l is a projector on partial wave l. However, since the coordinate system is not orthogonal, the naive forms of projectors $P_{l_1}(1)$ and $P_{l_2}(2)$ consisting in using $V_{\rm cn}^{(l_1)}(r_1)$ in partial wave l_1 and $V_{\rm cn}^{(l_2)}(r_2)$ in partial wave l_2 are also not orthogonal. Correct projectors can in principle be established but would have such a complicated form that the simplicity of the LMM would be lost. This problem affects the quantitative results of all models using the core–nucleon coordinate system with l-dependent interactions such as in Refs. [216–218] as first observed in Ref. [11] but the error is small and scales as the inverse of the core mass. Hence, qualitative conclusions are not affected. In particular, the exponential decrease of the Lagrange–Laguerre functions allows a detailed analysis of the asymptotic properties of the halo of the ^{6}He nucleus [224].

8. Miscellaneous applications

8.1. Real and imaginary time propagation

The Lagrange-mesh method is useful for solving the time-dependent Schrödinger equation

$$i\hbar \frac{d}{dt}\psi(t) = H(t)\psi(t). \tag{8.1}$$

Many methods exist to solve this equation. Among them, propagation methods with a unitary operator are particularly interesting because they preserve the norm. The time evolution is approximated with a propagation over a time step Δt by the evolution operator U,

$$\psi(t + \Delta t) = U(t + \Delta t, t)\psi(t). \tag{8.2}$$

Tractable approximations of U are obtained with the splitting methods where this operator is approximately factorized as a product of simpler unitary operators [225–227].

The time-dependent Hamiltonian can be written as

$$H(t) = H_0 + V(t), \tag{8.3}$$

where H_0 may include a time-independent part V_0 of the potential. In splitting methods, one is looking for approximations where H_0 and $V(t)$ are in separate exponentials. At second order, this can be achieved with the well-known expression

$$U = e^{-i\frac{1}{2}\Delta t V(t+\Delta t)} e^{-i\Delta t H_0} e^{-i\frac{1}{2}\Delta t V(t)} + O(\Delta t^3). \tag{8.4}$$

This expression has been generalized at fourth order in various ways [227–229]. The simplest variant reads [228]

$$U = e^{-i\frac{1}{6}\Delta t V(t+\Delta t)} e^{-i\frac{1}{2}\Delta t H_0} e^{-i\frac{2}{3}\Delta t \widetilde{V}(t+\frac{1}{2}\Delta t)} e^{-i\frac{1}{2}\Delta t H_0} e^{-i\frac{1}{6}\Delta t V(t)} + O(\Delta t^5), \tag{8.5}$$

where

$$\widetilde{V} = V + \frac{\Delta t^2}{48}[V, [H_0, V]] = V - \frac{\Delta t^2}{48}(\nabla V)^2. \tag{8.6}$$

It has also been extended at sixth and higher orders [227], i.e. with an error of order at least $O(\Delta t^7)$. Tests show that, except if very high accuracies are necessary, the fourth order should be optimal since it provides a good balance between accuracy and simplicity [230]. Higher-order algorithms are more accurate but their additional complication and computer-time cost do not make them optimal.

Very similar expressions appear in the imaginary-time method which provides a calculation of the energy of the lowest state of a given symmetry in a time-independent Hamiltonian H. Indeed, one easily checks that the ground-state wave function ψ_0 is given by

$$\psi_0 = \lim_{\tau\to\infty} e^{-\tau H}\phi \tag{8.7}$$

where ϕ is arbitrary except that it must contain a lowest-energy component with the studied symmetry. The equation can be solved by iteration with some imaginary-time step $\Delta\tau$

$$\psi(\tau + \Delta\tau) = e^{-\Delta\tau H}\psi(\tau) \tag{8.8}$$

with $H = H_0 + V$ and $\psi(0) = \phi$. The imaginary-time method has been made very efficient with the use of high-order factorizations of the exponential imaginary-time propagator [225,219,228,227,229–231]. As suggested in Ref. [231], the

fourth-order algorithm

$$\psi(\tau+\Delta\tau)=e^{-\frac{1}{6}\Delta\tau V(\tau)}e^{-\frac{1}{2}\Delta\tau H_0}e^{-\frac{2}{3}\Delta\tau\widetilde{V}(\tau)}e^{-\frac{1}{2}\Delta\tau H_0}e^{-\frac{1}{6}\Delta\tau V(\tau)}\psi(\tau), \tag{8.9}$$

where $\widetilde{V}$ is given by (8.6) with $\Delta\tau$ replacing Δt, provides an error of order $\Delta\tau^4$ with reasonable computing times. The potential may depend on τ in self-consistent calculations (Section 8.3). In this algorithm, for simplicity, the potential is evaluated only at imaginary time τ (compare with Eq. (8.5)). Here, contrary to the real-time case, it is crucial that all the coefficients in the exponentials are negative. Otherwise, the accuracy is strongly reduced by the exponential factors leading to an expansion of the wave function.

The splitting methods easily and efficiently combine with the LMM. The use of a Lagrange mesh leads to small sizes for the time-dependent matrices representing the evolution operator. This property is extremely important when there are several spatial dimensions. Let us first consider the case of one spatial dimension in a time-dependent problem. The time-independent part of the Hamiltonian may contain a static potential $V_0(x)$ in addition to the kinetic energy T. A Lagrange basis is used for the space coordinate x,

$$\psi(x,t)=h^{-1/2}\sum_{j=1}^{N}c_j(t)f_j(x/h). \tag{8.10}$$

The coefficients $c_j(t)=(h\lambda_j)^{1/2}\psi(hu_j,t)$ [Eq. (2.26)] show the evolution of the wave function at the different locations hu_j. The exponentials of the different operators are represented by the exponentials of their Lagrange-mesh approximations. Let H_0 be represented by a matrix $\boldsymbol{H}_0$ with elements

$$H_{0ij}=h^{-2}T_{ij}+V_0(hu_i)\delta_{ij}. \tag{8.11}$$

The matrix representing H_0 can be diagonalized as

$$\boldsymbol{H}_0=\boldsymbol{O}\,\mathrm{diag}(E_0,E_1,\ldots,E_{N-1})\,\boldsymbol{O}^T \tag{8.12}$$

where the E_i are the eigenvalues of $\boldsymbol{H}_0$ and the orthogonal matrix $\boldsymbol{O}$ contains its eigenvectors. The exponential of H_0 is a non-diagonal matrix but it is constant. The matrix representing $\exp(-i\Delta t H_0)$ can thus be obtained with a single diagonalization as

$$e^{-i\Delta t\boldsymbol{H}_0}=\boldsymbol{O}\,\mathrm{diag}(e^{-i\Delta tE_0},e^{-i\Delta tE_1},\ldots,e^{-i\Delta tE_{N-1}})\,\boldsymbol{O}^T. \tag{8.13}$$

The matrix representing the operator $\exp(-i\Delta tV(t))$ is diagonal,

$$e^{-i\Delta tV(t)}\longrightarrow e^{-i\Delta tV(hu_i,t)}\delta_{ij}. \tag{8.14}$$

Because of the small size of the Lagrange-mesh matrices, the propagation on the mesh is very fast.

In a three-dimensional propagation, the size of the complex vector $\Psi(t)$ representing the wave function $\psi(t)$ takes the much larger value $N_xN_yN_z$. However, as long as H_0 is separable in Cartesian coordinates,

$$H_0=H_{0x}+H_{0y}+H_{0z}, \tag{8.15}$$

$\exp(-i\Delta tH_0)$ can be factorized as

$$e^{-i\Delta tH_0}=e^{-i\Delta tH_{0x}}e^{-i\Delta tH_{0y}}e^{-i\Delta tH_{0z}}. \tag{8.16}$$

The decomposition (8.15) is always possible for at least the kinetic-energy operator (in this case, $H_0\equiv T$). Each operator H_{0x}, H_{0y}, H_{0z} acts on a single coordinate. The action of each partial exponential matrix can be programmed simply. For example, the multiplication of vector $\boldsymbol{\Psi}(t)$ by the $N_xN_yN_z\times N_xN_yN_z$ matrix $\exp(-i\Delta t\boldsymbol{H}_{0x})$ only involves a non-trivial $N_x\times N_x$ block. It can thus be performed with $N_x^2N_yN_z$ multiplications of complex numbers. The matrix representing $\exp(-i\Delta tV(t))$ is diagonal,

$$e^{-i\Delta tV(x,y,z,t)}\longrightarrow e^{-i\Delta tV(h_xu_i,h_yv_j,h_zw_k,t)}\delta_{ii'}\delta_{jj'}\delta_{kk'}. \tag{8.17}$$

One never needs a multiplication by a large square matrix as long as the potential is local.

The same comments apply to the imaginary-time evolution on a Lagrange mesh. Some applications however involve a non-local potential $V(\tau)$ (Section 8.4). In three dimensions, they then require multiplications by $N_xN_yN_z\times N_xN_yN_z$ square matrices.

8.2. Forced harmonic oscillator

As a one-dimensional example of resolution of the time-dependent Schrödinger equation, let us consider the Hamiltonian of a forced oscillator [232,233]

$$H(t)=-\frac{1}{2}\frac{\partial^2}{\partial x^2}+\frac{1}{2}x^2-f(t)x \tag{8.18}$$

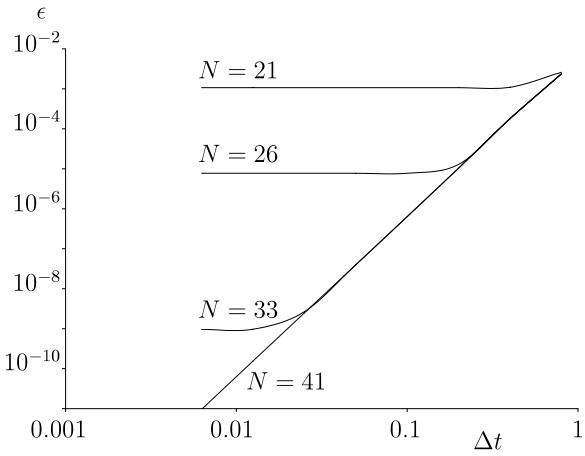

Fig. 22. Error ϵ on the wave function at $t = 2$ for the time-dependent Hamiltonian (8.18) as a function of the time step Δt, calculated with Eq. (8.21) on a Lagrange-sinc mesh with $N = 21, 26, 33$ and 41 mesh points.

where

$$f(t) = \sin^2 \frac{\pi}{2} t \tag{8.19}$$

like in Ref. [230]. This time-dependent term starts from zero at $t = 0$ and vanishes again at $t = 2$. At $t = 0$, the system is in the oscillator ground state $\varphi_0(x)$. This problem has an exact analytical solution [232,233]

$$\psi_{\rm ex}(x, t) = \varphi_0[x - x_0(t)] e^{i[p_0(t)x - \chi(t)]}. \tag{8.20}$$

See Ref. [230] for the expressions of $x_0(t)$, $p_0(t)$ and $\chi(t)$ when $f(t)$ is given by (8.19), and for details.

In the present Lagrange-mesh approach, the first two terms of the Hamiltonian are interpreted as operator H_0. The last term is the time-dependent potential $V(t)$. Calculations with H_0 equal to the kinetic-energy term T and $V(t) = \frac{1}{2}x^2 - f(t)x$ lead to very similar results. Errors with respect to the exact solution are presented in Fig. 22 as a function of the time step Δt for various calculations on a sinc mesh. This equal-spacing mesh is well adapted to non-stationary problems since a motion of the wave function can be described with a uniform accuracy.

The calculations are performed with mesh points in the interval $(-x_M, +x_M)$. They correspond to a scale parameter $h = 2x_M/(N - 1)$. The accuracy is evaluated as

$$\epsilon = \|\psi_{\rm ex}(t) - \psi(t)\| \approx \left\{ h \sum_{i=1}^{N} \lambda_i [\psi_{\rm ex}(hu_i, t) - (h\lambda_i)^{-1/2} c_i(t)]^2 \right\}^{1/2} \tag{8.21}$$

for $t = 2$ (and $\lambda_i = 1$ for the sinc mesh). With $x_M = 8$, results are displayed in Fig. 22 for $N = 21$ ($h = 0.8$), 26 ($h = 0.64$), 33 ($h = 0.5$) and 41 ($h = 0.4$) mesh points. The results with $N = 51$ ($h = 0.32$) are indistinguishable from those with $N = 41$. One observes that the accuracy improves like Δt^4, as expected. To optimally reach a given accuracy, one needs enough Lagrange mesh points. With at least $N = 41$, the Δt^4 accuracy is obtained down to 10^{-11}. However, if the required accuracy is 10^{-5}, $N = 26$ points are enough. Similar results are obtained with the Hermite mesh since the motion of the wave function is not large at $t = 2$.

8.3. Bose–Einstein condensates

The Gross–Pitaevskii equation describes the behaviour of a Bose–Einstein condensate at zero temperature within the mean-field approximation [234]. This non-linear Schrödinger equation involves an external trapping potential and a non-linear term due to the interactions between atoms. The atom–atom interaction within the dilute condensate is modelled only by its scattering length. The common individual wave function of each boson of the condensate is a self-consistent solution of this equation.

The imaginary-time method (Section 8.1) is used in many subfields of quantum physics and in particular to solve the Gross–Pitaevskii equation [235,231,10]. The fourth-order factorization algorithm (8.9) of the imaginary-time propagator combined with the LMM is well adapted to find a fast and accurate solution of the Gross–Pitaevskii equation [231].

In the absence of interactions between the bosons, the wave function of a boson is an eigenfunction of the Hamiltonian

$$H_0 = -\frac{1}{2}\Delta + V_{\rm conf}(x, y, z), \tag{8.22}$$

where $V_{\rm conf}$ is the external confinement potential and $\hbar = m = 1$. In most descriptions of experiments, this potential is well approximated by an oscillator trap

$$V_{\rm conf}(x,y,z) = \frac{1}{2}(\omega_x^2 x^2 + \omega_y^2 y^2 + \omega_z^2 z^2). \tag{8.23}$$

The angular frequencies ω_x, ω_y, ω_z are expressed as a function of some additional unit $\omega = 1$. Under the assumption of a dilute system, the behaviour of a condensate containing n bosons is described by the wave function ψ which is the normed ground-state solution of the Gross–Pitaevskii equation [234]

$$(H_0 + \lambda|\psi(x,y,z)|^2)\psi(x,y,z) = \mu\psi(x,y,z). \tag{8.24}$$

The dimensionless parameter in the non-linear term is defined as

$$\lambda = 4\pi n a\sqrt{\frac{m\omega}{\hbar}} \tag{8.25}$$

where a is the scattering length. Parameter λ can be positive or negative according to whether the interaction is repulsive or attractive.

The eigenvalue μ in Eq. (8.24) is the chemical potential,

$$\mu = \langle H_0\rangle + \lambda\langle|\psi|^2\rangle. \tag{8.26}$$

This expression is useful when Eq. (8.24) is not solved directly. The energy per boson is given by

$$E = \langle H_0\rangle + \frac{1}{2}\lambda\langle|\psi|^2\rangle. \tag{8.27}$$

The chemical potential, the energy per boson and the confinement potential satisfy a virial theorem,

$$E + \mu - 4\langle V_{\rm conf}\rangle = 0. \tag{8.28}$$

It can serve as a test of the accuracy of numerical calculations.

Let us consider three sets of N_x, N_y, N_z Lagrange functions $f_i^{p_x}(x/h_x)$, $g_j^{p_y}(y/h_y)$, $h_k^{p_z}(z/h_z)$ with parities p_x, p_y, p_z and the three-dimensional mesh $(h_x u_i, h_y v_j, h_z w_k)$ with the scaling parameters h_x, h_y, h_z. The corresponding weights are λ_i, μ_j, ν_k. Normed three-dimensional Lagrange functions (Section 2.8) can be defined as the products

$$F_{ijk}^{p_x p_y p_z}(x,y,z) = (h_x h_y h_z)^{-1/2} f_i^{p_x}(x/h_x) g_j^{p_y}(y/h_y) h_k^{p_z}(z/h_z). \tag{8.29}$$

The wave function of the condensate with parities p_x, p_y, p_z is then approximated as

$$\psi^{p_x p_y p_z}(x,y,z) = \sum_{i=\frac{1}{2}}^{\frac{1}{2}(N_x-1)} \sum_{j=\frac{1}{2}}^{\frac{1}{2}(N_y-1)} \sum_{k=\frac{1}{2}}^{\frac{1}{2}(N_z-1)} c_{ijk} F_{ijk}^{p_x p_y p_z}(x,y,z) \tag{8.30}$$

where N_x, N_y, N_z are chosen even for simplicity (Section 2.6). The matrix elements of Hamiltonian (8.22) are given by

$$H_{ijk,i'j'k'}^{p_x p_y p_z} = \frac{1}{2}h_x^{-2} T_{ii'}^{p_x}\delta_{jj'}\delta_{kk'} + \frac{1}{2}h_y^{-2}\delta_{ii'}T_{jj'}^{p_y}\delta_{kk'} + \frac{1}{2}h_z^{-2}\delta_{ii'}\delta_{jj'}T_{kk'}^{p_z} + V_{\rm conf}(h_x u_i, h_y v_j, h_z w_k)\delta_{ii'}\delta_{jj'}\delta_{kk'}, \tag{8.31}$$

where $T_{ii'}^{p_x}$, $T_{jj'}^{p_y}$, and $T_{kk'}^{p_z}$ are given by (2.55), (3.40) and (3.41) for the Lagrange–Hermite mesh or by (3.297) and (3.298) for the Lagrange-sinc mesh. The matrix representing the confinement potential is diagonal. The non-linear term is also diagonal,

$$\langle F_{ijk}^{p_x p_y p_z}|\lambda(\psi^{p_x p_y p_z})^2|F_{i'j'k'}^{p_x p_y p_z}\rangle = \frac{\lambda c_{ijk}^2}{8h_x h_y h_z \lambda_i \mu_j \nu_k}\delta_{ii'}\delta_{jj'}\delta_{kk'}. \tag{8.32}$$

The simple structures of Eqs. (8.31) and (8.32) are the main causes of the simplicity of the numerical algorithm.

The confining potential is chosen as $\omega_x = \omega_y = \omega_z = 1$. The calculation is performed with the Hermite and sinc meshes. The starting point of the iteration is the harmonic-oscillator wave function for $\lambda \le 10^3$ and the Thomas–Fermi approximation [234] for $\lambda > 10^3$ [10]. Three parameters must be chosen: the common number $N = N_x = N_y = N_z$ of mesh points, the scaling parameter $h = h_x = h_y = h_z$ and the imaginary-time step $\Delta\tau$. Except for h which is roughly optimized, the choice of the other parameters depends on the required accuracy. The convergence with respect to the number N of mesh points is illustrated for $\lambda = 1000$ in Fig. 23 with the Hermite mesh, $\Delta\tau = 0.01$ and the optimal parameter $h = 0.8$. The error $\epsilon = |\mu - \mu_{\rm exact}|$ on the chemical potential, where the exact value $\mu_{\rm exact}$ is approximated by a calculation with $N = 50$, is depicted with squares as a function of N. The convergence is approximately exponential from $N = 10$ to about 26–30. Beyond $N = 30$, the accuracy still improves but more slowly. The absolute value of the virial residue, i.e. the left-hand member of Eq. (8.28), is represented by triangles in the same figure. Its decrease is also slower beyond about $N = 30$. Clearly, it can serve as a measure of the accuracy on the chemical potential.

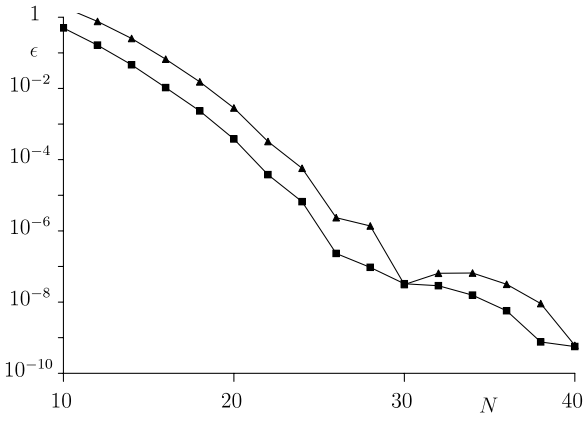

Fig. 23. Error $\epsilon = |\mu - \mu_{\rm exact}|$ on the chemical potential (squares) and absolute value of the virial residue $|E + \mu - 4\langle V_{\rm conf}\rangle|$ (triangles) for the Hermite mesh at $\lambda = 1000$ as a function of the number N of mesh points with $h = 0.8$ and $\Delta\tau = 0.01$.

Table 31
Chemical potential μ and energy E with optimal Hermite and sinc meshes for $\omega_x = \omega_y = \omega_z = 1$ as a function of the number N of mesh points, scale parameter h, time step $\Delta\tau$ and number $N_{\rm iter}$ of iterations. The last column displays the virial expression.

λ	Mesh	N	h	$\Delta\tau$	$N_{\rm iter}$	E	μ	Virial
1	Her.	20	0.9	0.05	206	1.530 891 280	1.560 971 500	−0.000 000 001
	sinc	20	0.5	0.05	265	1.530 891 280	1.560 971 499	−0.000 000 023
10^3	Her.	30	0.8	0.05	153	6.308 834 870	8.670 315 379	−0.000 000 012
	sinc	40	0.35	0.05	176	6.308 834 862	8.670 315 346	0.000 000 031
10^6	sinc	70	0.5	0.005	570	96.319 303 8	134.827 76	0.000 12

Calculations with reasonable numbers of mesh points for both Hermite and sinc meshes are compared in Table 31 as a function of positive values of parameter λ. The time step $\Delta\tau$ and the number $N_{\rm iter}$ of iterations are indicated. For small λ values, the convergence is faster with the Hermite mesh which is optimal for $\lambda = 0$. The sinc mesh becomes more efficient at higher λ values where the condensate wave functions flatten [10]. Hermite-mesh calculations do not converge for $\lambda > 10^5$ with $N \leq 80$.

8.4. Hartree–Fock calculations with a finite-range nuclear force

The Hartree–Fock method is important both in atomic and nuclear physics. At present, in atomic physics, the LMM cannot be applied with accuracy because of the singularity of the Coulomb potential. The situation is different in nuclear physics where effective forces are employed [236]. Nuclear Hartree–Fock calculations are often performed with effective Skyrme forces. They have a zero-range two-body part and depend on the density. They are devised in a way which simplifies the potential terms in the Hartree–Fock equation. The resulting equation has some similarity with the Gross–Pitaevskii equation. Hartree–Fock calculations are also performed with finite-range forces but the equations become then much more complicated to solve. The Hartree–Fock equation is non-local but still remains rather simple on a Lagrange mesh though the matrix representing the potential is full.

In self-consistent calculations involving an $A \times A$ Slater determinant Φ, the single-particle energies ϵ_m and orbitals ϕ_m verify the Hartree–Fock equations [236]

$$-\frac{\hbar^2}{2m_N}\Delta\phi_m(\boldsymbol{r}) + \left(\sum_{m'=1}^{A}\int d\boldsymbol{r}'\phi^*_{m'}(\boldsymbol{r}')V(\boldsymbol{r}-\boldsymbol{r}')\phi_{m'}(\boldsymbol{r}')\right)\phi_m(\boldsymbol{r})$$
$$-\int d\boldsymbol{r}'\left(\sum_{m'=1}^{A}\phi^*_{m'}(\boldsymbol{r}')V(\boldsymbol{r}-\boldsymbol{r}')\phi_{m'}(\boldsymbol{r})\right)\phi_m(\boldsymbol{r}') = \epsilon_m\phi_m(\boldsymbol{r}), \tag{8.33}$$

where V is a nucleon–nucleon potential independent of spin and isospin. This non-linear equation is solved by iteration.

The literature on nuclear Hartree–Fock calculations is enormous. Here I want to show a simple example with a spin- and isospin-dependent finite-range force. This example aims at illustrating the convergence of the method but not at giving realistic physical results. To this end, I consider the ^{16}O closed-shell nucleus with the Minnesota effective nucleon–nucleon interaction [222] and no Coulomb force. The Minnesota force involves a linear combination of Gaussians. In units of MeV and fm, its central part reads [222]

$$V = \left[V_R(r_{ij}) + \frac{1}{2}(1+P^\sigma_{ij})V_t(r_{ij}) + \frac{1}{2}(1-P^\sigma_{ij})V_s(r_{ij})\right]\frac{1}{2}[u + (2-u)P^M_{ij}] \tag{8.34}$$

where $\boldsymbol{r}_{ij}$ is the relative coordinate between nucleons i and j, operator P_{ij}^{σ} exchanges the spin coordinates of these nucleons and the Majorana operator P_{ij}^{M} exchanges their space coordinates $\boldsymbol{r}_i$ and $\boldsymbol{r}_j$. The repulsive-core, triplet and singlet parts of the interaction are $V_R(r) = 200\exp(-1.487r^2)$, $V_t(r) = -178\exp(-0.639r^2)$ and $V_s = -91.85\exp(-0.465r^2)$, respectively.

Also, a simplified centre-of-mass correction is used, i.e. only its one-body part. This simplification avoids the calculation of the two-body part of the correction. It amounts to multiply the kinetic-energy term by 15/16. This example gives a typical order of magnitude of the accuracy in 3D calculations. This accuracy can be assessed by a simple one-dimensional Hartree–Fock calculation exploiting the spherical symmetry of the ^{16}O nucleus.

The spatial parts $\varphi_m(x, y, z)$ of the single-particle orbitals $\phi_m(\boldsymbol{r})$ forming the 16×16 Slater determinant Φ are expanded for each orbital $m = 1$ to 4 (for $0s$, $0p_x$, $0p_y$ and $0p_z$) as

$$\varphi_m(x, y, z) = \sum_{i,j,k=1}^{N} C_{ijk}^{(m)} F_{ijk}(x, y, z) \tag{8.35}$$

where F_{ijk} is defined in Eq. (2.74) with $N = N_x = N_y = N_z$ points, and with the same Lagrange functions and scaling parameter h in the directions x, y and z corresponding to the mesh (hu_i, hu_j, hu_k). For the ^{16}O nucleus, the four orbitals are given by the N^3 equations

$$\begin{aligned}
&\sum_{i',j',k'=1}^{N} \left\{ \frac{15}{16} \frac{\hbar^2}{2m_N h^2} \left(T_{ii'}\delta_{jj'}\delta_{kk'} + \delta_{ii'}T_{jj'}\delta_{kk'} + \delta_{ii'}\delta_{jj'}T_{kk'} \right) \right. \\
&\quad + 2\delta_{ii'}\delta_{jj'}\delta_{kk'} \sum_{m'=1}^{4} \sum_{i'',j'',k''=1}^{N} [C_{i''j''k''}^{(m')}]^2 \mathcal{V}^D[h(u_i - u_{i''}), h(u_j - u_{j''}), h(u_k - u_{k''})] \\
&\quad \left. + 2\sum_{m'=1}^{4} C_{ijk}^{(m')} \sum_{i',j',k'=1}^{N} C_{i'j'k'}^{(m')} \mathcal{V}^E[h(u_i - u_{i'}), h(u_j - u_{j'}), h(u_k - u_{k'})] \right\} C_{i'j'k'}^{(m)} \\
&= \epsilon_m C_{ijk}^{(m)}
\end{aligned} \tag{8.36}$$

where

$$\mathcal{V}^D = (5u - 2)V_R + \left(\frac{9u}{2} - 3\right) V_t + \left(\frac{u}{2} + 1\right) V_s \tag{8.37}$$

and

$$\mathcal{V}^E = (5u - 8)V_R + \left(\frac{9u}{2} - 6\right) V_t + \left(\frac{u}{2} - 2\right) V_s. \tag{8.38}$$

The kinetic part is made of blocks like in Eq. (2.80). The direct part is diagonal but the exchange part is a full matrix. The four lowest eigenvalues of the matrix in Eq. (8.36) are the single-particle energies ϵ_m of the occupied levels. This process can be iterated. The corresponding eigenvectors provide the coefficients of the orbitals of these levels. The convergence and accuracy can be checked by comparing two expressions of the Hartree–Fock total energy [236]

$$E = \langle \Phi | H | \Phi \rangle = 4\sum_{m=1}^{4} \epsilon_m - \langle \Phi | V | \Phi \rangle. \tag{8.39}$$

For the sake of comparison, a spherical Hartree–Fock calculation is first performed on a regularized $\alpha = 0$ Laguerre mesh (3.50) with N mesh points and a scaling parameter $h = 0.12$. The exact expressions (3.77) are used for the matrix elements of $-d^2/dr^2$. The value of $\hbar^2/2m_N$ is 20.736 MeV fm^2. For simplicity, the exchange parameter is chosen as $u = 1$. The calculations converge to a stable value for all displayed digits after 12 iterations independently of N, starting from harmonic-oscillator orbitals. The results are displayed in Table 32. With $h = 0.12$, the convergence is very fast with respect to N. An accuracy of 2 keV is reached with only 12 points. Beyond $N = 16$, the accuracy reaches a few eV. For $N = 20$, the corresponding single-particle energies are $\epsilon_{0s} = -92.600\,071$ MeV and $\epsilon_{0p} = -47.443\,006$ MeV. More realistic values of the single-particle and total energies of ^{16}O (given the neglect of the Coulomb force and of the two-body part of the centre-of-mass term) can be obtained with $u \approx 0.85$.

The 3D Hartree–Fock calculations are performed on Hermite meshes (3.33) and sinc meshes (3.286) with N mesh points in each direction and a roughly adapted scaling parameter h. For the Hermite mesh, the exact expressions (3.42) are used for the matrix elements of $-\partial^2/\partial x^2$, $-\partial^2/\partial y^2$ and $-\partial^2/\partial z^2$. For the sinc mesh, they are given by (3.292) and (3.293). Rather than using Eq. (8.36), it is convenient to perform a parity projection to reduce the size of the matrix. Each orbital is projected on parity along each of the x, y and z axes with parities $(+1, +1, +1)$ for $0s$, $(-1, +1, +1)$ for $0p_x$, $(+1, -1, +1)$ for $0p_y$ and $(+1, +1, -1)$ for $0p_z$. This choice is consistent with the assumed spherical symmetry in the 1D calculation. This reduces the

Table 32
Comparison of energies E of ^{16}O (in MeV) obtained with a spherical Hartree–Fock calculation performed on a regularized Laguerre mesh ($\alpha = 0$) with N mesh points and a scaling parameter $h = 0.12$ and a 3D Hartree–Fock calculation performed on Hermite and sinc meshes with N points and the same scaling parameter h in the three directions. The total number of points in the projected 3D meshes is also given.

N	Laguerre (1D)	$\frac{1}{8}N^3$	Hermite (3D)	sinc (3D)	
	E ($h = 0.12$)		E ($h = 1$)	h	E
10	−223.097 319	125	−223.031 559	0.75	−221.839 707
12	−223.140 902	216	−223.114 082	0.70	−222.826 834
14	−223.142 725	343	−223.139 562	0.65	−222.826 834
16	−223.142 789	512	−223.141 273	0.65	−223.116 478
18	−223.142 791	729	−223.142 488	0.60	−223.137 265
20	−223.142 791	1000	−223.142 637	0.60	−223.140 950

total number of mesh points to $\frac{1}{8}N^3$. Tests show that the same results are obtained with Eq. (8.36) but with much longer computing times.

The energies obtained with 3D calculations are also presented in Table 32 (see Ref. [37] for preliminary results). The matrix sizes of the projected case are given in the table. In all cases, the convergence on all the displayed digits is reached after about 16 iterations, starting from harmonic-oscillator wave functions. With the Hermite mesh, $h = 1$ is optimal independently of N. An error of a few keV is obtained with $N = 14$, i.e. with only seven points on each positive semi-axis. When N increases to 20, the accuracy is better than 0.2 keV. Notice that the three $0p$ single-particle energies converge to the same value, confirming the spherical symmetry. With the sinc mesh, the optimal choice for h decreases when N increases. The accuracy is always slightly less good than with the Hermite mesh. With $N = 20$, it is better than 2 keV. This remains very good given the small number of 3D mesh points.

8.5. Translations and rotations on a Lagrange mesh

Translations and rotations are important to restore the symmetries of approximate wave functions, i.e. to eliminate spurious centre-of-mass components or to construct eigenstates with good angular momentum, respectively [237,236]. Such symmetry operations can be accurately performed on a Lagrange mesh [4].

Let us consider a translation of a one-dimensional function $\psi(x)$ over a distance a to the right. The resulting function is $\psi_a(x) = \psi(x - a)$. An obvious way of performing this translation over mesh points $x_i = hu_i$ is by an interpolation,

$$\psi_a(x) \approx \sum_{j=1}^{N} \lambda_j^{1/2} \psi(x_j) f_j[(x - a)/h] \tag{8.40}$$

where (2.44) and (2.45) are used. This method can be accurate but may be slow. It requires the evaluation of the Lagrange functions for each a value, i.e. a large number of calculations of orthogonal polynomials or trigonometric functions. The problem is even more serious on three-dimensional meshes.

Another approach is based on matrix representations of operators. With $\hbar = 1$, the operator $\exp(-iap_x)$ performs a translation over a distance a along the x axis of an arbitrary infinitely differentiable function $\psi(x)$. It can be approximately represented on a Lagrange mesh as

$$\exp(-iap_x) = \exp\left(-a\,\frac{d}{dx}\right) \longrightarrow \exp(-a\boldsymbol{D}/h) \tag{8.41}$$

where matrix $\boldsymbol{D}$ contains matrix elements (3.14) of the first derivative between Lagrange functions. This is an approximation since the matrix element of an exponential is replaced by the exponential of a matrix element. Let $\boldsymbol{O}$ be a matrix diagonalizing $\boldsymbol{D}$,

$$\boldsymbol{D} = \boldsymbol{O}\,\mathrm{diag}(d_1, d_2, \ldots, d_N)\,\boldsymbol{O}^T. \tag{8.42}$$

The approximate translation on the mesh is performed with the matrix

$$\exp(-a\boldsymbol{D}/h) = \boldsymbol{O}\,\mathrm{diag}(e^{-ad_1/h}, e^{-ad_2/h}, \ldots, e^{-ad_N/h})\,\boldsymbol{O}^T. \tag{8.43}$$

The values of the translated function $\psi_a(x)$ at mesh points x_i are given by

$$\lambda_i^{1/2} \psi_a(x_i) \approx \sum_{j=1}^{N} [\exp(-a\boldsymbol{D}/h)]_{ij}\, \lambda_j^{1/2} \psi(x_j). \tag{8.44}$$

An important particular case is given by the Fourier mesh (Section 3.7.1), where translations with unit step can be exactly performed, except at boundaries. On this mesh, the exponential operator is equivalent to an interpolation. Moreover, matrix

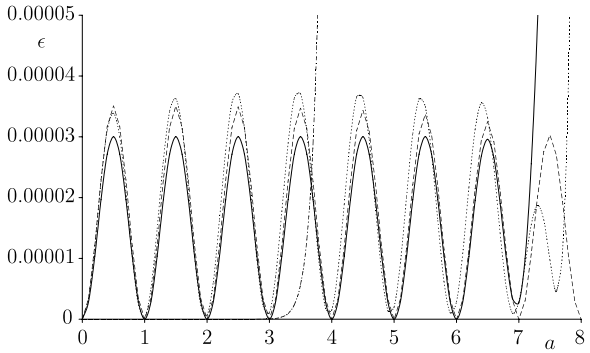

Fig. 24. Mean-square error ϵ [Eq. (8.48)] with respect to the exact translation $\psi_a(x)$ of the function $\psi(x) = \pi^{-1/4}\exp(-\frac{1}{2}x^2)$ for various mesh approximations: interpolation on a sinc mesh (dashed line), approximate translation operator on a sinc mesh (dotted line) and on a Hermite mesh (dash-dotted line), and both methods on a Fourier mesh (full line). In all cases, $N = 20$ and $h = 1$ are used.

$\boldsymbol{D}$ can be diagonalized analytically. Indeed, with $h = 1$ for simplicity, the functions (3.230),

$$\varphi_k(x) = N^{-1/2}e^{i2\pi kx/N} = \sum_{j=1}^{N}\varphi_k(x_j)f_j(x), \tag{8.45}$$

are exact eigenfunctions of d/dx with eigenvalues $i2\pi k/N$, $k = -\frac{1}{2}(N-1), \ldots, \frac{1}{2}(N-1)$. Hence the orthogonal matrix $\boldsymbol{O}$ with elements $O_{ij} = \varphi_j(x_i)$ diagonalizes $\boldsymbol{D}$ and the eigenvalues of $\exp(-a\boldsymbol{D})$ are $\exp(-i2\pi ka/N) = \sqrt{N}\varphi_k(-a)$. One deduces with (3.233) and (2.16),

$$[\exp(-a\boldsymbol{D})]_{ij} = \sqrt{N}\sum_{k=1}^{N}\varphi_k(x_i)\varphi_k(-a)\varphi_k^*(x_j) = f_j(x_i - a). \tag{8.46}$$

The action (8.44) of the translation operator on the mesh is

$$\psi_a(x_i) \approx \sum_{j=1}^{N} f_j(x_i - a)\psi(x_j) \tag{8.47}$$

i.e. one recovers Eq. (8.40) at mesh points, since $\lambda_j = 1$ and $h = 1$. This property is related to Eq. (3.237). Repeated multiplications by matrix $\exp(-a\boldsymbol{D})$ can be rapidly and easily done and provide exactly the same results as a number of interpolations performed with the Lagrange–Fourier functions. This would not be true for other Lagrange meshes.

Different translation techniques on a mesh are tested in Fig. 24. The translated function is the normed Gaussian $\psi(x) = \pi^{-1/4}\exp(-\frac{1}{2}x^2)$. The error is expressed as

$$\epsilon = \int [\psi_a(x) - \psi_a^{\text{approx}}(x)]^2 dx \approx h\sum_{j=1}^{N}\lambda_j[\psi(x_j - a) - \psi_a^{\text{approx}}(x_j)]^2 \tag{8.48}$$

where ψ_a^{approx} is given either by (8.40) or by (8.44). The integration domain is $(-\infty, +\infty)$ except for the Fourier mesh where it is approximated by $(-\frac{1}{2}N, \frac{1}{2}N)$. For a Fourier mesh with $N = 20$ mesh points and $h = 1$, approximations (8.40) and (8.44) give identical results as explained above. The error is periodic and positive. It remains smaller than 3×10^{-5}. It is represented by a full line. As expected, ϵ vanishes at mesh points. It starts increasing rapidly for $a > 7$ when the translated function hits the boundary $\frac{1}{2}N = 10$ of the domain. For a sinc mesh with $N = 20$ mesh points and $h = 1$, the two approximations are different but almost indistinguishable (dashed and dotted lines). The error is quasi (but not exactly) periodic and slightly smaller than for the Fourier mesh. It also starts to increase beyond 8 when there are no more mesh points (see Fig. 16 in Section 3.7.5). For a Hermite mesh with $N = 20$ mesh points and $h = 1$, approximation (8.44) is extremely precise for $a < 3$ ($\epsilon < 10^{-7}$) but becomes rapidly very bad beyond $a = 4$ (dash-dotted curve) because the translated function hits the last mesh point ($x_{19/2} \approx 5.4$). Amusingly, interpolation (8.44) is here *exact* for all a values because of Eq. (3.9). Indeed, the translated function is the square root of the weight function $w(x)$ of the Hermite mesh and the translation is exact. This accidental property does not occur for other functions but the translation remains very accurate for $a < 3$. The Hermite mesh is not interesting for large translations.

Three-dimensional translations on a Cartesian mesh with (N_x, N_y, N_z) mesh points (x_i, y_j, z_k) are obtained with the factorized representation

$$\exp(-i\boldsymbol{a}\cdot\boldsymbol{p}) \longrightarrow \exp(-a_x\boldsymbol{D}_x/h_x)\exp(-a_y\boldsymbol{D}_y/h_y)\exp(-a_z\boldsymbol{D}_z/h_z) \tag{8.49}$$

where $\boldsymbol{D}_x/h_x$, $\boldsymbol{D}_y/h_y$ and $\boldsymbol{D}_z/h_z$ represent $\partial/\partial x$, $\partial/\partial y$ and $\partial/\partial z$ on some Lagrange meshes. Like in Section 8.1, the translation can be performed with about $(N_x+N_y+N_z)N_xN_yN_z$ multiplications.

A rotation of angle α around the z axis of a function $\psi(x,y)$ can be performed by interpolation on a mesh $(x_i,y_j) = (h_x u_i, h_y v_j)$ like in Eq. (8.40),

$$\psi_\alpha(x,y) \approx \sum_{i=1}^{N_x}\sum_{j=1}^{N_y}(\lambda_i\mu_j)^{1/2}\psi(x_i,y_j)f_i[(x\cos\alpha - y\sin\alpha)/h_x]f_j[(x\sin\alpha + y\cos\alpha)/h_y]. \tag{8.50}$$

However this technique involves many calculations of Lagrange functions to determine the values $\psi_\alpha(x_i,y_j)$ of the rotated function at all mesh points. A matrix-multiplication technique is usually faster.

Matrix representations of rotation operators have been introduced in Ref. [238] in the context of finite differences. They have been extended to the Lagrange–Fourier mesh in Ref. [4]. A rotation of angle α of an infinitely differentiable function $\psi(x,y)$ around the origin of the (x,y) plane is performed with operator $\exp(-i\alpha L_z)$. This operator can be represented on a Lagrange mesh as

$$\exp(-i\alpha L_z) = \exp\left[-\alpha\left(x\frac{\partial}{\partial y} - y\frac{\partial}{\partial x}\right)\right]$$
$$\longrightarrow \exp(-i\alpha\boldsymbol{\mathcal{L}}_z) = \exp[-\alpha(\boldsymbol{X}\otimes\boldsymbol{D}_y/h_y - \boldsymbol{D}_x/h_x\otimes\boldsymbol{Y})] \tag{8.51}$$

where $\boldsymbol{X}$ and $\boldsymbol{Y}$ are diagonal matrices containing the mesh points x_i and y_j on their diagonal, respectively. The direct products in (8.51) lead to an $N_xN_y \times N_xN_y$ matrix. Matrix $\exp(-i\alpha\boldsymbol{\mathcal{L}}_z)$ can be calculated with a diagonalization of matrix $\boldsymbol{\mathcal{L}}_z$ with elements

$$(\boldsymbol{\mathcal{L}}_z)_{ij,i'j'} = -i[x_i\delta_{ii'}(D_{y,jj'}/h_y) - (D_{x,ii'}/h_x)y_j\delta_{jj'}] \tag{8.52}$$

like in (8.42) but its size is of course much larger. This size can be reduced if function $\psi(x,y)$ possesses parity symmetries [238].

The Hermitian matrix $\boldsymbol{\mathcal{L}}_z$ can be diagonalized as

$$\boldsymbol{\mathcal{L}}_z = \boldsymbol{O}\,\mathrm{diag}(\nu_1,\nu_2,\ldots,\nu_N)\,\boldsymbol{O}^\dagger. \tag{8.53}$$

Many of the eigenvalues ν_j of matrix $\boldsymbol{\mathcal{L}}_z$ are very close to integer values resembling the integer eigenvalues of operator L_z as shown by Table 4 of Ref. [4], even for rather small Fourier meshes. The eigenvalues and eigenvectors corresponding to non-zero eigenvalues can be found by diagonalizing the real symmetric matrix $\boldsymbol{\mathcal{L}}_z^2$ [238]. In Ref. [238], one also finds a way to reduce the size of the matrix to about $\frac{1}{4}N_xN_y$ by exploiting its symmetries.

The values of the rotated function $\psi_\alpha(x,y)$ at mesh points are given by

$$(\lambda_i\mu_j)^{1/2}\,\psi_\alpha(x_i,y_j) = \sum_{i'=1}^{N_x}\sum_{j'=1}^{N_y}[\exp(-i\alpha\boldsymbol{\mathcal{L}}_z)]_{(ij),(i'j')}\,(\lambda_{i'}\mu_{j'})^{1/2}\,\psi(x_{i'},y_{j'}) \tag{8.54}$$

where (ij) represents the index numbering the ordered functions $\psi_\alpha(x_i,y_j)$. The approximate rotation on the mesh is performed with the matrix with elements

$$[\exp(-i\alpha\boldsymbol{\mathcal{L}}_z)]_{(ij),(i'j')} = \delta_{ii'}\delta_{jj'} + \sum_{k=1,\nu_k\neq0}^{N_xN_y} O_{(ij)k}(e^{-i\alpha\nu_k}-1)O^*_{(i'j')k}. \tag{8.55}$$

This expression does not require the knowledge of the eigenvectors corresponding to zero eigenvalues ν_k.

Rotation techniques on a Lagrange mesh were first performed on the Fourier mesh [4]. They are tested in Fig. 25 by rotating the function

$$\psi(x,y) = (2\pi^2)^{-1/4}\exp\left[-\left(\frac{1}{4}x^2 + \frac{1}{2}y^2\right)\right]. \tag{8.56}$$

The same mesh is used for x and y ($N_x = N_y = N$ and $h_x = h_y = h$). The partial derivatives are calculated with Eqs. (3.234). The interpolation method requires $2N^4$ evaluations of sine functions while the matrix technique only requires N^2 evaluations of complex exponentials. The mean-square error ϵ is calculated at the Gauss approximation like in Eq. (8.48). The errors of the interpolation and of the matrix multiplication may have quite different behaviours. Their main differences are visible in the figure. While the error on the matrix multiplication has a rather smooth behaviour, the error on the interpolation displays peaks in the vicinity of 45 and 135 degrees. These peaks are due to the fact that non-negligible ghosts of the wave function appear in the corners of the two-dimensional mesh. They are thus related to the periodicity of the basis. This does not occur with the matrix multiplication, probably because of the elimination of zero (or close to zero) eigenvalues in Eq. (8.55). The error is more sensitive to the size of h than to N. For $h = 0.8$, increasing N from 14 to 18 does not improve the accuracy of the matrix method. On the contrary, it reduces the problem with the interpolation since the interval grows from

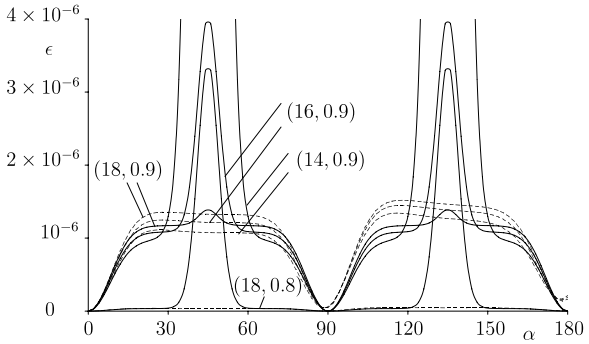

Fig. 25. Mean-square error ϵ with respect to the exact rotated function $\psi_\alpha(x, y)$ by an angle α of function $\psi(x, y)$ defined in (8.56) with approximations on a Fourier mesh: interpolation (full lines) and matrix multiplication (dashed lines). The curves are labelled with (N, h).

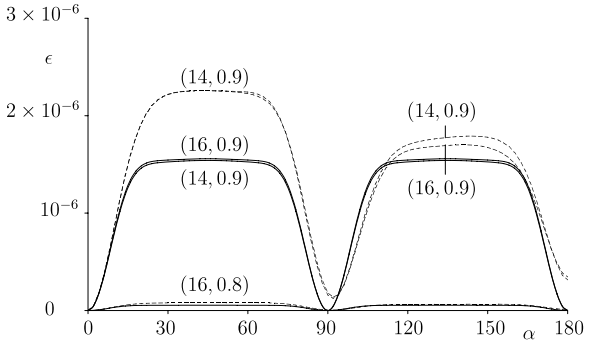

Fig. 26. Mean-square error ϵ with respect to the exact rotated function $\psi_\alpha(x, y)$ by an angle α of function $\psi(x, y)$ defined in (8.56) with approximations on a sinc mesh: interpolation (full lines) and matrix multiplication (dashed lines). The curves are labelled with (N, h).

$(-6.3, 6.3)$ to $(-8.1, 8.1)$. For $N = 18$ and $h = 0.9$, the two techniques give very close accuracies. When h decreases to 0.8, the error on the matrix multiplication drops by more than an order of magnitude while the problems of the interpolation near 45 and 135 degrees reappear. The interpolation method with a Fourier mesh should be used with care as these problems might affect the calculation of some observables.

The interpolation problems on a Fourier mesh are due to the periodicity of the basis functions. One can thus expect them to disappear with a sinc mesh. This is indeed what is observed in Fig. 26. The partial derivatives are calculated with Eqs. (3.291). The errors are now more uniform around 45 and 135 degrees. Again, the size of the error mainly depends on h (provided that the interval is large enough). The errors with the interpolation and with the matrix multiplication are very similar. The accuracy with the matrix multiplication is slightly less good than with the Fourier mesh.

A three dimensional rotation with Euler angles (α, β, γ) can be represented as [238]

$$\exp(-i\alpha L_z)\exp(-i\beta L_y)\exp(-i\gamma L_z) \longrightarrow \exp(-i\alpha \pounds_z)\exp(-i\beta \pounds_y)\exp(-i\gamma \pounds_z) \tag{8.57}$$

where $\pounds_y$ is defined like in Eq. (8.52). Each interpolation or matrix multiplication by $\exp(-i\gamma \pounds_z)$ for example can be performed independently in successive $z = z_k$ planes. The rotation by matrix multiplication requires $3N^2$ evaluations of complex exponentials and is thus faster than by interpolations with Lagrange functions.

9. Conclusion and outlook

The Lagrange-mesh method has developed significantly over the years. Initially, it was a curiosity, an original way of solving simple quantum-mechanical problems. To date, it has become an accurate technique of resolution, probably giving the best ratio of accuracy over computing time for some problems. It has been found very economical in scattering problems where the evaluation of potential terms is very long [156] or with a large number of channels [12–14,164]. It can also be useful to solve in a simple way the Dirac equation or three-body problems. It provide fast and accurate solutions of non-linear Schrödinger-like equations. In all these cases, the wave functions are available and easy to use for calculations of matrix elements of various observables or various types of transitions. Moreover, its elegance and simplicity have interesting pedagogical aspects and can provide a good training for students.

A large variety of examples in quantum physics are given in this review. Most two-body problems have been chosen to be comparable with simple exact solutions. The reader should be able to reproduce their results as simple exercises without too much effort. Of course, the LMM can also provide accurate results for potentials without exact solutions. Three-body

and non-linear applications require more work but I think that they nevertheless lead to simpler treatments than many other approaches. In particular, the approximate wave functions have a simple analytical form and can easily be used in applications [45,205,188,199].

The available meshes seem to be linked to orthogonal polynomials, classical or not, with the exception of the sinc mesh. The number of known Lagrange meshes is therefore limited until now. For a given family of polynomials, several types of Lagrange functions may exist and be useful, differing by a change of variables or by a regularization. However, I think that a number of useful meshes and Lagrange functions have still to be discovered, based on non-classical orthogonal polynomials. For some problems, adapted meshes should prove superior to those listed in Section 3. This requires a search for optimal weight functions $w(x)$ as a function of the studied problem.

Given the author's specialization, the applications in the present review are limited to quantum physics, i.e. the resolution of Schrödinger-like equations or the Dirac equation. The LMM should also be useful for other fields. Some related methods have already proved efficient to solve the Fokker–Planck equation. I expect that the LMM could also be useful in optics where non-linear Schrödinger equations are encountered. The LMM is particularly interesting in problems where one of the coordinates can be infinite. This may raise a difficulty for discretization or finite-elements methods but not for a global method like the LMM.

A big challenge is to extend the applicability of the LMM to problems where several singular terms appear at different locations such as in atomic Hartree–Fock calculations. The future should tell us whether this is possible.

Acknowledgements

I warmly thank Marc Vincke and Michel Hesse who significantly contributed to the development of the LMM. I am also indebted to Laurence Malegat, Pierre Descouvemont and Jean-Marc Sparenberg for fruitful collaborations on some topics. I acknowledge illuminating discussions on the principles of the method with Ernest Mund and Bernie Shizgal. I thank A. Adahchour, P. Capel, J. Dohet-Eraly, T. Druet, L. Filippin, M. Godefroid, G. Goldstein, P.-H. Heenen, A. Joos de ter Beerst, R. Kamouni, M. Kruglanski, R. Lazauskas, H. Masui, V.S. Melezhik, H. Olivares Pilón, J. Roland, C. Semay, K. D. Sen, B. Silvestre-Brac, E. Tursunov, Y. Suzuki and R. Yarmukhamedov for contributing to the development of some application(s) and/or for useful discussions. I am glad to mention that a number of undergraduate students in physics engineering contributed to some applications of the LMM and enjoyed using that method. This text presents research results of the interuniversity attraction pole programme P7/12 initiated by the Belgian-state Federal Services for Scientific, Technical and Cultural Affairs.

Appendix A. Proof of relation (2.68)

Let us consider Lagrange functions $\hat{f}_i(x)$ based on classical orthogonal polynomials $p_n(x)$ over the interval (a, b) and regularized by x. Relation (3.25) for non-regularized Lagrange functions $f_i(x)$ provides after multiplication by x/x_i,

$$\langle \hat{f}_i | \hat{f}_j \rangle = \delta_{ij} + (-1)^{i-j} \frac{\sqrt{\sigma(x_i)\sigma(x_j)}}{d_{2N} x_i x_j}. \tag{A.1}$$

Hence vector $\boldsymbol{v}$ in (2.68) has components

$$v_i = (-1)^i \sqrt{\frac{\sigma(x_i)}{d_{2N}}} \frac{1}{x_i}. \tag{A.2}$$

Now let us consider the expansion (2.25) in Lagrange functions,

$$\psi(x) = \sum_{j=1}^{N} c_j \hat{f}_j(x). \tag{A.3}$$

It can be seen as a polynomial of degree $N-1$ multiplied by x and by the square root of the weight function $w(x)$. The function $x^{-1}\psi(x)$ is thus orthogonal to $p_{N+1}(x)\sqrt{w(x)}$,

$$\int_a^b x^{-1} \psi(x) p_{N+1}(x) \sqrt{w(x)} dx = 0. \tag{A.4}$$

When this integral is approximated with the Gauss quadrature, one obtains

$$\sum_{j=1}^{N} \lambda_j x_j^{-1} \psi(x_j) p_{N+1}(x_j) \sqrt{w(x_j)} \approx 0. \tag{A.5}$$

Replacing $\psi(x_j)$ by its value calculated with (2.26) and using the value (3.23) of the Gauss weight λ_j, one obtains

$$\frac{k_N h_{N-1}}{k_{N-1}} \frac{1}{\sqrt{h_N d_{2N}}} \sum_{j=1}^{N} c_j \frac{\sqrt{\sigma(x_j)}}{x_j} \frac{p_{N+1}(x_j)}{|p_{N-1}(x_j)|} \approx 0. \tag{A.6}$$

The recurrence relation (3.3) then leads with (A.2) to

$$\sum_{j=1}^{N}(-1)^j c_j \frac{\sqrt{\sigma(x_j)}}{\sqrt{d_{2N}}\,x_j} = \sum_{j=1}^{N} c_j v_j \approx 0 \tag{A.7}$$

where various factors independent of j have been dropped. This is nothing but the property (2.68).

Other similar, but maybe more complicated, relations can be derived by modifying the power of x and/or the degree of the polynomial in Eq. (A.4). For example, one also has

$$\sum_{j=1}^{N}(-1)^j c_j \sigma(x_j) = \sum_{j=1}^{N} c_j x_j v_j \approx 0. \tag{A.8}$$

Appendix B. Summation formulas

In this appendix, several summation formulas employed in Section 3.7 are provided [32]. The geometric progression

$$\sum_{k=1}^{N}\exp[i(ka+b)] = \exp[i(a+b)]\frac{1-\exp iNa}{1-\exp ia} \tag{B.1}$$

is easily summed. Its real and imaginary parts provide respectively

$$\sum_{k=1}^{N}\cos(ka+b) = \cos\left(\frac{N+1}{2}a+b\right)\frac{\sin\frac{N}{2}a}{\sin\frac{1}{2}a} \tag{B.2}$$

and

$$\sum_{k=1}^{N}\sin(ka+b) = \sin\left(\frac{N+1}{2}a+b\right)\frac{\sin\frac{N}{2}a}{\sin\frac{1}{2}a}. \tag{B.3}$$

Appendix C. Polarizabilities

The polarizability is the response to a perturbation $r^\lambda Y_{\lambda\mu}(\Omega)$. In the non-relativistic case, the static polarizability of state nlm of a system described by a potential $V(r)$, where n is the radial quantum number or the principal quantum number in the hydrogen case, are given by [123]

$$\alpha_{\lambda\mu}^{(nlm)} = (2l+1)\sum_{l'}\begin{pmatrix} l' & \lambda & l \\ -m-\mu & \mu & m\end{pmatrix}^2 \alpha_\lambda^{(nll')}. \tag{C.1}$$

The reduced polarizabilities read

$$\alpha_\lambda^{(nll')} = 2(2l'+1)\begin{pmatrix} l' & \lambda & l \\ 0 & 0 & 0\end{pmatrix}^2 \sum_{n'}\frac{[\int_0^\infty \psi_{n'l'}(r)r^\lambda\psi_{nl}(r)dr]^2}{E_{n'l'}-E_{nl}} \tag{C.2}$$

where E_{nl} and $\psi_{nl}(r)$ are the energy and wave function of the studied state, i.e. ψ_{nl} is an eigenfunction of (5.2) with energy E_{nl}. The energies $E_{n'l'}$ and wave functions $\psi_{n'l'}(r)$ of the virtual final states are also solutions of (5.2) but for orbital momentum l'. The sum over n' should be understood as representing a sum over discrete states and an integral over the continuum. States degenerate with the initial state are excluded from the sum. The average or scalar polarizabilities are defined by

$$\alpha_\lambda^{(nl)} = \frac{1}{2l+1}\sum_{m=-l}^{l}\alpha_{\lambda\mu}^{(nlm)} = \frac{1}{2\lambda+1}{\sum_{l'=|l-\lambda|}^{l+\lambda}}' \alpha_\lambda^{(nll')} \tag{C.3}$$

where the prime means that the sum runs by steps of two and contains in general $\lambda+1$ terms.

A variant without the sum in Eq. (C.2) is obtained by using the summation technique of Dalgarno and Lewis [124]. An inhomogeneous Schrödinger equation is first solved,

$$(H_{l'}-E_{nl})\,\psi_{nll'}^{(1)}(r) = r^\lambda\psi_{nl}(r) \tag{C.4}$$

where $H_{l'}$ is defined by (5.2) with l replaced by l'. The reduced polarizabilities then read [123]

$$\alpha_\lambda^{(nll')} = 2(2l'+1)\begin{pmatrix} l' & \lambda & l \\ 0 & 0 & 0\end{pmatrix}^2 \int_0^\infty \psi_{nll'}^{(1)}(r)r^\lambda\psi_{nl}(r)dr. \tag{C.5}$$

A generalization to three-body systems described in perimetric coordinates is presented in Ref. [188].

The respective merits of (C.2) and (C.5) are different. The comparison is particularly interesting in the hydrogen case. Eq. (C.5) leads to simpler analytical calculations. The elimination of degenerate states is much easier with (C.2). Numerically, for an arbitrary potential $V(r)$, Eq. (C.2) is more convenient. In this case, the sum over n' is usually replaced by a finite sum over pseudostates, i.e. approximate solutions at negative and positive energies obtained with a square-integrable basis. When the matrix representing the l.h.s. of (C.4) in the LMM is inverted by using a spectral decomposition, the numerical code is then identical to a code based on (C.2). In hydrogenic cases with the LMM, Eq. (C.4) shows that the choice $h = n/2$ is optimal since it leads to exact results for $N > n + \lambda$. Hence Eq. (C.2) with its sum truncated in the same way also leads to exact results in that case.

Eq. (C.2) requires a diagonalization of the matrix corresponding to the final orbital momentum l' while Eq. (C.5) requires the resolution of an algebraic system, or the inversion of a matrix. Hence, for the large basis sets encountered in more complicated problems, generalizations of Eq. (C.5) are simpler to use than generalizations of Eq. (C.2) [188].

In the relativistic case, for a system described with the Dirac Hamiltonian H_D [Eq. (5.70)] with potential $V(r)$, these equations become [125]

$$\alpha_{\lambda\mu}^{(n\kappa m)} = (2j+1)\sum_{\kappa'}\begin{pmatrix} j' & \lambda & j \\ -m-\mu & \mu & m\end{pmatrix}^2 \alpha_\lambda^{(n\kappa\kappa')}. \tag{C.6}$$

The reduced polarizabilities read

$$\alpha_\lambda^{(n\kappa\kappa')} = 2(2j'+1)\begin{pmatrix} j' & \lambda & j \\ -1/2 & 0 & 1/2\end{pmatrix}^2 \sum_{n'} \frac{\{\int_0^\infty [P_{n'\kappa'}(r)P_{n\kappa}(r) + Q_{n'\kappa'}(r)Q_{n\kappa}(r)]r^\lambda dr\}^2}{E_{n'\kappa'} - E_{n\kappa}} \tag{C.7}$$

where $P_{n\kappa}(r)$ and $Q_{n\kappa}(r)$ are solutions of (5.73) with energy $E_{n\kappa}$. Here the sum over n' also involves the negative-energy continuum. The average or scalar polarizabilities are defined by

$$\alpha_\lambda^{(nl)} = \frac{1}{2j+1}\sum_{m=-j}^{j}\alpha_{\lambda\mu}^{(n\kappa m)} = \frac{1}{2\lambda+1}\sum_{\kappa'}\alpha_\lambda^{(n\kappa\kappa')}. \tag{C.8}$$

The inhomogeneous equation corresponding to (C.4) reads

$$(H_{\kappa'} - E_{n\kappa})\begin{pmatrix} P_{n\kappa\kappa'}^{(1)}(r) \\ Q_{n\kappa\kappa'}^{(1)}(r)\end{pmatrix} = r^\lambda \begin{pmatrix} P_{n\kappa}(r) \\ Q_{n\kappa}(r)\end{pmatrix} \tag{C.9}$$

where $H_{\kappa'}$ is defined in (5.73) with κ' replacing κ. The reduced polarizabilities are given by

$$\alpha_\lambda^{(n\kappa\kappa')} = 2(2j'+1)\begin{pmatrix} j' & \lambda & j \\ -1/2 & 0 & 1/2\end{pmatrix}^2 \int_0^\infty [P_{n\kappa\kappa'}^{(1)}(r)P_{n\kappa}(r) + Q_{n\kappa\kappa'}^{(1)}(r)Q_{n\kappa}(r)]r^\lambda dr. \tag{C.10}$$

Contrary to the non-relativistic case, the polarizabilities of the hydrogenic atoms are not always given exactly by the LMM. They are exact for $|\kappa'| = |\kappa|$ but not for $|\kappa'| \neq |\kappa|$ where Eq. (C.9) does not have simple solutions [125].

Appendix D. Dirac hydrogenic atom with two mesh points

The LMM provides exact solutions of the Coulomb–Dirac problem (Section 5.9) as illustrated here analytically with the simplest case. For $N = 2$, the Laguerre zeros given by (3.50) and (5.87) are

$$x_{1,2} = 2\gamma \mp \sqrt{2\gamma} \tag{D.1}$$

where γ is defined in Eq. (5.82). With (5.76)–(5.78), (3.72), (5.80) and $\kappa = -1$, the 4×4 Hamiltonian matrix reads with (5.88) ($h = 1/2Z$),

$$\boldsymbol{H}_{-1} = \begin{pmatrix} -\frac{2Z^2}{x_1} & 0 & -\frac{Z}{\alpha x_1} & -\frac{2Z}{\alpha}\sqrt{\frac{x_2}{x_1}}\frac{1}{x_2-x_1} \\ 0 & -\frac{2Z^2}{x_2} & -\frac{2Z}{\alpha}\sqrt{\frac{x_1}{x_2}}\frac{1}{x_1-x_2} & -\frac{Z}{\alpha x_2} \\ -\frac{Z}{\alpha x_1} & -\frac{2Z}{\alpha}\sqrt{\frac{x_1}{x_2}}\frac{1}{x_1-x_2} & -\frac{2Z^2}{x_1}-\frac{2}{\alpha^2} & 0 \\ -\frac{2Z}{\alpha}\sqrt{\frac{x_2}{x_1}}\frac{1}{x_2-x_1} & -\frac{Z}{\alpha x_2} & 0 & -\frac{2Z^2}{x_2}-\frac{2}{\alpha^2}\end{pmatrix}. \tag{D.2}$$

One of its eigenvalues

$$E_{1s1/2} = -\frac{Z^2}{\gamma+1} \tag{D.3}$$

is the exact energy for the Dirac ground state of the hydrogenic atom. The corresponding eigenvector is given by

$$(\boldsymbol{p}^T_{1s1/2}, \boldsymbol{q}^T_{1s1/2}) = -\frac{1}{2}\sqrt{\frac{\gamma+1}{2\gamma}}\left(\sqrt{x_1}, \sqrt{x_2}, -\frac{Z\alpha\sqrt{x_1}}{\gamma+1}, -\frac{Z\alpha\sqrt{x_2}}{\gamma+1}\right). \tag{D.4}$$

The Lagrange functions (3.70) associated with the mesh (D.1) read

$$\hat{f}^{(\alpha')}_{1,2}(x) = \mp[2\Gamma(2\gamma+1)(2\gamma \mp \sqrt{2\gamma})]^{-1/2}(x - 2\gamma \pm \sqrt{2\gamma})\, x^\gamma e^{-x/2}. \tag{D.5}$$

Hence the radial function of the large component is given by

$$\begin{aligned} P_{1s1/2}(r) &= -\frac{1}{2}\sqrt{\frac{\gamma+1}{2\gamma}}[\sqrt{x_1}\hat{f}^{(\alpha')}_1(2Zr) + \sqrt{x_2}\hat{f}^{(\alpha')}_2(2Zr)] \\ &= \sqrt{\frac{(\gamma+1)Z}{\Gamma(2\gamma+1)}}\,(2Zr)^\gamma e^{-Zr} \end{aligned} \tag{D.6}$$

and the radial function of the small component reads

$$Q_{1s1/2}(r) = -\frac{Z\alpha}{\gamma+1}P_{1s1/2}(r). \tag{D.7}$$

These components provide the exact Dirac spinor of the ground state. Notice that $\boldsymbol{p}_{1s1/2}$ and $\boldsymbol{q}_{1s1/2}$ are both orthogonal to vector $\boldsymbol{v}$ defined by Eq. (5.23). There is thus no difference in using the Gauss-quadrature expressions (3.72) or the exact expression (3.74) for the matrix elements of the first derivative (see Eq. (5.89) and its discussion).

The mean radius is exactly given by the Gauss-quadrature formula (5.91) as

$$\langle r\rangle = h\frac{x_1^2+x_2^2}{x_1+x_2} = Z^{-1}\left(\gamma+\frac{1}{2}\right). \tag{D.8}$$

This is also true for $\langle r^{-1}\rangle = 2/h(x_1+x_2) = Z/\gamma$ and $\langle r^{-2}\rangle = 1/h^2x_1x_2 = Z^2/\gamma(\gamma-\frac{1}{2})$.

Appendix E. System with separable imaginary part

The system of equations

$$(\boldsymbol{A} + i\alpha\boldsymbol{v}\boldsymbol{v}^T)\boldsymbol{x} = \boldsymbol{b}, \tag{E.1}$$

involving matrix $\boldsymbol{A}$, constant α and vectors $\boldsymbol{v}$ and $\boldsymbol{b}$, is solved with

$$\begin{aligned} \boldsymbol{x} &= (\boldsymbol{A} + i\alpha\boldsymbol{v}\boldsymbol{v}^T)^{-1}\boldsymbol{b} \\ &= \left(\boldsymbol{A}^{-1} - i\alpha\frac{\boldsymbol{A}^{-1}\boldsymbol{v}\boldsymbol{v}^T\boldsymbol{A}^{-1}}{1+i\alpha\boldsymbol{v}^T\boldsymbol{A}^{-1}\boldsymbol{v}}\right)\boldsymbol{b} \\ &= \boldsymbol{A}^{-1}\boldsymbol{b} - \frac{i\alpha(\boldsymbol{v}^T\boldsymbol{A}^{-1}\boldsymbol{b})}{1+i\alpha(\boldsymbol{v}^T\boldsymbol{A}^{-1}\boldsymbol{v})}\boldsymbol{A}^{-1}\boldsymbol{v}. \end{aligned} \tag{E.2}$$

If α, $\boldsymbol{A}$, $\boldsymbol{v}$ and $\boldsymbol{b}$ are real, the imaginary part of the solution is

$$\mathrm{Im}\,\boldsymbol{x} = -\frac{\alpha(\boldsymbol{v}^T\boldsymbol{A}^{-1}\boldsymbol{b})}{1+\alpha^2(\boldsymbol{v}^T\boldsymbol{A}^{-1}\boldsymbol{v})^2}\boldsymbol{A}^{-1}\boldsymbol{v}. \tag{E.3}$$

References

[1] J. Villadsen, M.L. Michelsen, Solution of Differential Equation Models by Polynomlal Approximation, Prentice-Hall, Englewood Cliffs NJ, 1978.
[2] C. Canuto, M.Y. Hussaini, A. Quarteroni, T.A. Zang, Spectral Methods in Fluid Dynamics, Springer, Berlin, 1988.
[3] J.P. Boyd, Chebyshev and Fourier Spectral Methods, Dover, New York, 2001.
[4] D. Baye, P.-H. Heenen, Generalised meshes for quantum mechanical problems, J. Phys. A 19 (1986) 2041.
[5] M. Vincke, L. Malegat, D. Baye, Regularization of singularities in Lagrange-mesh calculations, J. Phys. B 26 (1993) 811.
[6] D. Baye, Lagrange-mesh method for quantum-mechanical problems, Phys. Status Solidi b 243 (2006) 1095.
[7] D. Baye, M. Hesse, M. Vincke, The unexplained accuracy of the Lagrange-mesh method, Phys. Rev. E 65 (2002) 026701.
[8] M. Hesse, D. Baye, Lagrange-mesh calculations of three-body atoms and molecules, J. Phys. B 32 (1999) 5605.
[9] M. Vincke, D. Baye, Hydrogen molecular ion in an aligned strong magnetic field by the Lagrange-mesh method, J. Phys. B 39 (2006) 2605.
[10] D. Baye, J.-M. Sparenberg, Resolution of the Gross–Pitaevskii equation with the imaginary-time method on a Lagrange mesh, Phys. Rev. E 82 (2010) 056701.

[11] P. Descouvemont, C. Daniel, D. Baye, Three-body systems with Lagrange-mesh techniques in hyperspherical coordinates, Phys. Rev. C 67 (2003) 044309.
[12] P. Descouvemont, E.M. Tursunov, D. Baye, Three-body continuum states on a Lagrange mesh, Nuclear Phys. A 765 (2006) 370.
[13] T. Druet, D. Baye, P. Descouvemont, J.-M. Sparenberg, CDCC calculations with the Lagrange-mesh technique, Nuclear Phys. A 845 (2010) 88.
[14] P. Descouvemont, D. Baye, The *R*-matrix theory, Rep. Prog. Phys. 73 (2010) 036301.
[15] G. Szegö, Orthogonal Polynomials, Am. Math. Soc, Providence, RI, 1967.
[16] A. Nikiforov, V. Ouvarov, Eléments de la théorie des fonctions spéciales, MIR, Moscow, 1976.
[17] W. Yang, A.C. Peet, The collocation method for bound solutions of the Schrödinger equation, Chem. Phys. Lett. 153 (1988) 98.
[18] J.C. Light, I.P. Hamilton, J.V. Lill, Generalized discrete variable approximation in quantum mechanics, J. Chem. Phys. 82 (1985) 1400.
[19] J.C. Light, T. Carrington, Discrete-Variable Representations and their Utilization, in: Advances in Chemical Physics, Vol. 114, Wiley, Hoboken, NJ, 2007, p. 263.
[20] B. Shizgal, R. Blackmore, A discrete ordinate method of solution of linear boundary value and eigenvalue problems, J. Comput. Phys. 55 (1984) 313.
[21] B.D. Shizgal, H. Chen, The quadrature discretization method (QDM) in the solution of the Schrödinger equation with nonclassical basis functions, J. Chem. Phys. 104 (1996) 4137.
[22] M. Abramowitz, I.A. Stegun, Handbook of Mathematical Functions, Dover, New York, 1965.
[23] D. Baye, M. Vincke, Magnetized hydrogen atom on a Laguerre mesh, J. Phys. B 24 (1991) 3551.
[24] E.A. Hylleraas, B. Undheim, Numerische Berechnung der 2*S*-Terme von Ortho- und Par-Helium, Z. Phys. 65 (1930) 759.
[25] J.K.L. Macdonald, Successive approximations by the Rayleigh–Ritz variation method, Phys. Rev. 43 (1933) 830.
[26] C. Schwartz, High-accuracy approximation techniques for analytic functions, J. Math. Phys. 26 (1985) 411.
[27] C.C. Marston, G.G. Balint-Kurti, The Fourier grid Hamiltonian method for bound state eigenvalues and eigenfunctions, J. Chem. Phys. 91 (1989) 3571.
[28] M. Hesse, J. Roland, D. Baye, Solving the resonating-group equation on a Lagrange mesh, Nuclear Phys. A 709 (2002) 184.
[29] V. Szalay, T. Szidarovszky, G. Czak, A. Csszr, A paradox of grid-based representation techniques: Accurate eigenvalues from inaccurate matrix elements, J. Math. Chem. 50 (2012) 636.
[30] J. Dohet-Eraly, Private communication.
[31] R.G. Littlejohn, M. Cargo, T. Carrington, K.A. Mitchell, B. Poirier, A general framework for discrete variable representation basis sets, J. Chem. Phys. 116 (2002) 8691.
[32] D. Baye, Constant-step Lagrange meshes for central potentials, J. Phys. B 28 (1995) 4399.
[33] D.T. Colbert, W.H. Miller, A novel discrete variable representation for quantum mechanical reactive scattering via the *S*-matrix Kohn method, J. Chem. Phys. 96 (1992) 1982.
[34] V.S. Melezhik, Polarization of harmonics generated from a hydrogen atom in a strong laser field, Phys. Lett. A 230 (1997) 203.
[35] P. Capel, D. Baye, V.S. Melezhik, Time-dependent analysis of the breakup of halo nuclei, Phys. Rev. C 68 (2003) 014612.
[36] Y.-S. Choi, J. Javanainen, I. Koltracht, M. Kotrun, P.J. Mckenna, N. Savytska, A fast algorithm for the solution of the time-independent Gross–Pitaevskii equation, J. Comput. Phys. 190 (2003) 1.
[37] D. Baye, Nuclear calculations on Lagrange meshes, in: H. Horiuchi, et al. (Eds.), Innovative Computational Methods in Nuclear Many-body Problems Proceedings of the XVII RCNP International Symposium, Osaka, Japan, 1997, World Scientific, Singapore, 1998, p. 179.
[38] D. Dundas, Accurate and efficient non-adiabatic quantum molecular dynamics approach for laser-matter interactions, J. Phys. B 37 (2004) 2883.
[39] X. Chu, S.-I. Chu, Time-dependent density-functional theory for molecular processes in strong fields: Study of multiphoton processes and dynamical response of individual valence electrons of N_2 in intense laser fields, Phys. Rev. A 64 (2001) 063404.
[40] D. Baye, Integrals of Lagrange functions and sum rules, J. Phys. A 44 (2011) 395204.
[41] V. Szalay, Discrete variable representations of differential operators, J. Chem. Phys. 99 (1993) 1978.
[42] D. Baye, M. Hesse, J.M. Sparenberg, M. Vincke, Analysis of the *R*-matrix method on Lagrange meshes, J. Phys. B 31 (1998) 3439.
[43] M. Hesse, J.M. Sparenberg, F. Van Raemdonck, D. Baye, Coupled-channel *R*-matrix method on a Lagrange mesh, Nuclear Phys. A 640 (1998) 37.
[44] D. Baye, M. Vincke, M. Hesse, Simple and accurate calculations on a Lagrange mesh of the hydrogen atom in a magnetic field, J. Phys. B 41 (2008) 055005.
[45] D. Baye, M. Hesse, M. Vincke, Electromagnetic transitions of the hydrogen atom in a magnetic field by the Lagrange-mesh method, J. Phys. B 41 (2008) 185002.
[46] D. Baye, A. Joos de ter Beerst, J.-M. Sparenberg, Non-aligned hydrogen molecular ion in strong magnetic fields, J. Phys. B 42 (2009) 225102.
[47] H. Olivares-Pilón, D. Baye, A.V. Turbiner, J.C. López Vieyra, One-electron atomic-molecular ions containing lithium in a strong magnetic field, J. Phys. B 43 (2010) 065702.
[48] H. Olivares-Pilón, He_2^{+++} and HeH^{++} molecular ions in a strong magnetic field: The Lagrange-mesh approach, Phys. Lett. A 376 (2012) 1608.
[49] C. Bloch, Une formulation unifiée de la théorie des réactions nucléaires, Nuclear Phys. 4 (1957) 503.
[50] D. Baye, J. Goldbeter, J.-M. Sparenberg, Equivalence of the Siegert-pseudostate and Lagrange-mesh *R*-matrix methods, Phys. Rev. A 65 (2002) 052710.
[51] D. Baye, K.D. Sen, Confined hydrogen atom by the Lagrange-mesh method: Energies, mean radii, and dynamic polarizabilities, Phys. Rev. E 78 (2008) 026701.
[52] D. Baye, J. Dohet-Eraly, Confined helium on Lagrange meshes, in preparation.
[53] G.H. Golub, J.H. Welsch, Calculation of Gauss quadrature rules, Math. Comput. 23 (1969) 221.
[54] W. Gautschi, Algorithm 726: ORTHPOL-A package of routines for generating orthogonal polynomials and Gauss-type quadrature rules, ACM Trans. Math. Softw. 20 (1994) 21.
[55] B.I. Schneider, Accurate basis sets for the calculation of bound and continuum wave functions of the Schrödinger equation, Phys. Rev. A 55 (1997) 3417.
[56] H. Karabulut, E.L. Sibert III, Distributed Gaussian polynomials and associated Gaussian quadratures, J. Math. Phys. 38 (1997) 4815.
[57] D. Baye, M. Vincke, Lagrange meshes from nonclassical orthogonal polynomials, Phys. Rev. E 59 (1999) 7195.
[58] K. Varga, Z. Zhang, S.T. Pantelides, "Lagrange functions": A family of powerful basis sets for real-space order-*n* electronic structure calculations, Phys. Rev. Lett. 93 (2004) 176403.
[59] H. Karabulut, M. Kalay, Distributed Gaussian discrete variable representation, Int. J. Quant. Chem. 104 (2005) 16.
[60] R. Meyer, Trigonometric interpolation method for one-dimensional quantum-mechanical problems, J. Chem. Phys. 52 (1970) 2053.
[61] A.A. Mostofi, P.D. Haynes, C.-K. Skylaris, M.C. Payne, Preconditioned iterative minimization for linear-scaling electronic structure calculations, J. Chem. Phys. 119 (2003) 8842.
[62] G.W. Wei, Discrete singular convolution for the solution of the Fokker–Planck equation, J. Chem. Phys. 110 (1999) 8930.
[63] Y. Liu, D.A. Yarne, M.E. Tuckerman, Ab initio molecular dynamics calculations with simple, localized, orthonormal real-space basis sets, Phys. Rev. B 68 (2003) 125110.
[64] K. Varga, J.A. Driscoll, Computational Nanoscience: Applications for Molecules, Clusters, and Solids, Cambridge University Press, 2011.
[65] C. Schwartz, Numerical integration of analytic functions, J. Comput. Phys. 4 (1969) 19.
[66] J.T. Muckerman, Some useful discrete variable representations for problems in time-dependent and time-independent quantum mechanics, Chem. Phys. Lett. 173 (1990) 200.
[67] D. Baye, Lagrange bases for the Fourier, generalized Fourier and Riccati-Bessel grids, J. Phys. B 27 (1994) L187.
[68] P. Amore, M. Cervantes, F.M. Fernández, Variational collocation on finite intervals, J. Phys. A 40 (2007) 13047.
[69] R. Guardiola, J. Ros, On the numerical integration of the Schrödinger equation: Numerical tests, J. Comput. Phys. 45 (1982) 390.
[70] H. Karabulut, E.L. Sibert III, Trigonometric discrete variable representations, J. Phys. B 30 (1997) L513.
[71] E.G. Layton, The Fourier-grid formalism: Philosophy and application to scattering problems using *R*-matrix theory, J. Phys. B 26 (1993) 2501.
[72] E.G. Layton, E. Stade, Generalized Fourier-grid *R*-matrix theory; a discrete Fourier-Riccati-Bessel transform approach, J. Phys. B 26 (1993) L489.

[73] P. Amore, A variational sinc collocation method for strong-coupling problems, J. Phys. A 39 (2006) L349.
[74] F. Stenger, Numerical Methods based on Sinc and Analytic Functions, Springer, New York, 1993.
[75] M. Bollhöfer, Y. Notay, JADAMILU: a software code for computing selected eigenvalues of large sparse symmetric matrices, Comput. Phys. Commun. 177 (2007) 951.
[76] D.O. Harris, G.G. Engerholm, W.D. Gwinn, Calculation of matrix elements for one-dimensional quantum-mechanical problems and the application to anharmonic oscillators, J. Chem. Phys. 43 (1965) 1515.
[77] A.S. Dickinson, P.R. Certain, Calculation of matrix elements for one-dimensional quantum-mechanical problems, J. Chem. Phys. 49 (1968) 4209.
[78] D.E. Manolopoulos, R.E. Wyatt, Quantum scattering via the log derivative version of the Kohn variational principle, Chem. Phys. Lett. 152 (1988) 23.
[79] J.V. Lill, G.A. Parker, J.C. Light, Discrete variable representations and sudden models in quantum scattering theory, Chem. Phys. Lett. 89 (1982) 483.
[80] K. Sakimoto, Excitation and ionization in $\bar{p}$ + H collisions calculated by direct numerical solution using Laguerre meshes, J. Phys. B 33 (2000) 5165.
[81] K. Sakimoto, Protonium formation in collinear collisions between antiprotons and hydrogen molecular ions: Quantum-classical hybrid method versus adiabatic approximation, Phys. Rev. A 69 (2004) 042710.
[82] V.S. Melezhik, Three-dimensional hydrogen atom in crossed magnetic and electric fields, Phys. Rev. A 48 (1993) 4528.
[83] M.J. Rayson, Lagrange-Lobatto interpolating polynomials in the discrete variable representation, Phys. Rev. E 76 (2007) 026704.
[84] V. Szalay, G. Czak, A. Nagy, T. Furtenbacher, A.G. Csszr, On one-dimensional discrete variable representations with general basis functions, J. Chem. Phys. 119 (2003) 10512.
[85] L. Tao, C.W. McCurdy, T.N. Rescigno, Grid-based methods for diatomic quantum scattering problems: A finite-element discrete-variable representation in prolate spheroidal coordinates, Phys. Rev. A 79 (2009) 012719.
[86] D. Lemoine, The discrete Bessel transform algorithm, J. Chem. Phys. 101 (1994) 3936.
[87] R.G. Littlejohn, M. Cargo, Bessel discrete variable representation bases, J. Chem. Phys. 117 (2002) 27.
[88] D. Lemoine, A note on orthogonal discrete Bessel representations, J. Chem. Phys. 118 (2003) 6697.
[89] K.M. Dunseath, J.-M. Launay, M. Terao-Dunseath, L. Mouret, Schwartz interpolation for problems involving the Coulomb potential, J. Phys. B 35 (2002) 3539.
[90] L.-Y. Peng, A.F. Starace, Application of Coulomb wave function discrete variable representation to atomic systems in strong laser fields, J. Chem. Phys. 125 (2006) 154311.
[91] S.-L. Zeng, S.-Y. Zou, J. Yan, Generalized pseudospectral method for solving the time-dependent Schrödinger equation involving the Coulomb potential, Chinese Phys. Lett. 26 (2009) 053202.
[92] V. Szalay, The generalized discrete variable representation. An optimal design, J. Chem. Phys. 105 (1996) 6940.
[93] B. Shizgal, Eigenvalues of the Lorentz Fokker–Planck equation, J. Chem. Phys. 70 (1979) 1948.
[94] B. Shizgal, A Gaussian quadrature procedure for use in the solution of the Boltzmann equation and related problems, J. Comput. Phys. 41 (1981) 309.
[95] R. Blackmore, B. Shizgal, Discrete-ordinate method of solution of Fokker–Planck equations with nonlinear coefficients, Phys. Rev. A 31 (1985) 1855.
[96] H. Chen, B.D. Shizgal, A spectral solution of the Sturm–Liouville equation: comparison of classical and nonclassical basis sets, J. Comput. Appl. Math. 136 (2001) 17.
[97] H. Chen, B.D. Shizgal, The quadrature discretization method (QDM) in the solution of the Schrödinger equation, J. Math. Chem. 24 (1998) 321.
[98] J. Lo, B. Shizgal, Pseudospectral methods of solution of the Schrödinger equation, J. Math. Chem. 44 (2008) 787.
[99] J.Q.W. Lo, B.D. Shizgal, An efficient mapped pseudospectral method for weakly bound states: vibrational states of He_2, Ne_2, Ar_2 and Cs_2, J. Phys. B 41 (2008) 185103.
[100] B.D. Shizgal, The quadrature discretization method (QDM) in the calculation of the rotational-vibrational transitions in rare gas dimers, J. Mol. Struct.: Theochem 391 (1997) 131.
[101] J. Lo, B.D. Shizgal, Spectral convergence of the quadrature discretization method in the solution of the Schrödinger and Fokker–Planck equations: Comparison with sinc methods, J. Chem. Phys. 125 (2006) 194108.
[102] G.W. Wei, Solving quantum eigenvalue problems by discrete singular convolution, J. Phys. B 33 (2000) 343.
[103] D. Kosloff, R. Kosloff, A Fourier method solution for the time dependent Schrödinger equation as a tool in molecular dynamics, J. Comput. Phys. 52 (1983) 35.
[104] C. Semay, Fourier grid Hamiltonian method and Lagrange-mesh calculations, Phys. Rev. E 62 (2000) 8777.
[105] E. Fattal, R. Baer, R. Kosloff, Phase space approach for optimizing grid representations: The mapped Fourier method, Phys. Rev. E 53 (1996) 1217.
[106] R. Littlejohn, M. Cargo, Multidimensional discrete variable representation bases: Sinc functions and group theory, J. Chem. Phys. 116 (2002) 7350.
[107] F. Calogero, Matrices, differential operators, and polynomials, J. Math. Phys. 22 (1981) 919.
[108] M. Godefroid, J. Liévin, P.H. Heenen, Laguerre meshes in atomic structure calculations, J. Phys. B 22 (1989) 3119.
[109] L. Malegat, M. Vincke, Regularized Lagrange-mesh calculations and electron correlation in the ground states of helium-like atoms, J. Phys. B 27 (1994) 645.
[110] M. Plummer, C.J. Noble, Multichannel atomic scattering calculations using Lagrange mesh bases and the R-matrix method, J. Phys. B 32 (1999) L345.
[111] L. Fernández-Menchero, H.P. Summers, Stark effect in neutral hydrogen by direct integration of the Hamiltonian in parabolic coordinates, Phys. Rev. A 88 (2013) 022509.
[112] F. Calogero, On the zeros of Hermite polynomials, Lett. Nuovo Cim. 20 (1977) 489.
[113] P.M. Morse, H. Feshbach, Methods of Theoretical Physics, Part II, McGraw-Hill, New York, 1953.
[114] S. Flügge, Practical Quantum Mechanics I, Springer, Berlin, 1971.
[115] D. Lemoine, Optimized grid representations in curvilinear coordinates: The mapped sine Fourier method, Chem. Phys. Lett. 320 (2000) 492.
[116] J.P. Boyd, C. Rangan, P. Bucksbaum, Pseudospectral methods on a semi-infinite interval with application to the hydrogen atom: a comparison of the mapped Fourier-sine method with Laguerre series and rational Chebyshev expansions, J. Comput. Phys. 188 (2003) 56.
[117] B.I. Schneider, N. Nygaard, Discrete variable representation for singular Hamiltonians, Phys. Rev. E 70 (2004) 056706.
[118] A.A. Krylovetsky, N.L. Manakov, S.I. Marmo, Quadratic Stark effect and dipole dynamic polarizabilities of hydrogen-like levels, Laser Physics 7 (1997) 781.
[119] A.A. Krylovetsky, N.L. Manakov, S.I. Marmo, Comment on analytical calculations of two-photon transition amplitudes for the hydrogen atom, J. Phys. B 38 (2005) 311.
[120] K. Mcdowell, Exact static dipole polarizabilities for the excited S states of the hydrogen atom, J. Chem. Phys. 65 (1976) 2518.
[121] M.I. Bhatti, K.D. Coleman, W.F. Perger, Static polarizabilities of hydrogen in the B-spline basis set, Phys. Rev. A 68 (2003) 044503.
[122] J. Mitroy, M.S. Safronova, C.W. Clark, Theory and applications of atomic and ionic polarizabilities, J. Phys. B 43 (2010) 202001.
[123] D. Baye, Exact nonrelativistic polarizabilities of the hydrogen atom with the Lagrange-mesh method, Phys. Rev. A 86 (2012) 062514.
[124] A. Dalgarno, J.T. Lewis, The exact calculation of long-range forces between atoms by perturbation theory, Proc. Roy. Soc. London Ser. A 233 (1955) 70.
[125] L. Filippin, M. Godefroid, D. Baye, Relativistic polarizabilities with the Lagrange-mesh method, Phys. Rev. A 90 (2014) 052520.
[126] R.A. Buckingham, The quantum theory of atomic polarization I — Polarization by a uniform field, Proc. Roy. Soc. London Ser. A 160 (1937) 94.
[127] N. Aquino, G. Campoy, H.E. Montgomery, Highly accurate solutions for the confined hydrogen atom, Int. J. Quantum Chem. 107 (2007) 1548.
[128] S. Cohen, S.I. Themelis, Numerical solution of Dalgarno-Lewis equations by a mapped Fourier grid method, J. Chem. Phys. 124 (2006) 134106.
[129] S. Cohen, S.I. Themelis, K.D. Sen, Dynamic dipole polarizabilities of the ground and excited states of confined hydrogen atom computed by means of a mapped Fourier grid method, Int. J. Quantum Chem. 108 (2008) 351.
[130] Y.P. Kravchenko, M.A. Liberman, B. Johansson, Exact solution for a hydrogen atom in a magnetic field of arbitrary strength, Phys. Rev. A 54 (1996) 287.
[131] Y.P. Kravchenko, M.A. Liberman, B. Johansson, Highly accurate solution for a hydrogen atom in a uniform magnetic field, Phys. Rev. Lett. 77 (1996) 619.

[132] C. Stubbins, K. Das, Y. Shiferaw, Low-lying energy levels of the hydrogen atom in a strong magnetic field, J. Phys. B 37 (2004) 2201.
[133] L.B. Zhao, P.C. Stancil, Photoionization of hydrogen in white dwarf strength magnetic fields, Phys. Rev. A 74 (2006) 055401.
[134] H. Nakashima, H. Nakatsuji, Solving the Schrödinger and Dirac equations for a hydrogen atom in the universe's strongest magnetic fields with the free complement method, Astrophys. J. 725 (2010) 528.
[135] M. Vincke, D. Baye, Centre-of-mass effects on the hydrogen atom in a magnetic field, J Phys B 21 (1988) 2407.
[136] A.Y. Potekhin, A.V. Turbiner, Hydrogen atom in a magnetic field: The quadrupole moment, Phys. Rev. A 63 (2001) 065402.
[137] G. Lacroix, C. Semay, Lagrange-mesh calculations and Fourier transform, Phys. Rev. E 84 (2011) 036705.
[138] G. Lacroix, C. Semay, F. Buisseret, Lagrange-mesh calculations in momentum space, Phys. Rev. E 86 (2012) 026705.
[139] C. Semay, D. Baye, M. Hesse, B. Silvestre-Brac, Semirelativistic Lagrange mesh calculations, Phys. Rev. E 64 (2001) 016703.
[140] M. Moshinsky, A. Szczepaniak, The Dirac oscillator, J. Phys. A 22 (1989) L817.
[141] R. Szmytkowski, M. Gruchowski, Completeness of the Dirac oscillator eigenfunctions, J. Phys. A 34 (2001) 4991.
[142] F. Calogero, On the zeros of the classical polynomials., Lett. Nuovo Cim. 19 (1977) 505.
[143] F. Buisseret, C. Semay, Lagrange mesh, relativistic flux tube, and rotating string, Phys. Rev. E 71 (2005) 026705.
[144] F. Buisseret, C. Semay, Bound-state equivalent potentials with the Lagrange mesh method, Phys. Rev. E 75 (2007) 026705.
[145] D. Baye, L. Filippin, M. Godefroid, Accurate solution of the Dirac equation on Lagrange meshes, Phys. Rev. E 89 (2014) 043305.
[146] I.P. Grant, Relativistic Quantum Theory of Atoms and Molecules, Springer, New York, 2007.
[147] P.J. Mohr, B.N. Taylor, D.B. Newell, CODATA recommended values of the fundamental physical constants: 2010, Rev. Modern Phys. 84 (2012) 1527.
[148] V.M. Shabaev, Virial relations for the Dirac equation and their applications to calculations of hydrogen-like atoms, in Precision Physics of Simple Atomic Systems, in: Lecture Notes in Physics, vol. 627, Springer, Berlin, 2003, p. 97.
[149] V. Yakhontov, Relativistic linear response wave functions and dynamic scattering tensor for the $ns_{1/2}$ states in hydrogenlike atoms, Phys. Rev. Lett. 91 (2003) 093001.
[150] R. Szmytkowski, K. Mielewczyk, Gordon decomposition of the static dipole polarizability of the relativistic hydrogen-like atom: application of the Sturmian expansion of the first-order Dirac-Coulomb Green function, J. Phys. B 37 (2004) 3961.
[151] L.-Y. Tang, Y.-H. Zhang, X.-Z. Zhang, J. Jiang, J. Mitroy, Computational investigation of static multipole polarizabilities and sum rules for ground-state hydrogenlike ions, Phys. Rev. A 86 (2012) 012505.
[152] E.P. Wigner, L. Eisenbud, Higher angular momenta and long range interaction in resonance reactions, Phys. Rev. 72 (1947) 29.
[153] A.M. Lane, R.G. Thomas, *R*-matrix theory of nuclear reactions, Rev. Modern Phys. 30 (1958) 257.
[154] L. Malegat, Lagrange-mesh *R*-matrix calculations, J. Phys. B 27 (1994) L691.
[155] D. Baye, M. Hesse, R. Kamouni, Lagrange mesh calculation of the effective range expansion, Phys. Rev. C 63 (2000) 014605.
[156] S. Quaglioni, P. Navrátil, Ab initio many-body calculations of n-^{3}H, n-^{4}He, p-^{3,4}He, and n-^{10}Be scattering, Phys. Rev. Lett. 101 (2008) 092501.
[157] P. Navrátil, S. Quaglioni, Ab initio many-body calculations of the ^{3}H(d,n)^{4}He and ^{3}He(d,p)^{4}He fusion reactions, Phys. Rev. Lett. 108 (2012) 042503.
[158] K. Wildermuth, Y.C. Tang, A Unified Theory of the Nucleus, Vieweg, Braunschweig, 1977.
[159] Y. Yamaguchi, Two-nucleon problem when the potential is nonlocal but separable. I, Phys. Rev. 95 (1954) 1628.
[160] H. Masui, S. Aoyama, D. Baye, Jost function method on a Lagrange mesh, Prog. Theor. Exp. Phys. 2013 (2013) 123A02.
[161] O.I. Tolstikhin, V.N. Ostrovsky, H. Nakamura, Siegert pseudo-states as a universal tool: Resonances, *S* matrix, Green function, Phys. Rev. Lett. 79 (1997) 2026.
[162] O.I. Tolstikhin, V.N. Ostrovsky, H. Nakamura, Siegert pseudostate formulation of scattering theory: One-channel case, Phys. Rev. A 58 (1998) 2077.
[163] O.L. Ramírez Suárez, J.-M. Sparenberg, Precise determination of the effective-range parameters up to an arbitrary order, Phys. Rev. C 88 (2013) 014601.
[164] T. Druet, P. Descouvemont, Continuum effects in the scattering of exotic nuclei, Eur. Phys. J. A 48 (2012) 1.
[165] B. Buck, H. Friedrich, C. Wheatley, Local potential models for the scattering of complex nuclei, Nuclear Phys. A 275 (1977) 246.
[166] J.-M. Sparenberg, B.F. Samsonov, F. Foucart, D. Baye, Multichannel coupling with supersymmetric quantum mechanics and exactly-solvable model for the Feshbach resonance, J. Phys. A 39 (2006) L639.
[167] Y. Suzuki, D. Baye, A. Kievsky, Solving a coupled-channels scattering problem by adding confining potentials, Nuclear Phys. A 838 (2010) 20.
[168] J.C. Light, R.B. Walker, An *R* matrix approach to the solution of coupled equations for atom-molecule reactive scattering, J. Chem. Phys. 65 (1976) 4272.
[169] K. Sakimoto, Dissociative recombination of antiprotonic helium ions: $e + \bar{p}He^{2+} \to \bar{p} + He^+$, Phys. Rev. A 79 (2009) 042508.
[170] D. Baye, Breakup reaction models for exotic nuclei, Eur. Phys. J. Special Topics 156 (2008) 93.
[171] M. Pont, R. Shakeshaft, Theory of double photoionization of a two-electron atom: Circumventing the boundary conditions, Phys. Rev. A 51 (1995) 494.
[172] Y. Suzuki, W. Horiuchi, D. Baye, Green's function method for strength function in three-body continuum, Progr. Theoret. Phys. 123 (2010) 547.
[173] R. Suzuki, T. Myo, K. Katō, Level density in the complex scaling method, Progr. Theoret. Phys. 113 (2005) 1273.
[174] A. Csótó, B. Gyarmati, A.T. Kruppa, K.F. Pál, N. Moiseyev, Back-rotation of the wave function in the complex scaling method, Phys. Rev. A 41 (1990) 3469.
[175] Y. Ho, The method of complex coordinate rotation and its applications to atomic collision processes, Phys. Reports 99 (1983) 1.
[176] S. Aoyama, T. Myo, K. Katō, K. Ikeda, The complex scaling method for many-body resonances and its applications to three-body resonances, Progr. Theoret. Phys. 116 (2006) 1.
[177] C.Y. Lin, Y.K. Ho, Complex scaling in Lagrange-mesh calculations for Stark shifts and widths of the screened Coulomb potential, J. Phys. B 44 (2011) 175001.
[178] H. Suno, L. Andric, T.P. Grozdanov, R. McCarroll, Iterative calculations of photoionization cross sections by using the Lanczos algorithm and the complex coordinate method in the discrete variable representation, Phys. Lett. A 265 (2000) 377.
[179] M. Hesse, Three-body bound-state calculations by the Lagrange-mesh method: Selection of a coordinate system, Phys. Rev. E 65 (2002) 046703.
[180] A.S. Coolidge, H.M. James, On the convergence of the Hylleraas variational method, Phys. Rev. 51 (1937) 855.
[181] C.L. Pekeris, Ground state of two-electron atoms, Phys. Rev. 112 (1958) 1649.
[182] Z. Zhen, Effect of logarithmic terms on the energy level and wave function of a dtμ system, Phys. Rev. A 41 (1990) 87.
[183] E.M. Tursunov, D. Baye, P. Descouvemont, Comparative variational studies of 0^+ states in three-α models, Nuclear Phys. A 723 (2003) 365.
[184] L.M. Delves, Tertiary and general-order collisions, Nuclear Phys. A 9 (1959) 391.
[185] J. Raynal, J. Revai, Transformation coefficients in the hyperspherical approach to the three-body problem, Nuovo Cimento A 39 (1970) 612.
[186] M. Hesse, D. Baye, Lagrange-mesh calculations of the ground-state rotational bands of the H_2^+ and D_2^+ molecular ions, J. Phys. B 36 (2003) 139.
[187] M. Hesse, D. Baye, Lagrange-mesh calculations of excited states of three-body atoms and molecules, J. Phys. B 34 (2001) 1425.
[188] H. Olivares-Pilón, D. Baye, Static and dynamic polarizabilities of the hydrogen molecular ion, J. Phys. B 45 (2012) 235101.
[189] B. Grémaud, D. Delande, N. Billy, Highly accurate calculation of the energy levels of the H_2^+ molecular ion, J. Phys. B 31 (1998) 383.
[190] B.I. Schneider, L.A. Collins, S.X. Hu, Parallel solver for the time-dependent linear and nonlinear Schrödinger equation, Phys. Rev. E 73 (2006) 036708.
[191] H. Nakashima, H. Nakatsuji, Solving the Schrödinger equation for helium atom and its isoelectronic ions with the free iterative complement interaction (ICI) method, J. Chem. Phys. 127 (2007) 224104.
[192] A.M. Frolov, Two-stage strategy for high-precision variational calculations, Phys. Rev. A 57 (1998) 2436.
[193] C. Laughlin, S.-I. Chu, A highly accurate study of a helium atom under pressure, J. Phys. A 42 (2009) 265004.
[194] S. Kar, Y.K. Ho, Bound states of helium atom in dense plasmas, Int. J. Quant Chem. 106 (2006) 814.
[195] L.U. Ancarani, K.V. Rodriguez, Correlated expansions of n^1S and n^3S states for two-electron atoms in exponential cosine screened potentials, Phys. Rev. A 89 (2014) 012507.

[196] D. Wintgen, D. Delande, Double photoexcitation of $1P_0$ states in helium, J. Phys. B 26 (1993) L399.
[197] L. Hilico, N. Billy, B. Grémaud, D. Delande, Ab initio calculation of the $J = 0$ and $J = 1$ states of the H_2^+, D_2^+ and HD^+ molecular ions, Eur. Phys. J. D 12 (2000) 449.
[198] M. Hesse, D. Baye, Helium atoms in a strong magnetic field studied with the Lagrange-mesh method, J. Phys. B 37 (2004) 3937.
[199] H. Olivares-Pilón, D. Baye, Dipole transitions in the bound rotational-vibrational spectrum of the heteronuclear molecular ion HD^+, Phys. Rev. A 88 (2013) 032502.
[200] H. Olivares-Pilón, Quadrupole transitions in the bound rotational-vibrational spectrum of the deuterium molecular ion, J. Phys. B 46 (2013) 245101.
[201] R.E. Moss, Calculations for the vibration-rotation levels of H_2^+ in its ground and first excited electronic states, Mol. Phys. 80 (1993) 1541.
[202] Y. Hijikata, H. Nakashima, H. Nakatsuji, Solving non-Born-Oppenheimer Schrödinger equation for hydrogen molecular ion and its isotopomers using the free complement method, J. Chem. Phys. 130 (2009) 024102.
[203] H. Li, J. Wu, B.-L. Zhou, J.-M. Zhu, Z.-C. Yan, Calculations of energies of the hydrogen molecular ion, Phys. Rev. A 75 (2007) 012504.
[204] Z.-C. Yan, J.-Y. Zhang, Energies of the hydrogen molecular ions in high-angular-momentum states, J. Phys. B 37 (2004) 1055.
[205] H. Olivares-Pilón, D. Baye, Quadrupole transitions in the bound rotational-vibrational spectrum of the hydrogen molecular ion, J. Phys. B 45 (2012) 065101.
[206] Z.-C. Yan, J.-Y. Zhang, Y. Li, Energies and polarizabilities of the hydrogen molecular ions, Phys. Rev. A 67 (2003) 062504.
[207] T. Yamazaki, N. Morita, R.S. Hayano, E. Widmann, J. Eades, Antiprotonic helium, Phys. Reports 366 (2002) 183.
[208] Y. Kino, H. Kudo, M. Kamimura, High-precision Coulomb three-body calculation of antiprotonic helium atoms, Modern Phys. Lett. A 18 (2003) 388.
[209] Y. Kino, M. Kamimura, H. Kudo, Numerical accuracy of the energy levels of antiprotonic helium atoms, Nuclear Instrum. Methods Phys. B 214 (2004) 84.
[210] M. Hesse, D. Baye, The antiprotonic helium atom by the Lagrange-mesh method, in: N. Kalantar-Nayestakani, R.G.E. Timmermans, B.L.G. Bakker (Eds.), Few-Body Problems in Physics, in: AIP Conference Proceedings, vol. 768, American Institute of Physics, 2005, p. 328.
[211] F.T. Smith, Generalized angular momentum in many-body collisions, Phys. Rev. 120 (1960) 1058.
[212] E.C. Pinilla, P. Descouvemont, D. Baye, Three-body breakup of ^{11}Li with the eikonal method, Phys. Rev. C 85 (2012) 054610.
[213] E. Nielsen, D.V. Fedorov, A.S. Jensen, The structure of the atomic helium trimers: halos and Efimov states, J. Phys. B 31 (1998) 4085.
[214] M. Gattobigio, A. Kievsky, M. Viviani, Spectra of helium clusters with up to six atoms using soft-core potentials, Phys. Rev. A 84 (2011) 052503.
[215] M. Zhukov, B. Danilin, D. Fedorov, J. Bang, I. Thompson, J. Vaagen, Bound state properties of Borromean halo nuclei: ^{6}He and ^{11}Li, Phys. Reports 231 (1993) 151.
[216] D. Baye, M. Kruglanski, M. Vincke, Lagrange-mesh calculation of a three-body model for ^{6}He, Nuclear Phys. A 573 (1994) 431.
[217] A. Adahchour, D. Baye, P. Descouvemont, ^{14}Be in a Lagrange-mesh calculation, Phys. Lett. B 356 (1995) 445.
[218] D. Baye, Lagrange-mesh calculations of halo nuclei, Nuclear Phys. A 627 (1997) 305.
[219] Y. Suzuki, The ground-state structure and the soft dipole mode of the ^{6}He nucleus, Nuclear Phys. A 528 (1991) 395.
[220] V.M. Krasnopol'skii, V.I. Kukulin, Exclusion of occupied states from the nuclear optical amplitudes and potentials, Sov. J. Nuclear Phys. 20 (1975) 470.
[221] D. Baye, Supersymmetry between deep and shallow nucleus–nucleus potentials, Phys. Rev. Lett. 58 (1987) 2738.
[222] Y.C. Tang, M. LeMere, D.R. Thompson, Resonating-group method for nuclear many-body problems, Phys. Reports 47 (1978) 167.
[223] H. Kanada, T. Kaneko, S. Nagata, M. Nomoto, Microscopic study of nucleon-^{4}He scattering and effective nuclear potentials, Progr. Theoret. Phys. 61 (1979) 1327.
[224] R. Yarmukhamedov, D. Baye, C. Leclercq-Willain, Asymptotics of three-body bound state radial wave functions of halo nuclei, Nuclear Phys. A 705 (2002) 335.
[225] M. Suzuki, Fractal decomposition of exponential operators with applications to many-body theories and Monte Carlo simulations, Phys. Lett. A 146 (1990) 319.
[226] M. Suzuki, General theory of fractal path integrals with applications to many-body theories and statistical physics, J. Math. Phys. 32 (1991) 400.
[227] I.P. Omelyan, I.M. Mryglod, R. Folk, Construction of high-order force-gradient algorithms for integration of motion in classical and quantum systems, Phys. Rev. E 66 (2002) 026701.
[228] S.A. Chin, C.R. Chen, Gradient symplectic algorithms for solving the Schrödinger equation with time-dependent potentials, J. Chem. Phys. 117 (2002) 1409.
[229] D. Baye, G. Goldstein, P. Capel, Fourth-order factorization of the evolution operator for time-dependent potentials, Phys. Lett. A 317 (2003) 337.
[230] G. Goldstein, D. Baye, Sixth-order factorization of the evolution operator for time-dependent potentials, Phys. Rev. E 70 (2004) 056703.
[231] S.A. Chin, E. Krotscheck, Fourth-order algorithms for solving the imaginary-time Gross–Pitaevskii equation in a rotating anisotropic trap, Phys. Rev. E 72 (2005) 036705.
[232] K. Husimi, Miscellanea in elementary quantum mechanics, II, Progr. Theoret. Phys. 9 (1953) 381.
[233] E.H. Kerner, Note on the forced and damped oscillator in quantum mechanics, Can. J. Phys. 36 (1958) 371.
[234] F. Dalfovo, S. Giorgini, L.P. Pitaevskii, S. Stringari, Theory of Bose–Einstein condensation in trapped gases, Rev. Modern Phys. 71 (1999) 463.
[235] C.M. Dion, E. Cancès, Spectral method for the time-dependent Gross–Pitaevskii equation with a harmonic trap, Phys. Rev. E 67 (2003) 046706.
[236] P. Ring, P. Schuck, The Nuclear Many-Body Problem, Springer, New York, 1980.
[237] R.E. Peierls, J. Yoccoz, The collective model of nuclear motion, Proc. Phys. Soc. A 70 (1957) 381.
[238] D. Baye, P.-H. Heenen, Angular momentum projection on a mesh of cranked Hartree–Fock wave functions, Phys. Rev. C 29 (1984) 1056.